The removal of radionuclides from contaminated water samples using graphene oxide nano-flakes

Nicholas Robert Laver

A thesis submitted for the degree of

Doctor of Philosophy in Computational Chemistry

Department of Chemistry

University College London

September, 2018

I, Nicholas Robert Laver confirm that the work presented in this thesis is my own. Where information has been derived from other sources, I confirm that this has been indicated in the thesis.

Impact Statement

The advancement of industry from the latter part of the 20th century up to the current day, particularly in the areas of mining and nuclear power production has produced significant volumes of water contaminated with toxic and radioactive material[1]. The composition of which is heterogeneous and changing in different environments[2]. The majority of the waste produced from civil nuclear power production is currently stored in ponds, silos and tanks, many of which are approaching the end of their intended lifespan so require a remediation solution[3]. The transport of radionuclides and other heavy metals from such activities as uranium mining in contaminated groundwater and accumulation in soil can be a major pathway to human exposure[4], so also require a remediation solution.

Recent experimental research[1] into the use of graphene oxide (GO) as a sorption material for the removal of radionuclides and heavy metals from contaminated water has shown it to be very promising under laboratory conditions. GO can be produced using widely available chemicals and laboratory equipment[5], at low cost and in an environmentally friendly way[6,7]. Its production is also scalable.

The research in this thesis presents an investigation in computational chemistry to understand the binding interactions between radionuclides and the surface and edge of GO nano-flakes to assist in the development of GO based decommissioning solutions.

A model of GO is developed in density functional theory (DFT) based on the widely accepted Lerf-Klinowski[8] model of GO. An insensitivity to lateral size is identified for the stability of functional groups on the GO surface at high levels of oxidation, which has not been reported previously. The model of GO developed in this thesis could be useful for other similar studies.

The sorption of radionuclides to the surface and edge of GO is also investigated using DFT. A potential route towards radionuclide selectivity is identified in low pH environments. It is also established that highly oxidised GO is best for radionuclide removal and a study of non-idealised GO reveals that radionuclide sorption is largely insensitive to the presence of defects in the GO lattice.

The research presented in this thesis can be used to directly influence the design of new GO based decommissioning solutions in the nuclear industry. The study of non-idealised GO can also be used to influence the constraints on the production and reusability of GO, and the tolerance to defects, which can develop during synthesis and repeated sorption and desorption cycles. Beyond the direct applications presented in this thesis, the research could be used to influence the development of robust, affordable and environmentally friendly solutions to improve the water quality in developing countries and in countries immediately following natural disasters. The research presented in this thesis has applications both internal and external to the nuclear industry, domestically and internationally, and in both nuclear capable countries and those which require an accessible solution for removing heavy metal from drinking water.

Abstract

One of the main challenges currently facing the nuclear industry is the management, removal and disposal of radioactive material from aqueous environments. Water contaminated with nuclear material has arisen in a number of ways. The majority of nuclear material in aqueous environments is from normal nuclear activities and is currently stored in ponds, silos and tanks. Many of the waste storage facilities in the UK are however nearing the end of their intended lifetime so will shortly need processing. The contamination of water with nuclear material is also not confined directly to activities in a nuclear site, activities such as uranium mining can significantly increase the concentration of radionuclides and other heavy metals in groundwater. There are solutions within the nuclear industry to remediate contaminated water, there is also an ongoing need for more efficient and low-cost solutions.

Graphene oxide (GO) has been shown under laboratory conditions to be a highly effective sorbent material for the removal of cations from aqueous environments. The research presented in this thesis is a computational study to better understand the binding interactions between GO and cations to influence its development as a decommissioning solution in the nuclear industry.

The research begins in Chapter 3 where a model of GO is developed in density functional theory (DFT) and an insensitivity to the lateral size of the nano-flake for functional group stability on the surface at high level of oxidation is revealed, which had not been reported previously. It was also found from calculations that the formation of epoxy groups is unlikely at low levels of surface oxidation and functional groups tend to aggregate on GO surfaces, which is consistent with experimental observations.

The research then continues in Chapter 4 with an investigation into the binding interactions between GO and radionuclide cations. It is found, in agreement with experimental results that tetravalent cations mostly form inner-sphere complexes with GO and divalent cations mostly form outer-sphere complexes. A correlation between formal charge and binding energy is also revealed which is consistent with

experimental results. Th(IV) is found to have a low affinity towards the neutral COOH group which exists on GO edges in low pH environments, which is identified as a potential route towards radionuclide selectivity using chemically modified GO.

An investigation into the effect of defects in the GO lattice on sorption ability is presented in Chapter 5. It is found that defects have little to no effect on binding to the edge of the GO nano-flake and binding to the surface of defected GO is broadly similar to binding to the surface of defected-free GO. It is found however that the presence of a pore in the GO lattice can promote the hydrolysis of the Th(IV) aquocomplex which significantly increases the stability of the system. Binding to areas of the GO surface containing Stone-Wales defects is also enhanced by a greater density of functional groups.

The thesis then concludes in Chapter 6 with a summary of results and a discussion of the potential applications of GO in nuclear decommissioning.

Acknowledgements

I would firstly like to thank my supervisor Andy Kerridge for his continuous support, guidance and limitless patience throughout my research.

I would also like to thank the Nuclear Decommissioning Authority for providing funding for my research and everybody at National Nuclear Laboratory for support. I am particularly grateful to Jonathan Austin, my industrial supervisor for providing expertise.

I would like to thank also everybody in G19, especially Reece Beekmeyer, without whose football chat and occasional witty anecdotes to break up the days I am sure I would not have survived.

I would like to give special thanks to my parents, Doug and Karen, who despite serious illness have remained consistent in their support, belief and optimism for my studies, and without whom I would not be here.

I'd like also to give a big thanks to my sister, Kelly, just for being who she is.

I'd like to thank my new mother-in-law and grandmother-in-law, Mandy and Lynn, for welcoming me into both their home and their family, and supporting me whilst I finished writing up.

At last but no means least, I would especially like to thank my beautiful new wife Rachael, who has shown me unwavering love, support and patience over a turbulent couple of years. We got there in the end!

Contents

List of Tables

List of Figures

Chapter 1 Introduction

Historical and recent activities in nuclear industry have produced a significant volume of water contaminated with radioactive and toxic material. The composition of which is heterogeneous and can change in different environments. It contains both transuranic elements and nuclear fission products which can be both long- or short-lived, soluble, and very mobile[2] so difficult to contain. The remediation of contaminated groundwater and liquid waste effluent which arises from nuclear activities is one of the main technological challenges which currently faces the nuclear industry. The containment, management and eventual disposal of radioactive material present in water is very expensive and time consuming. The cost of nuclear decommissioning in the UK alone is forecast to be many tens of billions of pounds[9], with projected costs in the USA and Russia set to be even higher. The majority of the legacy waste from the infancy of the civil nuclear industry is currently stored in ponds, silos and tanks which are nearing the end of their intended lifetime and will need processing[3]. The creation of contaminated water is also not confined directly to power production and activities within nuclear sites. Activities such as mining yield significant volumes of so called naturally occurring radioactive materials (NORMs) and technologically enhanced naturally occurring radioactive materials (TENORMs), which can easily contaminate ground water. Due to the wide variety of contaminants, each of which posing a slightly different remediation challenge, and the variability of environments in which it exists, a versatile and robust remediation solution is sought.

There are many methods currently used for the removal of radioactive material from contaminated water. Some of the most commonly adopted methods are based on the use of activated carbon[10], bentonite clay[11], zerovalent iron[12], ion exchange techniques[13], and reverse osmosis and nanofiltration[14], other more novel techniques which have been proposed include, such things as, the uses of fungi[15], and hazelnut and almond shells[16] (which are discussed in further detail in Chapter 4). Many of the techniques currently used however are expensive or usefully only for the extraction of a limited number of ions, for example in the multi-nuclide removal equipment (ALPS) used at Fukushima a series of 7 different types of adsorbent material were used[17]. There is hence a need for more cost effective and versatile solutions for remediation of contaminated water.

There has been, over the last decade or so, an increased and continued interest in the use of emergent carbon materials for environmental applications. One which is receiving particular attention is graphene oxide (GO). GO has been shown under laboratory conditions to be a very promising absorbent for the removal of a wide range of radionuclides and heavy metals from aqueous environments[1], it can also be produced in large quantities at low cost and in an environmentally friendly way[6,7].

The aim of the research presented in this thesis is to better understand the underlying mechanisms governing the high adsorption capacity of GO for the removal of radionuclides and other heavy metals from aqueous environments. Chapter 2 gives an overview of the theoretical and computational methodology used throughout this thesis. A model for GO is developed in Chapter 3 using density functional theory (DFT), the binding interactions between radionuclides and the surface and edge of idealised defect-free GO are then studied and presented in Chapter 4. Chapter 5 then presents a study into the effect of defects on the adsorption of radionuclides by GO. A short summary of all of the research presented in this thesis is presented in Chapter 6 along with a discussion on outlook and potential future research.

1.1 Graphene Oxide (GO)

Graphene oxide (GO) is a 2-dimensional carbon material which was first synthesised over a century ago[18,19], its chemical and physical structure are still a point of debate and an active area of research. Many methods for structural characterisation require a sample to be in a bulk crystal form and produce unreliable results in the presence of water, GO is however of most interest when it is in solution. In solution it can be exfoliated under mild sonication to form sheets of one to a few atoms in thickness. Due to the oxygen containing functional groups, it is extremely hydrophilic, and disperses readily in water. The large surface area of GO and availability of reactive oxygen groups, make it a promising material for heavy metal extraction, which is discussed in Chapter 4. The need to be in solution however has led to challenges in characterising the structure of GO, hence it remains still a point of debate. The most widely accepted model for GO, the Lerf-Klinowski model is shown in Figure 1.

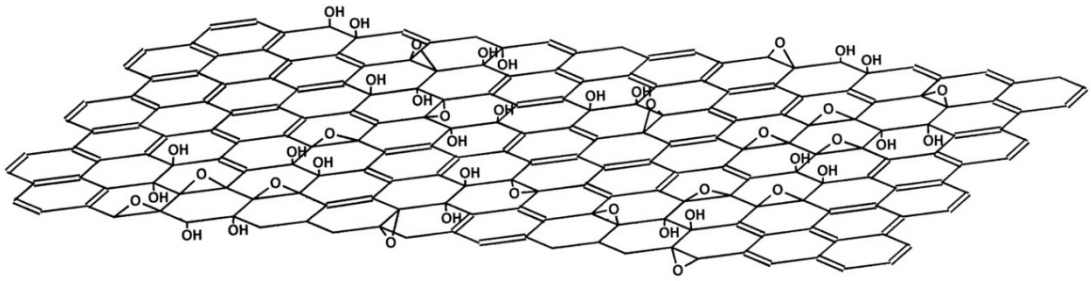

Figure 1: The Lerf-Klinowski structural model for GO [reproduced with permission from ref 20]

1.1.1 Methods of GO Production

GO can be produced by a number of different methods, each producing GO with a slightly different form. Synthesis of GO can be carried out using standard laboratory equipment and inexpensive chemicals which are widely available, its accessibility and wealth of possible uses have made it widely studied. The most commonly used chemical methods for producing GO are, the Brodie[19], Staudenmaier[18], and Hummers[21] methods, or some variation or modification of these methods. The three chemical methods each involve the oxidation of graphite flakes to varying degrees. The methods differ based on oxidising agents used and the exact procedure followed. The Brodie and Staudenmaier methods primarily use potassium chlorate ($KClO_3$) with nitric acid (HNO_3) for oxidation, whilst the Hummers method uses potassium permanganate ($KMnO_4$) with sulphuric acid (H_2SO_4). The Brodie method involves the addition of $KClO_3$ to a graphite suspension in fuming nitric acid. Staudenmaier later improved upon the Brodie method by adding the $KClO_3$ gradually in a series of small quantities rather than in a single addition. The Staudenmaier method produces GO with a similar oxygen content to the Brodie method but is much more suited to synthesis in a single vessel, it is however more time consuming and potentially more hazardous. The method developed by Hummer and Offeman replaced $KClO_3$ and HNO_3 with a concentrated mixture of H_2SO_4, $KMnO_4$, and sodium nitrate ($NaNO_3$). The resulting GO typically has a higher degree of surface oxidation than GO produced by the Brodie or Staudenmaier methods, and synthesis can typically be completed in less than 2 hours, making it much less time consuming than the other methods. Modifications are often made to each of the methods in order to control the nature and degree of

oxidation, and hence the final GO product. More recently Marcano *et. al.*[22] introduced another method for producing GO. The Marcano method follows a similar methodology to the Hummers method but uses phosphoric acid (H_3PO_4) rather than H_2SO_4 and an increased amount of $KMnO_4$ with the absence of $NaNO_3$. The Marcano method avoids the production of poisonous gases such as NO_2 and N_2O_4 which reduced the hazard in its production. The method also typically produces GO with a greater oxygen content to the other three methods, making it more suitable for some applications. A "bottom-up" methodology for GO production was also proposed Tang *et. al.*[7] in 2012. The bottom up method is a hydrothermal method which uses glucose as a sole reagent. Although not widely accepted as a preferred method for GO production, the bottom up method offers much greater control over lateral nano-flake size and thickness when compared to traditional methods, and the absence of strong oxidising agents makes it much safer and more environmentally friendly. In addition to a "bottom-up" method for synthesising GO, Tang *et. al.* also developed a method to reduce GO by thermal annealing and hence reduce the degree of oxidation without significantly degrading the GO structure, which is safer than the use of hydrazine and other strong chemicals, which are commonly used to control the oxygen content of GO. Since the degree and nature of oxidation of the surface and edges of GO can be controlled chemically, or thermally, and tailored towards specific purposes, GO can be considered as a collection of very similar materials with common characteristics, rather than having a single well-defined form. Extensive experimental, computational, and theoretical research has been carried out to identify and characterise the geometrical structure and common characteristics of GO, an outline and timeline of accepted GO structures follows.

1.1.2 Characterisation of the GO structure

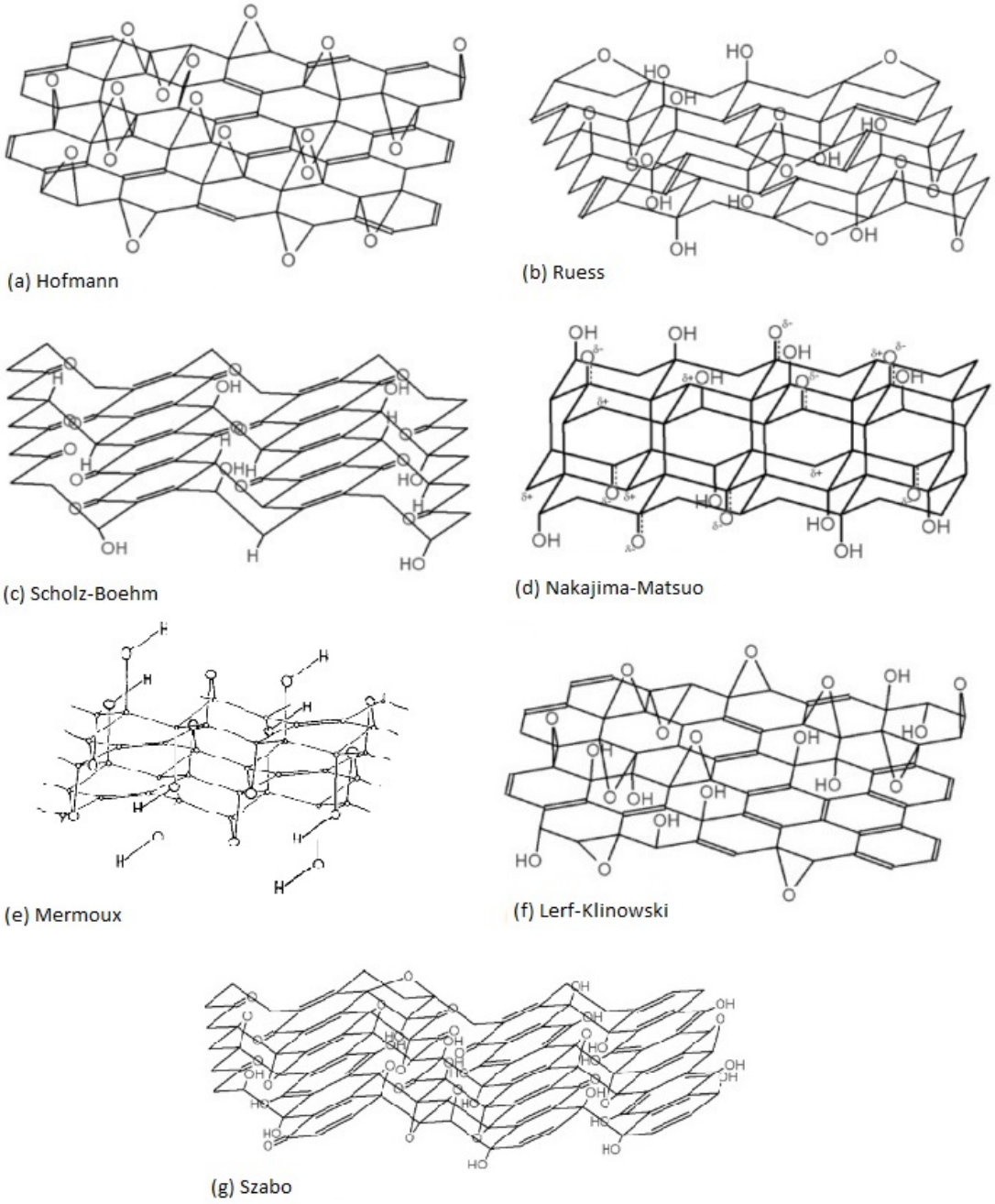

Figure 2: Historical proposed structural models of GO [reproduced with permission from ref 20 and 21]

The exact chemical structure of GO is still a point of debate. There are many reasons for this but the main contributing factors are the complexity of the material, particularly its irregular crystalline structure, considerable sample to sample variability due to both the method of synthesis, degree of oxidation, and condition of the starting graphite flakes, the non-stoichiometric atomic composition of GO which can be inhibitive to

many characterisation techniques, and a lack of precise techniques to characterise such materials or mixture of materials. The accepted structure for GO has evolved with the introduction of new and more precise characterisation techniques, today however there is still an ongoing debate around the structure of GO, a debate to which theoretical and computational studies are now beginning to contribute.

The history of GO extends back over 150 years, when it was first reported independently by Schafhaeutl[23] in 1840 and more famously by Brodie[19] in 1859. The early production of GO occurred serendipitously for both Schafhaeutl and Brodie whilst they were investigating the structure and chemical properties of graphite. Brodie noted that the resulting material which he had produced by the addition of potassium chlorate ($KClO_3$) to a graphite suspension in fuming nitric acid had a distorted crystalline structure, small size, limited thickness, dispersed readily in water but not acidic media, and contained hydrogen, oxygen and carbon. Whilst GO is known to have been synthesised as early as 1840 significant interest in determining its structure did not begin until the early 20th century.

One of the earliest models was proposed by Hofmann, Frenzel, and Csal in 1934[24] with later development by Hofmann and Konig in 1937[25] and further development into its final structural form by Hofmann and Holst in 1939[26]. Within the Hofmann model it is proposed that GO is a regular lattice structure consisting of repeating hexagonal carbon subunits, the model postulates that epoxy groups form across the basal plane with a net molecular formula C_2O, shown in Figure 2(a). The model was proposed based on ion exchange reactions, combustion analysis to determine chemical composition, and limited x-ray diffraction data. X-ray diffraction analysis of GO is problematic, due to its amorphous structure and hygroscopic nature. Combustion characterisation of a series of GOs by the Hofmann group using the half-micron method determined a C/O ratio of 2.5 to 33, based on this they proposed a theoretical limiting ratio of 2, and limiting net molecular formula C_2O. They stated that the limiting composition could not be realised due to safety concerns regarding the temperature and conditions required to synthesis GO with ultra-high oxygen content, which would not be advisable given the potential explosiveness of the strong oxidising agents used. X-ray analysis of their GO samples gave interference patterns almost identical to those from graphite, suggesting that the 6-membered ring structure is

maintained in GO. The model proposed by Hofmann *et. al.* determines a model for the basic physical shape of GO, however it does not account for the known hydrogen content.

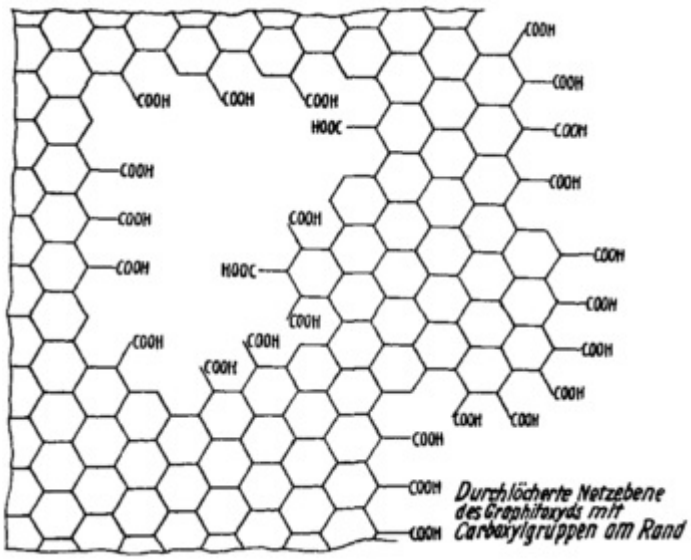

Figure 3: The proposed formation of carboxylic acid groups in GO pores [reproduced with permission from ref 25]

The Hofmann group also observed that GO turned litmus red when moistened, it was unclear to them whether this was due to an inherent acidic property of the chemistry of GO, or due to residual sulphuric acid from synthesis that would be difficult to remove completely from washing. They did however suggest the formation of carboxylic acid (COOH) groups along the flake edges and in pores formed by the liberation of carbon monoxide (CO) and carbon dioxide (CO_2) (Figure 3). They stated also that the formation of COOH groups on the surface was unlikely from a mechanistic point of view. Additionally, to the proposed formation of COOH groups, Hofmann *et. al.* later made reference in their 1939[26] paper to a model for GO proposed by Heinrich Thiele[27] around the same time. Thiele proposed a structural model for GO based on salt formation and base extraction experiments, along with known composition analysis and X-ray diffraction results available at the time. The Thiele model consists of an ordered hexagonal carbon lattice similar to that in the Hofmann model, which is functionalised with three hydroxyl groups on each ring to produce a limiting molecular formula $C_6(OH)_3$. Hofmann *et. al.* suggested that based on the work of Thiele, it was possible that epoxy and hydroxyl groups co-exist on the GO surface. Additionally, in the 1939 Hofmann *et. al.* paper they present results from methylation

experiments carried out on GO, from reactions with methyl alcohol and hydrogen chloride, which compound readily with carboxylic acid, and dimethyl sulphate, especially they noted that both –COOH and –OH groups are likely to exist. The combined work of Hofmann *et. al.*[24–26] and Thiele[27] in the 1930's predict a remarkably similar model to that of Lerf-Klinowski[8] (see Figure 1) which is the most accepted model today, albeit Hofmann and Thiele predicted the structure to be ordered, and have a limiting composition of between C_2O and $C_2(OH)$.

A new model was proposed by Ruess in 1946[28], the Ruess model accepts the existence of both the epoxy in the Hofmann model, and the hydroxyl groups proposed by Thiele. Unlike the models that preceded it however the model rejects the hexagonal sp^2 hybridised carbon lattice, and instead proposes an ordered sp^3 hybridised system in which a quarter of the cyclohexanes in the chair configuration contain epoxides in the 1,3 configuration and are hydroxylated in the 4 position, forming a lattice structure (shown in Figure 2(b)). The new model was proposed due to C-C bond lengths which they measured in GO to be 1.52 Å using a prism interference technique, which presumably had a large error, but was in close agreement with the C-C bond length of 1.54 Å[29] measured by Ruff and Brettscheider around the same time in tetracarbon monofluoride. Planar sp^2 hybridised C-C bond lengths like those in the Hofmann and Thiele models would be expected to be much closer to those measured in graphene (1.42 Å[30]). The structure proposed by Ruess of course does not allow for the range of compositions and C/O ratios reported for GO samples in the literature, he reasoned that this could be due to the content of OH and COOH being fictitious due to GO being highly hygroscopic and the complete drying of GO not being possible. Increased water content could lead to increased hydrogen content in combustion experiments, and misleading results.

Scholz and Boehm[31] proposed another structural model for GO in 1969, which consists of planar carbon layers with C=C bonds regularly cleaved, in which carbonyl and hydroxyl are the only functional groups (see Figure 2(c)). The Scholz-Boehm model was developed based on infrared (IR) spectroscopy and electron diffraction experiments, and the adsorption behaviour of a range of GO samples prepared by different methods. IR spectroscopy carried out with potassium bromide (KBr), which is a useful technique for identifying functional groups, showed no significant

difference in spectra between samples prepared by different methods, which suggested GO does not undergo configurational change at higher levels of oxidation, and has one single structure. Spectra obtained by Scholz and Boehm were also in good agreement with those found elsewhere in the literature at the time. They however gave a different interpretation for some of the absorption bands they observed. Bands which were present at 3400 cm^{-1} and 1620 cm^{-1} they assigned to molecular water between GO layers and KBr. A band at 1720 cm^{-1} which had been previously thought to be due to the presence of large amounts of COOH, they assigned instead to carbonyl groups. They found that in the presence of sodium salt the band at 1720 cm^{-1} disappears: since carboxylate (COO^-) ions are known to produce two bands in the ranges 1550 cm^{-1} – 1610 cm^{-1}, and 1300 cm^{-1} – 1400 cm^{-1}, in which ranges they found no significant change in the presence of sodium salt, they reasoned that the band should be reassigned to indicate the presence of carbonyl groups rather than COOH. Further proof for the existence of carbonyl groups, they suggested, came from an absorption band observed at 1620 cm^{-1}, as well as being a bending mode of water, this is an absorption frequency for carbonyl in quinone systems, which are hence included in their model. Due to the intensity of the band they reasoned that it was unlikely that it was solely from the deformation of water molecules. Following methylation with diazomethane they found that C-H valence oscillations occurred at 2875 cm^{-1}, 2925 cm^{-1}, and 1450 cm^{-1}, attributable to the formation of methyl groups, at the same time a band at 1380 cm^{-1}, which is generally accepted to be from deformation vibrations of C-OH, increased in intensity. Additional absorption bands at 1070 cm^{-1} which had previously been assigned to the stretching vibration of C-OH bonds[32] they say is uncertain, as is the assignment of bands at 970 cm^{-1} and 830 cm^{-1}. They suggested the latter absorption bands could be due to skeletal vibrations of the GO layers, or the three uncertain bands together could be indicative of the presence of tertiary alcohols, peroxide and hydroperoxide groups.

Nakajima *et. al.* presented another noteworthy structural model in 1988[33] with further revision of the structure in 1994[34]. The model proposed by Nakajima was based on characterisation following the fluorination of GO, and an attempt to reinterpret some of the then accepted physical features, such as six-fold (hexagonal) symmetry of the carbon lattice, the existence of carbonyl and hydroxyl groups, the presence of water absorbed between GO layer, and interlayer spacing of 6 to 11Å, which increases by

the absorption of water. Nakajima found that fluorinated GO under mild conditions gave an X-ray diffraction peak at almost exactly the same position as graphite fluoride $(C_2F)_n$, with a shoulder which corresponded to a similar peak in non-fluorinated GO, indicating unreacted GO. IR spectroscopy carried out on GO showed the presence of hydroxyl (1070 cm^{-1}), carbonyl (1720 cm^{-1}) and absorbed water (1600 cm^{-1} and 3200 cm^{-1}) consistent with previous studies. They found after fluorination of GO, however, that the hydroxyl peak disappeared and was replaced by a previously absent peak at 1120 cm^{-1}. The peak at 1120 cm^{-1} was interpreted to be the stretching vibration of peripheral CF_2, CF_3 or tertiary CF. They noted also that the (002) diffraction peak for $(C_2F)_n$ is around 10° 2θ(by Cu Kα)[35] (8.8 – 9.0 Å), fluorinated GO also gave a diffraction peak around 10°. If GO consists of single carbon layers, as in most structural models which have been proposed, then it would have been expected that fluorinated GO would give a diffraction peak much closer to that of $(CF)_n$, which gives a strong (002) peak at 14 to 15° 2θ(Cu Kα) (5.9 – 6.3 Å)[35]. Based on these results, Nakajima *et. al.* concluded that there was a very high likelihood that the basic GO structure is very similar to that of $(C_2F)_n$. $(C_2F)_n$ consists of a double carbon layer that is combined by C-C bonds orthonormal to the lattice in which fluorine atoms are bonded above and below the double carbon layers[36]. In the Nakajima GO model (Figure 2(d)) hydroxyl and carbonyl groups replace fluorine in the $(C_2F)_n$ structure to give a GO structure with two carbon layers which are sp^3 hybridised and linked together.

Intermediate to publication of the two Nakajima papers, Mermoux *et. al.*[37] proposed a new model based on GO characterised by FTIR and ^{13}C nuclear magnetic resonance (NMR) studies. ^{13}C NMR, unlike some of the characterisation techniques discussed above, is not sensitive to water content and as such is expected to be reliable for the characterisation of GO, in which complete drying is problematic. FTIR spectra obtained for well-dried GO prepared by the Brodie, Staudenmaier, and Hummer methods, it was found, can be characterised by a few medium and strong bands, the main features of which were found to be independent of method of preparation. When the dried GO was exposed to the atmosphere and moisture, changes were found to occur in the 3200 to 3600 cm^{-1} range and a new band appeared at 1620 cm^{-1}. Mermoux *et. al.* concluded from this that a previously ambiguous band at 3450 cm^{-1}, assigned by Nakajima and others to absorbed water, can be assigned to the presence of hydroxyl

groups with certainty. Further analysis of GO neutralised by sodium ethoxide in anhydrous ethanol allowed the identification of bands consistent with the presence of nonconjugated carboxylic-carbonyl groups, tertiary hydroxyl groups, and an apparent shift in C-O bond frequencies, indicating that they had acquired double bond character under neutralisation, which is not known to occur in purely aliphatic C-O_{OH} bonds. They stated the assignment of these frequencies with caution however, IR evidence alone is not justification enough to unequivocally assign bands, a band at 980 cm^{-1} for example, which can be characteristic of epoxy, ether, or peroxide groups would require further investigation. Using ^{13}C NMR analysis they found that spectra taken against tetramethylsilane (TMS) produce three lines at 62.2 ppm, 71.2 ppm, and 132 ppm, which they assigned to ether-oxygen, hydroxyl groups, and sp^2 hybridised carbon atoms, respectively. They found also that the same spectra was produced for GO which had been exposed to moisture, as well as GO produced by different methods, proving NMR to be a reliable analysis method for GO characterisation, which is independently of hydration, which had rendered the results from some other analytical methods questionable. The determination of C-O bonds using NMR did not show the presence of COOH groups which are widely accepted to exist along GO edges. The presence of COOH was however indicated by FTIR spectra produced for the same GO, suggesting that COOH is present in GO but in an abundance too low for NMR resolution, supporting previous models in which it exists only at GO flake edges and in defect pores. Moreover Mermoux highlights the absence of NMR spectral lines at 180 to 200 ppm which would be observed for keto groups, putting the model proposed by Scholz and Boehm, and Nakajima in to doubt, and the prominence of sp^2 hybridised carbon atoms puts both the Ruess and Nakajima models into further doubt, as both suggest sp^3 hybridised carbon atoms. The functional groups identified by FTIR and NMR studies by Mermoux, and the carbon environments they identified by NMR match most closely with the earliest proposed models by Thiele and the Hofmann group, and the most widely accepted model for GO proposed by Lerf and Klinowski, which is discussed below. Further NMR analysis carried out by Mermoux *et. al.* to test dipolar phasing characteristics showed that the hydroxyl and ether lines have approximately equal dipolar relaxation times, suggesting that the protons responsible for dipolar interactions are at equal distance from the carbon atoms bonded to both hydroxyl and ether groups, and hence the functional groups are ordered. Based on these results, Mermoux suggested a new model for GO in which hydroxyl and

ether-oxygen groups (in the 1,3 configuration) are regularly distributed on a puckered sp^2 hybridised carbon skeleton containing ethylenic bonds with an ideal composition $C_8O_2(OH)_2$ (see Figure 2(e)), which has a similar chair configuration as the Ruess model, differing in the prediction of sp^2 rather than sp^3 hybridised carbon skeleton, and employment of isolated carbon double bonds.

Currently the most widely accepted structural model for GO, and the one in which the GO model in this thesis is based upon, was proposed by Lerf *et. al.*[8,20,38] in 1998. The so called Lerf-Klinowski model is based predominately on the results of NMR investigations, as in the Mermoux model, and NMR characterisation of GO treated with a number of reagents which were specifically chosen to give further insight into the nature of some of the oxygen containing groups in GO. ^{1}H NMR carried out on GO prepared according to the Hummers method confirmed the presence of C-OH groups and H_2O. They found that the resonance associated with water was broad, indicating that water molecules trapped between GO layer are fairly immobile, presumably due to strong electrostatic interactions with GO surface functional groups. ^{13}C NMR spectra obtained by Lerf *et. al.* displayed the same features as those obtained by Mermoux (lines around 60, 70 and 130 ppm), which Mermoux had interpreted to indicate the presence of hydroxyl, 1,3-ether and C=C double bonds, on which they proposed their GO model. ^{13}C NMR spectra for GO which had been treated with potassium iodide (KI) by Lerf *et. al* however suggested that reconsideration of the physical features in the Mermoux model was needed, particularly the assignment of the line around 60 ppm to 1,3-ether. After 7 days of treatment with KI, Lerf *et. al.* found a significant decrease in the intensity of resonance around 60 and 70 ppm, and appearance of a broad line centred at 130 ppm, with a shoulder towards higher chemical shift, a new line around 110 ppm also appeared. They interpreted these spectral changes as major structural change amongst carbon atoms, and the formation of phenol or aromatic diol groups. Formation of such entities, they point out, would require a number of conditions to be satisfied. The conversion of attached OH groups to phenol/aromatic diols would need to take place, at least one double bond would need to be present in the ring, or would need to be formed by deoxygenation of an epoxy group, and bonds would need to be broken at the position of the OH groups during a process of re-aromatisation. Iodide, they stated, would be capable of such deoxygenation. The reduction in intensity of the line around 60 ppm suggests that the

deoxygenation of epoxide groups by I^- does occur, likewise reduced intensity of the 70 ppm line and chemical shift above 130 ppm suggests the transformation of C-OH to phenol/aromatic diol groups also takes place. It was also reported by Hofmann *et. al.*[24,26] that iodine is liberated when GO is reacted with hydrogen iodide (HI), which presents further indication of the presence of epoxide groups rather than 1,3-ethers, as 1,3-ether groups do not show this kind of reaction. Moreover, for GO which had been thermally decomposed by heating to 100 °C in vacuum, Lerf *et. al.* found that the 60 and 70 ppm lines disappeared and a dominant peak appeared around 122 ppm. The 110 – 160 ppm region of the NMR spectrum obtained following thermal decomposition, resembled that obtained from GO treated with KI closely, with resonance at 110 – 120 ppm and 160 ppm showing the formation of phenolic or aromatic diol groups and deoxygenation of epoxide. The decomposition of GO was not found to liberate oxygen, instead carbon monoxide (CO) and carbon dioxide (CO_2) were the decomposition products. It has long been suggested that the absence of oxygen as a decomposition product is due to oxygen reacting with the GO surface to form CO and CO_2. GO treated at extremely high temperatures becomes disordered and not easily detectable with NMR, the thermally decomposed GO presented by Lerf *et. al.* however had a definite spectral shape, suggesting that an intermediate GO decomposition product had being observed, presumably due to the vacuum and moderate conditions they used. Taken in part along with similarities to the spectra they presented for KI treated GO, spectra for thermally decomposed GO presented by Lerf *et. al.* provided further evidence for the presence of epoxide groups rather than 1,3-ethers. Based on the above results and further reasoning Lerf *et. al.* suggested a new model for GO (see Figure 2(f)). The Lerf-Klinowski model contains OH groups in agreement with previous models, which were confirmed by ^1H and ^{13}C NMR spectra and epoxide groups which were confirmed by ^{13}C NMR spectra obtained from GO treated with KI and thermally decomposed GO, additionally Lerf *et. al.* highlighted a complex sequence of reactions which are required for the formation of 1,3-ethers, which are unlikely to be realised in $KMnO_4/H_2SO_4$. Additionally, they reassigned the 130 ppm peak to aromatic entities and conjugated double C-C bonds, reasoning that isolated double bonds like those in models proposed by Mermoux and Scholz are easily oxidised, so are likely to be rare. The formation of phenol groups suggests that the epoxy and hydroxyl groups are very close to one another, but it is not necessary for the distribution of functional groups in every oxidised ring to be identical. Instead it is

suggested that GO consists or aromatic islands of various sizes which are not oxidised, separated by aliphatic 6-membered rings containing C-OH and epoxy groups and double bonds. In the Lerf-Klinowski model, functional groups form above and below the carbon lattice, and layer edges are terminated with C-OH and –COOH groups, consistent with results presented in other GO models.

Dimiev *et. al.*[39] proposed a modification to the Lerf-Klinowski model in 2013 which they termed the dynamic structural model (DSM). DSM was proposed due to no GO model previously proposed properly accounted for the observed level of acidity of GO. Carboxyl groups in the Lerf-Klinowski particularly, and acid groups in other models, account for a certain degree of acidity but not the degree of acidity that is known to exist. In DSM new functional groups constantly develop and transform, the key role belonging to water. Water incorporates into GO, transforms its structure and leaves by a number of different reactions. In the Dimiev model acidity is explained by the generation of hydrogen cation, which is driven by the accumulation of negative charge on GO layers, rather than the dissociation of pre-existing acidic groups, whose abundance would be too small. Prolonged exposure to water would degrade the GO flakes, gradually converting them in to humic acid-like structures. This gradual degradation could also lead to the formation of vacancy defects.

Although the Lerf-Klinowski model is now widely accepted, research, and new structural models are still being suggested. One such model of note was proposed in 2006 by Szabo *et. al.*[40]. Transmission electron microscopy (TEM) images they obtained showed GO has relatively thick stacking, and oxidised samples have distinctly different micro-structural features. During oxidation they found that graphite is delaminated to form very thin GO membranes with much smaller lateral dimensions than the course aggregate, they found also that even for their GO with the lowest level of oxidation (C/O ≈ 2.6) that there was very few areas resembling the original graphite slab. They found that GO sheets are not totally flat and smooth, but exhibit some folding, the extent of which increases with increased oxidation. X-ray diffraction (XRD) analysis carried out showed that the basal spacing of air-dried GO (equilibrium at 70% humidity) increases from 0.339 nm to 0.691 - 0.696 nm with oxidation, due to the expansion of layers to accommodate the various oxygen species. XRD spectra for GO showed no reflection corresponding to the main spectral line

(at $2\theta = 26.28°$) in the XRD spectrum on their parent graphite, within the detection limits of their equipment and the methodology used, they determined that this indicates that less than 0.1% of intact graphite crystallites remains in GO, in stark contrast to the large aromatic regions predicted in the Lerf-Klinowski model. Electron spin resonance (ESR) analysis of their GO samples showed a sharp and intense peak with small width which was only present for their GO with lowest oxidation, peaks were hardly observed for GO at higher oxidation levels. The small width of the peak, they stated, implies that there are no conduction carriers in GO, as in graphite, and hence there are no highly extended aromatic regions to develop a conduction band. Such narrow peaks, they concluded are due to condensed poly-aromatic domains across the GO lamellae, since other sources of such electronic behaviour would not vanish with increased oxidation. X-ray photoelectron spectroscopy (XPS) analysis showed the presence of 4 peaks, a peak at 284.4 eV, indicative of the presence of some aromatic carbon which is present in GO with $C/O \approx 2.6$, but disappears at higher levels of oxidation, the 3 remaining peaks at 287.2 eV, 289.3 eV, and 290.8 eV were assigned to alcohols, phenols and ether, ketones, and carboxylic groups respectively. Based on these results and with reference to their previous work[41], in which they demonstrated the likely presence of ketones and quinones, by greater consideration of the strong band in IR spectroscopy of GO at 1714 cm^{-1} by diffuse reflectance infrared fourier transform (DRIFT) spectroscopy, Szabo *et. al.* proposed a new model of GO (see Figure 2(g)). The Szabo model is a slight modification to that proposed by Scholz, in order to account for their improved IR spectroscopy results. The Szabo model was also proposed to give an improved account for the acidity of GO which is not satisfied in the Lerf-Klinwoski model, this was however resolved later in the Dimiev[39] DSM model. It should be noted that Szabo *et. al.* assume certain physical features of GO such as lack of graphite crystalline structure based on their GO sample having a low degree of oxidation, early combustion analysis by Hofmann *et. al*[26] revealed GO with $C/O \approx 2.5$ to 33, suggesting that Szabo *et. al.* examined exclusively GO, with what can be considered high level of oxidation. Such levels of oxidation, it has been shown in previous studies, have greater disorder and reduced graphite structure, and make results from some analytical techniques less certain. GO compositions vary greatly depending on a number of conditions, what constitutes high and low levels of oxidation is therefore subjective, knowledge of the existence of such GO however, casts doubt

on the reliability of the range C/O ≈ 2.0 – 2.6 to consider the complete range of GO surface oxidation levels.

Recent analytical experimental work has given further support to the GO structure proposed by Lerf *et. al.*. GO samples have been characterised by, amongst other analytical techniques, annular dark field imaging (ADF)[42], scanning transmission electron microscopy (STEM)[42], electron energy-loss spectroscopy (EELS)[42,43], Raman spectroscopy[44,45], selected area electron diffraction (SAED)[45], atomic force microscopy (AFM)[46,47], transmission electron microscopy (TEM)[43,45,48,49], atomic force microscopy coupled with infrared spectroscopy (AFM-IR)[50] and scanning electron microscopy (SEM)[51], all of which have given some level of additional validity to the Lerf-Klinowski model. For example, a recent study combining ADF, STEM, and EELS results reveal that GO is rough with an electronic structure distinct from both graphene and amorphous carbon. It was found to have average thickness of 6 Å and its structure is predominately amorphous due to distortions from the high fraction of sp^3 C-O bonds. It was found that around 40% of carbon atoms were sp^3 hybridised in a typical GO sample[42]. Raman spectroscopy in another studies[52] showed there are two characteristic bands for GO, a broad, blue shifted G-band at 1590 cm^{-1} (band in graphene[53] is 1580 cm^{-1}) which is characteristic of sp^2 hybridised carbon atoms, and a broad intense peak at 1330 cm^{-1}, the disorder induced D-band which indicates disorder induced in sp^2 hybridised carbon lattice by oxidation. SAED patterns for GO show clear crystalline structure with a 6-fold pattern, consistent with an hexagonal lattice.

Chapter 2 Computational Methodology

Computational chemistry can provide information on a wide range of microscope processes which may be difficult to obtain experimentally. High power computational resources continue to become less expensive and more widely available, whilst at the same time the costs associated with laboratory-based research remain the same, and in many cases are becoming more expensive, there is hence an ever-increasing interest in computational studies.

The aim of this chapter is to introduce the theoretical and practical background to the computational methodology on which the work in this thesis is based. The chapter begins with an introduction to the Schrödinger equation, which is central to quantum physics and computational chemistry, the discussion then moves on to a number of assumptions and simplifications which can be made in order to simplify the wavefunction to find quantitative solutions for many electron systems. The chapter then carries on, introducing the history and underlying principles of Density Functional Theory (DFT) and the evolution of DFT in both complexity and practicality with time. The chapter then concludes with a description of the specific uses of DFT in the research presented in this thesis.

2.1 The Schrödinger Equation

The Schrödinger equation is the fundamental equation, central to quantum chemistry and physics for describing the electronic structure of matter.

The non-relativistic, time-independent Schrödinger equation is given by the equation:

$$\hat{H}\Psi = E\Psi \qquad \textbf{(2.1)}$$

Where $\hat{H}$ is the non-relativistic Hamiltonian operator, Ψ is the wavefunction of the system, and E is the corresponding energy.

The wavefunction of the system (Ψ) depends on the spatial and spin coordinates of electrons ($\boldsymbol{x}_i = (\boldsymbol{r}_i, \sigma_i)$) and the spatial coordinates of nuclei ($\boldsymbol{R}_A$).

$$\Psi = \Psi(\boldsymbol{x}_1, \boldsymbol{x}_2 \ldots, \boldsymbol{x}_N, \boldsymbol{R}_1, \boldsymbol{R}_2, \ldots, \boldsymbol{R}_M) \tag{2.2}$$

The Hamiltonian operator represents the total energy of the system, a sum of kinetic ($\hat{T}$) and potential ($\hat{V}$) energy operators, and can be expressed, in atomic units (in which the mass of the electron (m_e), elementary charge (e), the reduced Planck's constant ($\hbar$), and Coulomb's constant (k_e) are all unity by definition), which are used hereafter:

$$\hat{H} = \hat{T} + \hat{V} \tag{2.3}$$

$$\hat{T} = \hat{T}_e + \hat{T}_n = -\frac{1}{2}\sum_{i=1}^{N} \nabla_i^2 - \frac{1}{2}\sum_{A=1}^{M} \frac{1}{M_A} \nabla_A^2 \tag{2.4}$$

$$\hat{V} = \hat{V}_{ne} + \hat{V}_{ee} + \hat{V}_{nn} = -\sum_{i=1}^{N}\sum_{A=1}^{M} \frac{Z_A}{r_{iA}} + \sum_{i=1}^{N}\sum_{j>i}^{N} \frac{1}{r_{ij}} + \sum_{A=1}^{M}\sum_{B>A}^{M} \frac{Z_A Z_B}{R_{AB}} \tag{2.5}$$

The kinetic energy operator (equation (2.4)) contains contributions from the kinetic energy of electrons ($\hat{T}_e$) and nuclei ($\hat{T}_n$), and the potential energy operator (equation (2.5)) is made up of the Coulombic potential energy operator ($\hat{V}_{ne}$) which acts between electrons and nuclei, and the interelectron ($\hat{V}_{ee}$) and internuclear ($\hat{V}_{nn}$) potential energy operators. The indices A and B run over M nuclei, i and j denote the electrons in the system, M_A and Z_A are the nuclear mass and nuclear charge respectively, r_{iA} is the distance between electron i and nucleus A, and r_{ij} is the distance between the electrons i and j.

Solving the Schrödinger equation for molecular systems is intractable, the wavefunction contains all nuclear and electronic degrees of freedom, which are coupled in the Hamiltonian operator. There are however a number of simplifications, assumptions, and approximations which can be made in order to allow solutions to be found.

2.2 The Born-Oppenheimer Approximation

As a first approximation towards solving the Schrödinger equation, the Born-Oppenheimer approximation allows the decoupling of the motion of electrons from the motion of nuclei. Such an assumption can be made due to nuclei being much larger in mass and moving much more slowly than electrons, the total wavefunction can then be considered as a product of separate nuclear (Ψ^{nc}) and electronic (Ψ^{el}) wavefunctions.

$$\Psi = \Psi^{nc}(\boldsymbol{R}_1, \boldsymbol{R}_{2,\dots}, \boldsymbol{R}_M)\Psi^{el}(\boldsymbol{x}_1, \boldsymbol{x}_{2,\dots}, \boldsymbol{x}_N; \{\boldsymbol{R}_A\}) \quad \textbf{(2.6)}$$

Where $\{\boldsymbol{R}_A\}$ denotes that the electronic wavefunction has only a parametric dependence on nuclear coordinates.

The nuclei move so much more slowly in fact, that electrons can be considered as being able to rearrange themselves into a stable configuration instantly when the nuclei move i.e. it is assume that nuclei are completely stationary ($\hat{T}_n = 0$ in equation (2.4)). This assumption allows consideration of solutions to the Schrodinger equation using an electron only Hamiltonian operator (also termed the clamped nucleus Hamiltonian), for a set of nuclei in fixed positions that acts on functions of only the degrees of freedom of the electrons. For example when considering a simple molecule such as benzene which has 12 atomic nuclei and 42 electrons, solutions of the Schrodinger equation to obtain the energy and wavefunction are obtained from equations with 162 variables (spatial coordinates for all electrons and nuclei), under the Born-Oppenheimer approximation however the electronic wavefunction depends on only 126 spatial coordinates.

2.3 Basis Sets

It is discussed in Section 2.4 that a molecular orbital approximation can be employed to express the many electron wavefunction as a product of one-electron molecular orbitals (MOs). A basis set in computational chemistry is a set of [basis] functions used to approximate MOs. The MOs used in the Hartree-Fock and Kohn-Sham methodology presented in this chapter (see equations (2.26) and (2.36) respectively)

are formed using an approach based on the superposition of atomic orbits (AO) to calculate MOs, this approach is commonly referred to as the linear combination of atomic orbitals (LCAO). AOs in general terms are functions used to describe the discrete, quantised energy levels of atoms, needed to determine the probability of finding an electron at any given point in space. AO are most commonly represented by functions which are centred on atoms, although functions centred in bonds or lone pairs have also been used[54–56].

Whilst the superposition of AO functions is the most commonly used method for calculating MOs, it is sometimes easier and more convenient to use plane-wave basis functions. Plane-wave basis functions are commonly used in calculations carried out using periodic boundary conditions (PBC), such calculations are not presented in this thesis, there are however comparisons made between results from molecular models and those from models using PBC (where available). As such the following discussion relates exclusively to a LCAO approach, as used in the calculations carried out for the results presented in this thesis.

The construction of MOs can be described by the general expression:

$$\emptyset_i = \sum_{\alpha}^{M} C_{\alpha i}\chi_\alpha \qquad \textbf{(2.7)}$$

Where $\emptyset_i$ is a MO, $C_{\alpha i}$ are the expansion coefficients, χ_α is the α^{th} AO, and M is the number of AOs in the basis set. As M is increased the size of the basis set tends towards infinity, and the complete basis set limit is reached. MOs formed in this way are in their most complete form. In practice however an appropriately large finite value for M must be chosen due to restraints on resources. Criteria for selecting an appropriately large basis set includes amongst others, the inclusion of a physically meaningful number of atomic orbitals, the satisfaction of the required level of energy accuracy, sufficient AOs to consider such things as loosely bound electrons, and the associated computational expense. The size of the basis set required to perform calculations of a specific quality increases non-linearly with the size of the atoms and molecules in the system. It is therefore incredibly important, particularly for large systems, and systems containing heavy elements (albeit, effective core potentials (see Section 2.3.3.3) and

other methods can be used to control computational cost), to choose appropriate basis sets to give sufficient accuracy and maximum efficiency. The mathematical functions which best describes AOs, are known as a Slater-type orbitals (STOs).

2.3.1 Slater-type Orbitals (STOs)

STOs are functions which are used to describe AOs, they were first introduced by American physicist John Slater in 1930[57], they can be represented in the general form;

$$\chi_{\zeta,n,l,m}(r,\theta,\varphi) = NY_{l,m}(\theta,\varphi)r^{n-1}e^{-\zeta r} \quad \textbf{(2.8)}$$

Where N is a normalisation factor, $Y_{l,m}$ is the spherical harmonic, n, l, and m are the principal, angular, and magnetic quantum numbers respectively, and ζ is a constant which is related to the effective charge on the nucleus, which can be estimated by Slater's rules[57]. STOs are particularly well suited for describing AOs because they describe behaviour both close to the nucleus and at long range correctly, displaying a cusp close to the nucleus and the correct exponential decay at long range. Additionally, relatively few STO functions are required to describe MOs. One important term to note in equation (2.8) however is the exponential term $e^{-\zeta r}$, which defines the decay of the basis function far from the nucleus, dependence of the exponent of r makes evaluation of integrals analytically difficult, and as such an alternative is commonly used. Gaussian-type orbitals (GTOs) are the most commonly preferred alternative as their integrals can be evaluated much more efficiently.

2.3.2 Gaussian-type Orbitals (GTOs)

The use of GTOs as an alternative to STOs was first proposed in 1950[58] by Samuel Boys. GTOs can be defined using the general formula;

$$\chi_{\zeta,n,l,m}(r,\theta,\varphi) = NY_{l,m}(\theta,\varphi)r^{2n-2-l}e^{-\zeta r^2} \quad \textbf{(2.9)}$$

Where terms share exact meaning with those in equation (2.8) expect ζ which cannot be obtained from Slater's rules for GTOs. The main difference between GTOs and STOs is in their radial component, whilst STOs depends upon r which makes them

accurate for describing the AOs, but mathematically awkward, GTOs depend upon r^2 which makes them less representative of AOs in terms of radial decay, but much more suitable for analytical integration. STOs, as mentioned, display a cusp close to the nucleus, GTOs however have zero gradient which is unphysical, similarly they decay too quickly in the radial region whilst the asymptotic decay of STOs is correct. The difference in shape between the STO and GTO functions for a representative 1s orbital is shown in Figure 4. Due to their characteristic and unrepresentative shape GTOs are often combined to give a better description of each AO (or to fit to a STO).

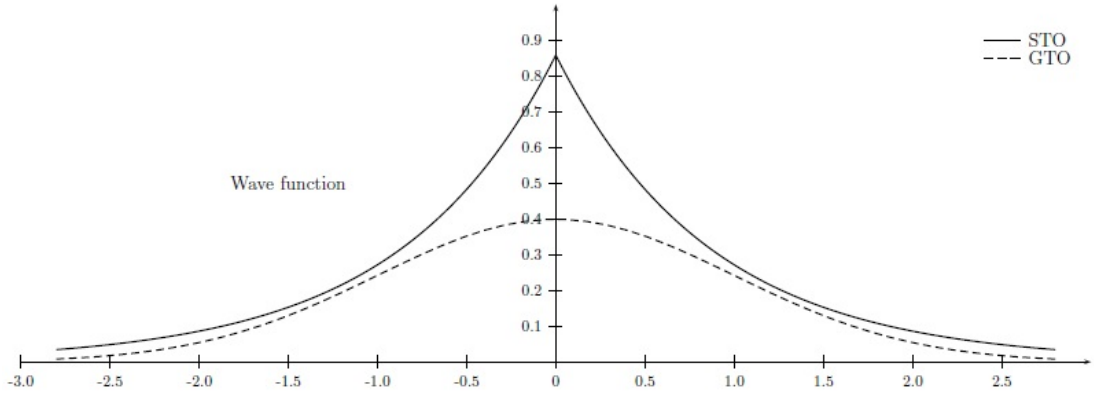

Figure 4: Comparison of the shape of an STO and GTO function [reproduced with permission from ref 59]

The product of a combination of GTOs is known as a contracted Gaussian-type orbital (CGTO), and their constituent functions termed primitive Gaussian-type orbitals (PGTOs). Figure 5 gives a graphical representation of the evolution in shape of the combination of 1 (STO-1G), 2 (STO-2G), and 3 (STO-3G) PGTOs to fit to a single STO, note the unusual naming convention and that even the combination of 3 PGTOs provides poor fitting to the STO function. Basis sets of this quality are poor, they are however useful for calculations on large systems and for determining preliminary geometries to reduce the computation cost of later, higher quality calculations.

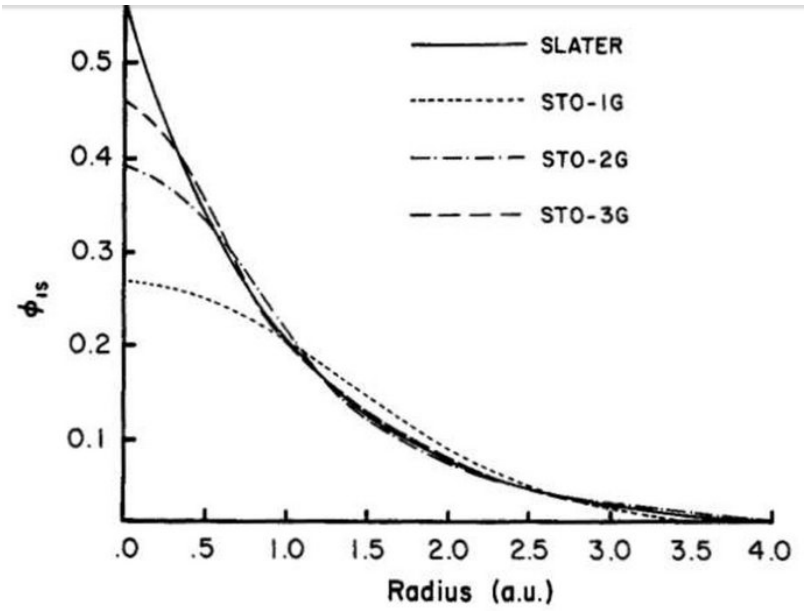

Figure 5: Approximation of an STO by the linear combination of GTOs [reproduced from ref 60]

The convergence of the atomic energy from CGTOs with increased constituent PGTOs towards the value from a single STO is presented for carbon in Table 1. Although the combination of several PGTOs is required to closely match the value obtained from a single STO, the associated computational expense is still expected to be significantly lower due to the GTO integrals being much simpler to solve, for this reason in the overwhelming majority of calculations carried out for polyatomic molecules, a finite basis of Gaussian-type functions is used to represent MOs, which in turn approximate the many electron wave-functions[61].

Table 1: Atomic energy with optimised exponents (energy in a.u.) [data from ref 62]

Atom	STO-3G	STO-4G	STO-5G	STO-6G	STO
C(^{3}P)	-37.22866	-37.51069	-37.58578	-37.60906	-37.62182

It is necessary as a basic requirement to include a sufficient number of basis functions to describe all of the electrons in each of the atoms within a system. The smallest possible basis set, the minimal basis set (also known as a single zeta (single-ζ) basis set) contains only functions for occupied atomic orbitals in the ground state. The minimum basis set for hydrogen for example comprises of only a single 1s function,

with no additional functions, the minimum basis set for boron comprises only functions for 1s, 2s, and the three 2p orbitals, and so on and so forth. Single zeta basis sets produce low quality results, insufficient for contemporary research, a number of improvements can however be made.

2.3.3 Improved Basis Sets

One of the main reasons that minimum basis sets produce such low-quality results is their poor description of variation in the radial components of AOs, which is required in an accurately description of bonding. It is desirable therefore to increase the number of basis functions which are used, particularly in valence orbitals which are involved in bonding. It is found that orbitals in the core are almost identical in atoms and molecules, a well-designed minimum basis set is hence usually sufficient for describing orbitals not involved in bonding. Alternatively a pseudopotential (Section 2.3.3.3) is often used to describe the core of heavy elements, and an increased number of basis functions is used to describe valence orbitals[63,64].

The naming convention for improved basis sets is usually derived from the number of functions used to describe each of the orbitals. When two functions are used to describe each orbital for example, they are termed "double-zeta(ζ)" (DZ), likewise if three are used they are referred to as being "triple-zeta(ζ)" (TZ), four is "quadruple-zeta(ζ)" (QZ), and so on and so forth, where "ζ" originates from Slater's original use of the term in equation (2.8). Typically however, as mentioned above, a greater number of basis functions is used routinely only to describe valence orbitals, in order to minimise computational cost. Basis sets with greater AOs in the valence region than in the core are as such termed "split valence" (SV), which is equivalent to "valence double-zeta(ζ)" (DZV), "valence triple-zeta(ζ)" (TZV), "valence quadruple-zeta(ζ)" (QZV) and so on. A number of further improvements can also be made to the formation of basis sets.

2.3.3.1 Polarisation Functions

Within molecules, the influence of nuclei in neighbouring atoms distorts and polarises electron density, hence orbitals in molecule must have much greater flexibility in shape than those in free atoms. Increased flexibility can be achieved by adding basis

functions representing orbitals with higher angular momentum, in general a basis function with angular momentum l is mixed with a basis function of $l + 1$. In the 1s orbital, for example, greater flexibility can be achieved by mixing in an orbital with p character. The positive p lobe works to emphasis one side of the orbital, whilst the negative lobe decreases the other, hence allowing polarisation in the s-orbital.

Likewise, p-orbitals can be polarised by the introduction of orbitals with d character.

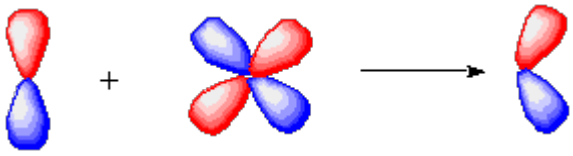

The inclusion of polarisation in AO functions gives basis sets which are termed "polarisation split valence" (SVP), TZVP, QZVP, and so on.

2.3.3.2 Diffuse Functions

The basis functions as they are have been described until now are only completely adequate for modelling cationic and neutral systems in the ground-state, further improvements are required where loosely bound electrons are present i.e. for calculations of excited states and for the description of anions, for this diffuse basis functions are used. Diffuse functions share the same angular momentum as existing orbitals, but use much smaller values for the ζ exponents to provide an improved description of the radial tail of the orbitals.

The basis sets used throughout the work presented in this thesis were developed by Ahlrichs and co-workers[65,66], and follow the naming conventions outlined in this sections. Other basis sets, such as those developed by Dunning[67], and Pople[62] are also very popular. Naming conventions vary between development groups, the underlying principles outlined above, and the way in which they are developed and implemented, however, is similar.

2.3.3.3 Effective Core Potentials (ECPs) and Relativistic Effects

The theory presented up to this point has been for a model of quantum mechanics which is both time-independent, i.e. it gives no description of how the system would evolve in time, and does not account for the relativistic effects from high velocity electrons orbiting the nucleus. At all but velocities close to the speed of light relativistic effects are negligible so are not usually encountered in day to day life, they do however play in an important role in chemistry, particularly for heavy elements. Relativistic effects are responsible for such phenomena as the unique colour of gold[68], and mercury being liquid at room temperature[69]. The degree to which relativistic effects contribute to a chemical system correlates with the atomic number of the elements in the system, their consideration is particularly important therefore in research presented in Chapter 4 and Chapter 5, in which f-block elements are considered.

One of the most commonly known consequences of relativity, along with the dilation of time, is the relativistic mass effects, the mass increase at very high velocity is defined by the expression:

$$m_{rel} = \frac{m_o}{\sqrt{1 - {v^2}/{c^2}}} = \gamma m_o \qquad \textbf{(2.10)}$$

Where m_{rel} is the relativistic mass, m_o is rest mass, v is velocity, c is the speed of light in a vacuum, and γ is known as the Lorentz factor. Relativistic effects are negligible except for bodies moving close to the speed of light.

An approximation of the speed of electrons in atoms can be obtained from knowledge of the Bohr model of the atom and classical mechanics. Using the Bohr model the energy levels of atoms can be determined by an approximation to the hydrogenic system, which can be determined by the expression:

$$E_n = \frac{-Z^2 R_E}{n^2} = \frac{-(k_e e^2)^2 m_e Z^2}{2\hbar^2 n^2} \quad \textbf{(2.11)}$$

Where Z is the atomic number, R_E is the Rydberg energy, and k_e is Coulomb's constant. It is more commonly expressed in atomic units (outlined in Section 2.1), where many of the terms can be normalised to unity:

$$E_n = \frac{-Z^2}{2n^2} \quad \textbf{(2.12)}$$

Coulomb's constant can also be used to derive an approximate value for the speed of light in atomic units:

$$k_e = \frac{\alpha\hbar c}{e^2} = \frac{1}{4\pi\varepsilon_0} \rightarrow c = \frac{1}{\alpha} \approx 137 \quad \textbf{(2.13)}$$

Where α is the fine structure constant.

It is also known from classical mechanics that the average kinetic energy of an electron over time can be given by (in a.u.):

$$\bar{T} = \frac{1}{2}\bar{v}^2 \quad \textbf{(2.14)}$$

Combining expressions for the potential and kinetic energy of electrons from the Bohr and classical models respectively using the virial theorem, which states that for an ideal system, the potential energy when averaged over time is equal to twice the average kinetic energy (i.e. $E = \bar{T} + \bar{V} = -\bar{T}$), a general expression relating atomic number to electron velocity is obtained:

$$E_n = \frac{Z^2}{2n^2} = \frac{1}{2}\bar{v}^2 \quad \textbf{(2.15)}$$

Which for the 1s atomic orbital is simply:

$$\bar{v} = Z \tag{2.16}$$

It is noted from equation (2.15) that electrons move much more quickly in heavy elements, and in low energy core orbitals. The velocities calculated from equation (2.15) can be used to approximate the degree of contraction of core electrons (and electrons in higher energy orbitals) by the modified Bohr radius with the reintroduction of the Lorentz factor from equation (2.10):

$$a_o = \frac{(4\pi\varepsilon_o)\hbar^2}{m_e e^2 Z} \rightarrow a_o' = \frac{(4\pi\varepsilon_o)\hbar^2}{\gamma m_e e^2 Z} = \frac{1}{\gamma Z} \tag{2.17}$$

The relativistic core contraction becomes increasingly significant for heavy elements. While relativistic effects can generally be ignored for light elements, their consideration is paramount in importance for heavy elements: they cause the contraction of all s- and to a lesser extent p-orbitals (due to orthogonality conditions between orbitals with the same angular momentum), and cause d- and f- orbitals to expand indirectly due to nuclear shielding effects from the contracted s- and p-orbitals.

Within relativity, space and time are united into the single 4-dimensional spacetime continuum, as such they should be treated on the same basis in any relativistic calculation and a dependency on time must be introduced to the Schrodinger equation used. The time dependent Schrodinger equation is known, and is given by the expression:

$$\hat{H}\Psi(\boldsymbol{r}, t) = i\hbar\frac{\partial}{\partial t}\Psi(\boldsymbol{r}, t) \tag{2.18}$$

Unfortunately, the time dependent Schrodinger equation relies on second order partial derivatives with respect to spatial components, and only first order derivatives with respect to time, making is incompatible with the implementation of relativistic effects, as the four dimensions cannot be considered on the same terms. Dirac proposed an alternative equation which is compatible with both quantum mechanics and special relativity, which can be expressed in general terms:

$$(c(\boldsymbol{\alpha}\cdot\boldsymbol{p})+\boldsymbol{\beta}mc^2)\Psi = i\hbar\frac{\partial}{\partial t}\Psi \qquad \textbf{(2.19)}$$

$$\boldsymbol{\alpha}_{x,y,z}=\begin{bmatrix}\mathbf{0} & \boldsymbol{\sigma}_{x,y,z}\\ \boldsymbol{\sigma}_{x,y,z} & \mathbf{0}\end{bmatrix} \qquad \boldsymbol{\beta}=\begin{bmatrix}\boldsymbol{I} & \mathbf{0}\\ \mathbf{0} & -\boldsymbol{I}\end{bmatrix}$$

$$\boldsymbol{\sigma}_x=\begin{bmatrix}0 & 1\\ 1 & 0\end{bmatrix} \qquad \boldsymbol{\sigma}_y=\begin{bmatrix}0 & -i\\ i & 0\end{bmatrix} \qquad \boldsymbol{\sigma}_z=\begin{bmatrix}1 & 0\\ 0 & -1\end{bmatrix} \qquad \boldsymbol{I}=\begin{bmatrix}1 & 0\\ 0 & 1\end{bmatrix}$$

Where $\boldsymbol{\alpha}$ is a 4x4 matrices constructed from 2x2 Pauli spin matrices $\boldsymbol{\alpha}_{x,y,z}$, $\boldsymbol{\beta}$ is a 4x4 matrix, and $\boldsymbol{p}$ is the momentum operator. The solutions to the Dirac equation are column vectors of length 4 known as spinors. Electron spin and the existence of the positron come directly out of the solutions to the Dirac equation. Antimatter had not been previously observed, and its existence was not suspected until it was predicted by Dirac, it was discovered experimentally 5 years after publication of the Dirac equation paper by Carl Anderson[70]. Owing to the predicted existence of the positron, spinors can be considered as having two components, large (L) and small (S), the large spinor component is associated with electronic solutions, and the small component corresponds to a coupling of electrons and positrons. For non-relativistic calculations, i.e. those in which the speed of light is assumed to be infinite, the small component disappears and solutions to the Dirac equation reduce to those of the Schrodinger equations. The standard form of the spinors is given by the equation:

$$\Psi(\boldsymbol{r},t)=\begin{bmatrix}\Psi_{L,\alpha}(\mathbf{r},t)\\ \Psi_{L,\beta}(\mathbf{r},t)\\ \Psi_{S,\alpha}(\mathbf{r},t)\\ \Psi_{S,\beta}(\mathbf{r},t)\end{bmatrix} \qquad \textbf{(2.20)}$$

As well as the contraction of s- and p- orbitals, and subsequent expansion of d- and f-orbital from the introduction of relativistic effects, another consequence which arises conveniently from the Dirac equation is spin-orbit coupling. Spin-orbit coupling is an effect based on the coupling of intrinsic electron spin and the orbital angular momentum associated with the motion of the electron moving around the nucleus, which is responsible for such physical effects as the fine structure splitting of spectral

lines. Spin-orbit coupling arises from the magnetic field generated by the atomic nucleus when the nuclear system is observed from the electron's frame of reference. The magnetic field from the nucleus is directly related to the orbital angular momentum of the electron, and also creates a torque on the electron from interaction with the magnetic dipole moment created by the electron spin, creating the observed changes in the energy levels of electrons in the atom. When considering quantum mechanics using the Schrodinger equation, the quantum states of electrons are described using the principle (n), angular (l), magnetic (m), and spin (s) quantum numbers, in the Dirac equation however, only the total angular momentum (j) is conserved. In the Dirac interpretation it is no longer reasonable to consider the angular momentum of electrons around the nucleus and the electron spin separately.

When constructing an *ab initio* (from first principles) calculation, particularly those containing heavy elements where relativistic effect may need to be considered, there are tremendous computational costs associated, and an all electron description may be too expensive. There is a need to find computational savings and suitable approximations. One such approximation, which can be used for systems containing heavy elements like those in Chapter 4 and Chapter 5, originates from the earlier mentioned observation that core electrons are almost inert to changes in chemical bonding and almost identical in atoms and molecules. The effect of core electrons on valence electrons can be represented accurately by a potential energy term (commonly referred to as a relativistic effective core potential (RECP), ECP, or pseudopotential). The potential energy term can effectively incorporate scalar relativistic effects without the need to explicitly solve the Dirac equation. As well as reducing computational costs greatly compared to an all electron approach, the use of a potential energy term reduces the problem computationally to dealing only with valence electrons in atoms. Germanium, for example, when calculated with a pseudopotential describing core electrons becomes as computationally inexpensive as carbon, whilst producing results which are almost in perfect agreement with all electron calculations[63].

2.3.3.4 Basis Set Superposition Error (BSSE)

The use of the finite atomic basis sets used in the research presented in this thesis can introduce an error into energy calculations, beside that inherently associate with the

use of approximations based on GTOs and the use of an incomplete set of basis functions.

The so-called basis set superposition error (BSSE) arises because over short distances basis functions centred on the nucleus of one atom can describe the electron density close to the nucleus of neighbouring atoms. The consequence of this in energy calculations products are treated using basis functions from both reactants. This means that the energy of a product is calculated using a more complete basis set, which in itself is not an error, it does however cause an artificial lowering of the energy of the product and an overestimation of binding strength.

BSSE is most significant in calculations carried out with small basis sets. A simple solution therefore is to increase the size of the basis sets used. This is however, at significantly increased computational cost, so is not always practical. The most common approach therefore is to attempt to find an approximation for the energy bias towards the product. The most popular method for this is known as Counterpoise Correction (CP)[71].

CP involves the use 'ghost functions' to effectively improve the basis set used for the treatment of the constituent reactant up to the level of that used in the treatment of the product. This is achieved through the use of 'ghost functions', basis functions located at the nuclear position of the other reactants in the product, without the nuclei or electrons.

If we consider two reactants A and B, which come together to form the product AB, the complexation energy using conventional the conventional approach would simply be:

$$E_c = E_{AB} - E_A - E_B \qquad \textbf{(2.21)}$$

It is discussed however that using the approach outlined in equation (2.21), the product E_{AB} is not treated on the same terms as the reactants E_A and E_B, using CP the BSSE can be estimated using the formula:

$$BSSE = (E_A^{AB} - E_A^A) + (E_B^{AB} - E_B^B) \quad \textbf{(2.22)}$$

Where superscripts indicate the set of basis functions used in the calculation and subscripts indicate the reactant being calculated, i.e. E_A^{AB} is the energy of the reactant A, calculated using the basis set associated with reactant and ghost functions from reactant B.

The corrected energy, combining equations (2.21) and (2.22) then becomes:

$$E_c^{CP} = E_c - BSSE \quad \textbf{(2.23)}$$

2.4 Hartree-Fock Theory

The Born-Oppenheimer Approximation (Section 2.2) tells us that the wavefunction of many electron systems can be considered as having two distinct components, one for nuclei and one for electrons. Electrons and nuclei can be considered separately due to the considerable difference in their mass and velocity at which they move. The many-body wavefunctions which consider only the electronic component (of interest for electronic structure calculations) then becomes;

$$\Psi = \Psi^{el}(\boldsymbol{x}_1, \boldsymbol{x}_2, \dots, \boldsymbol{x}_N) \quad \textbf{(2.24)}$$

Solutions to even the electronic Schrodinger equation are tractable only for simple atoms with one electron, solutions for large system do not exist. The Hartree-Fock theory allows for solutions to be found for large systems. The first step in development of the Hartree-Fock theory is to assume that poly-electronic and poly-atomic systems can be considered as systems of individual electrons, that do not formally interact with one another. This is often referred to as the Hartree product wavefunction.

$$\Psi_{HP}(\boldsymbol{r}_1, \boldsymbol{r}_2, \dots, \boldsymbol{r}_N) = \phi_1(\boldsymbol{r}_1)\phi_2(\boldsymbol{r}_2) \dots \phi_N(\boldsymbol{r}_N) \quad \textbf{(2.25)}$$

The Hartree product wavefunction as described in equation (2.25) has orbitals which depends only on the spatial distribution of electrons (where $\emptyset(\boldsymbol{r})$ are known as spatial

orbitals), electrons however do not have only spatial degrees of freedom, spin must also be included into the wavefunction.

$$\emptyset(\boldsymbol{r}) \rightarrow \chi(\boldsymbol{x}) = \phi(\boldsymbol{r})\sigma \tag{2.26}$$

The Hartree product now becomes;

$$\Psi_{HP}(\boldsymbol{x}_1, \boldsymbol{x}_2, \dots, \boldsymbol{x}_N) = \chi_1(\boldsymbol{x}_1)\chi_2(\boldsymbol{x}_2) \dots \chi_N(\boldsymbol{x}_N) \tag{2.27}$$

Where $\chi(\boldsymbol{x})$ are spin orbitals, and as in equation (2.24), $\boldsymbol{x}$ defines space-spin coordinates which are a product of spatial $(\boldsymbol{r})$ and spin (σ) coordinates. The approximation for spin orbitals are usually defined by linear combination of atomic orbitals (LCAO) as outlined in Section 2.3. The Hartree product however, whilst being convenient, provides an unsatisfactory description of systems of electrons. Its solutions are not antisymmetric with respect to electron exchange, which is a requirement of Fermions. The Pauli exclusion principle, which states that two or more identical electrons in a system cannot occupy the same quantum state simultaneously, arises directly from a need for antisymmetry.

To overcome the issue of antisymmetry it is assumed within Hartree-Fock theory that a single Slater determinant can be used to approximate an exact N-body wavefunction. Antisymmetry is maintained within the Slater determinant due to the interchange of either two rows or two columns resulting in a change of sign of the determinant, likewise the Pauli exclusion principle is obeyed because if two rows or columns are equal, the determinant is zero, the Slater determinant is defined as;

$$\Psi_{SD}(\boldsymbol{x}_1, \boldsymbol{x}_2, \dots, \boldsymbol{x}_N) = \frac{1}{\sqrt{N!}} \begin{bmatrix} \chi_1(\boldsymbol{x}_1) & \cdots & \chi_N(\boldsymbol{x}_1) \\ \vdots & \ddots & \vdots \\ \chi_1(\boldsymbol{x}_N) & \cdots & \chi_N(\boldsymbol{x}_N) \end{bmatrix} \tag{2.28}$$

There are a number of consequences associated with using a Slater determinant, the first being that electrons in the system are indistinguishable from one another, that being that all electrons are associated with all orbitals, a consequence that fits in well with the understanding that electrons are indistinguishable (or identical) particles from quantum statistics. The second is that electrons are assumed to move independently

of one another, there is a Coulombic repulsion (an approximate interelectron ($\hat{V}_{ee}$) potential) from the average position of all electrons, and an exchange interaction (sometimes referred to as Pauli repulsion), which is a direct consequence of antisymmetrisation, Hartree-Fock is a mean field theory.

In a mean field theory, effective one electron energy operators can be defined within the many electron Schrodinger equation, within Hartree-Fock theory, these are known as Fock operators and are defined by the equation:

$$\hat{f}_i = -\frac{1}{2}\nabla_i^2 - \sum_{A=1}^{M}\frac{Z_A}{r_{iA}} + V_i^{HF}\{j\} \tag{2.29}$$

The first two terms in the Fock operator are one electron terms, they are the kinetic energy of a single electron, and the potential energy between the electron and nuclei respectively. The third term is known as the Hartree-Fock potential, which is a two electron operator, and relates to how electrons interact with one another. The Hartree-Fock potential can be expressed in terms of the Coulomb ($\hat{J}_{ij}$) and exchange ($\hat{K}_{ij}$) operators, which defines the repulsive and exchange energy between the i^{th} and j^{th} electrons respectively, it can be expressed more explicitly as:

$$V_i^{HF}\{j\} = \sum_{j=1}^{N/2}[2\hat{J}_{ij} - \hat{K}_{ij}] \tag{2.30}$$

Exchange is a consequence of antisymmetry and has no physical analogue from classical theories. Although the Hartree-Fock theory provides a method for finding solutions for the Hamiltonian of many body wavefunctions by solving for a single N-electron wavefunction in terms of N-one electron wavefunctions, the operators relating to each electron still depends upon solutions of Fock operators for all other electrons due to the Hartree-Fock potential. The Fock operator can be used to form a matrix (the Fock matrix (***F***)) for all electrons, finding solution in Hartree-Fock theory then become a search for the set of spin orbitals, which correspond to eigenvalues of the Fock matrix. Solutions can obtained iteratively by using the Roothaan-Hall[72,73] method which was developed by Clemens Roothaan and George Hall, whom it is

named after, independently in 1951. The Roothaan-Hall method is given by the equation:

$$\boldsymbol{FC} = \varepsilon \boldsymbol{SC} \tag{2.31}$$

Where $\boldsymbol{F}$ is the Fock matrix, $\boldsymbol{C}$ is the coefficient matrix which is comprised of the expansion coefficients and denotes how atomic orbitals combine in molecular orbitals, $\boldsymbol{S}$ is an overlap matrix, and ε is an energy vector. This leads to a self-consistent field (SCF) method in which the constituent C_i vectors from the coefficient matrix are systematically varied from a set of trial molecular orbitals until the ground state energy is obtained. The Hartree-Fock wavefunction is a Slater determinant constructed from the orbitals obtained by this iterative method. Within the confines of Hartree-Fock theory and within the limits of the assumptions made, these wavefunctions can be used to compute any physical or chemical properties for which corresponding operators can be defined.

2.5 Density Functional Theory (DFT)

The discussion in this chapter so far has focused on simplifications and approximations which can be made within a wavefunction approach to find solutions for many-body systems. Whilst the use of Hartree-Fock theory (Section 2.4) and the Born-Oppenheimer approximation (Section 2.2) (which is inherently assumed within Hartree-Fock), greatly simplify wavefunction calculations, its underlying mathematics are still too cumbersome for many applications. There are also other limitations and inaccuracies associated with the description of the wave function using a Slater determinant, such as Hartree-Fock not considering aspects of "electron correlation", the explicit effect of an electron on all other electrons within a system. Fortunately, a wavefunction approach is not the only method by which to solve the Schrodinger equation. This section outlines the development of density functional theory (DFT), which formulates solutions to the Schrodinger equation in terms of the electronic density, as an alternative to a wavefunction approach. A functional in mathematics takes functions as arguments and outputs numerical values, they are denoted by the use of square brackets. Calculations in DFT reduce the consideration of three spatial

degrees of freedom for every single electron in the many-electron wavefunction, to just three for the whole system.

2.5.1 Hohenberg-Kohn Theorems

The development of modern DFT began with the work of Hohenberg and Kohn who proved two theorems in 1964, which have become the basis of the theory. The first Hohenberg-Kohn theorem (the so-called existence theorem), states that:

> "…the ground state of an interacting many particle system… is a unique function of the electron density ρ(**r**)"[74]

The second theorem (the so-called variation theorem), can be summarised as:

"The ground state energy can be obtained variationally, the density that minimises the total energy is the exact ground state density"

$$E_0[\rho_0] = \min E[\rho] = \min(T[\,\rho] + E_{ne}[\rho] + E_{ee}[\rho]) \qquad \textbf{(2.32)}$$

Where E_o is the true ground state energy, $min\,E$ is the ground state energy obtain by variational principle, T is the ground state kinetic energy, and E_{ne} and E_{ee} are the ground state nuclear-electron, and inter-electron potential energies respectively.

2.5.2 Kohn-Sham DFT

Whilst the Hohenberg-Kohn theorems provide an interesting concept and potentially reduces solving the many body Schrodinger equation from a wavefunction problem containing $4N$ (N being the number of electron) degrees of freedom, to an electron density problem with only 3 degrees of freedom, there was no obvious method for calculating the ground state energy from the density, nor to finding the density without first knowing the wavefunction. This was addressed in 1965[75] by Kohn and Sham who considered a fictitious non-interacting system with an identical density to the ground state density of the real, interacting system. From a reference system dependent only on electron kinetic energy and a nuclear-electron attraction, which can be defined;

$$E_{ref}[\rho] = T_{NI}[\rho] + E_{ne}[\rho] \quad \textbf{(2.33)}$$

Other terms can be added to map the full interacting system on to the idealised non-interacting system to give a description of the interacting system.

$$E_{KS}[\rho] = T_{NI}[\rho] + E_{ne}[\rho] + J[\rho] + E_{xc}[\rho] \quad \textbf{(2.34)}$$

Where T_{NI} is the kinetic energy of the non-interacting reference system, E_{ne} is the Coulomb interaction energy between electrons and nuclei, J is the Coulombic repulsion between electrons, and E_{xc} is the exchange-correlation (*xc*-) energy which includes all interaction energies not otherwise considered, and acts as a correction term. $E_{xc}[\rho]$ can be defined as:

$$E_{xc}[\rho] = (T[\rho] - T_{NI}[\rho]) + (E_{ee}[\rho] - J[\rho]) \quad \textbf{(2.35)}$$

Where $T[\rho]$ and $E_{ee}[\rho]$ are functional descriptions of the kinetic and interelectronic energies of the interacting system, the terms on the right hand side of the equation define the difference between a non-interacting and interacting system, and the difference between a simple classical interpretation of interelectronic interactions and those in a real system. From the definition in equation (2.35) the *xc*- energy is the only term within Kohn-Sham DFT which cannot be calculated from classical models. If an exact expression for the *xc*-energy was known, Kohn Sham DFT would be an exact method. Unfortunately such an expression is not known, hence much of the development of DFT in the last 50 years has focused upon the development of improved approximations to *xc*-energy, these are outlined in Section 2.5.3. Once the *xc*-energy has been determined the ground state energy of the system can be found. Determining the ground state energy involves solving a set of one electron Kohn-Sham equations iteratively, in a similar manner to finding solutions in Hartree-Fock theory. Many of the early DFT codes worked on modified Hartree-Fock systems because the minimisation procedure is so similar, the one electron Kohn-Sham equations are in the form:

$$\hat{f}_i^{KS}\emptyset_i = \left(-\frac{1}{2}\nabla^2 + V_{KS}(\boldsymbol{r})\right)\emptyset_i = \varepsilon_i\emptyset_i \tag{2.36}$$

2.5.3 Exchange-Correlation (*xc*-) Functionals

Determination of the contribution of E_{xc} is the main obstacle in any DFT calculation. The main focus of DFT research and development over the last 50 years or so has been towards ascertaining which form a functional to approximate E_{xc} should take. Many xc-functionals have been proposed and developed both empirically and from first principles. In this section an overview of the form of the currently available approximations to the xc-functional is given, with particular attention to xc-functionals used in the research presented in this thesis. An overview of the development in complexity of xc-functionals is summarised in Perdew's Jacob's ladder, shown in Figure 6.

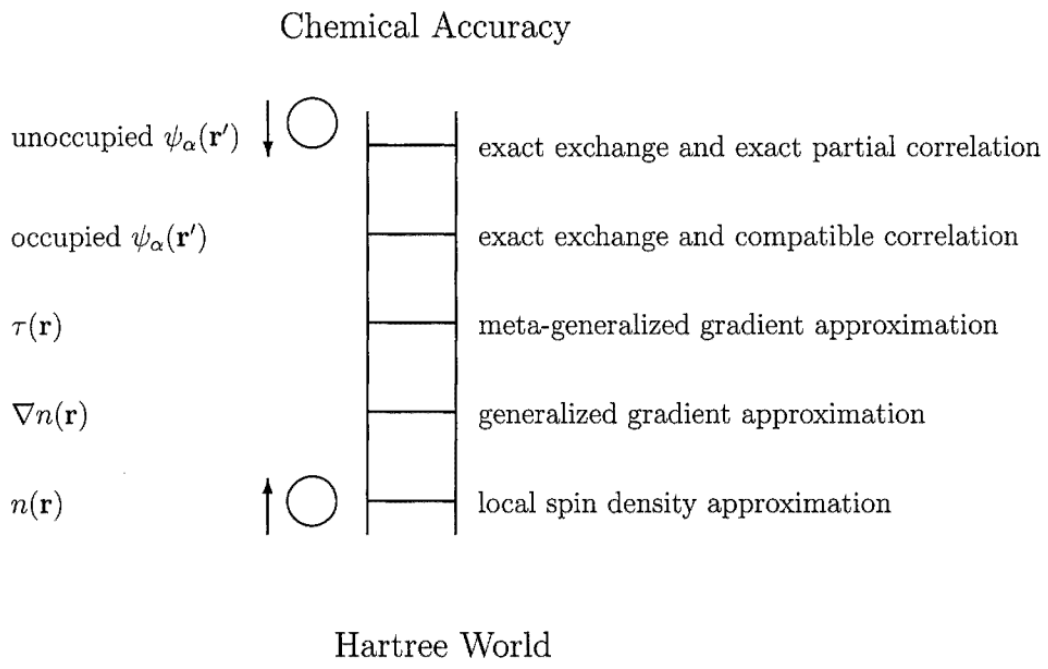

Figure 6: Jacob's ladder for the systematic improvement of DFT functionals [reproduced with permission from ref 76]

2.5.3.1 Local Density Approximation (LDA)

The local density approximation (LDA) is the simplest approximation to the *xc*-functional, it depends solely upon the value of electron density at each point in space. In LDA it is assumed that the *xc*-energy, as function of ρ, is the same as the *xc*-energy of a homogenous gas (HEG) at the same density, the *xc*-energy in LDA can thus be expressed:

$$E_{xc}^{LDA}[\rho] = \int \rho(\boldsymbol{r})\epsilon_{xc}^{unif}\big(\rho(\boldsymbol{r})\big)\, d\boldsymbol{r} \tag{2.37}$$

Where ϵ_{xc}^{unif} is the exchange-correlation energy density for a single electron in the interacting homogenous electron gas of density $\rho(\boldsymbol{r})$. In practice the contribution from exchange (E_x) and correlation (E_c) are considered separately.

$$E_{xc}^{LDA}[\rho] = E_x^{LDA}[\rho] + E_c^{LDA}[\rho] \tag{2.38}$$

The largest contribution to the *xc*- energy is from the exchange term whose analytical form can be expressed exactly;

$$E_x^{LDA}[\rho] = -\frac{3}{4}\left(\frac{3}{\pi}\right)^{1/3} \int \rho^{4/3}(\boldsymbol{r})\, d\boldsymbol{r} \tag{2.39}$$

The correlation term is however much more difficult to express analytically, it is obtained most commonly by fitting to stochastic data from quantum Monte Carlo simulations[77,78]. Given the simplicity of LDA, it's results are of surprisingly high quality, it however typically overbinds molecules by around 30kcal/mol, which makes it unacceptable for contemporary research[79].

2.5.3.2 Generalised Gradient Approximation (GGA)

An improvement in accuracy over LDA can be obtained by the Generalised Gradient Approximation (GGA). Similarly to LDA, GGA depends upon the values of density at each point in space, unlike the LDA however, GGA also depends upon the gradient of the electron density.

$$E_{xc}^{GGA}[\rho(\boldsymbol{r})] = \int \rho(\boldsymbol{r})\epsilon_{xc}\big(\rho(\boldsymbol{r}), \nabla\rho(\boldsymbol{r})\big)\ d\boldsymbol{r} \tag{2.40}$$

Most GGA functionals are developed as correction terms which are added to LDA functionals to account for the gradient in electron density. Whilst there is essentially only one LDA functional, there are many GGA functionals, developed both empirically and from first principles. Common empirical GGA functionals include B88[80] which is included in the popular hybrid xc-functional B3LYP, and common non-empirical functionals include PBE[81] which is used extensively throughout the research presented in this thesis, and is also included in the hybrid *xc*-functional PBE0.

GGA is found to generally be much more accurate than LDA for predicting total energy[82], lattice constants[82] and barrier heights[83], and is better suited to inhomogeneous electron densities. The GGA approach can be further improved by also considering the second order derivative of electron density ($\nabla^2\rho(\boldsymbol{r})$) or alternatively, and more commonly, kinetic energy density. This is known as meta-GGA and is the third step in Jacob's ladder of DFT functionals in Figure 6, the most popular meta-GGA functional is TPSS[84]. Meta-GGA functionals attempt to give the accuracy of hybrid functionals without the associated extra computational cost.

2.5.3.3 Hybrid Functionals

The next step up in complexity beyond GGA functionals on Jacob's ladder are hybrid functionals. They are referred to as being hybrid because they are *xc*–functionals which are a hybrid of LDA, GGA, and exact exchange obtained from Hartree-Fock theory. There are both benefits and disadvantages of hybrid functionals, they usually produce higher quality results than GGA functionals but this comes with significantly increased computational costs, typically up to 10-100 times[85]. The significantly increased computational cost is due in part to the increased mathematical rigour in calculating exact exchange, and additionally, approximations such as the resolution of the identity (RI-J) method (see Section 2.5.3.5) cannot be exploited as efficiently. The optimum amount of exact exchange to be included, and which LDA and GGA functionals it should be used alongside, is still a point of ongoing debate and research, as such there are too many hybrid functionals to describe here, the reader is however directed to a useful review article by Mardirossian *et. al.*[86] for more information. Two of the most

popular hybrid functionals are however PBE0[87], which is based upon the versatile non-empirical GGA *xc*-functional PBE, and is the most widely used hybrid functional in this research, and B3LYP[88] which is based upon the semi-empirical B88[80] GGA *x*-functional along with correlation from the LYP[89] functional and a contribution from LDA, they are constructed as follows;

$$E_{xc}^{PBE0} = \frac{1}{4}E_x^{HF} + \frac{3}{4}E_x^{PBE} + E_c^{PBE} \quad \textbf{(2.41)}$$

$$E_{xc}^{B3LYP} = E_x^{LDA} + a(E_x^{HF} - E_x^{LDA}) + b(E_x^{B88} - E_x^{LDA}) + E_c^{LDA} + c(E_c^{LYP} - E_c^{LDA}) \quad \textbf{(2.42)}$$

Where a = 0.20, b = 0.72, and c = 0.81

Due to the nature of their construction, B3LYP is found to perform better for elements around those that were used in the empirical fitting to form the functional, whereas PBE0 is found to perform better as an all-round functional, particularly useful for heavy elements[90].

There are a wide range of *xc*-functionals available for use in DFT that vary greatly in complexity, accuracy, and computational cost. The most commonly used functionals are fundamentally based on simple models of HEGs, with additional accuracy gained from consideration of the gradient of density in the HEGs and inclusion of exact exchange obtained from Hartree-Fock calculations. It is unlikely there will ever be an exact *xc*-functional, the research into improved functionals is however continually ongoing.

2.5.3.4 Dispersion Correction

Despite significant advances in DFT, particularly the development of increasingly accurate and complex *xc*-functionals, DFT is still inherently deficient at describing non-bonding interactions, especially van der Waals (dispersion) interactions. The incomplete description of dispersion interactions can significantly affect the accuracy of DFT calculations. The source of the deficiency is two-fold. Firstly, *xc*-functionals describe only the local properties of the exchange-correlation energy, so breakdown for long-range effects. Secondly, dispersion can be viewed as the attraction between

electrons in one region responding to instantaneous changes in charge density in another region, in DFT and other mean field theories however, electrons interact only with total charge density in a mean-field way.

The simplest way to include dispersion energies into DFT calculations is through the addition of a dispersion energy term. This can be described by the general expression:

$$E_D = -\sum_{A,B} f(r_{AB}, A, B) C_6^{AB} / r_{AB}^6 \quad \textbf{(2.43)}$$

Where E_D is the dispersion energy, C_6^{AB} is the dispersion coefficient, which depends on the position of atoms A and B, r_{AB} is the interatomic distance between atoms A and B, and $f(r_{AB}, A, B)$ is a *xc*-functional dependent dampening function which reduces to zero at very small interatomic distances.

The total energy can then be calculated using the general expression:

$$E_{total} = E_{DFT} + E_D \quad \textbf{(2.44)}$$

Where E_{DFT} is the energy calculated using DFT and E_D is the dispersion correction energy obtained using equation (2.43).

2.5.3.5 Resolution of Identity

Resolution of identity (RI-J) is an approximation which can be used in DFT to significantly increase the speed of calculations, without loss of accuracy[91]. The increased efficiency is obtained through the use of modified terms for the description of Coulomb interactions (J). This involves the use of auxiliary basis sets, which can be predefined, to form an approximated electron density which requires significantly fewer integrals to solve[92].

2.6 Geometry Optimisation and Vibrational Frequency Analysis

The chapter up to this point has outlined the theoretical background to computational chemistry and how the theories have evolved, I now move on to the practical applications exploited in this thesis, and some of the analysis techniques used.

A geometry optimisation can be carried out to obtain information about equilibrium geometries which are identified as local energetic minima on potential energy surfaces (PES), and transition states which are identified as saddle points on PES. Transition states are not sought within this research, so the methods used to obtain them are not explicitly discussed, much of the following mathematics and explanation is however universal for finding all stationary points on a PES. The main discussion is on the methods used to obtain and identify energetic minima, and how their correspondence to minima on a PES can be verified by vibrational frequency analysis. The motivation for performing geometry optimisation to find energetic minima, the end point in such calculations is often a true representation of the structure a molecular system is found in nature, knowledge of such structures is useful for a range of physical and experimental investigations.

Geometry optimisations, which is the main use of DFT in this thesis, is the process of finding the arrangements of atoms for which the net inter-atomic force on each atom is zero within a given tolerance, and the PES of the molecular system is at a stationary point. Stationary points are identified by studying the derivatives of the energy of the PES with respect to the position of nuclei. When the PES is at a stationary point the first derivative with respect to nuclear position vanishes, that is the forces acting on each nucleus are in equilibrium or the net force acting on them is acceptably close to zero. The nature of the stationary point is determined by the second derivatives of the energy, the second derivatives of energy in all directions are positive for local minima, there is a curvature in one direction which is negative for transition states.

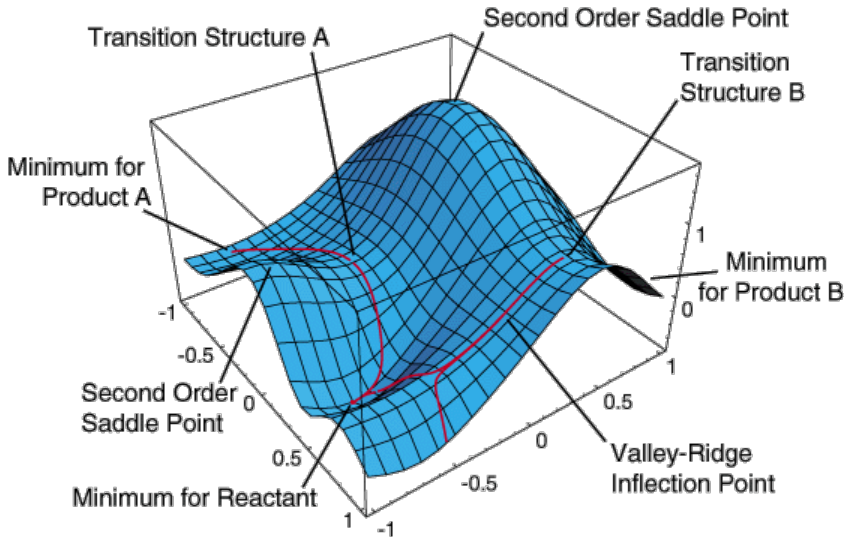

Figure 7: The potential energy surface (PES) showing minima corresponding to the optimised molecule structures and saddle points corresponding to transition states [reproduced with permission from ref 93]

Figure 7 provides a graphical representation of a PES with key features such as energetic minima relating to reactants and products, and saddle points relating to transition states highlighted. In this graphical representation it is easy to see how molecular systems evolve on a PES from reactant to products, and how each of the geometric features can be used to understand the system, i.e. the gradient at any point on the surface is related to force, and points of zero gradient (and zero force) are energetic minima or transition states. There are a range of mathematical techniques which can be employed to find equilibrium geometries on PES, the technique used within Turbomole, and the DFT calculations presented in this thesis is based up on quasi-Newton-Raphson methods[94,95].

Newton-Raphson techniques are very popular in geometry optimisation methodologies, although they are generally more computationally involved than other less popular techniques such as steepest descents, they are generally fast and reliable. They perform particularly well for convergence close to points of zero gradient. The Newton-Raphson methods use the second derivatives of energy to establish points of minimum and maximum energy on the PES, which for quadratic functions is an exact technique. The shape of PES are almost quadratic very close to energetic minima which is one of the reasons why the technique works so well.

Newton-Raphson methods require as starting input an exact gradient vector, and an approximation of the Hessian matrix (a square matrix of second order partial derivatives of scalar valued functions, also sometimes referred to as a "functional determinant"), the quality of which determines the rate at which convergence towards an optimised structure occurs. Computational costs can be greatly reduced by deriving the initial Hessian Matrix from preliminary calculations carried out using less sophisticated functionals or small basis sets. Such a method is used to a certain extent within the research presented in this thesis, data of PBE0 *xc*-functional quality in results chapters is obtained from calculations with an initial geometry and other parameters derived from equilibrium geometry in calculations of PBE quality. Geometry optimisations in general terms are performed iteratively, a flow chart of the steps involved in the Newton-Raphson method is shown in Figure 8.

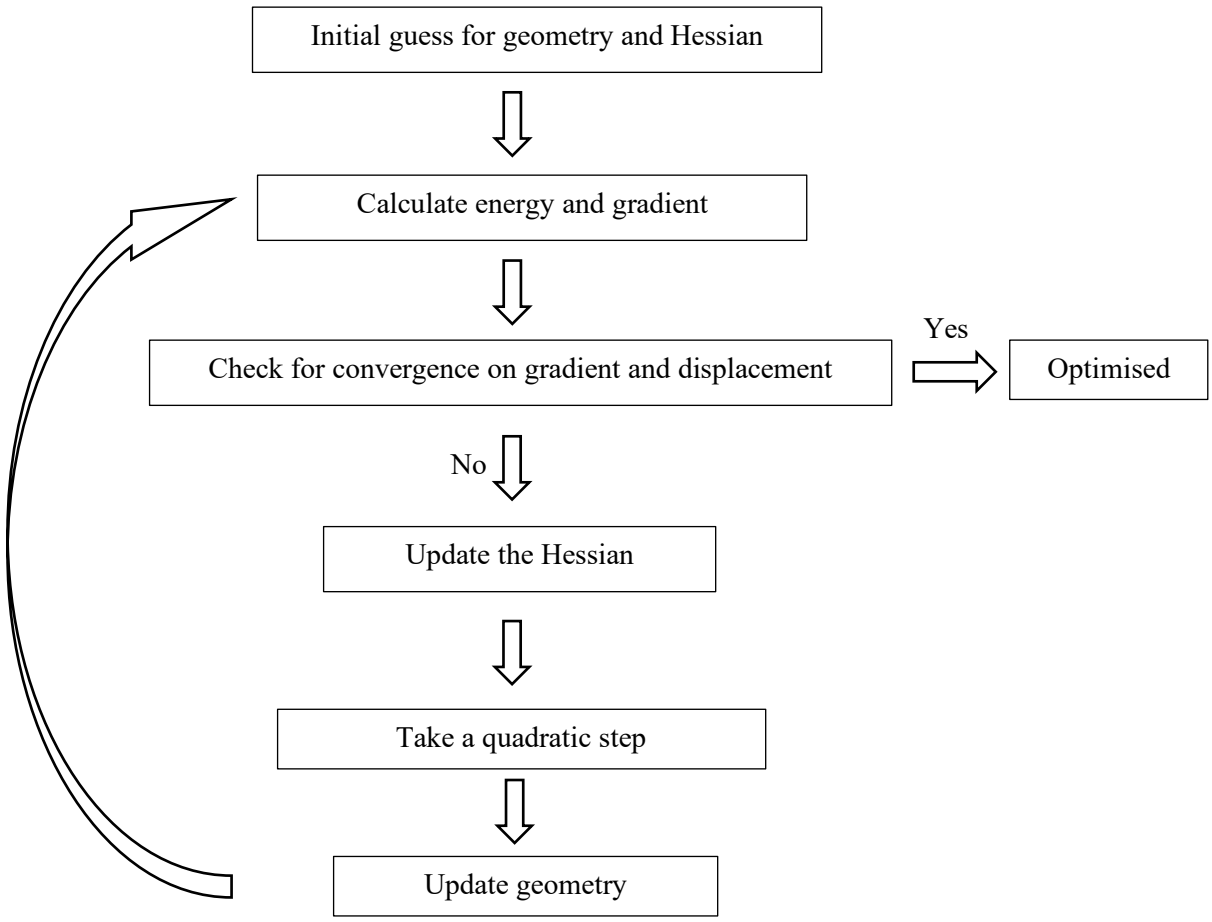

Figure 8: Geometry optimisation flow chart for the Newton-Raphson technique

Within each iteration (geometry optimisation step) the updated Hessian is computed from gradient history, leading to estimated Hessian matrices which become asymptotically more accurate as the gradient history grows. Using this approach means even poor initial Hessian matrices leads to geometry optimisations which are completed in a reasonably short number of steps. Further improvement to the accuracy and efficiency of geometry optimisations can be achieved by introduction of controls and restrictions which set requirements on such things as optimisation step length, and ensure that the updated Hessian after each step length has the correct eigenvalue structure.

The gradient and the Hessian matrix from optimised geometries can also be used to confirm the character of energetic minima and locate transition states[96], through vibrational frequency analysis. The energy landscape of the PES can be approximated almost exactly by a harmonic potential around a stationary point. The Hessian constructed from the second derivatives of the energy is known as the force constant matrix (in which forces act in the opposite direction to the gradient). When converted to Cartesian coordinates, the eigenvectors of the mass-weighted Hessian force constant matrix correspond to normal modes of vibration, plus five or six modes for translation and rotation. Vibrational frequencies are proportional to the square root of the eigenvalues of the mass weighted Hessian, hence vibrational frequencies at energetic minima are real, corresponding to the bottom of a potential well, where all eigenvalues of the Hessian corresponding to molecular vibrations are positive. A transition states on a PES is at the point of zero gradient in which the PES is a maximum in one direction (along the reaction path), which corresponds to a single negative eigenvalue in the Hessian, and a minimum in all other direction. Transition states are hence identified by a single imaginary vibrational frequency.

2.7 Charge Analysis

Often in computational chemistry it is desirable to obtain information about the electronic configuration and net charge associated with each atom in a polyatomic molecular model, such information can provide increased understanding of chemical phenomena and help to correlate it with experimental results.

The most commonly used method for analysing the distribution of net charge across atoms in polyatomic molecules is Mulliken analysis[97]. In Mulliken analysis, charges are obtained from multiplications of overlap and density matrices, which result directly from single determinant molecular wave functions calculated using MOs from the LCAO method. Mulliken analysis is however prone to errors, and often provides unreliable charge distribution characteristics. It is known for example to predict unphysically negative values for charge, due to the nonorthogonal basis sets used in modern calculations. It is also reported to give an unreasonable physical picture for the charge distribution in compounds with significant ionic character, and is highly basis set dependent[98]. For these reasons, amongst others, the preferred method for

charge analysis in calculations presented in this thesis, is natural population analysis[98–100] (NPA) which is available in Turbomole at similar computational cost to Mulliken analysis.

NPA is a method of population analysis based on the construction of natural atomic orbitals (NAOs) (from which its name originates) for the molecular system in an arbitrary atomic orbital basis set. The NAOs, and NBOs (natural bond orbitals) which they can be used to construct, correspond to natural Lewis structures (allowing a maximum orbital occupancy of 2), and are orthonormal, hence they are inherently positive, and occupations sum correctly to the total number of electrons. Additionally, the construction of NAOs is intrinsic to the wave function rather than the atomic basis set used, so is not susceptible to the basis set dependency encountered in Mulliken analysis. Construction of NAOs in NPA can be summarised in two steps. The first step involves the diagonalization of an atomic angular symmetry sub-block of the density matrix, the second involves the removal of interatomic overlap.

Implementation of the first step leads to a set of "pre-NAOs", which can be divided in to two sets based on their occupancy. There is a "minimal set" corresponding to high occupancy orbitals (close to 2.0), and a "Rydberg set" consisting of formally unoccupied orbitals (close to 0.0). The Rydberg set does not necessarily have a zero occupation, particularly in molecular environments, but they have only a secondary role in describing the electron density and charge. The overlap between pre-NAOs in adjacent centres in the Rydberg set increases without limit with increased basis set size so their orthogonalisation is treated separately from the "minimal set".

In the second step, a method of "occupancy-weighted-symmetric-orthogonalisation", developed specifically for NAO analysis is employed[98]. If occupancy weighting is not employed in the removal of the interatomic overlap, the desired NAOs are not obtained. The pre-NAOs in the occupied "minimal set" describe the atomic electron density in the SCF approximation exactly, the "Rydberg set" by contrast provides little accurate description of electron density, hence much greater weighting is given to the occupied pre-NAOs. NBO populations, and hence charge information, is obtained from the sum of the resulting NAOs calculated by the above method in the atom.

2.8 Solvation Models

The methodology and background theory presented so far in this chapter has focused on the study of properties in the gas phase, in solution these properties are likely to be significantly different. These differences have inspired the development of solvation models for quantum chemical calculations. The intention of solvation modelling is to include solvation effects into calculations which provide sufficient representation of the effect of a solvent environment on molecules, without the need for prohibitively complicated mathematics or unreasonable large computational costs.

Whilst it is possible to model a solvent explicitly, that is explicitly include a large number of solvent molecules, such calculations are incredibly computationally demanding, and do not always guarantee accurate solvation energies. This is due to the importance of long-range electrostatic interactions in solvent interactions which are not typically described well by DFT[101], for this reason solvation effects are typically included implicitly. Implicit solvation models, in general terms, replace a large number of explicit solvent molecules with a continuum dielectric which is a representation of the effect of the solvent molecules. The use of a continuum dielectric results in the loss of all structural information for the solvent but does provide a very practical solution for emulating the important solvent effects. The basic principle shared by all implicit solvation models is the construction of an interacting dielectric field or equivalent, which has a cavity for the solute molecules. A graphical representation of explicit and implicit solvation is shown in Figure 9.

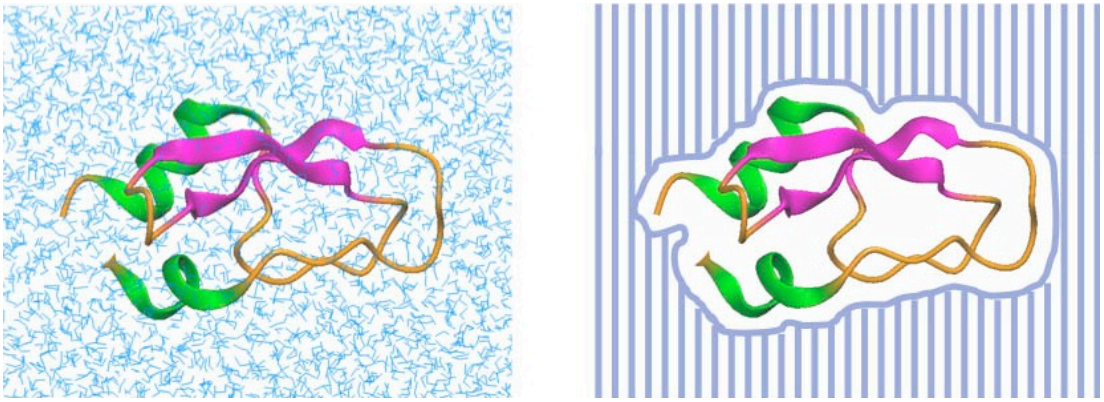

Figure 9: Basic comparison of explicit and implicit solvation around a protein [reproduced with permission from ref 102]

One of the earliest implicit solvation models was based on the work of John Kirkwood and Lars Onsager. The Kirkwood-Onsagar model[103–105] employs a spherical (ideal) cavity and an electrostatic potential represented by a single-centre, multi-pole expansion. The use of an ideal cavity allows for analytical solutions of Poisson's equations to be found exactly, which is mathematically convenient, but they do not fit the shape of anything other than very simple solutes well. The use of an ideal cavity has hence been replaced more commonly with the use of a molecular shaped cavity. Polarisable continuum models (PCMs) is the general term given to the class of implicit solvation models which have been developed more recently employing cavities more closely matched to the shape of molecules. PCMs improve upon the Kirkwood-Onsagar type approach in two ways, firstly, they employ cavities constructed of a series of atom-centred spheres rather than a simple sphere which matches the solute shape much more closely, and secondly, the exact electron density of the solute is used, rather than a multi-pole expansion, to polarise the continuum. The complete history and evolution of implicit solvation models is beyond the scope of this thesis but is covered in literature review by Tomasi and collegues[106]. The discussion here now focuses specifically on the conductor-like screening model (COSMO)[107] which is a PCM solvation used extensively within the research presented in this thesis.

COSMO is widely used throughout computational chemistry, it is included as standard in many popular codes such as Gaussian[108,109] and ADF[110], amongst others, and most importantly for the research presented in this thesis, Turbomole. The basic principle used in the development of the COSMO model and what sets it apart from many other dielectric continuum models, is the use of a scaled conductor model to approximate the dielectric fields. The use of a scaled conductor model rather than modelling a dielectric field allows the use of much more simple boundary conditions. The total potential vanishes at infinity in a conductor making them much less complicated to model than a rigorous dielectric continuum. The deviation in results between an approximation based on the model of a conductor and a rigorously defined dielectric continuum is found to be negligible for strong dielectrics (dielectric constant $\varepsilon > 20$) and less than 10% for non-polar solvents ($\varepsilon \approx 2$)[111], making it a good approximation for all systems.

The cavities used in COSMO are arbitrary in shape, they are produced by use of a generalised solvent-accessible surface (SAS), which is based on van der Waals radii of the atoms in the solute increased by 20%. SAS are a popular method for defining cavities in continuum solvent models as they produce cavities which are well matched to the solute shape. As mentioned earlier, the use of non-ideal (that is non-spherical or non-elliptical) cavities does not allow for the analytical calculation of solvation energy, the cavity is hence described by a surface constructed from finite elements known as segments, each segment of the cavity has a constant screening charge density which corresponds to a screening charge, by the expression:

$$q_i = s_i \sigma_i \tag{2.45}$$

Where q_i is the screening charge, a dampening effect from the presence of mobile charge carriers of the segment (i), s_i is the area of the segment and σ_i is screening charge density. A matrix is defined to represent the screening charge by introduction of the m-dimensional vector $\boldsymbol{q} = (q_1, \ldots, q_m)$, where m is the total number of segments in the cavity. The Coulomb interactions of the screening charge are represented by the symmetric matrix $\boldsymbol{A}$ which accounts for the self-interaction of the screening charge, a conductor boundary equation for a vanishing conductor potential can then be formed:

$$0 = \boldsymbol{\Phi^{tot}} = \boldsymbol{\Phi^{X}} + \boldsymbol{A q^{*}} \tag{2.46}$$

Where $\boldsymbol{\Phi^{X}}$ is the vector for the electrostatic potential of the solute X on each segment, and $\boldsymbol{q}^*$ denotes the screening charges in a conductor, i.e. corresponding to an infinite dielectric strength ($\varepsilon = \infty$), for a finite dielectric $\boldsymbol{q}^*$ is scaled by a function $f(\varepsilon)$ to give:

$$\boldsymbol{q} = f(\varepsilon)\boldsymbol{q}^{*} = \frac{\varepsilon - 1}{\varepsilon + x}\boldsymbol{q}^{*} \tag{2.47}$$

Where x can be any value between 0 and 1, but is most commonly 0.5 in Turbomole calculations. Combining equations (2.46) and (2.47) gives;

$$\boldsymbol{A q} = -f(\varepsilon)\boldsymbol{\Phi^{X}} \tag{2.48}$$

Which directly relates screening charge to the electrostatic potential of the solute, and hence to the charge density of the solute. Solvation effects from COSMO are implemented into DFT (or HF) to be solved self-consistently by adding the electrostatic potential obtained by solving equation (2.48) as an external potential. The polarisation energy which is required to generate the screening charges is accounted for by the subtraction of half of the solute-continuum interaction energy. A graphical representation of the SCF cycle in DFT with solvation effects from COSMO included is given in Figure 10, Q is used as the general notation for solute density.

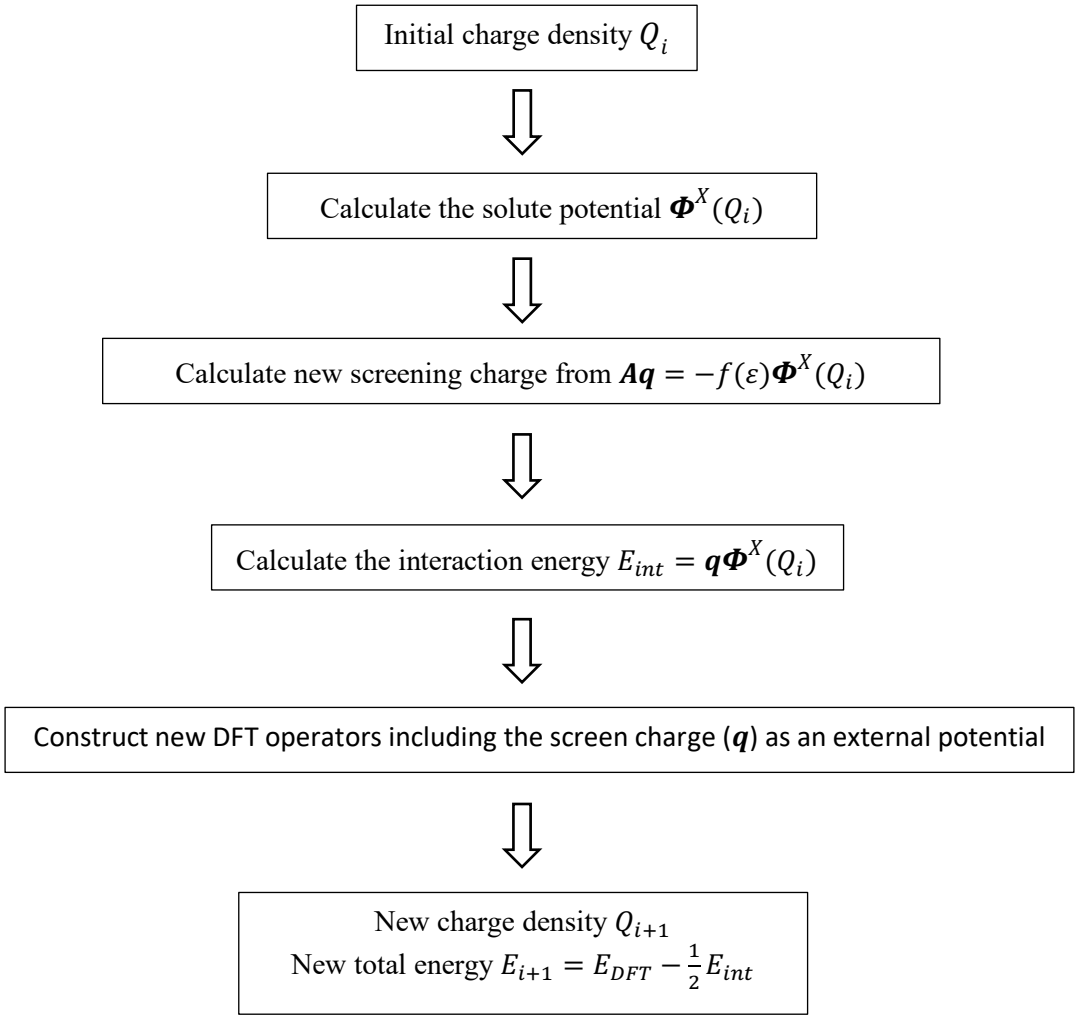

Figure 10: Flow chart of the SCF cycle in DFT calculations with COSMO

Chapter 3 Development of a Graphene Oxide (GO) Model Using Density Functional Theory (DFT)

3.1 Introduction

Graphene is a one atom thick, two dimensional layer of sp^2 hybridised carbon which has been shown to display a range of unique thermal, electrical, and mechanical properties[112,113]. Whilst the existence of unique and superior properties of graphene had been predicted for some time, it was not successfully isolated until 2004, work for which Geim and Novoselov were awarded the 2010 Nobel Prize in physics. Since its discovery, graphene has been studied extensively for a wide range of applications, which have shown favourable results. Whilst there is great interest in the use of graphene, large scale production is still however very difficult, which is a barrier to scalable commercial use, similar carbon materials are hence attracting increased research attention in the hope of exploiting some of their graphene-like properties. Amongst those receiving particular attention is the multifunctional hybrid material graphene oxide (hereafter GO). GO is a 2-dimensional carbon material which displays many of the desirable physical characteristics of graphene such as large surface area, it also has oxygen containing functional groups across its basal planes and along its edge, which give it further novel uses[114]. The large scale production of GO is inexpensive and much more trivial than graphene, and can be carried out in an environmentally friendly way[6,7]. GO is also being explored as a possible intermediate in a route to large scale production of graphene[115] and for environmental applications, one such application is as a scavenger in nuclear decommissioning, which is discussed in Chapters 4 and 5.

3.2 Literature Review

The exact chemical structure of GO is still a point of debate, due mainly to the complexity of the material and lack of precise techniques to characterise such materials. The difficulties in determining the physical structure of GO and the experimental characterisation techniques which have been used are presented in Chapter 1. Computational and theoretical studies are contributing towards a greater understanding of the underlying structure and properties of GO. This chapter provides

one such study into the formation and properties of GO based on its most widely accepted form, the Lerf-Klinowski model, which includes hydroxyl, epoxy and carbonyl functional groups on the GO surface, and carboxylic acid, carbonyl and hydroxyl groups along its edges. The model presented in this chapter does not consider the arrangement of functional groups along the GO edge, so carbon atoms are terminated with hydrogen atoms. Carbonyl groups are also thought to be relatively rare on GO surfaces, so are not included in the model presented in this chapter (see Figure 11).

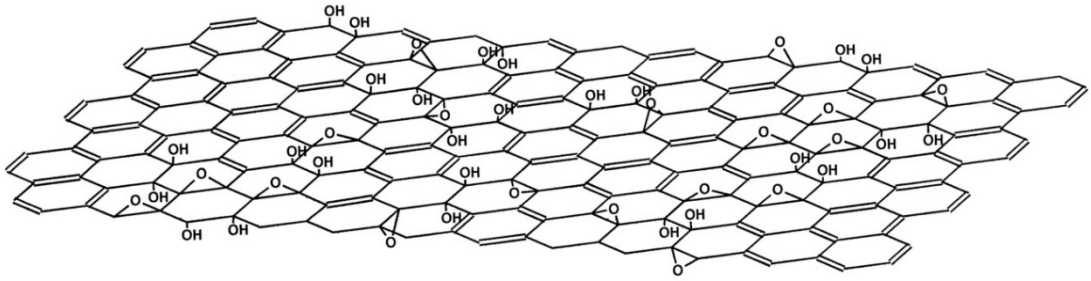

Figure 11: The Lerf-Klinowski structural model for GO [reproduced with permission from ref 20]

A density functional theory (DFT) study by Boukhvalov *et. al.*[116] found that the binding of hydroxyl functional group pairs to graphene sheets is most stable when binding occurs on neighbouring carbon atoms and when the functional groups are on the opposite side of the graphene flake. This was also observed in a separate investigation by Ghaderi *et. al.*[117] who also found that the binding energy of individual functional groups increases with increased surface coverage, consistent with an increase in calculated C-C bonds from 1.42 Å, the bond length for graphene[30], to 1.54 Å, the C-C bond length in diamond[118], and hence a transition towards rehybridisation of carbon atoms from sp^2 to sp^3. Tachikawa *et. al.*[119] found in a separate investigation that the binding energy of single OH radicals to GO surfaces is also dependent on the GO flake size. They investigated GO flakes with 7, 14, 19, 29, and 37 carbon rings and calculated binding energies of 0.18 eV, 0.41 eV, 0.29 eV, 0.32 eV, and 0.30 eV respectively, at the B3LYP/6-31(d) level of theory. They concluded that the binding energy increases and reaches a limiting value for large GO flakes, the highest binding energy is however calculated for the flake containing

14 carbon rings, and the flake containing 29 carbon rings also fails to fit the trend. Although not highlighted by the authors, this is presumably due to a geometric effect which would not manifest itself in larger flakes, the flakes containing 7, 19, and 37 carbon rings all have the same circular shape, whilst flakes containing 14 and 29 carbon rings cannot produce such a shape. Another DFT study by Lahaye *et. al.*[120] reported that the 1,3-ether group proposed in many GO model is energetically unstable so does not exist, providing support for the Lerf-Klinowski model which is most accepted. They also reported that OH groups are needed to stabilise the GO surface because epoxy groups create too much tension on the carbon lattice to be the sole functional group.

It is discussed in Chapter 1, that the accurate structural analysis of GO has been one of the most difficult problems in the field of graphite compounds and derivatives research, and is still an ongoing area of debate. This has arisen for many reasons, including GO being highly hygroscopic, and the presence of water makes results obtained from many analysis techniques less certain. There is also significant sample to sample variability, which is dependent on a number of factors, such as method of synthesis used, the conditions during synthesis, and variability in graphite flakes. The accepted structure for GO has evolved from early characterisation by Brodie and Schafhaeutl to the now almost universally accepted Lerf-Klinowski model based on the available characterisation techniques of the time. Early structural models for GO were based mostly on elemental analysis by combustion experiments, IR spectroscopy, X-ray and electron diffraction techniques, and chemical techniques such as methylation and ion exchange. More recently the availability of such characterisation techniques as NMR and electron microscopy, and advancements toward more sophisticated versions of traditional analysis techniques such X-ray and IR spectroscopy, and investigations in computational chemistry have improved our understanding of GO. The debate around the structure of GO is however still ongoing. The history of GO structural understanding has been paved with contradicting results and uncertainty, on reflection however the Lerf-Klinowski model best represents the majority of experimental results, and is hence the most widely accepted GO form, and the one used in the investigations presented in this thesis.

3.3 Computational Details

Geometry optimisations were performed using density functional theory (DFT) using version 6.5 of the TURBOMOLE[95] code. The PBE[81] exchange-correlation (*xc*-) functional, which is based upon the generalised gradient approximation (GGA), along with the related, and more computational expensive PBE0[87] hybrid-GGA *xc*-functional, which incorporates a 25% proportional of exact (Hartree-Fock) exchange, were used throughout. The functionals used do not include correction for dispersion energies. The def2-TZVP[121] atom-centred Ahlrich basis set of polarised triple-ζ quality for all atomic species was used in all calculations, calculations to correct for basis set superposition error were also not carried out.

Consideration of solvation effects were made using the conductor-like screening model (COSMO) with default parameters, *i.e.* a relative permittivity of $\varepsilon_r = \infty$, which is considered a suitable approximation for water, and molecular cavities constructed of spheres with radii 2.00 Å, 1.72 Å, and 1.30 Å for C, O, and H, respectively.

Numerical vibrational frequency calculations were carried out on all geometries optimised at the PBE level of theory without consideration of solvation effects, in order to confirm correspondence to local energetic minima. Correspondence to energetic minima was assumed for all other model chemistries. This assumption was made due to the large computational cost associated with numerical frequency analysis, especially those carried out with hybrid functionals.

3.4 Results and Discussion

3.4.1 Bulk Surface Formation

3.4.1.1 Hydroxylated Graphene Surfaces

The stability of single oxygen containing functional groups on graphene nano-flakes was investigated. The representative graphene flakes considered have n = 7, 19 and 37 carbon rings, corresponding to coronene ($C_{24}H_{12}$), circumcoronene ($C_{54}H_{18}$), and circumcircumcoronene ($C_{96}H_{24}$) respectively (as in Figure 12). Whilst graphene oxide

(GO) nano-flakes are typically in the range of tens of nanometres to several micron in diameter[122], significantly larger than those presented here, the aim is to understand the significance of using a smaller model system on the binding of hydroxyl groups and the formation of epoxy groups on GO surfaces whilst making consideration of computational costs. Computational costs are prohibitive to modelling GO nano-flakes with realistic dimensions in DFT.

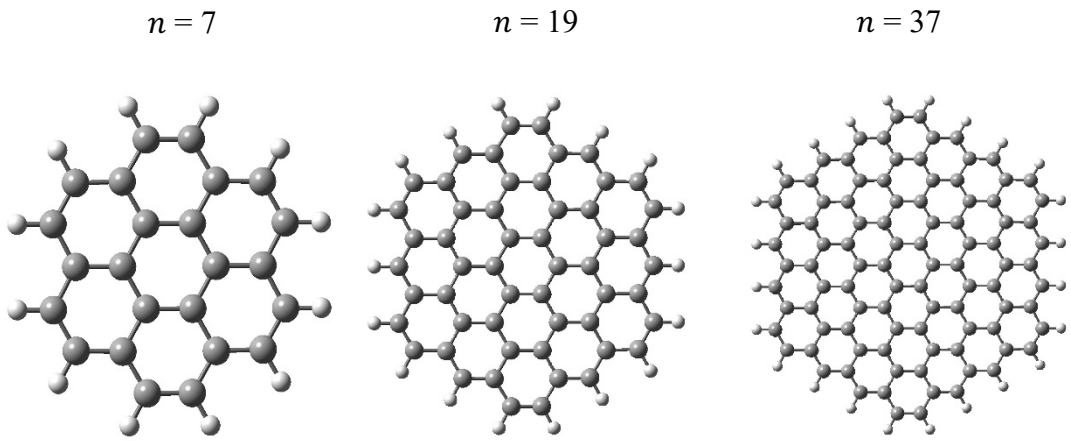

Figure 12: Model graphene nano-flakes incorporating 7, 19 and 37 carbon rings. Optimised at the PBE/TZVP level of theory.

The binding energy of a single hydroxyl group to the GO nano-flake surface was calculated in the conventional way using the standard formula:

$$E_b = E_{C_nH_mOH} - E_{C_nH_m} - E_{OH} \quad \textbf{(3.1)}$$

Where $E_{C_nH_mOH}$ is the total energy of the OH-bound nano-flake (see Figure 13), $E_{C_nH_m}$ is the energy of the pristine nano-flake, and E_{OH} is the energy of the hydroxyl radical.

Table 2: Binding energy of a single hydroxyl group bound to the graphene nano-flake surface as a function of flake size. All values are in eV. GP = Gas Phase. COSMO = continuum solvent.

Flake Size	PBE		PBE0	
	GP	COSMO	GP	COSMO
7	-0.49	-0.42	-0.26	-0.18
19	-0.63	-0.57	-0.37	-0.30
37	-0.65	-0.59	-0.38	-0.31

Calculated binding energies are presented in Table 2. It appears that the binding energy of a single hydroxyl group converges towards a maximum value as the size of the nano-flake increases, behaviour that can be attributed to the electronic structure of the flake converging on that of bulk graphene, and has also been reported previously in the literature[119]. The results are in excellent agreement with those reported elsewhere[119], results from a similar molecular model have been reported for n = 7, 19 and 37 nano-flakes of -0.18 eV, -0.29 eV and -0.30 eV respectively, for geometries optimised using the B3LYP hybrid *xc*-functional, displaying the same convergence towards a maximum value. Results are also in excellent agreement with those reported from periodic calculations of comparable quality, calculated values have been reported of -0.67 eV[123] and -0.70 eV[120] from calculation at the PW91 and PBE levels of theory, respectively. This goes some way towards establishing the validity of the molecular models presented here with existing research, particular confidence is obtained from comparison of values for n = 37 nano-flake and those for infinite systems obtained using periodic boundary conditions (PBC). The calculated binding energy for the n = 37 nano-flake is in very close agreement with values calculated from GO models using PBC of comparative quality, whilst there is very little increase between the value calculated for the n = 19 and n = 37 nano-flake presented here, suggesting the binding energy on both nano-flakes is close to the asymptotic value.

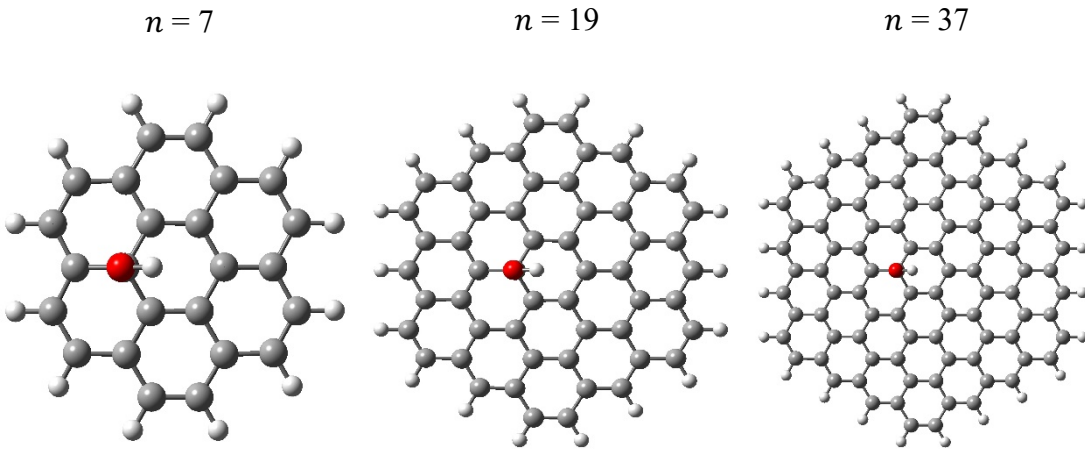

Figure 13: GO nano-flakes incorporating a single OH functional group at the central ring. Optimised at the PBE/TZVP level of theory.

When comparing binding energies calculated using the PBE and PBE0 *xc*-functionals, it is noted that there is a significant reduction in calculated binding energies when using

PBE0, which may be interpreted as over-binding with PBE, as has been reported previously in the literature[124]. Calculated C-O_{OH} bond lengths presented in Table 3 however, show that the PBE0 *xc*-functional predicts significantly shorter C-O_{OH} bonds, which is indicative of the formation of stronger bonds. It is noted also that the difference in calculated C-O_{OH} bond lengths between PBE and PBE0 is insensitive to nano-flake size.

Table 3: C-O_{OH} bond length for a single hydroxyl group adsorbed on a GO nano-flake surface. All values are in Å. GP = Gas Phase. COSMO = continuum solvent

Flake Size	PBE		PBE0	
	GP	COSMO	GP	COSMO
7	1.502	1.512	1.464	1.472
19	1.501	1.511	1.463	1.470
37	1.500	1.510	1.463	1.469

Single point energy calculations were performed on graphene nano-flakes held at their adsorption geometries with the hydroxyl group removed. These calculations give an estimation of the energy associated with nano-flake deformation in the adsorption process. Deformation energies are presented in Table 4. There are significantly larger (~0.2 eV) deformation energies associated with geometries optimised using the PBE0 *xc*-functional than those produced using PBE. It can therefore be stated with confidence that deformation energy is the main contributing factor to the smaller calculated binding energies using PBE0, rather than over-binding which has been previously associated with the PBE functional.

Table 4: GO nano-flake deformation energy for absorption of a single OH group. All values are in eV. GP = Gas Phase. COSMO = continuum solvent

Flake Size	PBE		PBE0	
	GP	COSMO	GP	COSMO
7	1.10	1.08	1.28	1.27
19	1.11	1.09	1.29	1.28
37	1.12	1.10	1.29	1.28

The inclusion of implicit solvation effects leads also to, an albeit, less-pronounced, reduction in OH stability, which is also *xc*-functional independent. C-O_{OH} bond lengths in Table 3 show that this is commensurate with a lengthening, and therefore weakening of C-O_{OH} bonds, which can be attributed to competing electrostatic interactions between oxygen atoms and the continuum solvent. It is noted that binding energies calculated from models in which a continuum solvent model is used to describe the first solvation shell may be unreliable due to limitations in this approach. Such an approach is useful however to understand how the physical system may be affected by solvation. Similar behaviour has also, however, been previously reported in models in which water molecules are explicitly modelled[125], providing some validation for the observations presented here.

3.4.1.2 Graphene Epoxide

The formation of single epoxy groups at GO flake centres was also investigated, geometries are presented in Figure 14. Formation energies were calculated by comparison of the energy of the graphene epoxide nano-flake to energies of the free oxygen dimer and pristine graphene nano-flake, in keeping with previous work[126], using the standard formula:

$$E_f = E_{C_nH_mO} - E_{C_nH_m} - E_{O_2}/2 \qquad \textbf{(3.2)}$$

Where $E_{C_nH_mO}$ is the total energy of the geometry in Figure 14, $E_{C_nH_m}$ is the energy of the pristine graphene nano-flake, and E_{O_2} is the energy of the oxygen dimer.

The formation energies presented in Table 5 imply that the formation of single epoxy groups is unstable, presumably due a large energetic penalty with respect to reorganising multiple carbon atoms from sp^2 to sp^3 hybridisation on a rigid GO nano-flake, whilst a high degree of planarity is maintained. It has been reported experimentally[127] also that epoxy groups do not form readily at low levels of GO surface oxidation and Lahaye *et. al.*[120] reported that OH groups are needed to stabilise the GO surface because epoxy groups create too much tension on the carbon lattice to be the sole functional group. The lack of epoxide groups at low levels of oxidation has been attributed experimentally to the low concentration of $KMnO_4$ and H_2SO_4 used in a modified Hummers method for the production of GO with low surface oxidation, and

a complicated sequence of chemical reactions is required to convert hydroxyl and carbonyl groups into epoxy groups under such conditions. Another explanation based on the calculations presented is that the formation of epoxy groups on pristine or near pristine nano-flakes is largely prohibited by the energetics of their formation and is hence not favourable.

Table 5: Formation energy of a single epoxy group on GO nano-flake surface. All values are in eV. GP = Gas Phase. COSMO = continuum solvent

Flake Size	PBE		PBE0	
	GP	COSMO	GP	COSMO
7	1.04	0.98	1.20	1.14
19	0.94	0.88	1.03	0.96
37	1.02	0.96	1.18	1.12

Conversely to the binding of single hydroxyl groups to GO surfaces, the inclusion of solvation effects leads to a relative stabilisation, when considering the formation of single epoxy groups. This increase in stability appears to be attributable to the weakening of the C-O bonds, due to electrostatic forces acting on the oxygen from the continuum solvent and a consequent reestablishment of greater sp^2 character amongst the carbon atoms close to the oxygen bridge. This is evident from the lengthening of the C-O bonds, and shortening of C-C bonds below the oxygen bridge, as shown in Table 6.

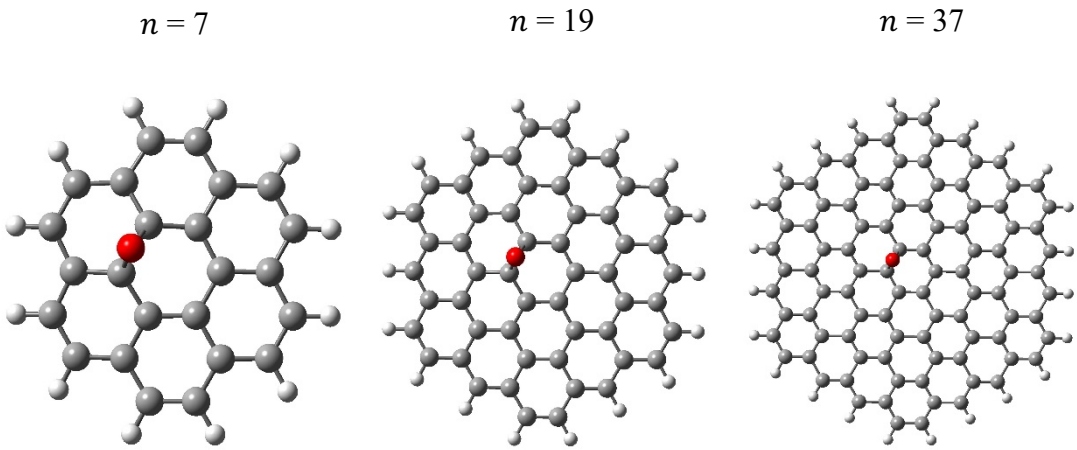

Figure 14: GO nano-flakes incorporating a single epoxy group at the central ring. Optimised at the PBE/TZVP level of theory.

As with the adsorption of single hydroxyl groups, calculations carried out using the PBE0 *xc*-functional predict the formation of single epoxy groups on pristine GO to be destabilised compared to those carried out using PBE. This again may be attributed to more pronounced distortion of the graphene nano-flake from planarity when using PBE0, confirmed by calculated flake deformation energies presented in Table 7.

Consideration of the effect of increased flake size on formation energies suggests that unlike the binding of single hydroxyl groups, there is no simple convergence towards a maximum value consistent with an infinitely large nano-flake predicted from the results in Table 5. The formation energies calculated for formation of a single epoxide group on the n = 7 and 37 nano-flakes are very similar, whilst those calculated for the n = 19 flake are significantly smaller.

Table 6: Average C-O bond lengths for a single epoxy group on a GO nano-flake surfaces. (Values in brackets correspond to C-C bond lengths under the oxygen bridge). All values are in Å. GP = Gas Phase. COSMO = continuum solvent

Flake Size	PBE		PBE0	
	GP	COSMO	GP	COSMO
7	1.436 (1.582)	1.443 (1.579)	1.413 (1.569)	1.420 (1.563)
19	1.453 (1.529)	1.463 (1.523)	1.428 (1.512)	1.436 (1.506)
37	1.454 (1.529)	1.462 (1.525)	1.428 (1.514)	1.433 (1.514)

Graphene is an extremely flexible material, and as discussed in Section 3.4.1.1, the adsorption of even single function groups can lead to significant distortion of the carbon lattice, and these distortions are crucially important to the energetics of the chemisorption process. From consideration of deformation energies presented in Table 7, it is noted that deformation energy is significantly greater in the smallest (n = 7) flake than the two larger nano-flakes, which is unsurprising since this flake would be expected to have least flexibility. When calculated deformation energies are taken in combination with the data presented in Table 5, a much clearer picture begins to emerge; the high instability of the smallest (n = 7) flake is due to flake distortion, which decreases as flake size increases, revealing an electronic instability for the formation of epoxy groups that increases with increasing nano-flake size, presumably up to a threshold which has not been realised here, in which the electronic structure of the carbon lattice more closely resembles that of bulk graphene.

Table 7: GO nano-flake deformation energy for the formation of a single epoxy group. All values are in eV. GP = Gas Phase. COSMO = continuum solvent

Flake Size	PBE		PBE0	
	GP	COSMO	GP	COSMO
7	1.10	1.07	1.21	1.17
19	0.89	0.85	0.97	0.93
37	0.87	0.85	0.95	0.96

3.4.2 Edge Formation

The position and orientation of single functional groups amongst carbon atoms on the bulk surface of GO, it is found, has no significant effect on binding strength (see Section 3.6.1). Small variations (~0.05 eV) are calculated when single hydroxyl groups are moved to different positions on the bulk surface, which are negligible and consistent with the energy associated with the rotation of the hydroxyl group[128]. One area which has not been investigated however, to the best of the authors knowledge, and which is of interest to the understanding of the structure of GO, is the oxidation of carbon atoms close to nano-flake edges. Whilst it is widely accepted that various functional groups can exist along GO edges, carboxyl (COOH), hydroxyl (OH), and

carbonyl (C=O) groups being the most common, it is assumed, for simplicity and consistency with calculations in the previous section that carbon atoms at the flake edge are terminated with hydrogen atoms.

3.4.2.1 Hydroxyl Adsorption

Binding energies for the adsorption of single hydroxyl groups close to the edge of GO flakes (see Figure 15), calculated using equation (3.1), are given in Table 8. The calculations reveal that binding close to the nano-flake edge is much stronger than to the bulk surface, and significantly shorter C-O_{OH} bonds are formed. It is found also that convergence towards an asymptotic value for binding energy is not as clear as it is for binding amongst the bulk surface, although binding energy increases with increasing nano-flake size.

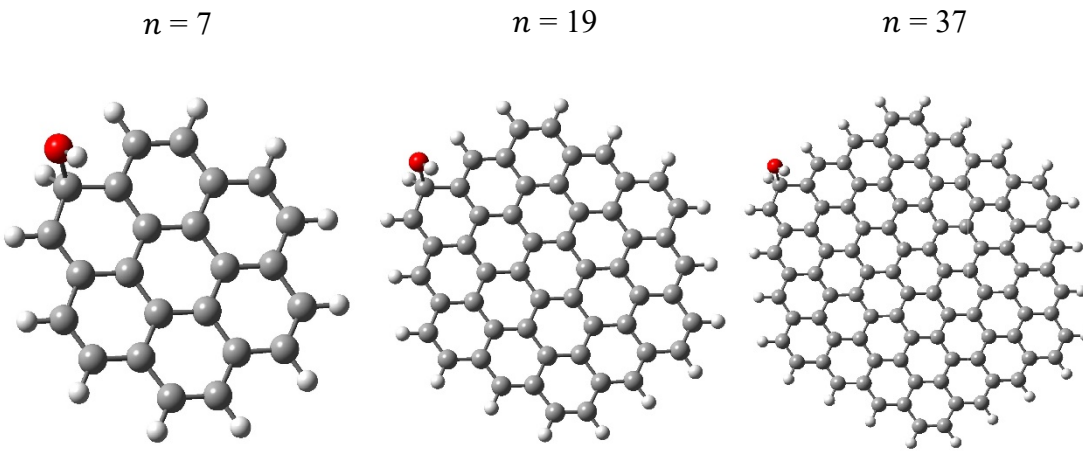

Figure 15: GO nano-flakes incorporating a single hydroxyl group close the flake edge. Optimised at the PBE/TZVP level of theory.

Greater stability of OH groups close to the GO flake edge, it can be reasoned, is due to a reduced penalty in energetics to binding there compared to the GO flake surface. The increased binding strength is attributed to both increased flexibility of the nano-flake at its edge, and the reduced energetic penalty to adopting sp^3 hybridisation in carbons atoms coordinated to two carbon atoms and one hydrogen atom, rather than to three carbon atoms, held rigidly on the bulk surface.

Table 8: Binding energy of a single hydroxyl group adsorbed close to the GO nano-flake edge. All values are in eV. GP = Gas Phase. COSMO = continuum solvent

Flake Size	PBE		PBE0	
	GP	COSMO	GP	COSMO
7	-1.30	-1.19	-1.15	-1.03
19	-1.40	-1.30	-1.28	-1.16
37	-1.45	-1.35	-1.35	-1.25

Similarly, to the adsorption of a hydroxyl group to the bulk nano-flake surface, there is an, albeit less significant, reduction in calculated binding energy when the PBE0 *xc*-functional is used. The reduction can again be attributed to the known increase in energy associated with flake deformation energy when using this functional: the impact of flake deformation energy is however presumably less significant for adsorption close to the flake edge due to reduced rigidity and greater freedom to easily distort the flake in that region.

Table 9: C-O_{OH} bond length for a single hydroxyl group adsorbed close to a GO nano-flake edge. All values are in Å. GP = Gas Phase. COSMO = continuum solvent

Flake Size	PBE		PBE0	
	GP	COSMO	GP	COSMO
7	1.461	1.466	1.431	1.435
19	1.459	1.466	1.430	1.433
37	1.458	1.463	1.429	1.432

The inclusion of implicit solvation again leads to a small reduction in calculated binding energies, this is again commensurate with a lengthening of the C-O_{OH} bonds (Table 9). Bond elongation is much less pronounced at the nano-flake edge site than on the bulk surfaces, this is most probably due to shorter, stronger bonds being less easily affected by the competing electrostatic force from the continuum solvent.

3.4.2.2 *Epoxy Formation*

When considering the formation of epoxy groups close to the nano-flake edges, two possible configurations are identified. Epoxy group formation can either occur involving two carbon atoms along the flake edge (C_1), or with one carbon at the flake edge and one resembling a bulk surface carbon (C_2), both configurations are presented in Figure 16.

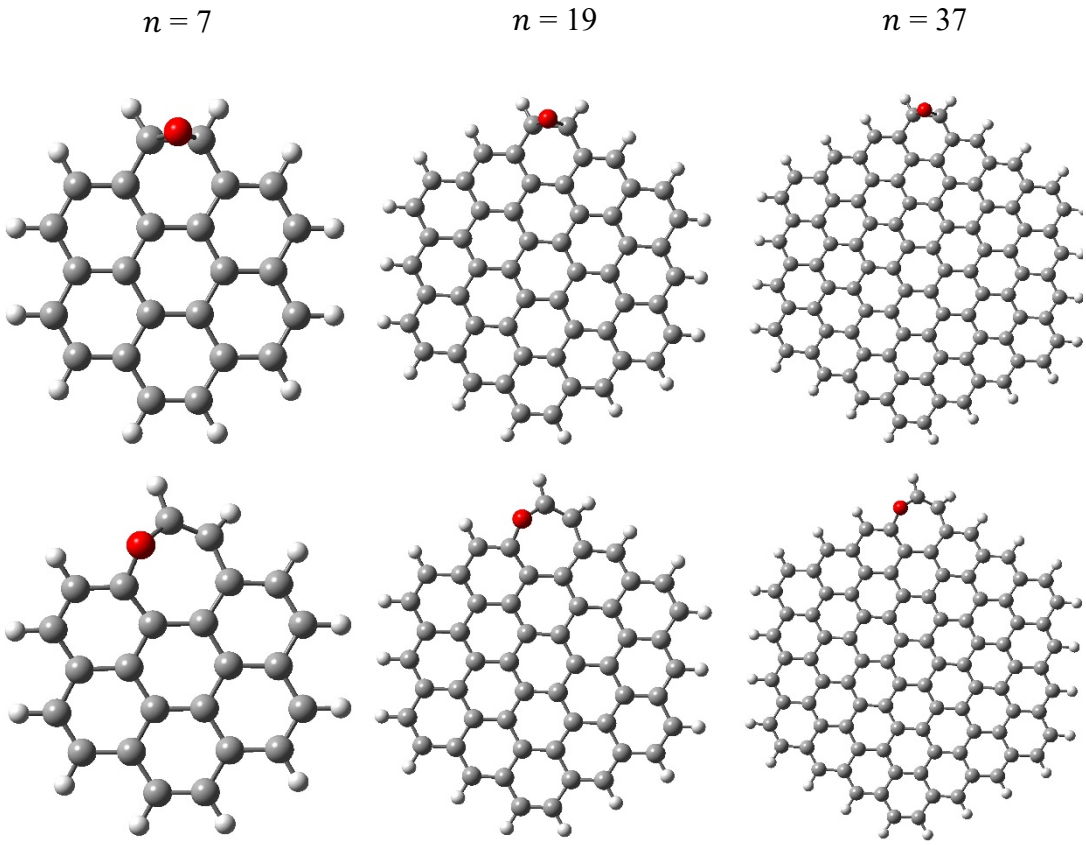

Figure 16: GO nano-flakes incorporating the formation of a single epoxy group at the flake edge (top: C_1; bottom: C_2). Optimised at the PBE/TZVP level of theory.

Formation energies for both configurations, calculated using equation (3.2), are presented in Table 10. It is found that formation close to the flake edge is exothermic, unlike the formation of single epoxy groups on the bulk surface of the flake. There appears also to be convergence towards an asymptotic value for both configurations, which is also not found for calculations on the bulk surface. The convergence towards an asymptotic value is however much slower than in calculations for adsorption of a single hydroxyl group. The stability of formation in both configurations can be attributed to increased flexibility and reduced penalty to disrupting the hybridisation

of carbon atoms at flake edges. The formation of epoxy groups close to the flake edge, whilst being exothermic, is still significantly less favourable than binding of single hydroxyl groups anywhere on the GO surface. This suggests, again, that the formation of hydroxyl groups is most favoured at very low levels of GO surface oxidation, and supports hydroxyl groups as the dominant group on GO surfaces, in agreement with experimental observations[127].

When considering formation energies calculated using the PBE0 *xc*-functional, it is found, in contrast with other results, that there is a slight increase in stability predicted. It has already been shown that flake deformation energy is the main contributing factor for the difference between PBE and PBE0 *xc*-functional calculations. It is not unreasonable to conclude then, that reduced rigidity at the GO flake edge has reduced this effect, resulting in calculated values much closer to one another. A similar trend is observed for the binding of single hydroxyl groups, binding energies calculated at the PBE and PBE0 level of theory for hydroxyl groups close to the nano-flake are in closer agreement to one another than those on the central ring. Although a slightly different trend is observed than in data presented elsewhere in this chapter, both PBE and PBE0 calculated energies continue to show the same overall trends as one another. The inclusion of continuum solvent effects again, leads to an energetic stabilisation of the epoxy group at the nano-flake edge, consist with epoxy formation on the central ring of the nano-flake.

Table 10: Formation energy of a single epoxy group formed at a GO nano-flake edge. All values are in eV. GP = Gas Phase. COSMO = continuum solvent.

Flake Size	PBE				PBE0			
	GP		COSMO		GP		COSMO	
	C_1	C_2	C_1	C_2	C_1	C_2	C_1	C_2
7	-0.28	0.04	-0.37	0.05	-0.32	0.01	-0.41	0.01
19	-0.47	-0.12	-0.56	-0.15	-0.53	-0.13	-0.62	-0.16
37	-0.54	-0.19	-0.63	-0.21	-0.63	-0.21	-0.71	-0.24

It is noted from Figure 16 that the C-C bond below the oxygen bridge in the epoxy groups has broken in C_2, resulting in "unzipping" of the GO nano-flake, and

establishment of a 7-membered ring configuration. Breaking of C-C bonds is also know to occur on the GO bulk surface of GO nano-flakes after multiple epoxy groups have formed[129] (see Section 3.4.3.2). Additional calculations were carried out for the n = 7 nano-flake which suggests that formation of a single epoxy group in the same position without unzipping would be unstable.

Table 11: C-O & C-C (in brackets) bond lengths of single a epoxy group formed at the GO nano-flake edge. All values are in Å. GP = Gas Phase. COSMO = continuum solvent.

Flake Size	PBE		PBE0	
	GP	COSMO	GP	COSMO
7 [C_1]	1.448 (1.486)	1.457 (1.485)	1.424 (1.473)	1.433 (1.472)
7 [C_2]	1.387 (2.348)	1.392 (2.347)	1.372 (2.320)	1.377 (2.318)
19 [C_1]	1.449 (1.481)	1.458 (1.480)	1.425 (1.467)	1.434 (1.467)
19 [C_2]	1.383 (2.374)	1.388 (2.370)	1.369 (2.339)	1.373 (2.338)
37 [C_1]	1.449 (1.479)	1.459 (1.478)	1.425 (1.466)	1.434 (1.465)
37 [C_2]	1.382 (2.370)	1.386 (2.378)	1.367 (2.349)	1.371 (2.350)

Table 12: GO nano-flake deformation energy (C_1) for formation of a single epoxy group at a GO nano-flake edge. All values are in eV. GP = Gas Phase. COSMO = continuum solvent.

Flake Size	PBE		PBE0	
	GP	COSMO	GP	COSMO
7	0.71	0.67	0.78	0.75
19	0.68	0.64	0.74	0.71
37	0.67	0.64	0.72	0.69

Calculated bond lengths for both configurations (Table 11) show that much shorter, stronger C-O bonds have formed in C_2 when the C-C under the oxygen bridge has broken. Calculated flake deformation energies, presented in Table 12, confirm that disruption of the nano-flake structure towards the edge is much less significant than on the bulk surface, as would be expected.

3.4.3 Formation of Functional Group Pairs

3.4.3.1 Hydroxyl Pair Adsorption

The study of functional group stability was extended to investigate the oxidation of the GO bulk surface by multiple groups, considering first the binding of hydroxyl pairs. The investigation is limited to oxidation of the bulk surface in this and the following section due to limitations on computational resources and the relative rarity of edge binding sites, particularly on large flakes with real-world dimensions. Many possible configurations of hydroxyl pairs are possible, the focus is confined however, to the effect of oxidising both sizes of the GO surface compared to a single side (functional groups are known to form on both sides of the basal plane of GO[130]), and the effect of the proximity of hydroxyl groups to one another on binding energy. Four configurations were chosen, which are nearest neighbour same side (NNSS), nearest neighbour opposite side (NNOS), next nearest neighbour same side (NNNSS), and next nearest neighbour opposite size (NNNOS). Figure 17 shows the four configurations on the n = 7 nano-flake.

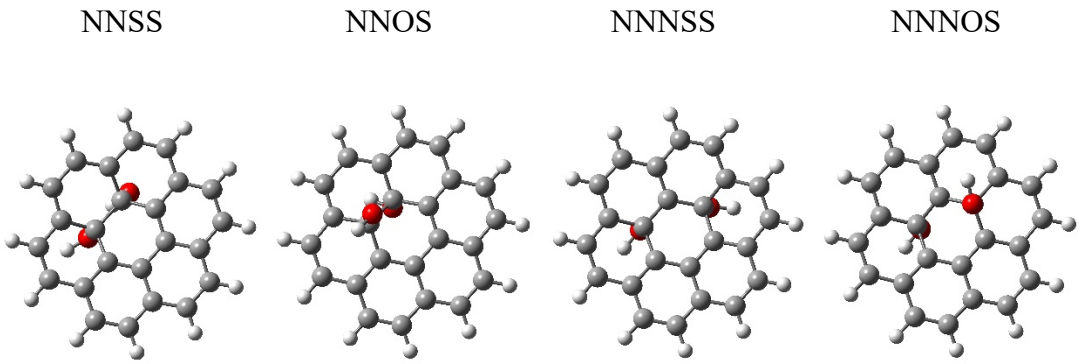

Figure 17: GO nano-flakes incorporating a pair of hydroxyl groups adsorbed on the central ring (n = 7). Optimised at the PBE/TZVP level of theory.

The binding energy of hydroxyl pairs was calculated using the standard formula;

$$E_b = \frac{E_{C_nH_m(OH)_2} - E_{C_nH_m} - 2E_{OH}}{2} \quad \textbf{(3.3)}$$

Where $E_{C_nH_m(OH)_2}$ is the total energy of the double OH-bound GO nano-flake, $E_{C_nH_m}$ is the energy of the pristine nano-flake, and E_{OH} is the energy of the hydroxyl radical.

The relative position of binding of hydroxyl groups to one another is found to have a profound effect on binding energy. As in similar studies[126,131], NNOS is found to be the most favourable configuration. The greatest contribution to stabilisation comes from functionalisation of neighbouring carbon atoms. A smaller contribution to stability is also found from oxidation of both side of the nano-flake surface, calculated binding energies are presented in Table 13.

A comparison of the binding energies calculated for a single hydroxyl groups (Table 2) with those for hydroxyl pairs, shows an increase in stability of more than 0.5 eV per OH when functionalisation occurs in the preferred nearest neighbour configuration. The increased stability can be attributed to the establishment of a greater degree of sp^3 character, which is confirmed by calculated C-C bond lengths. C-C bond lengths close to the oxidation site, in the n = 7 nano-flake for example, increased from 1.427 Å to 1.506 Å with adsorption of a single hydroxyl group, and to 1.527 Å with the adsorption of a second as measured at the NNOS geometry, which had been optimised at the PBE level without consideration of solvation effects. These are consistent with C-C bonds of 1.42 Å[30], measured experimentally in graphene (true sp^2 hybridisation), and appear to be approaching the 1.54 Å[118] measured in diamond (sp^3 hybridised carbon atoms). The increase in C-C bond length appears to be insensitive to both *xc*-functional and whether a continuum solvent model is included in calculations.

Conversely, adsorption to non-neighbouring carbons atoms has an associated energy penalty when compared to the value calculated for the adsorption of a single hydroxyl group. The energy penalty can be attributed to an increase in the disruption of the electronic structure of the aromatic carbon system to accommodate the second functional group. The energy penalty associated with functionalising non-neighbouring carbon atoms is most significant on the n = 7 nano-flake, and for calculations using PBE0, due presumably to the increased deformation energy effect demonstrated previously for the smallest nano-flake, and the increased deformation energy associated with using the hybrid functional.

Table 13: Binding energy of a pair of hydroxyl groups on a GO nano-flake surface (n = 7). All values are in eV. GP = Gas Phase. COSMO = continuum solvent.

Configuration	PBE		PBE0	
	GP	COSMO	GP	COSMO
NNSS	-1.14	-1.04	-0.91	-0.79
NNOS	-1.34	-1.24	-1.12	-1.03
NNNSS	-0.35	-0.31	0.07	0.11
NNNOS	-0.37	-0.30	0.07	0.13

When considering the effect of increased flake size on the adsorption energy of hydroxyl pairs to GO nano-flake surfaces (binding energies calculated at the PBE level of theory without consideration of solvation effects are giving in Table 14, other calculated are presented in Section 3.6.2), different pictures emerge for the functionalisation of neighbouring and non-neighbouring carbon atoms. When non-neighbouring carbon atoms are functionalised, there appears to be a simple convergence towards an asymptotic value, which is associated with convergence towards graphene-like properties. When neighbouring carbon atoms are functionalised however, a more complicated picture emerges, one that is similar to that seen in calculations for the formation of single epoxy groups. It has been shown repeatedly that there is a large impact on stability from flake distortion, especially for the smallest (n = 7) flake. It has also been shown that it is energetically favourable to functionalise neighbouring carbon atoms, previous observations taken along with data presented in Table 14, reveals again an electronic instability which increases with flake size when neighbouring carbon atoms are functionalised, similar to behaviour observed for the formation of single epoxide groups on the nano-flake central ring.

Table 14: Binding energy of a pair of hydroxyl groups on a GO nano-flake surface. All values are in eV. Calculations carried out in the gas phase using the PBE *xc*-functional.

Flake Size	NNSS	NNOS	NNNSS	NNNOS
7	-1.14	-1.34	-0.35	-0.37
19	-1.23	-1.46	-0.59	-0.51
37	-1.17	-1.41	-0.67	-0.56

3.4.3.2 *Epoxy Pair Formation*

The formation of pairs of epoxy groups on GO nano-flake surfaces was also investigated. The configurations considered, as with the adsorption of pairs of hydroxyl groups are NNSS, NNOS, NNNSS, and NNNOS. The formation of multiple epoxy groups with a common carbon atom cannot occur without breaking of a C-C bond since the resulting bonding geometry would exceed the carbon valency of 4, hence the four geometries are as in Figure 18.

The formation energy of pairs of epoxy groups was calculated using the following formula:

$$E_f = \frac{E_{C_nH_mO_2} - E_{C_nH_m} - E_{O_2}}{2} \quad \textbf{(3.4)}$$

Where $E_{C_nH_mO_2}$ is the total energy of the epoxy bound nano-flake, $E_{C_nH_m}$ is the energy of the pristine nano-flake, and E_{O_2} is the energy of the oxygen dimer.

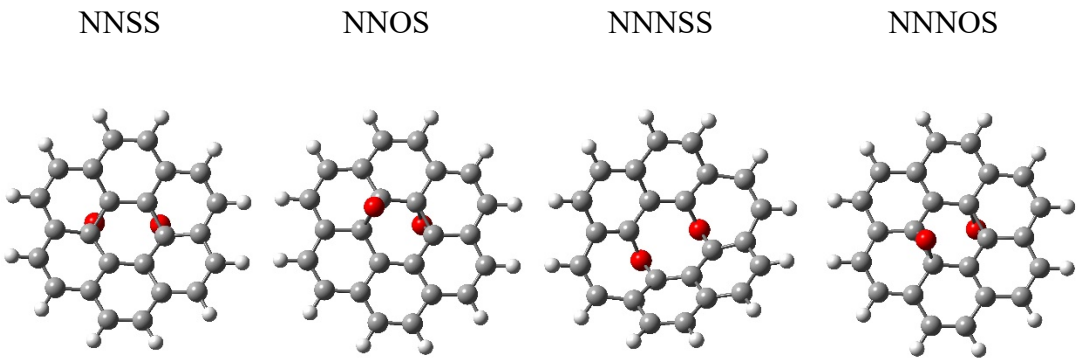

Figure 18: GO nano-flakes incorporating a pair of epoxy groups formed on the central ring (n = 7). Optimised at the PBE/TZVP level of theory.

As with the adsorption of pairs of hydroxyl groups, the relative position of epoxy groups to one another on the GO surface is found to have a profound effect on the energy of formation. Calculated formation energies (Table 15) show that the formation energy of epoxy pairs is endothermic in all configurations, and comparison of calculated energies with those for the formation of single epoxy groups found in Table 5, allows for analysis and characterisation of the effect of epoxy proximity to one another. From comparison with energy of formation of a single epoxy group, there is an energy penalty (0.3-0.5 eV/epoxy) for oxidation of non-neighbouring carbon

atoms, and likewise a reduction in instability when oxidising neighbouring carbon atoms (0.2-0.4 eV/epoxy). The reduction in instability associated with oxidising neighbouring carbon can be attributed to establishment of a greater sp^3 hybridisation amongst the carbon atoms in the nano-flake, likewise the increased instability from the oxidation of non-neighbouring carbon atoms can be attributed to increased disruption of the electronic structure of the aromatic carbon network to accommodate the second functional group, as in the formation of pairs of hydroxyl groups.

A special case is observed when formation takes place in the NNNSS configuration, as can be seen in Figure 18, and in Section 3.6.3 for the n = 19 and 37 nano-flakes, unzipping of the GO nano-flake occurs, similar to that observed for C_2 in Figure 16. Unzipping of the GO carbon lattice results in significantly less unstable systems, due to the release of strain in the C-C bonds below the oxygen bridges and relaxation into a configuration with an 8-membered central ring, behaviour which has also been reported previously in the literature[129].

Table 15: Formation energy of an epoxy group pair formed on a GO nano-flake surface. All values are in eV. GP = Gas Phase. COSMO = continuum solvent.

Configuration	PBE		PBE0	
	GP	COSMO	GP	COSMO
NNSS	0.77	0.70	0.91	0.84
NNOS	0.83	0.77	0.98	0.91
NNNSS	0.25	0.20	0.26	0.21
NNNOS	1.34	1.27	1.52	1.45

As with calculations for the formation of single epoxy groups, there is a small decrease in the instability of the system when continuum solvent effects are considered, this again is commensurate with weakening of C-O bonds due to competing electrostatic interactions, and reestablishment of a greater degree of sp^2 hybridisation amongst the carbon atoms close to the oxygen bridge. A comparison of formation energies calculated using the PBE and PBE0 *xc*-functionals show that PBE0 predicts greater functional group instability than PBE, in keeping with previous results, and attributable

again to the increased energy associated with deformation of the flake when using the PBE0 *xc*-functional.

Table 16: Formation energy of an epoxy group pair formed on a GO nano-flake surface. All values are in eV. Calculations carried out in the gas phase using the PBE *xc*-functional.

Flake Size	NNSS	NNOS	NNNSS	NNNOS
7	0.77	0.83	0.25	1.34
19	0.65	0.64	0.63	1.32
37	0.76	0.76	0.67	1.30

A seemingly complicated relationship begins to emerge when considering the effect of increased nano-flake size on calculated formation energy of epoxide pairs (Table 16, results from calculation using the PBE0 *xc*-functional and with consideration of continuum solvent effects are in Section 3.6.3), one that however becomes much clearer when taken in consideration with energies calculated for the deformation of the nano-flake backbone, presented in Table 17.

Table 17: GO nano-flake deformation energy from formation of a pair of epoxy groups. All values are in eV. Calculations carried out at the PBE level of theory in the gas-phase.

Flake Size	NNSS	NNOS	NNNOS
7	1.96	1.63	1.87
19	1.68	1.48	1.65
37	1.69	1.50	1.62

It is found in both nearest neighbour configurations (NNSS and NNOS) that the least unstable systems are predicted be the n = 19 nano-flake, while in the next nearest neighbour configuration, stability on all flakes is found to be approximately equal except for the NNNSS configuration on the n = 7 nano-flake which is significantly less unstable. Formation energies considered in combination with the energies associated with flake deformation reveal that there is an instability that increases with flake size, as in energies calculated for the formation of single epoxy groups, and the binding of hydroxyl pairs to neighbouring carbon atoms. It is found also from a

comparison of formation energies for the NNSS and NNOS geometries, there is greater functional group instability associated with oxidation of both sizes of the nano-flakes, which is in contrast to that found for hydroxyl pairs. It is found however that oxidation of both sides of the GO basal plane leads to reduced deformation energy of the carbon backbone, presumably due to greater planarity of the carbon lattice. Based on these results, it is proposed that electrostatic forces between functional groups which are in close proximity on the same side of the flake contributes to functional group stability.

3.4.4 Functional Group Stability at High Levels of Oxidation

It known from experimental data that the level of oxidation on GO surfaces is typically in the range 25% to 75%[116]. The effect of functional group stability at increased levels of surface oxidation in this range is therefore investigated here. With confidence from broadly similar results for different flake sizes in this chapter so far for lone functional groups, and functional groups pairs, and with consideration of the considerable computational costs associated with calculations on large systems, only the n =7 and n = 19 flakes are considered for the remainder of this chapter. It has also been shown that binding interactions close to GO nano-flakes edges display significantly different binding characteristics than those on the GO bulk surface. GO found experimentally is typically a few nm to several microns in diameter, so would have a much greater surface to edge ratio than those in DFT calculations presented here, and hence edge binding interactions would be much rarer; adsorption close to the nano-flake edge is therefore also not considered in this section.

3.4.4.1 Graphene Hydroxide

The effect of increased surface oxidation on binding energy was investigated initially for the adsorption of hydroxyl groups only. Surface oxidation at levels of 25%, 50%, and 75% were investigated, which correspond to the adsorption of 3, 6, and 9 hydroxyl groups on the surface of the n = 7 nano-flake, and 9, 18, and 27 groups on the n = 19 nano-flake. There is a wide range of possible configurations of functional groups on GO surfaces and an exhaustive study of every possible configuration is not practically possible. Guidance towards low energy configurations was however obtained by use of a random number generator (RNG) to ensure a range of configurations was considered. Modifications were also made to the configurations obtained by RNG

which gave systems with the lowest energies using knowledge obtained from the investigation of single and double hydroxyl adsorption, which in turn produced lower energy geometries. It was found, as predicted from previous calculations presented in this work, that functional groups in close proximity to one another and oxidation of both sides of the GO surface yields the most stable geometries, which is also in agreement with experimental[30,132–134] and other theoretical[128] studies. It has been consistently reported in the literature that functional groups aggregate on GO surfaces forming distinct sp^2 and sp^3 hybridised regions. The most stable configurations obtained by this approach are presented in Figure 19.

Binding energies were calculated using the following formula;

$$E_b = \frac{E_{C_nH_m(OH)_x} - E_{C_nH_m} - xE_{OH}}{x} \quad \textbf{(3.5)}$$

Where $E_{C_nH_m(OH)_x}$ is the energy of the hydroxylated GO, $E_{C_nH_m}$ is the energy of the pristine nano-flake, E_{OH} is the energy of the hydroxyl radical, and x is the number of hydroxyl groups adsorbed on the GO surface.

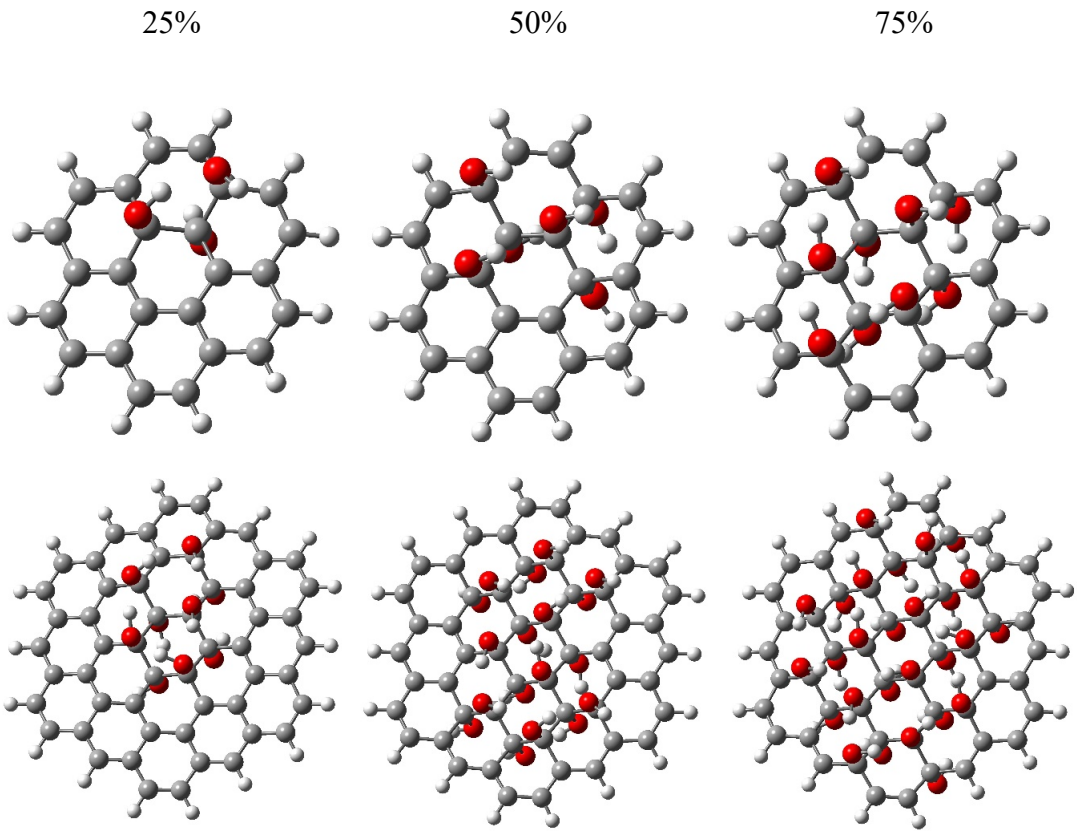

Figure 19: GO nano-flakes with n = 7 and 19 carbon rings incorporating hydroxyl groups at the 25%, 50% and 75% coverage levels. Optimised at the PBE/TZVP level of theory.

Binding energies calculated for the lowest energy configurations at the 25%, 50%, and 75% levels of oxidation for both the n = 7 and n = 19 nano-flakes, the binding energy calculated for a single hydroxyl group, and the lowest energy hydroxyl group pairs are presented in Figure 20. The stability of hydroxyl groups on the GO surface is seen to increase quickly with increased surface oxidation, then converge towards a maximum value, which is in agreement with behaviour reported previously[126]. Consideration of both the n = 7 and n = 19 nano-flakes and all level of surface oxidation simultaneously reveals an insensitivity to flake size at high levels of surface oxidation, which has not been reported previously. The observed insensitivity to flake size gives support for validity of the molecular model developed in this chapter for the description of finite regions of much larger systems. Increased stability with greater surface oxidation can be attributed to the convergence towards complete sp^3 hybridisation amongst carbon atoms. This is characterised by an increase in average C-C bond length, from 1.426 Å on the pristine nano-flake (calculated for the n = 7 nano-flake optimised at the PBE level of theory in the gas phase) to 1.463 Å at 25% surface oxidation, and to 1.545 Å at 75%. An increase from 1.426 Å to 1.468 Å at 25% oxidation and 1.554 Å

at 75% oxidation was calculated for the n = 19 flake using the same optimisation parameters.

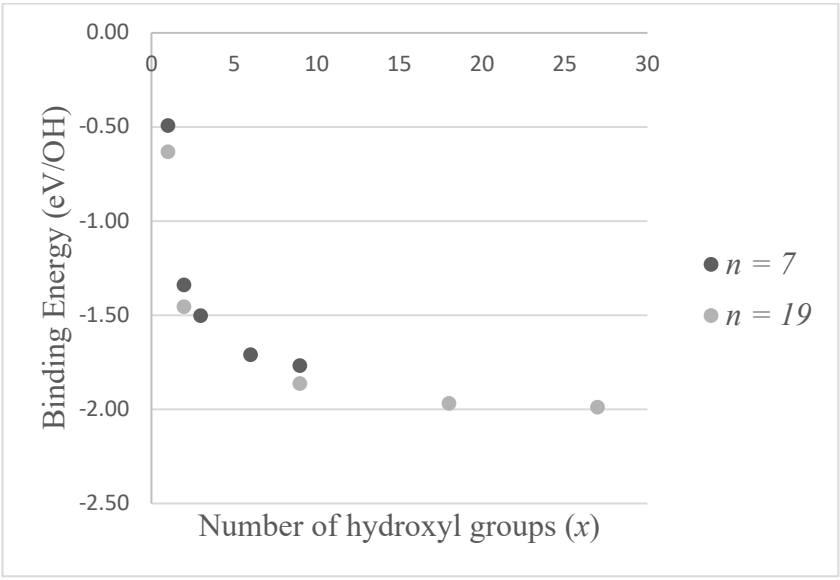

Figure 20: Binding energy of hydroxyl groups on the n = 7 and n = 19 nano-flakes. Calculations at the PBE/TZVP level of theory in the gas-phase.

Calculated binding energies are presented in Table 18. As with calculations for the adsorption of single hydroxyl groups and hydroxyl group pairs to GO surfaces, there is a significant reduction in calculated binding energy when using the PBE0 *xc*-functional. This again can be attributed to the known increase in flake deformation energy when using the hybrid *xc*-functional. Similarly, there is a reduction in calculated binding energy when considering solvation effect effects, which is also consistent with results reported previously in this chapter.

Table 18: Binding energies of hydroxyl groups bound to a GO nano-flake surface for $n = 7$ and $n = 19$ nano-flakes. All values are in eV per hydroxyl group. GP = Gas Phase. COSMO = continuum solvent

Coverage	PBE		PBE0	
Level (%)	GP	COSMO	GP	COSMO
25 ($n = 7$)	-1.50	-1.39	-1.36	-1.24
50 ($n = 7$)	-1.71	-1.57	-1.53	-1.39
75 ($n = 7$)	-1.90	-1.71	-1.76	-1.60
25 ($n = 19$)	-1.86	-1.69	-1.72	-1.55
50 ($n = 19$)	-1.97	-1.80	-1.83	-1.64
75 ($n = 19$)	-1.99	-1.83	-1.86	-

3.4.4.2 Mixed Surface Oxidation

Hydroxyl and epoxy groups coexist on GO surfaces[5], oxidation by both functional groups simultaneously was therefore investigated. Due to increased stability of hydroxyl groups on GO surfaces, established from previous calculations, and the ratio of hydroxyl to epoxy groups on GO surfaces that can be inferred from the experimentally obtained compositions for GO ($C_8H_2O_3$ to $C_8H_4O_5$), hydroxyl groups are retained as the dominant species on the GO surface. The lowest energy geometries obtained by oxidation with only hydroxyl groups (presented in Figure 19) were modified to incorporate a single epoxy group in place of two hydroxyl groups from neighbouring carbon atoms. This approach maintains the 25%, 50%, and 75% levels of surface oxidation, and gives low energy geometries comparable with those in the previous section. The range of chemical compositions investigated using this approach is $C_8H_{0.7}O_{1.3}$ to $C_8H_{5.5}O_{5.8}$, excluding hydrogen atoms terminating the flake edges, which brackets compositions which have been observed experimentally. Geometries modified to incorporate a single epoxy groups are shown in Figure 21, oxygen atoms which form part of the epoxy group are emphasised in lilac.

The binding/formation energy for mixed surface oxidation flakes was calculated using a standard approach and the following formula:

$$E_b = \frac{E_{C_nH_m(OH)_xO_y} - E_{C_nH_m} - xE_{OH} - yE_{O_2}/2}{(x+y)} \quad \textbf{(3.6)}$$

Where $E_{C_nH_m(OH)_xO_y}$ is the energy of the oxidised GO nano-flake, $E_{C_nH_m}$ is the energy of the pristine nano-flake containing n-carbon atoms and m-hydrogen atoms at flakes edges, E_{OH} is the energy of the hydroxyl radical, E_{O_2} is the energy of the oxygen dimer, x is the number of hydroxyl groups on the flake surface and y is the number of epoxy groups which have been formed.

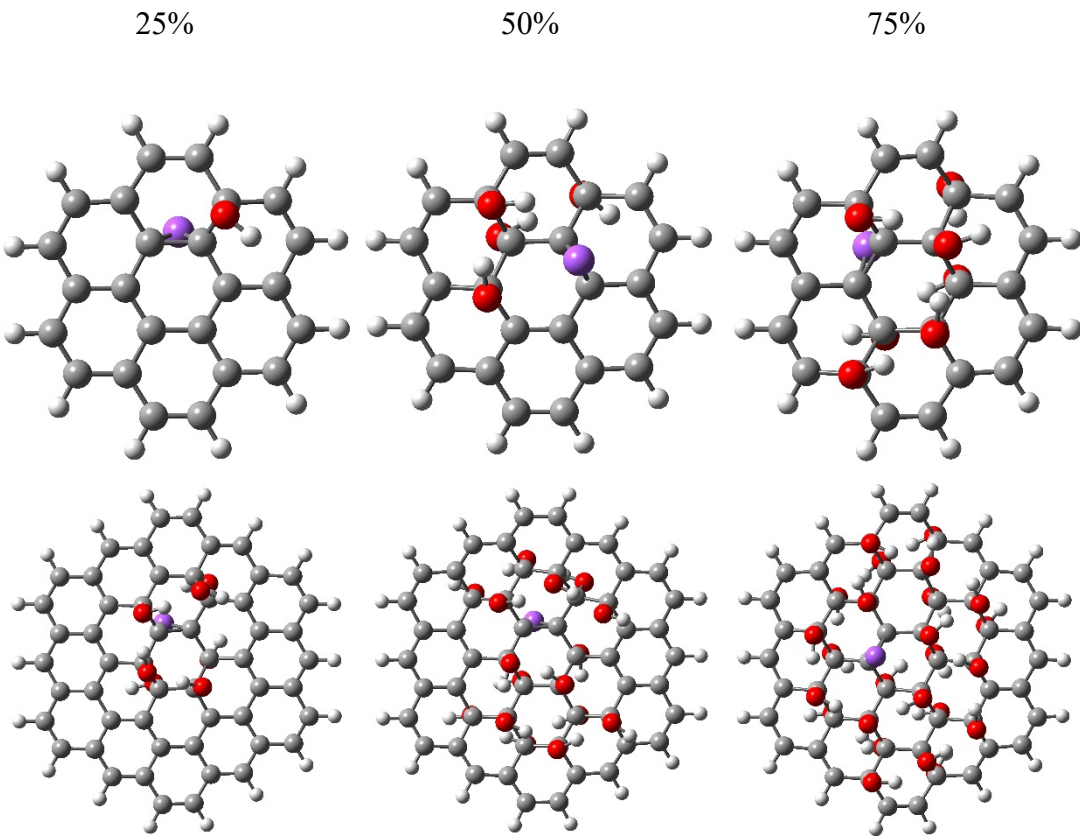

Figure 21: GO nano-flakes incorporating hydroxyl groups and a single epoxy group at the 25%, 50% and 75% level of surfaces oxidation. Optimised at the PBE/TZVP level of theory (Lilac is used to emphasis position of the epoxy group)

A comparison of results presented in Table 19 with those in Table 18 in the previous section, reveals a significant reduction in system stability from the introduction of an epoxy group. This is in agreement with the results reported elsewhere[116] and consistent

with results reported previously in this chapter, confirming much greater stability for hydroxyl groups than epoxy groups on GO surfaces. The reduction in stability is most significant at low levels of oxidation when the ratio of hydroxyl to epoxy groups is lowest. As surface oxidation is increased, and the population of hydroxyl groups begins to significantly outnumber epoxy groups, energies are much closer to the single species values in Table 18.

Considering of the effect of the continuum solvent model reveals a reduction in functional group stability, which is most significant at high levels of surface oxidation, when the ratio of hydroxyl and epoxy groups is greatest. It was shown in Section 3.4.1 that the stability of hydroxyl groups on GO surfaces is reduced by the inclusion of implicit solvent effects whilst the stability of epoxy increases, for mixed surface oxidation systems there are competing effects from the different responses of hydroxyl and epoxy groups to solvation effects. At low levels of oxidation, the two effects are balanced, and solvation effects become negligible, as the level of oxidation is increased however, hydroxyl groups significantly outnumber epoxy groups, and the destabilisation of hydroxyl groups becomes the dominant effect. The impact of the continuum solvent is *xc*-functional independent, in agreement with previous results. Consistent with previous results there is also a reduction in calculated binding with the PBE0 *xc*-functional, which again is almost certainly due to increased energy associated with the deformation of the GO carbon lattice, as observed previously in this chapter.

Table 19: Binding/formation energies of hydroxyl groups and a single epoxy species on a GO nano-flake surface for n = 7 and 19 nano-flakes. All values are in eV. GP = Gas Phase. COSMO = continuum solvent

Coverage	PBE		PBE0	
Level (%)	GP	COSMO	GP	COSMO
25 (7)	-0.16	-0.15	-0.07	-0.06
50 (7)	-1.25	-1.16	-1.09	-1.00
75 (7)	-1.58	-1.46	-1.46	-1.34
25 (19)	-1.49	-1.37	-1.37	-1.25
50 (19)	-1.84	-1.69	-1.70	-1.55
75 (19)	-1.90	-1.74	-	-

The stability of functional groups on highly oxidised GO surfaces with mixed oxidation appears to be determined only by the abundance and nature of oxidation, and is independent of the size of the GO flake, as in systems oxidised by only hydroxyl groups. This is an important result in the computational study of GO systems, that to the best of the authors knowledge has not been reported previously, and gives strong support for the validity of a molecular model for GO as a good approximation for large GO systems.

3.5 Discussion and Conclusion

A molecular model of GO has been developed using DFT, based on the structural model proposed by Lerf and Klinowski, that appears to be consistent with experimental data and existing theoretical studies. It has been found in particular that the stability of oxygen containing functional groups on graphene surfaces is insensitive to the lateral size of the nano-flake at high levels of surface oxidation. It is also shown from DFT calculation that the formation of epoxide groups at low levels of surface oxidation is unlikely, which is consistent with experimental results. It has been demonstrated, that:

(i) The binding energy of individual hydroxyl groups on pristine graphene surfaces increases with flake size and converges towards a maximum value consistent with values from periodic calculations of comparable quality.

(ii) Binding energies calculated with the hybrid PBE0 *xc*-functional are significantly lower than those calculated at the PBE level of theory, whilst PBE0 calculated C-O_{OH} bond lengths are shorter. Lower binding energies are found to be due greater energetic contributions from flake deformation with the hybrid functional, and not from the reported overbinding with PBE.

(iii) The inclusion of a continuum solvent model in DFT calculations stabilises epoxide groups on GO surfaces and destabilises hydroxyl groups.

(iv) Functional group are most stable when they are clustered together on GO surfaces, consistent with experimental data and other theoretical studies.

3.6 Appendix Information

3.6.1 The Effect of Functional Group Position on the Binding Energy of a Single Hydroxyl Group on the Surface of a Graphene Nano-flake

Position 1

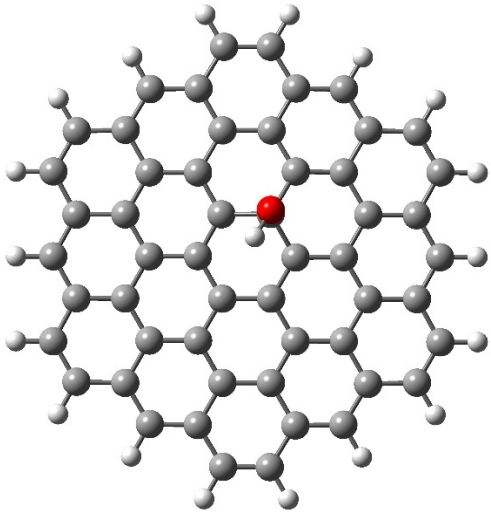

Position 2

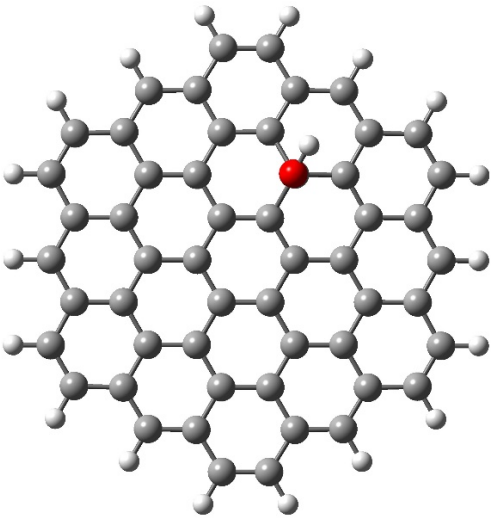

Position 3

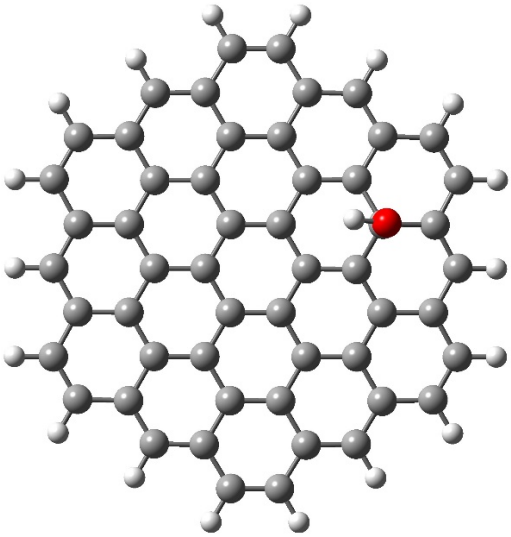

Position 4

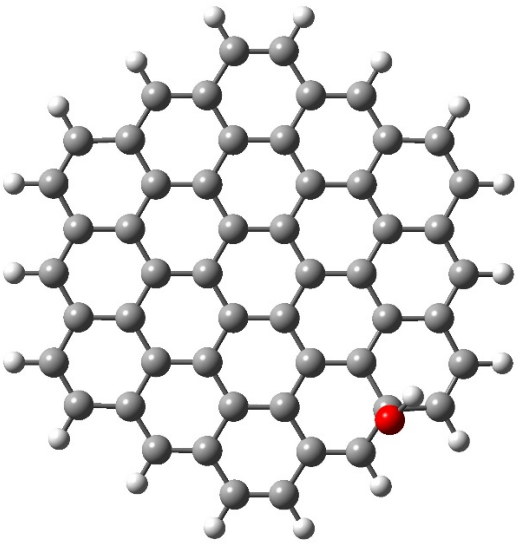

Figure 22: Graphene nano-flake incorporating a single hydroxyl group in four unique positions on the surface. Optimised at the PBE/TZVP level of theory.

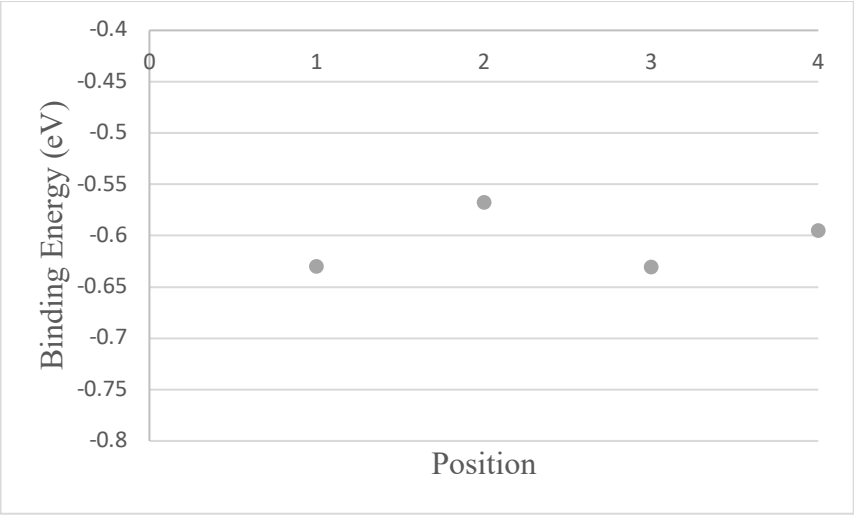

Figure 23: Binding energy of single hydroxyl groups in four unique positions on the surface of GO. Calculations at the PBE/TZVP level of theory in the gas-phase (relates to configurations in Figure 22)

3.6.2 Hydroxyl Pair Adsorption

Table 20: Binding energy of a pair of hydroxyl groups on a GO nano-flake surface (n = 19). All values are in eV. GP = Gas Phase. COSMO = continuum solvent.

Configuration	PBE		PBE0	
	GP	COSMO	GP	COSMO
NNSS	-1.23	-1.12	-1.02	-0.91
NNOS	-1.46	-1.37	-1.28	-1.19
NNNSS	-0.59	-0.52	-0.20	-0.13
NNNOS	-0.51	-0.46	-0.12	-0.07

Table 21: Binding energy of a pair of hydroxyl groups on a GO nano-flake surface (n = 37). All values are in eV. GP = Gas Phase. COSMO = continuum solvent.

Configuration	PBE		PBE0	
	GP	COSMO	GP	COSMO
NNSS	-1.17	-1.04	-0.92	-0.79
NNOS	-1.41	-1.31	-1.18	-1.09
NNNSS	-0.67	-0.60	-0.27	-0.19
NNNOS	-0.56	-0.51	-0.16	-0.11

3.6.3 Epoxy Pair Formation

Table 22: Formation energy of a pair of epoxy groups formed on a GO nano-flake surface (n = 19). All values are in eV. GP = Gas Phase. COSMO = continuum solvent.

Configuration	PBE		PBE0	
	GP	COSMO	GP	COSMO
NNSS	0.65	0.57	0.67	0.59
NNOS	0.64	0.57	0.66	0.59
NNNSS	0.63	0.60	0.75	0.71
NNNOS	1.32	1.27	1.54	1.49

Table 23: Formation energy of a pair of epoxy groups formed on a GO nano-flake surface (n = 37). All values are in eV. GP = Gas Phase. COSMO = continuum solvent.

Configuration	PBE		PBE0	
	GP	COSMO	GP	COSMO
NNSS	0.76	0.69	0.87	0.80
NNOS	0.76	0.70	0.88	0.82
NNNSS	0.67	0.64	0.74	0.71
NNNOS	1.30	1.23	1.50	1.44

Chapter 4 Investigation of the Interaction of Radionuclides with Graphene Oxide Nano-flakes in DFT

4.1 Introduction

It is discussed in Chapter 1 that nuclear activities produce a wide variety of potential contaminants in the form of transuranic elements and nuclear fission products, each posing a slightly different remediation challenge. The health risks associated with exposure to radioactive material, particularly the ingestion of radioactive material, are universal recognised. Radiation exposure is associated with many cancers and other negative health effects in humans. Radiation damage to DNA can occur both directly through the ionisation of DNA nucleobases and sugar-phosphate backbones and indirectly through the production of highly reactive free radical species from the radiolysis of water. Mining activities can also increase the concentration of heavy metals in the soil which can easily enter the water table. Heavy metals such as lead, mercury and cadmium are particularly detrimental to the health of humans and other living organisms. Long-term exposure to water polluted with heavy metals can cause serious disorders, such as anaemia, cancer and renal disease[135]. Metals are also distinguishable from many other toxins, as they are non-biodegradable and non-water soluble so can accumulate in cells and become concentrated throughout the food chain.

In addition to the contamination of water from recent and ongoing nuclear activities there is also a significant volume of legacy nuclear waste which requires a versatile decommissioning solution. Contamination has arisen from such activities as historical nuclear weapons testing and development, and the accidental release of nuclear materials into the environment from nuclear incidents such as Chernobyl, and more recently, Fukushima. There was also significant nuclear material released into the environment in the infancy of the modern nuclear industry when containment and disposal of nuclear materials was much less rigorously planned and the dangers of exposure to radioactive materials were much less well understood. Nuclear sites in the UK in particular have many unique decommissioning challenges to solve due to the evolution of the nuclear industry and the wide range of nuclear reactor and nuclear site designs which are currently the subject of decommissioning efforts. The first generation of nuclear reactors for power generation in the UK were Magnox

(**mag**nesium-**n**on-**ox**idising) reactors, so called because of the magnesium-aluminium alloy used for fuel cladding. Magnox reactors were not build to a standard specification[136] hence each site requires a slightly different long-term decommissioning solution. More recent nuclear power stations, and those still active in the UK that will be approaching the end of their lifetime and will require decommissioning in the near future, are predominately advanced gas-cooled reactors (AGRs), which adopt a more standardised design. Nuclear power will also likely play a significant role in meeting future energy demands both in the UK and abroad. The decline in non-renewable fossil fuels, an expanding global population and greater awareness of environmental impact and ambitions towards sources of low carbon emission energy solutions will drive nuclear expansion. There is hence now a greater need than ever for robust, versatile, environmentally friendly, and preferably low-cost solutions for decommissioning and remediating existing and future nuclear sites. The research presented in this and the following chapters focus upon one such emerging technology as a potential solution for the large-scale removal of radioactive and toxic materials from contaminated aqueous environments.

The history, physical structure, and production methods for GO are discussed in detailed in Chapter 1. The surfaces and edges of GO are functionalised with epoxy, hydroxyl, and carboxyl moieties which make it well suited as a sorbent material for the removal of cations and anions from aqueous environments. The large surface area of GO and lack of internal surfaces also lead to it displaying fast sorption kinetics and high adsorption efficiency[137]. GO has been studied extensively under laboratory conditions and has shown great promise as a highly efficient sorbent material for the removal of a wide range of fission products, transuranic elements, and other heavy metals from contaminated aqueous environments. GO can also be produced using cost effective and environmentally friendly methods, using common and inexpensive chemicals and laboratory equipment which are discussed in Chapter 1. GO is also made up of only CHON (carbon, hydrogen, oxygen, and nitrogen) elements so is not considered a significant environmental hazard and it can be completely incinerated at T = 800°C[1]. Studies have also indicated it is reusable, which can minimise the amount of secondary waste produced. The production of secondary waste is a major issue in the nuclear industry, due to the mixed levels of radioactivity it often contains and the toxicity of fission products and transuranic elements which creates unique challenges

for decommissioning. The contaminated material in secondary waste streams in the nuclear industry often needs to be stored and contained for many years before it can be disposed of or recycled by conventional methods.

The aim of the research presented in this chapter is to obtain a greater understanding of binding interactions between radionuclides and the surfaces and edges of GO nano-flakes. The research in this thesis can hopefully influence the design of future GO and aid in the large-scale remediation of effluent waste and other contaminated aqueous solutions arising from nuclear and other activities.

4.2 Literature Review

There has been, and continues to be, significant interest in the development of GO as a sorbent material for the removal of fission products and transuranic elements from contaminated aqueous environments. The potential use of GO as a sorbent material for water remediation is not confined to use in the nuclear industry, it is also being investigated for the removal of Pb, Cd, Zn and other toxic metals[138–140]. Although not the main focus of this research, greater understanding of the mechanism of adsorption of cations by GO may also influence the development of safe and cost-effective methods for removing heavy metals from contaminated water supplies. The use of GO as a solution to improving water quality, may be particularly useful in developing countries where financial factors may be an issue, and modern water treatments may not be available. In India for example, it is estimated that over 85% of the public water supply is currently sourced directly from ground water[141] which may be contaminated with heavy metals. India also has a rapidly evolving nuclear industry and boasts the world's largest natural thorium reserves[142]. These thorium reserves are central to India's long-term nuclear programme, as it strives towards meeting the energy demands of its large and growing population and achieve energy independence. It is heavily invested in thorium-based fast breeder and advanced heavy water reactor development, in which research and development efforts and expanding nuclear activities may lead to further contamination of ground water. India is also not unique in the need for a solution to improve water quality, many other developing countries would benefit from such a solution.

4.2.1 Experimental Research

The use of GO as a sorbent material for the removal of heavy metals and nuclear materials from aqueous environments has been studied extensively. Experimental investigates have been carried out for a wide range of heavy metals and radionuclides, in different environments. Experimental research has included, but is not limited to, the use of GO for the removal of Cs(I)[143], Cu(II)[140,144], Cd(II)[140,145,146], Zn(II)[140], Co(II)[145], Pb(II)[140,146–148], Sr(II)[1,143,149], Eu(III)[1,150], Am(III)[1], Th(IV)[1,151,152], Pu(IV)[1], Np(V)[1], U(VI)[1,146,153–155], Tc(VIII)[1].

One of the main issues which is preventing the effective removal of radionuclides from contaminated aqueous environments is the lack of low-cost and robust sorbent materials. Many materials have been shown under idealised laboratory conditions to be very promising, but their effectiveness has quickly diminished in more realistic environments where variations in pH and the presence of competing ions can significantly inhibit performance. The performance of GO has however been found to be very promising in a wide range of conditions and it has been shown to outperform most other sorbent materials and extraction methods. The adsorption capacity of GO towards Cu(II) for example is significantly greater than all other available materials and methods. Sikto *et. al.*[140] reported a maximum sorption capacity of 294 mg g^{-1} for the removal of Cu(II) using GO, which is much greater than more conventional sorbent materials such as activated carbon[156,157] (4–5 mg g^{-1}) and carbon nano-tubes (CNTs)[158] (24.49 mg g^{-1}). Other sorbent materials which have shown promising results under laboratories include the zeolite, scolecite, which was studied for the removal of Cu and other divalent cations[159] from aqueous solutions, it too however is found to have a maximum adsorption capacity an order of magnitude smaller than that typical obtained from GO sorption experiments (4.2 mg g^{-1}), and was found to be effective across a much smaller pH range. Scolecite was also found to be ineffective for the removal of other divalent cations such as Ni(II) (0.9 mg g^{-1}), Co(II) (0.23 mg g^{-1}), and Cd(II) (0.18 mg g^{-1}), which can also be effectively be removed using GO[145,160]. Algae[161] and crab shell[157] has also shown promise under laboratory conditions, Yu *et. al.* reported very high sorption capacities of algae from a study of nine common species of marine macro algae, sourced from 5 continents (63 – 76 mg g^{-1}), likewise An *et. al.* reported sorption capacities for crab shells (62.3 mg g^{-1}) which is much

higher than many other sorption materials, but significantly less than the value reported for GO.

Zhao *et. al.*[147] reported a maximum sorption capacity of 842 mg g^{-1} for the removal of Pb(II) from an idealised aqueous environment using highly oxidised GO at pH 6.0 and T = 293 K, a sorption capacity which was much greater than those reported elsewhere in the literature for other sorption materials. It has been reported for example that activated carbon[162] and oxidised MWCNTs[163] which are commonly used sorption materials have maximum sorption capacities of 21.8 mg g^{-1} and 2.06 mg g^{-1}, respectively, at pH 6.0 and T = 303 K with respect to Pb(II), sorption capacity for other materials such as sawdust[164] (34.25 mg g^{-1} at pH 7.0 and T = 303 K), iron oxide[165] (36.00 mg g^{-1} at pH 5.5 and T = 298 K), GMZ bentonite[166] (23.83 mg g^{-1} at pH 5 and T = 293 K) and hazelnut shells[16] (28.18 mg g^{-1} at pH 6.0 and T = 293 K) are all also significantly lower than GO. Similar results have also been reported for metal cations in higher oxidations states. Sun *et. al.*[150] calculated a maximum sorption capacity of 175.44 mg g^{-1} using GO for the removal of Eu(III), which compares extremely favourably with other adsorption materials used for Eu abstractions studied under similar experimental conditions, such as titanium dioxide[167] (TiO_2) (5.0 mg Eu g^{-1}), multiwall carbon nanotubes[168] (MWCNTs) (1.4 mg Eu g^{-1}) and Zeolite Socony Mobil-5[169] (ZSM-5) (3.28 mg Eu g^{-1}). Li. *et. al.*[155] reported a maximum sorption capacity of 299 mg g^{-1} for the removal of U(VI) from contaminated groundwater, other promising materials such as nanoporous and non-nanoporous alumina were reported by Sun *et. al.*[170] to have maximum sorption capacities of 11.6 and 3.99 mg g^{-1}, respectively. Carboni *et. al.*[171] reported a maximum sorption capacity of 97 mg g^{-1} for the removal of U(VI) from contaminated water using mesoporous carbon.

The calculated adsorption capacity for GO towards each of the radionuclides however varies greatly throughout the literature, which can make direct comparisons between results from different experiments and between different experimental groups difficult. Separate investigations by Sikto *et.al.*[140] and Yang *et.al*[144], for example, reported maximum adsorption capacity of GO for the removal of Cu(II) to be 294 mg g^{-1} and 46.6 mg g^{-1}, respectively. The experimental methodology used by the Sikto and Yang research groups were very similar, both experiments were carried out at ambient temperature and pressure, both were at pH = 5, and both also calculated maximum

sorption capacities by fitting initial and final concentrations to the Langmuir model after equilibrium conditions had been reached. The only noteworthy difference in experimental methodology between the two groups is the amount of time allowed for equilibrium conditions to be reached, the Sikto group allowed 120 minutes for the establishment of equilibrium conditions, whilst Yang *et. al.* allowed only 10 minutes. Similar sorption experiments by Romanchuk *et. al.*[1] however found that equilibrium conditions are typically reached in less than 5 minutes in such experiments, due to the extremely high accessible surface area and lack of internal surfaces in GO. The extra time allowed by the Sikto group is therefore not expected to have contributed significantly to the large difference in reported adsorption capacities. In similar studies which investigated the removal of U(VI) by GO, Wang *et. al*[154] and Li. *et. al.*[155] reported calculated maximum sorption capacities of 94.3 mg g^{-1} and 299 mg g^{-1}, respectively. Li *et. al.*[155] also reported, however, that following chemical modification to significantly reduce the oxygen content of their GO, the maximum sorption capacity reduced from 299 mg g^{-1} to 47 mg g^{-1}, in sorption experiments repeated under the same conditions. Zhao *et. al*.[147] also reported that the maximum sorption capacity of Pb(II) by GO in their investigation increased from 400 mg g^{-1} to 842 mg g^{-1} when a GO sample with higher oxygen content, and greater surface functional groups density was used. It is discussed in Figure 1 that the composition of GO can vary greatly between samples. The chemical composition of GO relies on a number of factors such as the conditions during synthesis, the chemical or physical method used to produce the GO, and the quality and source of the graphite flakes used. The large variability reported in sorption capacities throughout the literature, reveals a high sensitivity to oxygen content for radionuclide sorption. The large variability in calculated sorption capacities also limits the comparability of results between studies on different radionuclides and heavy metals and those carried out by different experimental research groups. Experimental results from all radionuclides, and from all experimental research groups can however be analysed, for which a number of observations are made, and trends emerge, which are now discussed.

The effect of ionic strength and pH on the sorption capacity of materials towards different ions is commonly investigated. Investigations carried out by Romanchuk *et. al.* and Yang *et. al.* into the adsorption of Cs(I)[143] and Sr(II)[143,149] by GO report that ionic strength has a large effect on the adsorption of Cs(I), and the

adsorption of Cs(I) has little dependence on pH, whereas the adsorption of Sr(II) is sensitive to pH and is insensitive to ionic strength at pH > 6. Zhao *et. al.*[145] investigated the effect of ionic strength on the adsorption of Cd(II) and Co(II), they also reported that the adsorption of both Cd(II) and Co(II) is sensitive to ionic strength at low pH and insensitive at high pH. Similar investigations into the adsorption of Pb(II)[146,147] using GO also reported a sensitivity to ionic strength at low pH (pH < 6), and no sensitivity at higher pH. Sensitivity to ionic strength can be used as a reliable, indirect method for identifying the formation of inner-sphere and outer-sphere complexes[172]. Investigations carried out for cations in higher oxidation states reported that the adsorption of Eu(III)[150], Th(IV)[151,152], and U(VI)[154] are all independent or have little dependency ionic strength, across a wide pH range (pH 3 to 11). An investigation by Showalter *et. al.*[146] also determined inner-sphere complexation between U(VI) and GO, and the formation of outer-sphere complexes between Cd(II) and GO surfaces, in the pH range 4.9 to 8.1 using X-ray adsorption fine structure spectroscopy (XAFS). It can be established therefore from available experimental results that the adsorption of the monovalent cation Cs(I) by GO is commonly by outer-sphere complexation, whereas both inner-sphere and outer-sphere surface complexes can form between GO and the divalent cations Sr(II), Cd(II), Co(II), and Pb(II) depending on the pH of the environment. Cations in oxidation states greater than 2 mostly form inner-sphere complexes with GO.

The effect of temperature on the adsorption of radionuclides by GO has also been investigated experimentally. Zhao *et. al.*[145] reported an increase in the maximum sorption efficiency of Cd(II) and Co(II) from 106.3 mg g^{-1} and 68.2 mg g^{-1}, to 167.5 mg g^{-1} and 79.8 mg g^{-1}, respectively, when the temperature in their experiments was increased from 303 K to 333 K, and all other parameters were maintained. Zhao *et. al.*[147] also reported that the sorption capacity of Pb(II) on GO increased from 842 mg g^{-1} to 1150 mg g^{-1} when the temperature was increased from 293 K to 313 K, it increased further to 1850 mg g^{-1} at 333 K, a greater than two-fold increase in sorption capacity with an increase in temperature of 40K. Sun *et. al.*[150] also reported an increase in the sorption capacity of about 30% for the removal of Eu^{3+} with an increase in temperature from 298 K to 338 K, and likewise it was reported by both Pan *et. al.*[151] and Ye *et. al.*[152] that the sorption of Th^{4+} increased with an increase in temperature.

The comparability of radionuclides in the same oxidation state has also been assessed, it has already been established from other experimental studies that monovalent cations form outer-sphere complexes with GO, divalent cations form both inner-sphere and outer-sphere complexes dependent on the pH of the system, and cations in higher oxidations states form predominately inner-sphere complexes with GO. Sitko *et. al.*[140] investigated the adsorption capacity of GO towards a number of divalent metal cations. They investigated the adsorption of Cu(II), Zn(II), Cd(II), and Pb(II) using GO produced by the same batch process, and maintaining all conditions. They calculated maximum adsorption capacities of 294, 345, 530 and 1119 mg g^{-1} for Cu(II), Zn(II), Cd(II), and Pb(II), respectively. When considered with relation to their respective masses, it was revealed that the Sikto *et. al.* GO adsorbed approximately 5 mmol of each of the divalent radionuclides per gram. A similar study by Zhao *et. al.*[145] found that GO produced by their batch experiment adsorbed approximately 1 mmol per gram of the divalent cations Cd(II) and Co(II). It was established earlier in this discussion that the adsorption capacity of GO has a strong dependence on functional group density. The results presented by Sikto[140] and Zhao[145] suggest there is an equivalency between all divalent cations, research carried out by Yang *et. al.*[160] however, who investigated the adsorption of Pb(II), Ni(II), and Sr(II) in competitive environments reported sorption capacities of 2.37, 1.75, and 0.62 mmol g^{-1} of Pb(II), Ni(II), and Sr(II) respectively, for GO produced by their batch process. The range of adsorption capacities for divalent metal calculated by Yang *et. al.* is presumably due to competition between metal cations in their experiment, and not an inherent difference between the bonding nature of the metals.

Romanchuk *et. al.*[1] reported in another investigation that there is also a correlation between pH sorption edge and cation formal charge. They reported that the complete adsorption of Th(IV) and Pu(IV) could be achieved at pH > 1.5 in their investigation, whilst complete sorption of Am(III) and Eu(III) did not occurred pH > 2.3. They reported also that the sorption of most cations they investigated is quantitative over a large pH range but the sorption of U(VI) decreased significantly above neutral pH, which is most likely due to the formation of U(VI) carbonate complexes at high pH. The adsorption of Tc(VII) is reported to be close to zero at pH > 1.5 but is very high at extremely low pH. Technetium exists mostly as the pertechnetate anion (TcO_4^-) so its adsorption is inhibited significantly by electrostatic repulsion between the

negatively charged pertechnetate ion and the anionic charge which accumulates on GO.

The pH at which there is zero charge (pH_{pzc}) on GO have been determined by a range of methods and by using a range of GO samples, with varying results. The surface charge on GO is positive at $pH < pH_{pzc}$ and negative at $pH > pH_{pzc}$. The most common method used to determine the pH_{pzc} for GO is mass titration, by which it is most commonly determined to be around pH 3.9[145,150,153]. Zhao *et. al.*[147] reported a pH_{pzc} value of 3.8 by titration experiment, they reported also that it increased to pH 4.1 for reduced GO (rGO), indicating a GO charge dependence on the degree of oxidation. Wang *et. al.*[154,173] also determined the pH_{pzc} of GO from a mass titration technique[174], they however reported it to be 2.09, which is perhaps more fitting with experimental observations reported by Romanchuk *et. al.*[1]. Who, as discussed, reported that the adsorption of the TcO_4^- anion was close to zero at pH > 1.5 due to electrostatic repulsion between TcO_4^- and the anionic charge accumulating on the GO nano-flake. They reported also that trivalent and tetravalent radionuclides can be completely adsorbed at pH > 2.3 and pH > 1.5, respectively, a process which seems unlikely in the presence of strong electrostatic repulsion. Zeta potential measurements carried out by Ye *et. al.*[152] also indicate that GO is negatively charged at pH > 2, and determined that the pH_{pzc} of GO is around 1.5 from interpolation of results. Konkena *et. al.*[175] also carried out zeta-potential measurements on GO and rGO, reporting that highly oxidised GO has a negative charge in the pH range 2 to 12, whilst rGO remains positively charged at low pH. Electrokinetic measurements carried out by Chowdhury *et. al.*[176] also revealed GO is negatively charged in the pH range 2 to 10. Additionally, Konkena *et. al.*[175] also established from zeta potential measurements, pH titrations and infrared spectroscopy that deprotonation of carboxylic acid groups is the primary cause of negative charge build up on GO nano-flakes, the deprotonation of hydroxyl groups occurs only in basic conditions when significant negative charge has already accumulated on GO nano-flakes.

The reversibility of radionuclide adsorption and the reusability of GO following desorption has also been investigated. Romanchuk *et. al.*[1] investigated the reversibility of the sorption of Pu(IV) and U(VI) from GO. They reported that when the pH in their experimental environment was reduced to 1 by the addition of $HClO_4$, new steady state

conditions were reached in less than 10 minutes, in which more than 60% of their Pu(IV) and nearly all of their U(VI) had been desorbed. Madadrang et. al[177] in a similar investigation found that the addition of ethylenediamine (EDTA) to GO improved the adsorption capacity of Pb(II), and Pb(II) could be almost completely desorbed from GO-EDTA at extremely low pH. Characterisation of the GO-EDTA after desorption also suggested that it could be reused. Bai *et. al.*[178] reported also from desorption experiments that 68%, 91%, and 97% of Th(IV) could be removed from GO using 0.1, 0.5 and 1.0 M nitric acid (HNO_3), respectively. The ready desorption of radionuclides from GO suggesting it is potentially reusable, scanning electron microscope (SEM) images of GO taken after desorption however indicated obvious surface morphology changes of the GO induced by the sorption of Th(IV), which may limit the reusability and lifetime of GO. Yang *et. al.*[160] carried out desorption experiments for Pb(II), Ni(II), and Sr(II), initiated by the replacement of the supernatant with metal-ion-free electrolyte solution, results indicated that the complete reversal of adsorption is not possible, but the reversibility can be strengthened by the presence of competing metal ions.

Another extremely desirable property of GO which has been observed and reported is the formation of manageable aggregates when it is mixed with water containing cations. Sheng-Tao *et. al*[144] reported almost immediate aggregate formation when Cu(II) was added to a GO suspension. Under an optical microscope they observed the formation of rod-like structures, approximately 100 μm in length, formed from stacked and folded GO-Cu sheets. Romanchuk *et. al.*[1] also reported almost immediate coagulation between GO and simulated liquid nuclear waste which contained a mixture of radionuclides and other cations, the aggregates which had formed were visible with the naked eye. Examination of the GO-cation precipitate using scanning transmission electron microscopy (STEM) also revealed the coagulated particles are on the scale of 100 μm. Jiang *et. al.*[113] also reported the rapid formation of an aggregate between GO and the divalent cations Ca(II), Ni(II), and Co(II) in aqueous environments. They proposed the formation of a three-dimensional, multi-layered coagulant structure in which GO sheets, water molecules, and the divalent ions assume the role of skeleton, filler, and linker, respectively (see Figure 24).

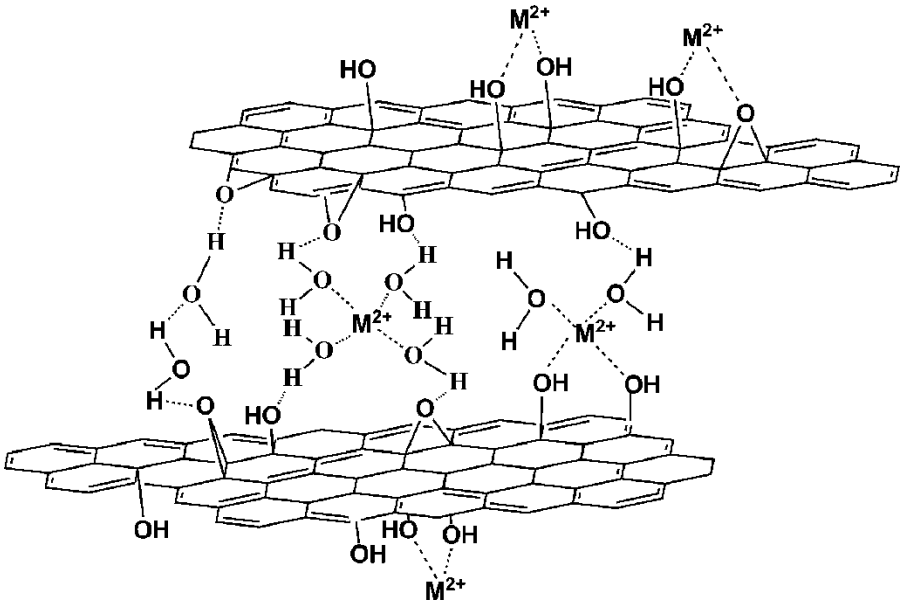

Figure 24: Schematic illustration of the formation of gel-like rGO cylinders with divalent ion linkage. [reproduced with permission from ref 113]

The literature discussed above shows that GO is a very promising sorbent material for the removal of wide range cations arising from nuclear activities and other sources from aqueous environments. It outperforms many conventional methods and other sorbent materials for cation removal and can be produced in a cost effective and environmentally friendly way. It has been shown under experimental conditions to be effective across a wide pH range and in different environmental conditions. It forms manageable aggregates and is potentially reusable. Spent GO can also be completely incinerated, reducing the amount of secondary waste produced.

4.2.2 Computational and Theoretical Research

Along with the considerable experimental interest which has been invested in the development of GO as a sorbent material for the remediation of water contaminated with nuclear material and other toxic cations, theoretical and computational research has also begun to emerge. Computational studies can provide microscopic insight into chemical environments which may not be accessible experimentally. They are also particularly useful for the investigation of actinide systems, where experimental investigations are often prohibited due to concerns around safety and security which is associated with handling toxic and highly radioactive materials. This section discusses some of the recent computational investigations into the nature and strength of binding

between radionuclides and GO nano-flakes. The computational investigations which can be currently found in the literature focus predominately on the sorption of higher actinides, although investigations into other metals are beginning to emerge. Recent studies include investigations into the use of GO to remove neptunium[179], plutonium[179], and thorium[178] containing complexes, the greatest interest to date however has been in the sorption of uranyl[154,180–183] (hereafter referred to as U(VI)). The study of U(VI) is an obvious choice due to it being both naturally occurring, excessively present in the environment due to nuclear activities[184], and soluble in water[185], so can be very mobile. It is also the most common fissile material used in the production of nuclear energy, so its recovery and extraction from aqueous environments is desirable for future energy needs. Recent studies have also explored the sorption of heavy metals such as Pb(II)[160,186], Ni(II)[160], and Sr(II)[160]. More novel computational research has also included such things as the adsorption of UF_6 by GO and similar[187], for potential route towards a new GO based uranium enrichment technique.

Wu *et. al.*[182] investigated the bonding nature of the U(VI) aquocomplex ($[UO_2(H_2O)_5]^{2+}$) with the functionalised edge of graphene nano-flakes using density functional theory (DFT). They investigated the inner-sphere complexation of U(VI) with mono-, ortho-, and meta-functional group pairs of carboxyl (-COOH), hydroxyl (-OH), amide (-$CONH_2$), and methylformamide (-$CONMe_2$). It is widely accepted that OH and COOH groups are found to functionalise the edges of GO nano-flakes, as discussed in greater detail in Chapter 1. There is however no experimental evidence for the existence of $CONH_2$ or $CONMe_2$ groups on the edge of GO nano-flakes, nor is there experimental reference to the presence of nitrogen in GO combustion experiments. Nitrogen containing groups are, however, they state, known to bind effectively towards U(VI) ions. GO can be chemical modified to control both the nature and degree of oxidation and the introduction of new functional species is possible, it is not unfeasible therefore that they could be introduced in future GO design. Wu *et. al.* also considered higher pH environments by deprotonation of the OH and COOH groups, and also explored the different binding interactions that occur to the oxygen and nitrogen atoms in the $CONH_2$ and $CONMe_2$ groups. Their calculations were carried out at the B3LYP level of theory using the 6-31G(d) basis set of double-ζ quality for light elements, and the ECP60MWB quasi-relativistic small

core pseudopotential and associated ECP60MWB-SEG valence basis sets for the uranium atom. They investigated solvation effects by performing single point energy calculations on gas-phase optimised geometries with the SMD solvation model, they also performed single point energy calculations on geometries optimised at the B3LYP level of theory using the M06-2X hybrid functional by the Minnesota groups, which had been found in a previous studie[188] to be more suitable for use with U(VI) containing systems than the more common hybrid functional B3LYP. They reported an increase in the length of both axial (U-O_{ax}) and water (U-O_w) oxygen bonds within the U(VI) aquocomplex when it was bound to the OH and COOH groups on the nano-flake edge, indicating the formation of strong bonds between U(VI) and GO (U-O_{GO}). When complexed to the anionic, deprotonated OH and COOH functional groups, longer U-O_{ax} and U-O_w bonds, and shorter U-O_{GO} bonds were also calculated than to the neutral functional groups, indicating an increase in stability due to electrostatic interactions between the cationic metal complex and anionic functional groups. They also reported stronger binding interactions between U(VI) and functional group pairs than to single functional groups, indicating a preference towards the formation of multiple U-O_{GO} bonds, and therefore to highly oxidised GO, in agreement with experimental results. Significantly shorter U-O_{GO} bonds were also calculated than those between the U(VI) metal centre and nitrogen atoms (U-N_{GO}) in binding interactions with the $CONH_2$ and $CONMe_2$ groups, suggesting that U(VI) has much stronger coordinating ability towards oxygen atoms than to nitrogen atoms. Their binding energies calculated in the gas phase and with continuum solvent effects showed broadly the same trends, however, the inclusion of solvation effects was found to have a profound effect on calculated binding energies. All binding energies they obtained from gas phase calculations were large and negative (strong binding was predicted), many of the binding energies calculated between U(VI) and the neutral functional groups on GO however, were positive in aqueous phase calculations. The binding energies calculated with the M06-2X *xc*-functional were also broadly similar to those calculated at the B3LYP level of theory, indicating the suitably of the B3LYP *xc*-functional in such calculations.

The adsorption of U(VI) was also investigated by Sun *et. al.*[180] in a combined experimental and computational study. They determined experimentally from EXAFS studies that U(VI) primarily forms inner-sphere complexes with GO across a wide pH

range as has been reported in other experimental investigations[146,154]. They found however that outer-sphere complexes formed at pH 4.0 on rGO. They determined their rGO to be 7.35% oxygen by weight, whilst their GO was 37.43% by weight. They found also that in high pH conditions, adsorption occurred by coprecipitation on both GO and rGO, presumably due to the formation of $(UO_2)_3(OH)_7^-$ and $UO_2(OH)_3^-$ species[189] which form at pH > 8.0. Their DFT calculations were carried out on a series of finite GO nano-flake models with hydroxyl and epoxy groups on the GO surfaces and carboxylic acid groups at the flake edges. They performed geometry optimisations in the aqueous phase using the popular PBE0 *xc*-functional, which is used in the research presented in this thesis, and the cc-pVDZ basis set of polarised double-ζ quality for light elements and an ECP and associated basis functional for uranium. They found that the formation of inner-sphere complexes with COOH groups on the GO nano-flake edge is preferred to outer-sphere binding to surface epoxy groups, in agreement with their experimental results. They found also, as in other studies, that calculated binding energies to COOH groups on the nano-flake edge increases significantly if the COOH deprotonates to form the anionic carboxylate groups (12.1 kcal mol^{-1} to 50.5 kcal mol^{-1} in their DFT calculations). They found also that the binding interaction with surface OH groups resulted in the abstraction of a OH group from the GO surface and formation of a stable $[GO\text{-}OH\text{---}U(OH)O_2]^{2+}$ with a calculated binding energy of 42.8 kcal mol^{-1}.

Another study by Wu *et. al.*[179] investigated the sorption of plutonium and neptunium ions to the surface and edge of GO. Their investigation studied the sorption of pentacoordinated neptunyl ($[Np(V)O_2(H_2O)_5]^+$) and plutonyl ($[Pu(VI)O_2(H_2O_5]^{2+}$), and nonacoordinated plutonium ions ($[Pu(IV)(H_2O)_9]^{4+}$)) to graphene nano-flakes functionalised with a single hydroxyl, carboxyl or carbonyl group on the flake edge or epoxy group on the GO surface (see Figure 25).

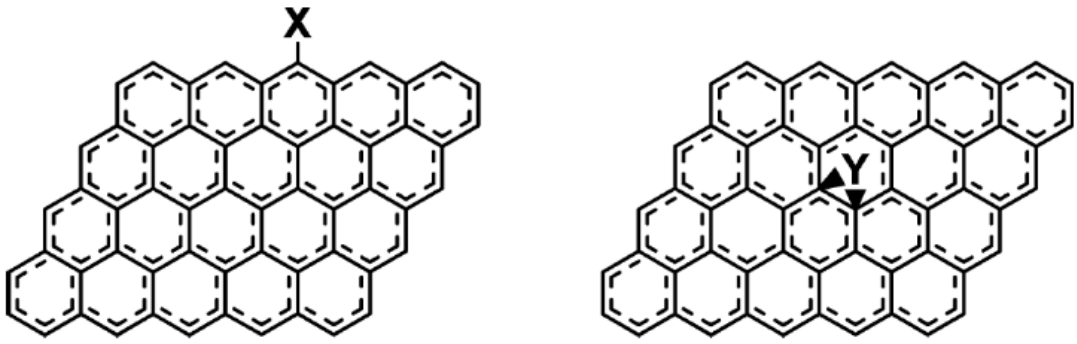

Figure 25: Structure of GO used by Wu *et. al.*, X = -OH, -COOH, and –CO groups, Y = -O- group.

Their geometry optimisations were initially carried out in the gas-phase at the B3LYP level of theory using the ECP60MWB effective core potential and associated ECP60MWB-SEG valence basis sets for neptunium and plutonium atoms and the 6-31G(d) Pople split valence basis set of double-ζ quality for light elements. They performed additional single point energy calculation on optimised geometries using the SMD implicit solvation model to consider solvation effects, and using the larger 6-311+G(d,p) basis set of polarised triple-ζ quality to investigate the effect of basis set quality in the energy calculations. Large basis sets, it is widely accepted, are better suited to energy calculations, as discussed in Chapter 2. They found from geometry optimisations that Np(V) and Pu(VI) are prone to retain pentacoordination when bonding to all functional groups, through coordination to 4 oxygen atoms in water molecules and one oxygen atom in the GO functional group. They observed also the formation of a hydrogen bond in complexes of Np(V) with the COOH and CO groups on the GO edge, which were thought to contributed to stabilisation. They found in complexes of Pu(IV) with GO that the plutonium ion can be either octa- or nonacoordinated. When binding with the COOH group on the GO edge, Pu(IV) was found to form two bonds to oxygen atoms in the functional group and retain coordination to 7 water molecules in the solvation shell. When binding to the OH or CO groups on the GO edge, or the epoxy group on the GO surface, Pu(IV) was found to be octacoordinated, forming one Pu-O_{GO} bond with the functional group and coordinating to 7 water molecules in the first solvation shell. The 8th water molecule from the solvation shell moved into the second solvation shell. They reported from their calculations that Pu(IV) binds more strongly than both Pu(VI) and Np(V) to all functional groups, and Np(V) binds least strongly, which is consist with experimental

observations. They found that Pu(IV) binds most preferentially to the epoxy groups on the GO surface, whilst complexation of Np(V) with the epoxy group was found to be the only endothermic reaction in their aqueous phase calculations. They reported that Pu(VI) binds preferentially with the OH groups on the GO flake edge, and Np(V) binds preferentially to the COOH group. They found, as in other studies, that the inclusion of solvation effects has a significant effect on calculated binding energies. They found also that the use of the larger triple-ζ basis set typically predicts binding energies which are approximately 30 kcal mol^{-1} greater than calculations carried out with a double-ζ basis set but the same general trends emerge. They also reported from calculated M-O_{GO} bond lengths that Pu(IV) binds more easily with GO than the other two ions studied. NBO and QTAIM analysis was also carried out by Wu *et. al.* which indicated that the bonds formed in the complexation of Pu(IV) and GO possessed greater covalency whilst electrostatic interactions were more dominant for complexation of Np(V) and Pu(VI) ions with GO.

Bai *et. al.*[178] studied the sorption of Th(IV) in complementary experimental and DFT investigations. Their experimental results were in agreement with observations made in other experimental studies. They found for example that sorption kinetics were fast and equilibrium conditions were reached in less than 10 minutes. They found also that sorption has a strong dependence on pH but is independent of ionic strength, indicating the formation of inner-sphere complexes with the GO nano-flake. They carried out EXAFS analysis on their Th(IV) complexes with GO which indicated Th(IV) is typically coordinated with 8 or 9 oxygen atoms with an average Th-O bond length of ~2.45 Å in the first coordination shell. Their DFT calculations were carried out to investigate the bonds formed between COOH and OH groups on the surface and edge of GO nano-flake, their Th(IV) fully coordinated with 4 nitrate (NO_3^-) groups in the first coordination shell. Nitrate groups were used due to a stronger coordination ability of NO_3^- than H_2O to Th(IV). They reported calculated bond lengths between GO functional groups and the Th(IV) metal centre (Th-O_{GO}) were longer to oxygen atoms in OH groups (Th-O_{OH}) than those to carboxyl oxygen atoms (Th-O_{COOH}), suggesting that COOH groups have stronger coordination ability towards Th(IV) than OH groups. They calculated Gibbs free energies (ΔG) for a range of binding configurations to the GO nano-flake surface and edge at the B3LYP level of theory using a small-core ECP for Th, a 6-31G(d) basis set of polarised double-ζ quality for light elements, and SMD

continuum solvent model to include bulk solvation effects. The Gibbs free energies reported were all around -2000 kcal mol^{-1} in the gas phase and -600 kcal mol^{-1} in the aqueous phase, indicating that all binding of Th with GO is favourable, and highlighting the significant role that solvation energies play in the sorption process of Th(IV) and other radionuclides on GO, which has been reported in other studies.

The adsorption of heavy metals using GO has also been studied by computational investigations. Wang *et. al.*[186] investigated the adsorption of Pb(II) by combined experimental and theoretical study. Using experimental studies they reported a sensitivity to ionic strength at pH < 6 and an insensitivity to ionic strength at pH > 6 for the adsorption of Pb(II) by GO which is consistent with other studies into the adsorption of divalent metals using GO. They reported also a small decrease in the pH of the solution following adsorption of Pb(II), which is associated with the progressive deprotonation of GO surface functional groups during the sorption process and hydrolysis of Pb(II) solvated complexes. They noted also a progressive decrease in the adsorption efficiency of Pb(II) at pH > 8 despite the known continued progressive deprotonation of the GO nano-flakes. The progressive decrease in binding efficiency is most likely due to the formation of $Pb(OH)^{+}$, $Pb(OH)_2^0$, and $Pb(OH)_3^-$ complexes which are known to form at various pHs[190]. The $Pb(OH)_3^-$ complex particularly, which forms at very high pH, experiences electrostatic repulsion from the increasingly deprotonated GO, which significantly inhibits sorption. They found also, as in other studies, that the sorption kinetics fit the Langmuir isotherm models better than the Freundlich models, suggesting that sorption on the GO surface is by monolayer coverage. FTIR spectra obtained before and after Pb(II) sorption indicated that the binding of Pb(II) is mainly due to the formation of Pb(II) complexes with COOH groups, presumably due to the deprotonation of COOH groups at relatively low pH and the accumulation of negative charge on COOH groups. Using DFT they calculated binding energies of 1.3 kcal mol^{-1} to a single surface epoxy group, and 16.5 kcal mol^{-1} to a pair of epoxy groups, binding energies calculated to COOH groups were 14.7 and 18.7 kcal mol^{-1} to a single COOH group and a COOH pair, respectively. Calculated binding energies indicate Pb(II) prefers binding to COOH groups than epoxy groups which is consist with their experimental results. Greater binding to functional group pairs also indicates preferred binding to highly oxidised GO which is consist with other experimental and theoretical studies. The increase in binding energy

reported by Wang *et. al.* for complexation with multiple oxygen functional groups was much less significant for binding interactions with COOH groups on the GO edge than epoxide groups on the GO surface.

Computational studies have also been useful in the investigation of the competitive adsorption of radionuclides in solution using GO. The study of competitive adsorption is important because radionuclides often co-exist in the solution in different concentrations. Greater understanding of their sorption in competitive environments can also provide insight into nuclide sorption in varying environmental conditions, in the presence of competing ions, it may also lead to possible routes towards the use GO for radionuclide selectivity and separation. Cheng *et. al.*[183] investigated the competitive adsorption of U(VI) and Sr(II) by GO using batch techniques and computational studies. They found from experimental results that the presence of U(VI) significantly inhibits the sorption of Sr(II) in the pH range 3.0 - 7.5, but not at higher pH. The presence of Sr(II) was found to have little effect on the sorption of U(VI) across the whole pH range, demonstrating a higher affinity of GO towards U(VI) than Sr(II). Their computational investigation compared the binding interactions of hydrated U(VI) and Sr(II) complexes ($[(UO_2)(H_2O)_5]^{2+}$ and $[Sr(H_2O)_9]^{2+}$) with model GO flakes functionalised with a single deprotonated OH group on the surface. Their calculations were carried out at the B3LYP/6-31G(d) level of theory with small-core ECP which replaces 60 and 28 core electrons from uranium and strontium, respectively, and solvation effects taken into account by the SMD continuum solvent model. The coordination numbers used for U(VI) and Sr(II) were determined by EXAFS calculations. They reported calculated Sr-O bond lengths in their $[Sr(H_2O)_9]^{2+}$ complex to be 2.650 Å, which was in excellent agreement with Sr-O bond lengths they measured experimentally using EXAFS of 2.64 Å. Visual analysis of their optimised geometries reveals however that U(VI) is always pentacoordinated in their calculations, whereas the Sr(II) aquocomplex is octacoordinated with the ninth water molecule in the second solvation shell. Sr(II) complexes with the functional groups on the GO surface are hepta- or octacoordinated dependent on the nature of the binding interaction. They calculated binding energies for both inner-sphere and outer-sphere binding interactions to the O^- functional group. Outer-shell binding energies for U(VI) were calculated to be 33.53, 33.12, 32.34 and 32.29 kcal mol^{-1} in 4 different binding configurations, suggesting there is little variability in the energetics of different

outer-sphere binding configurations. Calculated outer-shell binding energies for Sr(II) showed much greater variation. Binding energies in 5 configurations were calculated to be 19.50, 19.40, 18.88, 17.04 and 14.71 kcal mol^{-1}, it should be noted however that the two lowest value correspond to geometries in which an extra water molecule has migrated from the primary to the secondary solvation shell. Inner-sphere binding energies were calculated to be 37.77 and 37.17 kcal mol^{-1} for U(VI) in two difference configurations, suggesting again little sensitivity to a change in binding configuration, and 12.94 kcal mol^{-1} for Sr(II). Binding energies also indicated that U(VI) binds much more strongly to GO than Sr(II) and shows a preference towards inner-sphere binding interactions, Sr(II) shows a preference towards forming outer-sphere complexes, which are both in agreement with experimental results.

Yang *et. al.*[160] investigated the individual and competitive adsorption of the divalent metals Pb(II), Ni(II), and Sr(II) by GO, by combined experimental and theoretical studies. The individual investigations for each of the metal ions were in good agreement with other research into the sorption of divalent metal ions to GO. They calculated maximum adsorption capacities of 2.37, 1.75, and 0.62 mmol g^{-1} for Pb(II), Ni(II), and Sr(II) respectively at pH = 5 and T = 300K. When the metals were studied in competitive binary and ternary systems, they found that the adsorption of all metals decreased compared to single metal ion systems. The measured decrease in adsorption was relative to the adsorption affinity of the competing metal ions. The adsorption of Ni(II) for example decreased from 1.75 mmol g^{-1} in the individual metal ions system, to 1.43 mmol g^{-1} in a binary mixture with Sr(II), and to 0.92 mmol g^{-1} in a binary mixture with Pb(II), which are consistent with similar observations reported by Cheng *et. al.*[183] in the U(VI) and Sr(II) competitive sorption experiment. Desorption experiments, initiated by the replacement of the supernatant with metal-ion-free electrolyte solution indicated that the complete reversal of Pb(II), Ni(II), and Sr(II) adsorption is not possible, but the reversibility can be strengthened by the presence of competing metal ions. Their computational studies were carried out using DFT at the PBE0 level of theory with a cc-pVDZ basis set of polarised valence double-ζ quality for light elements, and suitable small-core ECPs and associated basis sets for Pb(II), Ni(II), and Sr(II). Their calculations were all carried out in the aqueous phase using a polarised continuum solvent model. They calculated binding energies for inner-sphere interactions between hexacoordinated Pb(II), Ni(II), and Sr(II), with lone functional

groups and functional group pairs of OH and epoxy groups. They reported calculated binding energies of 1.3, 3.9, and 3.3 kcal mol^{-1} for Pb(II), Ni(II), and Sr(II) to a single epoxy groups, respectively. Binding to pairs of epoxy groups were calculated to be 11.9, 15.9, and 15.4 kcal mol^{-1} for Pb(II), Ni(II), and Sr(II) respectively, a significant increase on the single epoxy group values. Binding energies indicate highly oxidised GO has a higher sorption capacity, consistent with experimental results and other theoretical studies. Binding energies to pairs of OH groups were calculated to be 18.7, 24.9, and 14.6 kcal mol^{-1} for Pb(II), Ni(II), and Sr(II) respectively, indicating both Pb(II) and Ni(II) preferentially bind to OH groups whilst Sr has comparable affinity towards both functional groups. Additionally to the calculated binding energies, transition state calculations at the same level of DFT showed that Pb(II) can easily abstract an OH group from the GO surface to form a $[GO(OH) \text{ --- } Pb(OH)(H_2O)_6]^{2+}$ complex which is much more stable, whilst Ni(II) and Sr(II) cannot, revealing a bonding order Pb > Ni > Sr which is in agreement with their experimental results.

4.3 Computational Details

4.3.1 Computational Details

Geometry optimisations were carried out using DFT in version 6.5 of the TURBOMOLE[95] code. The PBE[81] *xc*-functional, which is based upon the generalised gradient approximation (GGA), along with the associated PBE0[87] hybrid-GGA *xc*-functional, were used throughout. The functionals used do not include correction for dispersion energies. The def2-SVP[191,192] atom centred Ahlrich basis set of polarised double-ζ quality was used for H, C and O, and small-core effective core potentials (ECPs) with the associated basis set were used for Sr[193], La[194,195], and Th[196,197] to reduce computational cost, ECPs are discussed in Chapter 2. The ECPs used are those developed by Dolg *et. al.* and replace 28 core electrons in Sr and La, and 60 core electrons in Th, respectively. A polarised double-ζ quality basis set has been chosen due to prohibitively high computational cost when using the def2-TZVP triple-ζ basis set used for calculation in Chapter 3 for large systems. Although a polarised triple-zeta quality basis sets would be more accurate for energetic

calculations, the use of polarised double-ζ quality basis sets is common, and widely accepted to be sufficient for contemporary research on large systems[198]. Calculations to correct for basis set superposition error were not carried out, although it should be noted that calculations carried out using smaller basis set are more prone to the error. Wu *et. al.*[179] also reported that although calculations using triple-ζ basis sets typically predict binding energies around 30 kcal mol^{-1} greater than double-ζ basis set calculations, the same general trends emerge from calculations using both basis sets, so conclusions and general trends emergent from calculations carried out with a basis set of double-ζ quality would be expected to be representative of those obtained with a larger basis set.

Consideration of solvation effect was made using the conductor-like screening model (COSMO) with default parameters, *i.e.* a relative permittivity of $\varepsilon_r = \infty$, which is considered a suitable approximation for water, and molecular cavities constructed of spheres with radii which are 2.00 Å, 1.72 Å, and 1.30 Å for C, O, and H respectively, and 2.223 Å for Sr, La, and Th. It has been shown also that continuum solvation models can produce reliable free energies in solution for the actinide species with the first coordination sphere treated explicitly[199].

Numerical vibrational frequency calculations were carried out on geometries optimised at the PBE level of theory, in order to confirm correspondence to local energetic minima. Correspondence to energetic minima was assumed for geometry optimisations carried out using the PBE0 *xc*-functional. Such an assumption is made due to the large computational cost associated with numerical frequency analysis, especially those carried out on geometries optimised using hybrid-functionals.

4.3.2 Model of the Graphene Oxide (GO) Nano-flake

The model of the GO nano-flake used throughout this chapter is adapted from that developed in Chapter 3. It was discovered that the adsorption of hydroxyl groups on the GO surface is much more favourable energetically than the formation of epoxy groups, which is consist with typical GO compositions obtained from experimental results[5]. An insensitivity to GO nano-flake size on the adsorption of OH groups and formation of epoxy at high levels of surface oxidation was also revealed, which had

not been reported previously. The GO nano-flake model used in this chapter is based upon the n = 19 nano-flake developed in Chapter 3 which results have suggested provides a good representation of the physical and electronic structure of an infinite GO nano-flake. The n = 19 nano-flake model also allowed for sufficient spatial variation to study distinct surface and edge binding interactions, whilst also being conservative with respect to computational expense. The GO nano-flake model used in this chapter has 50% surface oxidation. It is based upon the 50% mixed oxidised flake presented in Figure 21 which is in the middle of the range of oxidation levels reported from experimental results. The surface chemistry has been modified to incorporate three additional epoxy groups in place of six hydroxyl groups (see Figure 26). This results in a GO nano-flake with a chemical composition of $C_{36}(OH)_{10}O_4$ (excluding edge groups) which is in close agreement with typical GO compositions observed experimentally.

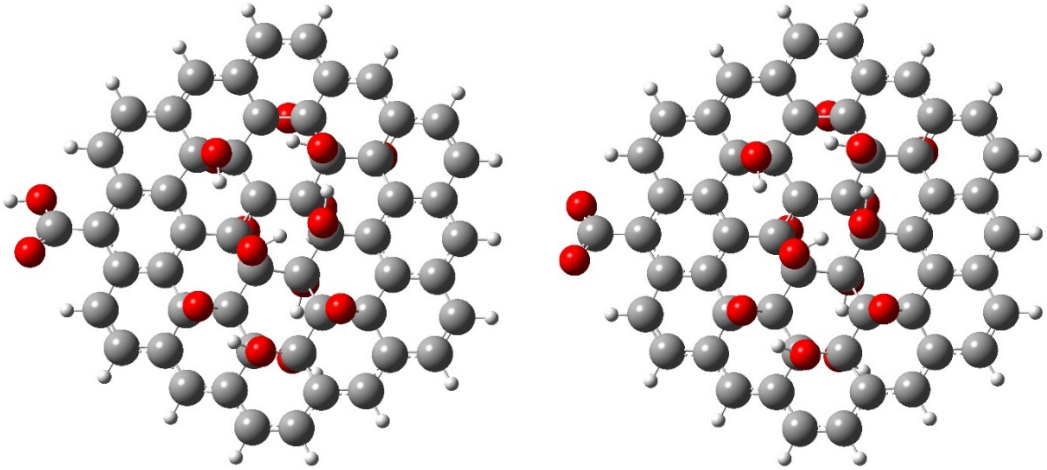

$C_{54}H_{17}(OH)_{10}(O)_4COOH$ $C_{54}H_{17}(OH)_{10}(O)_4COO^-$

Figure 26: GO nano-flakes incorporating both hydroxyl and epoxy groups at the 50% level of surface oxidation. Optimised at the PBE/SVP level of theory

The GO nano-flake edges were also modified to incorporate a single carboxylic acid (COOH) or carboxylate (COO^-) group in place of a hydrogen atom. COOH groups are known to exist on GO edges from experimental characterisation[5]. GO is also known to deprotonate at relatively low pH, and become increasingly deprotonated as pH is increased. The deprotonation of GO has been shown to significantly affect the sorption of cations. There is no direct method to explicitly simulate pH effects in DFT, the deprotonation of COOH edge groups to the anionic COO^- group, however, does allow

for the consideration of some degree of known pH effects in GO models, as has been done in other computational studies[180,182]. The anionic O^- surface functional groups is not considered, based on experimental results by Konkena *et. al.*[175] who reported that OH groups deprotonate at much higher pH than COOH groups, and COOH groups are the main anionic group in GO and the main source of the progressive negative charge accumulated on GO at increased pH.

4.3.3 Radionuclide Analogues

To understand the binding interactions between radionuclides and the surfaces and edges of GO nano-flakes, a single divalent, trivalent, and tetravalent cation were chosen. The radionuclide cations which are investigated are Sr(II), La(III), and Th(IV), these were chosen primarily because of their closed electron shells. The use of closed electron systems in DFT calculations is advantageous because calculations with open electron shell systems are prone to such effects as spin contamination,[200–202] which can make their results less reliable. Calculations carried out on closed shell electron systems are also typically less computational expensive. Sr(II) is also one of the most abundant divalent nuclear fission products so understanding of its interactions with GO is relevant to future industrial applications. The chemistry of the lanthanides are similar, so La(III) is a reasonable example of this series. There are perhaps more industrially relevant actinides than Th(IV), such as U or Pu, but it is quite representative of the typical size and one of the (many) possible oxidation states in the actinide series. There is also an abundance of experimental data on the adsorption of Th(IV) to GO to compare DFT results to.

The Sr(II) aquocomplex used is in the hexacoordinated triangular prism configuration, which was found to be the most favourable configuration in DFT investigations by Kerridge *et. al.*[203], and is the configuration used in similar DFT studies by Yang *et. al.*[149]. A recent Sr(II) hydration study by Makkos *et. al.*[204] also reported that Sr(II) is most stable when hexacoordinated with solvation shells containing 1-4 hydroxyl groups. La(III) and Th(IV) are both nonacoordinated, at the PBE level of theory both were found to form a tricapped prism configuration (see Figure 27) in geometry optimisations carried out without symmetry constraints, whilst at the PBE0

level of theory both formed the distorted monocapped square antiprism configuration (see Figure 28).

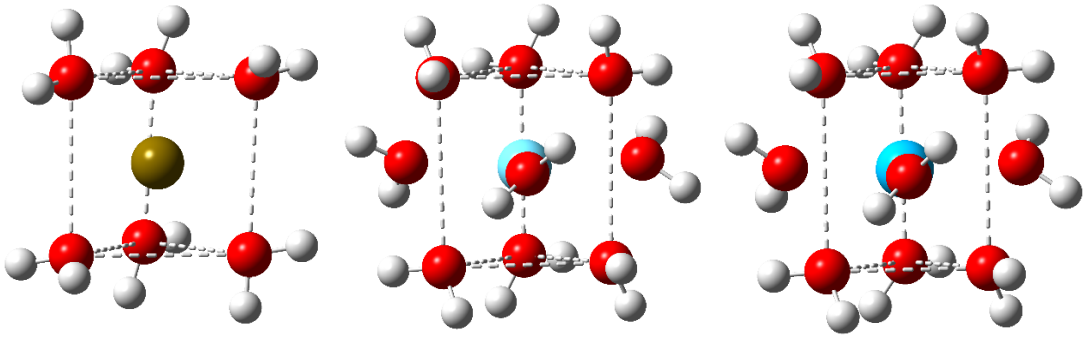

$[Sr(H_2O)_6]^{2+}$ $[La(H_2O)_9]^{3+}$ $[Th(H_2O)_9]^{4+}$

Figure 27: Hydrated Sr(II), La(III), and Th(IV) cations, in the six-coordinated triangular prism (Sr), and nine-coordinated tricapped prism (La and Th) configurations. Optimised at the PBE/SVP level of theory.

There have been many studies to determine the configurational and structural arrangement of La(III) and Th(IV) solvated complexes, both experimental and computational. Buzko *et. al*[205,206] investigated the hydration of La by 8 and 9 water molecules using Hartree-Fock (HF) and second-order Møller-Plesset perturbation theory (MP2) calculations. They determined that the La(III) ion in aqueous solution is primarily nonacoordinated, and the tricapped prism configuration was preferred at their level of theory. They also reported a continuous decrease in the cationic charge on La(III) with increased solvation from Mulliken charge analysis. In the nonacoordinated hydrated structure their calculations suggest about one-quarter of the tricationic charge was transferred to the water molecules in the aquocomplex solvation shell. Allen *et. al.*[207] used extended x-ray absorption fine structure (EXAFS) spectroscopy to investigate coordination in the first solvation shell of trivalent lanthanide and actinide ions, they determined an average coordination number of 9.2 for La(III) and a La-water (La-O_w) bond length of 2.54 Å. Yang *et. al.*[208] investigated the hydration of Th(IV) by DFT and molecular dynamics (MD) simulations to study the first and second hydration shells, respectively. They concluded based on DFT calculations that the primary hydration coordination number of Th(IV) is 9. They also reported from DFT calculations carried out at the B3LYP level of theory that the capped-square-antiprism configuration of hydrated Th(IV) is approximately

4 kcal mol^{-1} more stable than the tricapped prism configuration. The greater stability in Th(IV) nonahydrate they accredited to greater overlap between the Th 6*d* and 5*f* orbitals with O 2*p* orbitals in the higher symmetry capped square antiprism (C_{4v}) configuration than the tricapped prism configurations (D_{3h}). Torapava *et. al*[209] also reported that Th(IV) is most commonly hydrated with nine water molecules, based on EXAFS and large angle X-ray scattering (LAXS) investigations. They reported also that it most commonly exists in the tricapped trigonal prism and monocapped square antiprism configurations. Although results presented by Yang *et. al*[208] suggest that the capped square anti-prism is the most stable of the two common nonacoordinated Th(IV) hydrates, the difference in stability identified between the two configurations in the research carried out using the B3LYP *xc*-functional is not expected to significantly affect any trends in results. The tricapped prism configuration is hence used for Th(IV) in PBE calculations throughout this thesis.

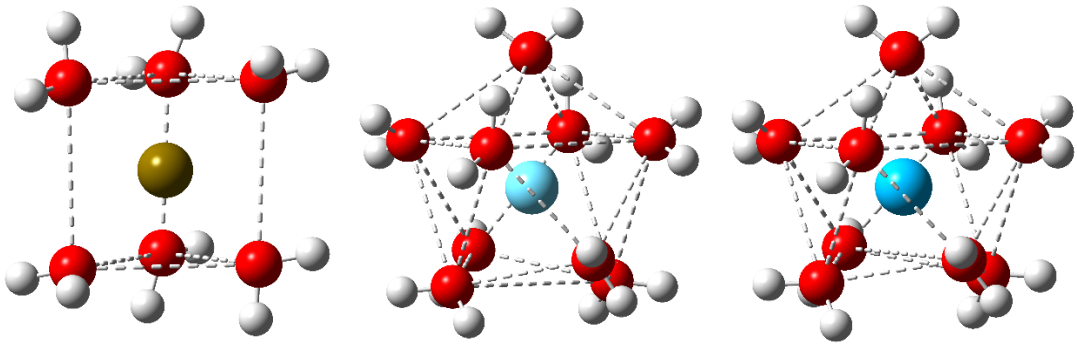

$[Sr(H_2O)_6]^{2+}$ $[La(H_2O)_9]^{3+}$ $[Th(H_2O)_9]^{4+}$

Figure 28: Hydrated Sr(II), La(III), and Th(IV) cations, in the six-coordinated triangular prism (Sr), and nine-coordinated monocapped square antiprism (La and Th) configurations. Optimised at the PBE0/SVP level of theory.

Natural population charge analysis (NPA) was also carried out on hydrated Sr(II), La(III), and Th(IV) complexes, the calculated charge on the metal ion are given in Table 24. The calculated charges suggest approximately 10% of the dicationic charge of Sr(II) is transferred to water molecules in the solvation shell, approximately 25-30% of the tricationic charge of La(III) is transferred to the solvation shell, consistent with Mulliken charge analysis calculations by Buzko et. al[205,206], and approximately half of the tetracationic charge of Th(IV) is transferred to the water molecules in the solvation shell.

Table 24: Charge on metal cations in hexacoordinated (Sr) and nonacoordinated (La & Th) aquocomplexes calculated by natural population analysis

Ion	PBE	PBE0
Sr(II)	1.78	1.83
La(III)	2.15	2.27
Th(IV)	1.93	2.13

4.3.4 Reaction Energy Calculations

The reaction energies for inner-sphere complexation of the radionuclide analogues with the surface and edges of the GO nano-flake were calculated in the standard way (see Section 4.3.4.2). Water molecules were eliminated from the solvation shell of the radionuclide analogues and deleted from the system to form M-O_{GO} bonds with the surface or edge of the GO nano-flake, the preferred hexacoordination for Sr(II), and nonacoordination for La(III) and Th(IV), respectively, were maintained. The reaction energies for outer-sphere complexations were calculated using a novel approach developed here specifically for calculations in solvated environments. The approach was developed to overcome some of the known inadequacies in the use of a continuum solvent to describe the first solvation shell in calculations. The use of an explicit solvation model in DFT calculations is prohibitive due to computational cost, particularly for large systems. Full explicit solvation models also do not always provide the most accurate results due to inherent inadequacies in the treatment of dispersion and other intermolecular forces when using DFT, some of which are discussed in Chapter 2. Continuum solvent models provide an effective solution for the inclusion of solvation effects at conservative increase in computational cost, and have been show in other computational studies[182] to have a profound effect on calculated binding energies for radionuclides to GO nano-flakes in DFT calculations, they do not however simulate local hydrogen bond interactions which will be important close to the GO surface. It was therefore deemed desirable to employ an approach in which explicit and implicit solvation models are combined.

4.3.4.1 *The Energy of a Water Molecule*

The energy of water molecules in the bulk explicit solvent was obtained from a 24 water cluster model of Ludwig and Weinhold[210], calculated at the appropriate level of theory for this research. Ludwig and Weinhold investigated water clusters containing between 1 and 26 water molecules in a range of configurations, their lowest energy system was found to be the 24 water molecule tetrakaidecadral configuration (see Figure 29).

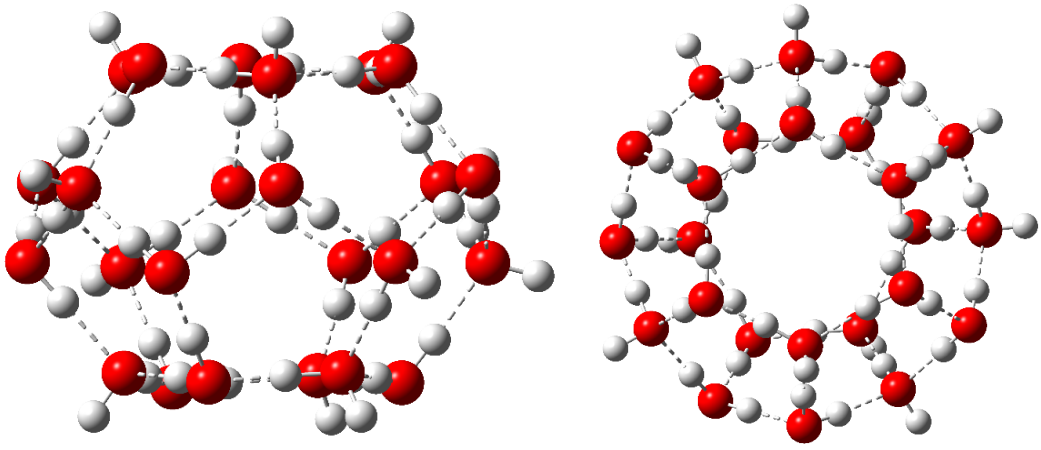

Side view Top view

Figure 29: 24 water molecule cluster in the tetrakaidecadral configuration. Optimised at the PBE/def2-SVP level of theory.

The approximate energy of a single water molecule was obtained using an approach also used in the thesis of Eszter Makkos[211], according to the following equation:

$$E_w = \frac{E_{W24}}{24} \qquad \textbf{(4.1)}$$

Where E_w is an estimation of the energy of an individual water molecule in a bulk water system and E_{W24} is the energy of the 24 water molecule system shown in Figure 29.

4.3.4.2 *Inner-Sphere Binding Interactions*

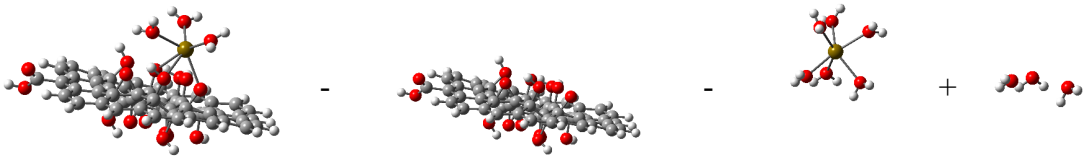

Figure 30: Visual description of inner-sphere binding energy calculation between a Sr(II) aquo-complex and a GO nano-flake surface

The binding energy for the formation of inner-sphere complexes between the radionuclide analogues and the surface or edge of the neutral GO nano-flake was calculated in the conventional way (see Figure 30) using the following equation;

$$E_b = E_{[GO+R]^{m+}} - E_{GO} - E_{[R]^{m+}} + E_{(H_2O)_x} \quad \textbf{(4.2)}$$

Where $E_{[GO+R]^{m+}}$ is the energy of the interacting system, E_{GO} is the energy of the neutral GO nano-flake, $E_{[R]^{m+}}$ is the energy of the radionuclide aquocomplex with charge m, and $E_{(H_2O)_x}$ is the energy of the water molecules eliminated from the solvation shell of the radionuclide aquocomplex during inner-sphere complexation of the radionuclide and the GO surface/edge, calculated from equation (4.1).

Calculations for the anionic GO nano-flake were calculated using the analogous equation;

$$E_b = E_{[GO+R]^{(m-1)+}} - E_{[GO]^-} - E_{[R]^{m+}} + E_{(H_2O)_x} \quad \textbf{(4.3)}$$

Where $E_{[GO+R]^{(m-1)+}}$ is the energy of the interacting system, $E_{[GO]^-}$ is the energy of the anionic GO nano-flake, $E_{[R]^{m+}}$ is the energy of the radionuclide aquocomplex, and $E_{(H_2O)_x}$ is the energy of the x water molecules eliminated from the solvation shell of the radionuclide aquocomplex during inner-sphere complexation of the radionuclide and the GO surface/edge calculated using equation (4.1).

4.3.4.3 *Outer-Sphere Binding Interactions*

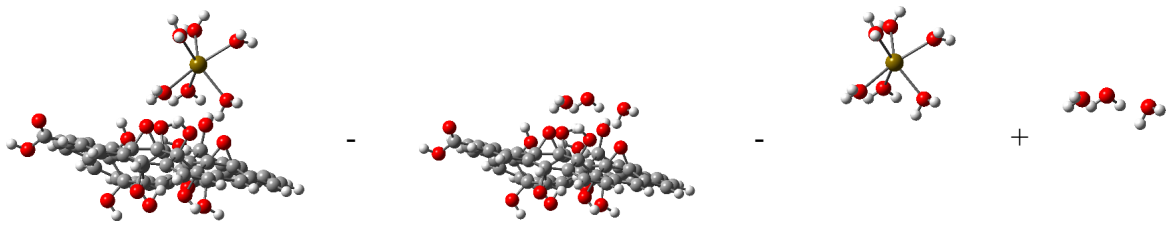

Figure 31: Visual description of outer-sphere binding energy calculation between a Sr(II) aquo-complex and a GO nano-flake surface

The reaction energies for outer-sphere binding interactions were calculated with respect to the displacement of water molecules which would have been interacting with the GO surface or edge (see Figure 31). Using the following equation:

$$E_b = E_{[GO+R]^{m+}} - E_{GO+(H_2O)_x} - E_{[R]^{m+}} + E_{(H_2O)_x} \quad \textbf{(4.4)}$$

Where $E_{[GO+R]^{m+}}$ is the energy of the interacting system, $E_{GO+(H_2O)_x}$ is the energy of the neutral GO nano-flake and water molecules interacting with the GO surface or edge, $E_{[R]^{m+}}$ is the energy of the radionuclide aquocomplex, and $E_{(H_2O)_x}$ is the energy of the x water molecules displaced from the GO surface or edge to accommodate the radionuclide aquocomplex, obtained from equation (4.1).

Calculations for the anionic GO nano-flake system were calculated using the following equation;

$$E_b = E_{[GO+R]^{(m-1)+}} - E_{[GO+(H_2O)_x]^-} - E_{[R]^{m+}} + E_{(H_2O)_x} \quad \textbf{(4.5)}$$

Where $E_{[GO+R]^{(m-1)+}}$ is the energy of the interacting system, $E_{[GO+(H_2O)_x]^-}$ is the energy of the anionic GO nano-flake and water molecules interaction with the GO surface or edge, $E_{[R]^{m+}}$ is the energy of the radionuclide aquocomplex, and $E_{(H_2O)_x}$ is the energy of the water molecules displaced from the GO surface or edge to accommodate the outer-sphere complexation of the GO nano-flake and the radionuclide aquocomplex obtained from equation (4.1).

4.4 Results

4.4.1 Neutral GO Nano-flakes

4.4.1.1 Surface Complexation

Analysis was first carried out on the binding of radionuclides to the surface of the neutral GO nano-flake by inner-sphere and outer-sphere interactions. A comparison of the two modes of binding interaction is made, and the binding preference of each of the analogues is compared to experimental results. Geometries optimised at the PBE level of theory in the aqueous phase for inner-sphere complexation between the radionuclide analogues and the GO nano-flake surface are presented in Figure 32, PBE0 geometries can be found in Appendix Section 4.6.1. Calculations were all carried out in the aqueous phase using the COSMO continuum solvent model, based on results from some initial calculations which indicated that gas phase calculations gave unphysically large binding energies. Unphysically large binding energies from gas phases calculations have also been reported in the literature[182]. The majority of similar studies also report only results from aqueous phase calculations[160,178–180], presumably for similar reasons. There are a wide range of possible geometric configurations in which the radionuclide analogues can bind with the GO surfaces and an exhaustive study of every possible configuration is not practically possible. Two different binding configurations were tested for each of the ions to the surface and edge of the model GO nano-flake in PBE calculations initially. Guidance towards other low energy configurations was then obtained by substituting the ions between low energy configurations (and removing equatorial waters when substituting Sr(II) into configurations which were found to be low for La(III) and Th(IV)). Exploration for low energy configurations was not carried out with PBE0 due to computational expense. PBE0 calculations are carried out only in configurations found to be the lowest from PBE calculations.

Inner-sphere binding for each of the analogues in the lowest energy geometry investigated involves the formation of 3 M-O_{GO} bonds with functional groups on the GO surface and the elimination of 3 water molecules from the system to maintain the preferred coordination number for each of the metal cations.

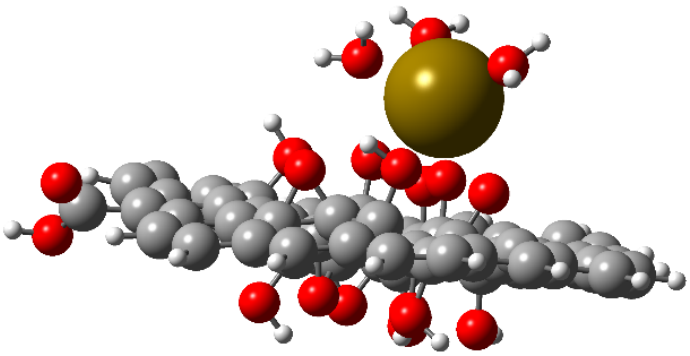

$[C_{54}H_{17}(OH)_{10}(O)_4COOH{\cdot}Sr(H_2O)_3]^{2+}$

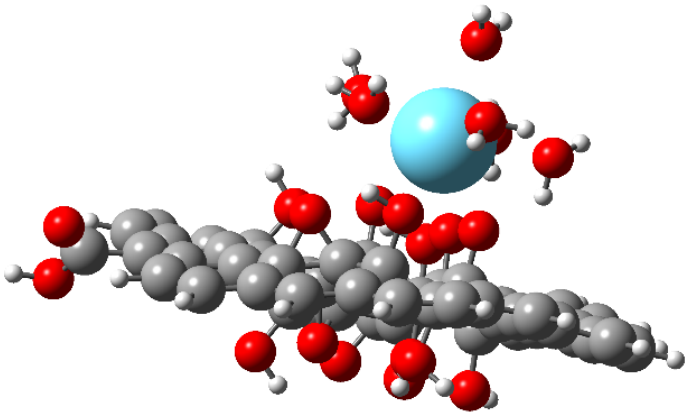

$[C_{54}H_{17}(OH)_{10}(O)_4COOH{\cdot}La(H_2O)_6]^{3+}$

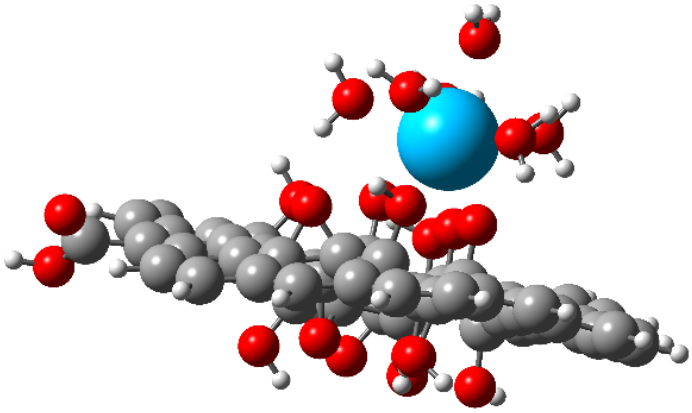

$[C_{54}H_{17}(OH)_{10}(O)_4COOH{\cdot}Th(H_2O)_6]^{4+}$

Figure 32: Inner-sphere binding of Sr(II), La(III), and Th(IV) aquocomplexes with the surface of the neutral GO nano-flake. Optimised at the PBE/SVP level of theory.

The inner-sphere and outer-sphere complexation binding energies were calculated using equations (4.2) and (4.4) respectively and are presented in Table 25.

Table 25: Binding energy for inner- and outer-sphere complexation of Sr(II), La(III), and Th(IV) aquocomplexes with the surface of a neutral GO nano-flake. All values are in eV. Calculations carried out in the aqueous-phase.

Ion	PBE		PBE0	
	Inner	Outer	Inner	Outer
Sr(II)	-0.63	-1.08	-0.47	-1.00
La(III)	-1.28	-1.14	-0.90	-0.93
Th(IV)	-1.84	-1.04	-1.46	-0.79

A clear correlation emerges between the formal charge of the radionuclide and the binding energy associated with inner-sphere complexation. The increase in calculated binding energy is commensurate with the formation of shorter bonds between the cation and the oxygen of the surface GO functional groups (M-O_{GO}), when differing ionic radii are taken into account (the ionic radii[212] used for Sr(II), La(III), and Th(IV) are 1.32 Å, 1.36 Å, and 1.23 Å respectively). The average M-O_{GO} bond length between Sr(II), La(III) and Th(IV), and the functional groups on the GO surface was calculated be 2.596 Å, 2.563 Å and 2.434 Å respectively, at the PBE level of theory. Consideration of the chemical structure on the GO nano-flake surface following binding reveals that Sr(II) has formed bonds with two hydroxyl groups and one epoxy group, whilst both La(III) and Th(IV) have altered the GO surface chemistry to form M-O_{GO} bonds with two OH groups and one carbonyl group. The carbonyl group has formed by breaking a C-O bond in the epoxy group. It is perhaps unsurprising that the surface chemistry has changed in the presence of electrostatic forces from the trivalent and tetravalent cation complexes, it is unsurprising also from results presented in Chapter 3 that the change in surface chemistry has occurred at an epoxy group. It was found that formation of epoxy groups on the GO surface is much less stable than the binding of OH groups, the energetic barrier to removal of the oxygen atom, or the conversion of the epoxy group to a carbonyl group was however not calculated. A comparison of the individual M-O_{GO} bonds which have formed with the GO surface groups suggests that Sr(II) more readily complexes with epoxy than OH groups. The

Sr-O_{epoxy} bond was calculated to be 2.529 Å in calculations carried out using the PBE *xc*-functional, whilst Sr-O_{OH} bonds were calculated to 2.642 Å and 2.616 Å, respectively. La(III) and Th(IV) are also found to form much shorter bonds to carbonyl groups than the OH groups. M-$O_{carbonyl}$ bonds for La(III) and Th(IV) were calculated to be 2.348 Å and 2.137 Å, whilst average M-O_{OH} were calculated to be 2.671 Å and 2.583 Å, respectively.

A comparison of inner-sphere binding energies calculated using PBE and PBE0 reveals, as in results presented in Chapter 3 that calculations carried out using PBE0 predict smaller binding energies than those carried out with PBE. The same general trends however emerge from calculations carried out with both *xc*-functionals. The difference in calculated binding energy is most significant for La(III) and Th(IV). There are several reasons why the calculated binding energy may be smaller in PBE0 calculations. It was found in Chapter 3 that smaller binding energies were due to larger energies associated with deformation of the graphene nano-flake during the adsorption process when using PBE0, which may also be a contributing factor here. It was also shown in Section 4.3.3 that the free La(III) and Th(IV) aquocomplexes calculated using PBE0 have greater point group symmetry than those from PBE calculations. There may be an energy penalty to breaking the symmetry of the aquocomplex, which was calculated to be about 4 kcal mol^{-1} for the Th(IV) aquocomplex by Yang *et. al.*[208] at the B3LYP level of theory. It may also be evidence of overbinding with the PBE *xc*-functional, as previously reported in the literature[124]. The largest difference in binding energy calculated between PBE and PBE0 is around 0.4 eV, significantly smaller than the energy variation expected from using a larger triple-ζ basis, as reported by Wu *et. al.*[179]. Binding energies calculated for inner-sphere complexation of Sr(II) with the GO surface are in excellent agreement with those in other theoretical studies. Yang *et. al*[160] calculated binding energies of 0.57 eV, and 0.54 eV for the binding of Sr(II) to pairs of epoxy and hydroxyl groups, respectively, in a similar study carried using DFT at the PBE0 level of theory. Calculated bond lengths are however not consistent with those reported by Yang, who calculated Sr-O_{GO} bond lengths of 2.628 Å and 2.596 Å to epoxy and hydroxyl groups respectively, a binding preference towards OH groups. Sr-O_{GO} bond lengths to epoxy and OH groups calculated in this research are 2.531 Å and 2.620 Å respectively, at the same level of theory as the investigation by Yang *et. al*.

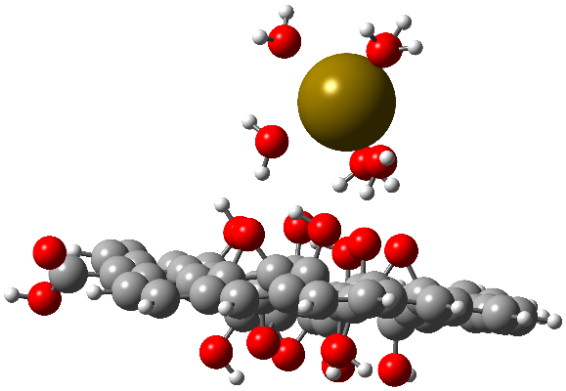

$[C_{54}H_{17}(OH)_{10}(O)_4COOH.Sr(H_2O)_6]^{2+}$

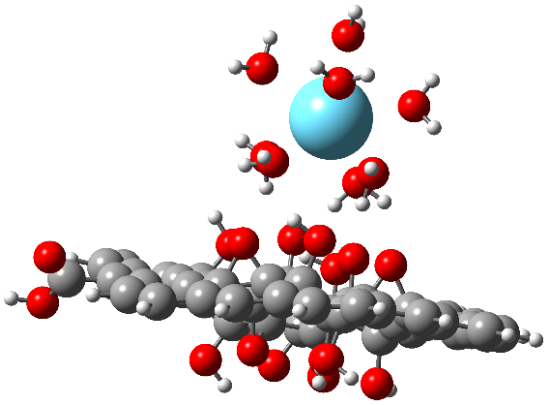

$[C_{54}H_{17}(OH)_{10}(O)_4COOH.La(H_2O)_9]^{3+}$

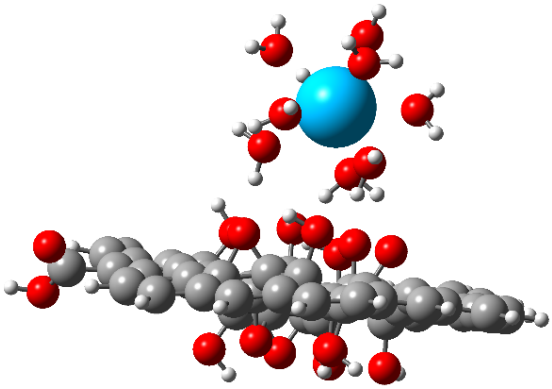

$[C_{54}H_{17}(OH)_{10}(O)_4COOH.Th(H_2O)_6]^{4+}$

Figure 33: Outer-sphere binding of Sr(II), La(III), and Th(IV) aquocomplexes with the surface of the neutral GO nano-flake. Optimised at the PBE/SVP level of theory.

Binding energies for outer-sphere complexation between the solvated radionuclide analogues and the surface of the neutral GO nano-flake, calculated using equation (4.4) are also presented in Table 25. Calculations carried out using the PBE *xc*-functional predict no correlation between formal charge and binding energy. All values are also within a range of 0.1 eV, which is within the expected error associated with the DFT methodology. A weak correlation emerges, which is inverse to formal charge in calculations carried out using PBE0, the binding energies too show little variability. An independence of formal charge is hence revealed in binding energy calculations. Binding is dominated by the formation of a H-bond network with the GO surface which is approximately equal for all radionuclides. Analysis of the hydrogen bond network which has formed between the solvation shell of the metal hydrates and the functional groups on the GO surface (see Figure 33) reveals that three water molecules from the Sr(II) solvation shell have formed hydrogen bonds with the GO surface, whilst four water molecules are involved in bonding from the La(III) and Th(IV) solvation shells. Although fewer water molecules are involved in the formation of the H-bond network between Sr(II) and the GO surface, water molecules in the Sr(II) form on average a greater number of bonds with the GO surface. Geometries optimised at the PBE level of theory show the formation of 5, 5, and 4 H-bonds between Sr(II), La(III), and Th(IV) and the GO surface respectively, PBE0 geometries show the formation of 4 H-bonds for all three of the radionuclides investigated.

Comparison of the binding energies calculated using PBE and PBE0 shows again that PBE predicts stronger binding interactions. The difference in calculated binding energy between the *xc*-functionals is approximately half that calculated for inner-sphere binding interactions with the GO surfaces. The binding energies calculated using PBE are 0.2 and 0.1 eV larger for inner-sphere and outer-sphere binding of Sr(II) to the GO surface, and approximately 0.4 and 0.2 eV larger for inner-sphere and outer-sphere binding of La(III) and Th(IV). The trends which emerge in the data between the two *xc*-functionals are however broadly the same. The origins of the reduction in binding energy for outer-sphere binding do not seem to be due to increased deformation energies (see Table 26) as was the case for calculated presented in Chapter 3, but rather something inherent to the *xc*-functionals used.

Table 26: Deformation energy of neutral GO nano-flakes, and Sr(II), La(III), and Th(IV) aquocomplexes following outer-sphere complexation with the GO surface. All values are in eV. Calculations carried out in the aqueous-phase

Ion	PBE		PBE0	
	Flake	Complex	Flake	Complex
Sr(II)	0.07	0.14	0.00	0.07
La(III)	0.13	0.24	0.08	0.25
Th(IV)	0.19	0.37	0.13	0.34

A comparison was also made between the binding energy calculated for inner-sphere and outer-sphere complexation for each of the radionuclide cations and the neutral GO surface (see Table 25). Binding energies predict that outer-sphere complexation is strongly preferred by Sr(II), whilst inner-sphere binding is strongly preferred for Th(IV). The binding energies calculated for La(III) and the surface of the neutral GO flake predict no clear preferred mode of interaction. Inner-sphere complexation is predicted to be slightly preferred by PBE calculations, whilst outer-sphere binding interactions are predicted to be preferred by calculations carried out using the PBE0 *xc*-functional. The results for Sr(II) and Th(IV) are in excellent agreement with experimental results. The neutral GO nano-flake is representative of conditions around the point of zero charge, which for GO is reported[147,174] to be between to pH 2 and pH 4, dependent on the method of GO characterisation and degree of oxidation of the GO sample. Experimental results have shown that divalent radionuclides typically form outer-sphere surface complexes with GO at pH < 6, whilst tetravalent radionuclides and those in higher oxidations states form inner-sphere surface complexes at much lower pH. Experimental investigations have reported the formation of inner-sphere complexes between GO and trivalent cations, these are typically carried out in a pH[1,150] range around 3 – 11, where some experimental characterisations suggest the GO is anionic. The change in binding preference for divalent radionuclides which occurs around pH 6 is well understood, and the DFT calculations presented here predict a similar transition may also be present for trivalent cations, which would require experimental verification. Interestingly, it was also reported by Sun *et. al.*[180] from experimental results that U(VI) forms outer-sphere complexes at pH 4 on rGO but forms inner-sphere complexes with GO with high

surface functional groups density at the same pH. The ionic charge on GO has been found experimentally to be dependent on both pH and the degree of oxidation of the GO nano-flakes, the Sun *et. al.* study may also be experimental evidence of a charge dependent transition in binding preference of cations in higher oxidation states.

4.4.1.2 Edge Complexation

The binding interactions between the radionuclide analogues and the carboxylic acid (COOH) group on the edge of the neutral GO flake was also investigated (see Table 27). Calculated binding energies suggests that outer-sphere binding is preferred by all ions. The greatest increase in binding energy between inner-sphere and outer-sphere complexation is predicted for Th(IV). An inverse correlation between formal charge and binding energy is predicted for inner-sphere binding to the COOH group on the GO edge. Sr(II) and La(III) have a much greater affinity towards the neutral COOH groups than Th(IV). The binding energies calculated for outer-sphere binding interactions also suggest an inverse correlation with formal charge, albeit, one much less pronounced than that predicted by inner-sphere binding.

Table 27: Binding energy of inner- and outer-sphere complexation of Sr(II), La(III), and Th(IV) aquocomplexes with the edge of a neutral GO nano-flake. All values are in eV. Calculations carried out in the aqueous-phase

Ion	PBE		PBE0	
	Inner	Outer	Inner	Outer
Sr(II)	-0.54	-0.71	-0.42	-0.58
La(III)	-0.38	-0.69	-0.31	-0.56
Th(IV)	-0.07	-0.54	0.10	-0.37

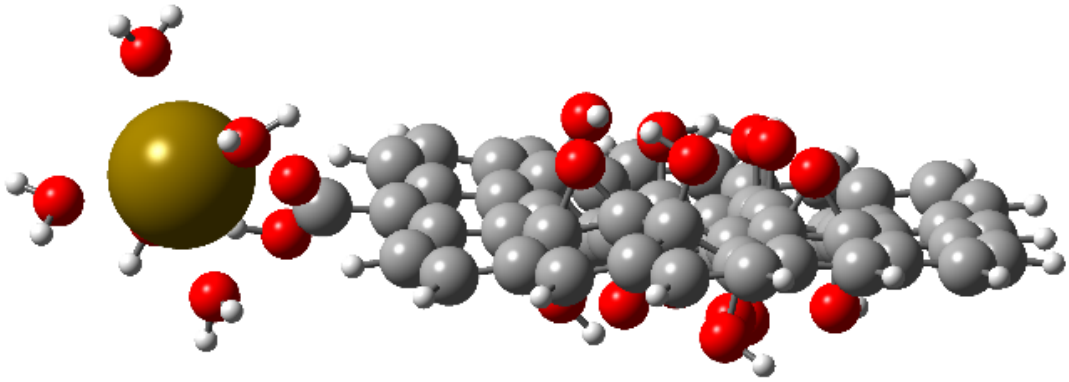

$[C_{54}H_{17}(OH)_{10}(O)_4COOH.Sr(H_2O)_5]^{2+}$

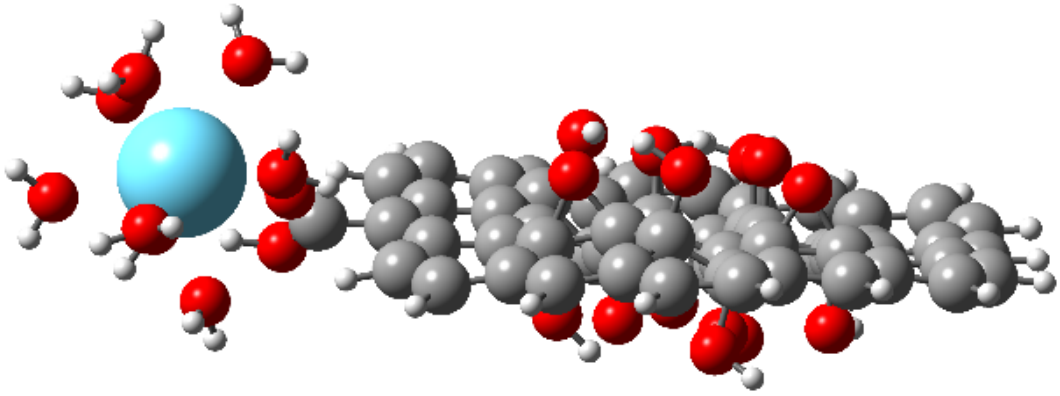

$[C_{54}H_{17}(OH)_{10}(O)_4COOH.La(H_2O)_8]^{3+}$

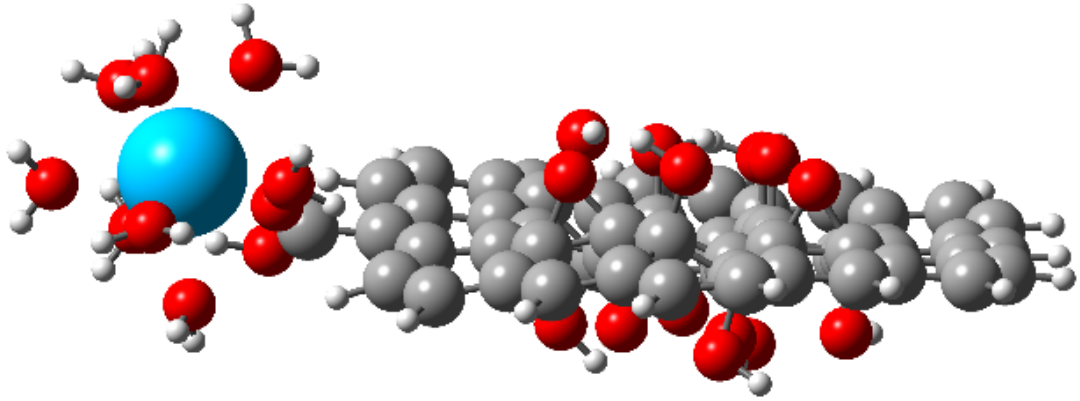

$[C_{54}H_{17}(OH)_{10}(O)_4COOH.Th(H_2O)_8]^{4+}$

Figure 34: Inner-sphere binding of Sr(II), La(III), and Th(IV) aquocomplexes with the edge of the neutral GO nano-flake. Optimised at the PBE/SVP level of theory.

Inner-sphere complexation occurs by the formation of a single M-O_{COOH} bond with the carboxyl oxygen and are stabilised further with an H-bond with the hydroxyl side of the COOH group (see Figure 34). The M-O_{COOH} bonds are calculated to be 2.516 Å, 2.516 Å, and 2.332 Å for Sr(II), La(III), and Th(IV), respectively, using the PBE *xc*-functional. M-O_{COOH} bonds are significantly shorter than M-O_{GO} bonds to functional groups on the GO surface. The M-O_{COOH} bond calculated for Th(IV) is much shorter than those calculated Sr(II) and La(III) when their respective ionic radii are taken into account, shorter bonds are usually indicative of the formation of stronger bonds, calculated binding energies however suggest that Th(IV) is significantly less stable on the neutral GO edge than the other radionuclides. Calculations carried out at the PBE0 level of theory predict it is unstable. The extremely low binding energy calculated for Th(IV) may be due to steric effects and the smaller Th(IV) ion being unable to fully develop interactions with the COOH group. There may also be a contribution from the water ion displaced during complexation being more tightly bound in the Th(IV) complex than others. It can be concluded however that Th(IV) does not bind readily with COOH groups on the edge of the neutral GO nano-flake. Calculated flake deformation energies also give further possible indication to the discrepancy between calculated bond lengths and binding energies. Single point energy calculations were carried out for the GO nano-flakes held at their adsorption geometries, energies associated with the deformation of the GO nano-flake are given in Table 28. Th(IV) is found to cause much more significant distortion of the GO flake during binding than Sr(II) and La(III), which is unsurprising due to its greater charge density, and hence greater electrostatic force exerted on the flake edge. The energy associated with the deformation of the nano-flake alone however does not fully account for Th(IV) being significantly less stable than Sr(II) and La(III) at the nano-flake edge, nor do nano-flake deformation energies account for Sr(II) being more stable than La(III). The flake deformation energies together with possible steric effects however produce an explanation for the calculated binding energies, and incoherence between calculated binding energies and calculated bond lengths.

The binding energies calculated for outer-sphere interactions with the neutral GO edge (see Table 27) predict that all metal cations are stabilised approximately equally.

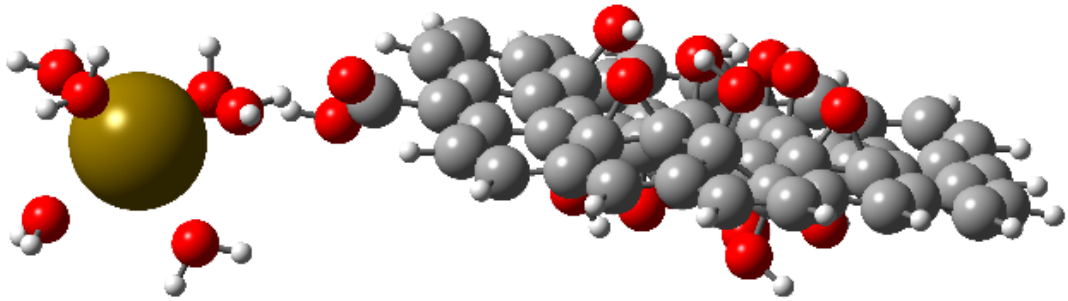

$[C_{54}H_{17}(OH)_{10}(O)_4COOH.Sr(H_2O)_6]^{2+}$

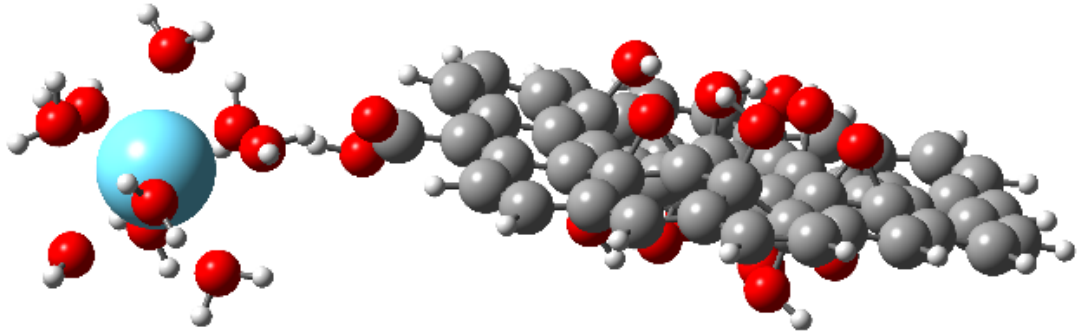

$[C_{54}H_{17}(OH)_{10}(O)_4COOH.La(H_2O)_9]^{3+}$

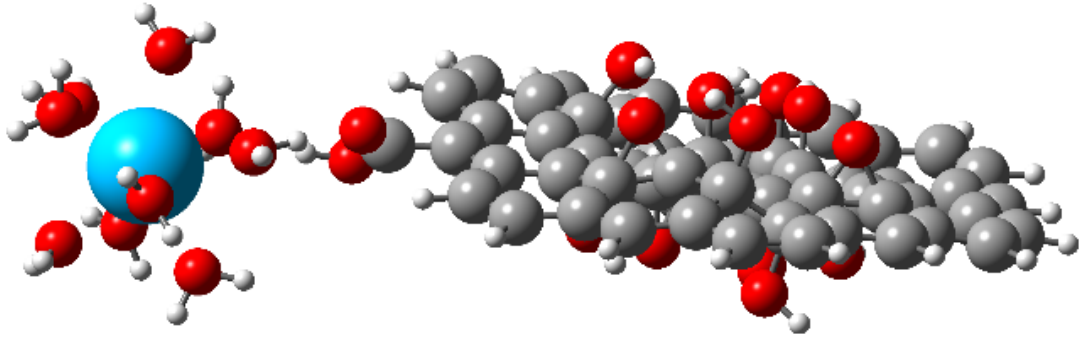

$[C_{54}H_{17}(OH)_{10}(O)_4COOH.Th(H_2O)_9]^{4+}$

Figure 35: Outer-sphere binding of Sr(II), La(III), and Th(IV) aquocomplexes with the edge of the neutral GO nano-flake. Optimised at the PBE/SVP level of theory.

Binding energies calculated for Sr(II) and La(III) differ by only 0.02 eV in calculations carried out using both PBE and PBE0, which is much smaller than the expected accuracy of the DFT methodology. Binding energies calculated for Th(IV) are however around 0.15 eV smaller than those calculated for Sr(II) and La(III) in calculations carried out using PBE, and about 0.2eV smaller in PBE0 calculations.

Analysis of the binding geometries (see Figure 35) reveals that two water molecules from the solvation shell of the radionuclide analogues are involved in the formation of H-bonds with the neutral GO edge. One water molecule forms an H-bond with the hydroxyl group of the carboxylic acid, the other forms an H-bond with the carbonyl group of the carboxylic acid. The H-bonds formed between Sr(II) and the COOH group are calculated to be 1.681 Å and 1.711 Å (formation with the carbonyl and hydroxyl group of COOH, respectively) at the PBE level of theory, they are calculated to be 1.626 Å and 1.724 Å in the La(III) geometry, and 1.871 Å and 1.488 Å for Th(IV). Further analysis of the Th(IV) complex reveals the elongation of the O-H bond in one of the water molecules interaction the GO edge, resulting in the formation of a much shorter Th-O_w bond. Th(IV) complexes are known experimentally to be prone to hydrolysis[209]. When calculated binding energies are considered in combination with the destabilisation of the O-H bond in the water molecule of the solvation shell of Th(IV), a clearer picture begins to emerges, one in which the outer-sphere complexation of aquo complexes to neutral GO edges is insensitive to formal charge, as it was to the surface of the neutral GO flake.

Table 28: Deformation energy of neutral GO nano-flakes following inner- and outer-sphere complexation of Sr(II), La(III), and Th(IV) aquocomplexes with the GO edge. All values are in eV. Calculations carried out in the aqueous-phase

Ion	PBE		PBE0	
	Inner	Outer	Inner	Outer
Sr(II)	0.06	0.03	0.04	0.03
La(III)	0.09	0.04	0.07	0.03
Th(IV)	0.20	0.04	0.18	0.03

A comparison was also made for binding preference for each of the radionuclide analogues, to the GO surface or edge. Surface and edge binding energies for the both inner-sphere and outer-sphere complexation formation are presented in Table 29, collated from result presented in other tables.

Table 29: Binding energies for inner-sphere (I) and outer-sphere (O) complexation of Sr(II), La(III), and Th(IV) aquocomplexes with the surface and edge of a neutral GO nano-flake. All values are in eV. Calculations carried out in the aqueous-phase. Data collated from results in other tables.

Ion	I/O	PBE		PBE0	
		Edge	Surface	Edge	Surface
Sr(II)	**I**	-0.54	-0.63	-0.42	-0.47
Sr(II)	**O**	-0.71	-1.08	-0.58	-1.00
La(III)	**I**	-0.38	-1.28	-0.31	-0.90
La(III)	**O**	-0.69	-1.14	-0.56	-0.93
Th(IV)	**I**	-0.07	-1.84	0.10	-1.46
Th(IV)	**O**	-0.54	-1.04	-0.37	-0.79

A comparison of inner-sphere binding energies with the surface and edge of neutral GO suggest that surface complexation is preferred for all radionuclides. This is unsurprising as there is an opportunity to form a greater number of M-O_{GO} bonds with the surface functional groups, it has been shown both experimentally and in other theoretical studies that greater radionuclide adsorption occurs with GO with a greater degree of oxidation. The comparative calculated binding energies for each of the radionuclide analogues predicts there is only a small increase in binding energy for Sr(II) to the GO surface compared to the edge, which is complementary to results by Yang *et. al.*[160] who reported that Sr(II) has approximately equal affinity towards OH and epoxy groups. Wang *et. al.*[186] also reported calculated binding energies for the divalent cation Pb(II) which were less than 0.1 eV greater to a pair of epoxy groups than to a single COOH group in DFT calculations. Comparison of the binding energies calculated for La(III) and Th(IV) however reveal a much greater affinity towards the surface functional groups on the neutral GO nano-flake, and a preference towards forming multiple M-O_{GO} bonds. Th(IV) in particularly shows very low affinity towards the neutral COOH group on the nano-flake edge, as discussed above.

The comparison of outer-sphere binding interactions with the GO surface and edge reveals that surface binding is also preferred for all radionuclides. The formation of outer-sphere complexes with the GO surface is by the formation of H-bonds between 3 or 4 water molecules in the solvation shell and surface functional groups, whilst

complexation with the edge is by the formation of H-bonds between 2 water molecules and the COOH group. The resulting surface complexes are approximately twice as stable as those on GO nano-flake edge, revealing a consistency in the formation energy of H-bonds, and reaffirming an insensitivity to formal charge for outer-sphere complexation with both the surface and the edge of the GO nano-flake established above.

4.4.2 Anionic GO Nano-flakes

The analysis of the binding interactions with GO nano-flakes now moves on to consider the anionic GO nano-flake which includes the carboxylate (COO^-) functional group on the edge. Analysis was first carried out on the binding interactions between the radionuclide analogues and the surface of the anionic GO nano-flake. A comparison of inner-sphere and outer-sphere binding is made, and the binding preferences of each of the radionuclide analogues is compared to experimental results, other theoretical studies, and results from the neutral GO nano-flake. The investigation then considers binding interactions with the edge of the GO nano-flake, again a comparison between inner-sphere and outer-sphere binding is made, and results are compared to other investigations. A comparison is also made between surface and edge binding to the anionic GO nano-flake, and results are summarised.

4.4.2.1 Surface Complexation

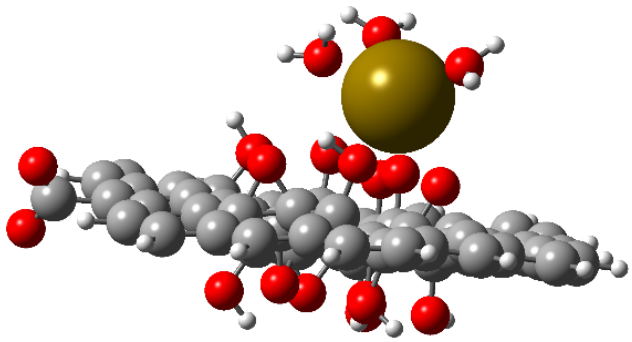

$[C_{54}H_{17}(OH)_{10}(O)_4COO.Sr(H_2O)_3]^{1+}$

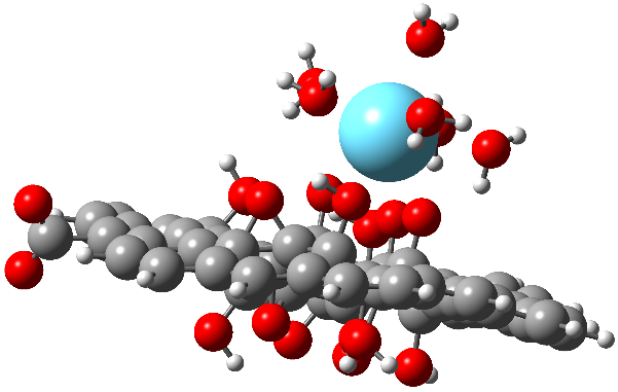

$[C_{54}H_{17}(OH)_{10}(O)_4COO.La(H_2O)_6]^{2+}$

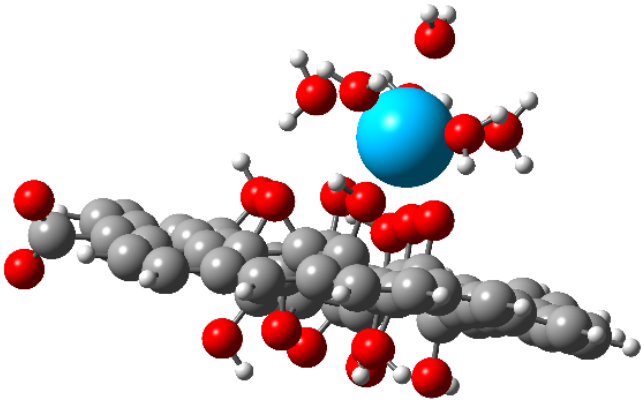

$[C_{54}H_{17}(OH)_{10}(O)_4COO.Th(H_2O)_6]^{3+}$

Figure 36: Inner-sphere binding of Sr(II), La(III), and Th(IV) aquocomplexes with the surface of the anionic GO nano-flake. Optimised at the PBE/SVP level of theory.

Geometries optimised at the PBE level of theory for inner-sphere binding of the radionuclide analogues to the surface of the anionic GO nano-flake are presented in Figure 36, geometries optimised at PBE0 level of theory are in Appendix 4.6.1. The trends which emerge and the binding energies calculated for both inner-sphere and outer-sphere binding interactions are found to be consistent with those calculated for binding to the neutral GO surface. Inner-sphere complexation of the radionuclides with the surface of the anionic GO flake is by the formation of 3 M-O_{GO} bonds, as in complexation geometries for the surface of the neutral GO flake (see Figure 32). The inner-sphere binding energies calculated using equation (4.3) are presented in Table 30. There is a correlation between the formal charge of the cations and the strength of binding by inner-sphere interactions, as in calculations for the neutral nano-flake. The increase in calculated binding energy with charge is also commensurate with formation of shorter M-O_{GO} bonds. The average calculated M-O_{GO} bond lengths from PBE calculations are 2.590 Å, 2.559 Å and 2.429 Å for Sr(II), La(III), Th(IV) respectively, which are consist with bonds calculated to the surface of the neutral GO nano-flake. Consideration of the surface chemical structure of anionic GO following inner-sphere complexation reveals that Sr(II) has formed M-O_{GO} bonds with two hydroxyl groups and one epoxy groups, whilst La(III) and Th(IV) have both modified the GO surface structure to form bonds with two hydroxyl groups and a carbonyl groups, as in complexes formed with the surface of neutral GO.

Table 30: Binding energy of inner- and outer-sphere complexation of Sr(II), La(III), and Th(IV) aquocomplexes with the surface of an anionic GO nano-flake. All values are in eV. Calculations carried out in the aqueous-phase

Ion	PBE		PBE0	
	Inner	Outer	Inner	Outer
Sr(II)	-0.68	-0.94	-0.49	-1.03
La(III)	-1.45	-1.18	-1.01	-0.96
Th(IV)	-2.01	-1.09	-1.60	-0.84

A comparison of the binding energies calculated for the inner-sphere complexation of radionuclide analogues to the surface of the anionic GO nano-flake with those for complexation with surface of the neutral GO nano-flake presented in Table 25 reveals

that the binding energy for Sr(II) is consistent between the two GO flakes, La(III) and Th(IV) are however calculated to be more stable on the anionic GO surface. Calculations carried out at the PBE level of theory predict that La(III) and Th(IV) are both around 0.2 eV more stable on the anionic GO nano-flake surface. The increase in binding energy may be due to the displacement of anionic charge from the carboxylate group on the GO nano-flake edge to the chemically altered GO nano-flake surface. NPA charge analysis carried out on the anionic GO nano-flake before and after adsorption suggests around 10% of the anionic charge is transferred to the GO surface during complexation with La(III) and Th(IV) and only around 3% is transferred during complexation with Sr(II).

Binding energies calculated for the outer-sphere complexation of the radionuclide analogues to the surface of the anionic GO nano-flake calculated using equation (4.5) are also presented in Table 30. Geometries optimised at the PBE level of theory are presented in Figure 37, PBE0 geometries are in Appendix 4.6.1. Binding energies calculated using the PBE *xc*-functional predict no relationship between formal charge and binding energy, whilst those calculated at the PBE0 level of theory predict a trend which anticorrelates with charge, consistent with calculations carried out for the neutral GO surface. Comparing calculated binding energies with those for complexation with the surface of the neutral GO nano-flake in Table 25 reveals that the binding energy for Sr(II) is 0.14 eV more stable on the neutral GO nano-flake at the PBE level of theory, while PBE0 calculations predict it to be 0.03 eV more stable on the anionic nano-flake. Binding energies calculated for La(III) and Th(IV) predict there is no significant difference in binding energy between the neutral and anionic GO nano-flake, revealing an independence to the chemistry at the GO nano-flake edge for the formation outer-sphere surface complexations.

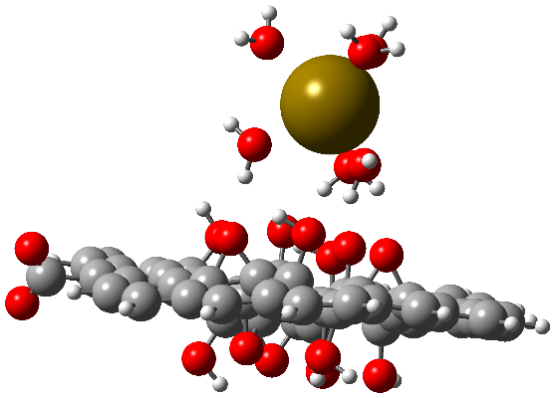

$[C_{54}H_{17}(OH)_{10}(O)_4COO.Sr(H_2O)_6]^{1+}$

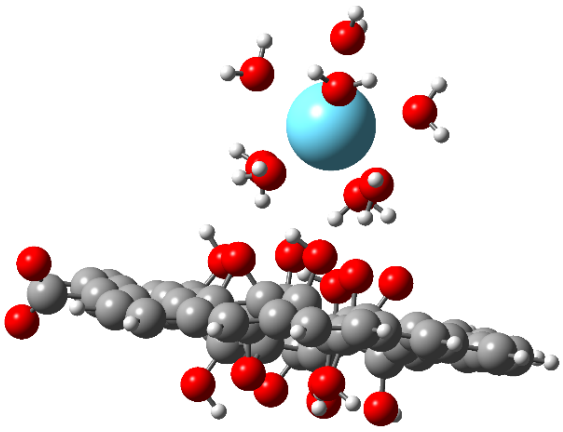

$[C_{54}H_{17}(OH)_{10}(O)_4COO.La(H_2O)_9]^{2+}$

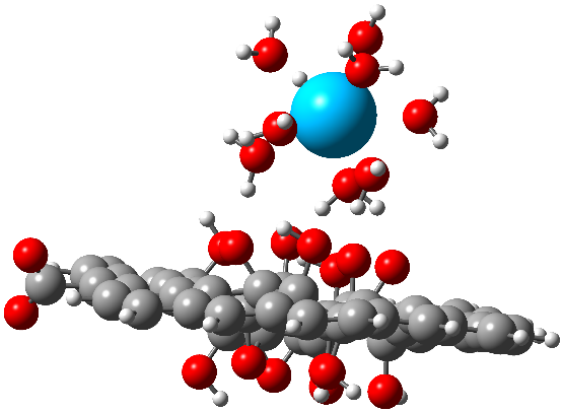

$[C_{54}H_{17}(OH)_{10}(O)_4COO.Th(H_2O)_9]^{3+}$

Figure 37: Outer-sphere binding of Sr(II), La(III), and Th(IV) aquocomplexes with the surface of the anionic GO nano-flake. Optimised at the PBE/SVP level of theory.

A comparison between the inner-sphere and outer-sphere binding energies for each of the radionuclide analogues with the surface of the anionic GO flake was also made. Calculated binding energies predict that outer-sphere binding interactions are strongly preferred by Sr(II), in agreement with calculations for the neutral GO nano-flake presented in Table 25, La(III) and Th(IV) are both predicted to prefer binding by inner-sphere surface complexation. The formation of inner-sphere complexes between Th(IV) and the anionic GO surface is predicted to be around twice as stable as the formation of outer-sphere complexes. The inner-sphere and outer-sphere binding energies calculated for La(III) are much more similar to one another, calculations carried out at the PBE level of theory predict a preference towards inner-sphere complexation, whilst PBE0 calculations predict no preference between the two binding interactions, which is consistent with calculations carried out for the neutral GO nano-flake.

4.4.2.2 Edge Complexation

The binding interactions between the radionuclide analogues and the edge of the anionic GO nano-flake were also investigated, calculated binding energies for the formation of both inner-sphere and outer-sphere complexes are presented in Table 31. The calculated binding energies reveal a clear correlation between the formal charge of the radionuclide and binding strength for the formation of both inner-sphere and outer-sphere complexes, which was not present in calculations for binding to the neutral GO edge. Analysis of the inner-sphere complexation geometries (see Figure 38) reveals that complexation is by the formation of two M-O_{COO^-} bonds.

Table 31: Binding energy of inner- and outer-sphere complexation of Sr(II), La(III), and Th(IV) aquocomplexes with the edge of an anionic GO nano-flake. All values are in eV. Calculations carried out in the aqueous-phase

Ion	PBE		PBE0	
	Inner	Outer	Inner	Outer
Sr(II)	-1.05	-1.48	-0.91	-1.29
La(III)	-1.26	-1.60	-1.09	-1.37
Th(IV)	-1.48	-2.01	-1.30	-1.76

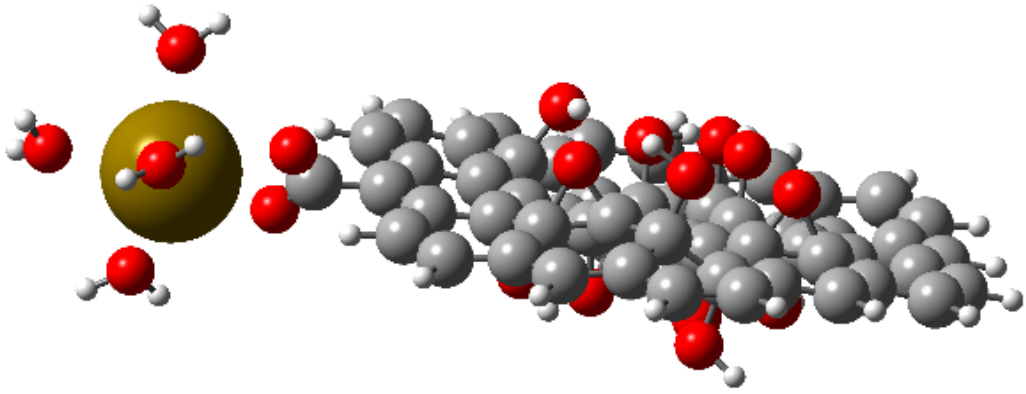

$[C_{54}H_{17}(OH)_{10}(O)_4COO.Sr(H_2O)_4]^{1+}$

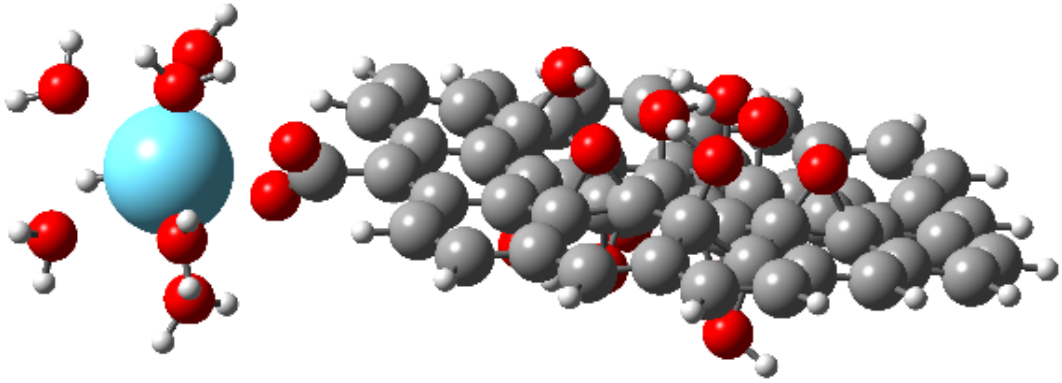

$[C_{54}H_{17}(OH)_{10}(O)_4COO.La(H_2O)_7]^{2+}$

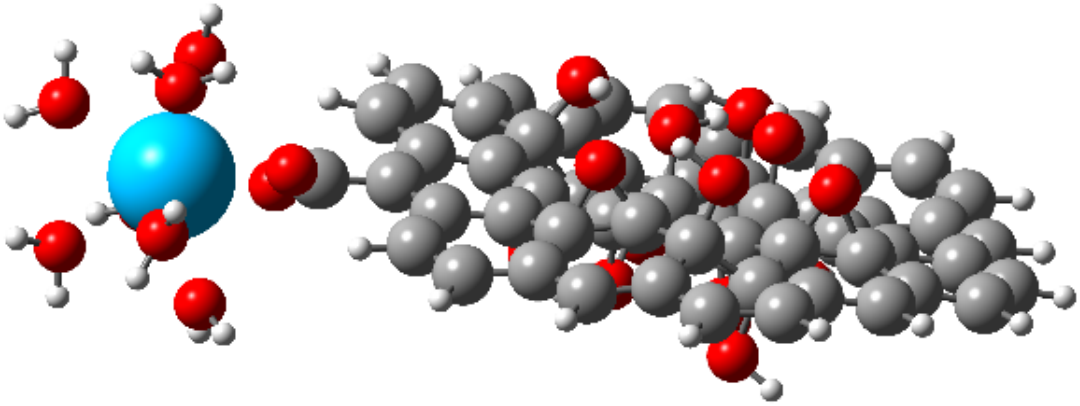

$[C_{54}H_{17}(OH)_{10}(O)_4COO.Th(H_2O)_7]^{3+}$

Figure 38: Inner-sphere binding of Sr(II), La(III), and Th(IV) aquocomplexes with the edge of the anionic GO nano-flake. Optimised at the PBE/SVP level of theory.

Two water molecules are also eliminated from the first solvation shell of each of the radionuclide aquocomplexes to maintain the preferred coordination number. Average $M\text{-}O_{COO^-}$ bond lengths were calculated to be 2.575 Å, 2.561 Å, and 2.407 Å for Sr(II), La(III), and Th(IV) respectively, which correlate with the calculated binding energies when differing ionic radii are taken into account. Calculated $M\text{-}O_{COO^-}$ bond lengths are longer than those calculated to the carbonyl oxygen on the carboxylic acid group on the edge of the neutral GO nano-flake ($M\text{-}O_{COOH}$), which is surprising, but may be due steric effect from a greater number of coordinating waters preventing as close a contact as would otherwise be possible. Wu *et. al.*[182] reported shorter bonds between U(VI) and COO^- than COOH, commensurate with the increased binding energy to the anionic edge group. A significant increase in stabilisation of U(VI) on anionic functional groups was also reported by Sun *et. al.*[180].

A comparison of the binding energies calculated for inner-sphere complexation with the edge of the anionic and neutral GO nano-flakes reveals a significant contribution to binding from electrostatic forces between the cationic radionuclide analogues and the anionic functional group. Binding energies for inner-sphere complexation of Sr(II), La(II), and Th(IV) with the carboxylate group are calculated to be 0.52, 0.88, and 1.41 eV greater, respectively, than those calculated with the neutral GO nano-flake edge in calculations carried with PBE, calculations carried out with PBE0 predict they will be 0.49, 0.78, and 1.40 eV greater, respectively.

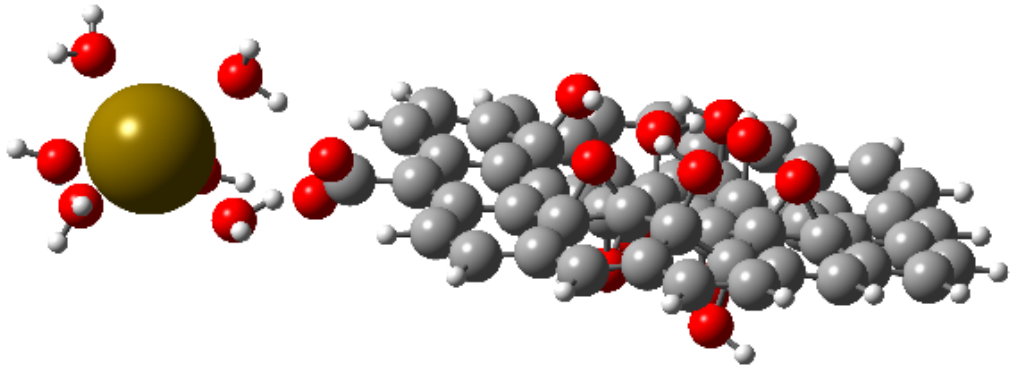

$[C_{54}H_{17}(OH)_{10}(O)_4COO.Sr(H_2O)_6]^{1+}$

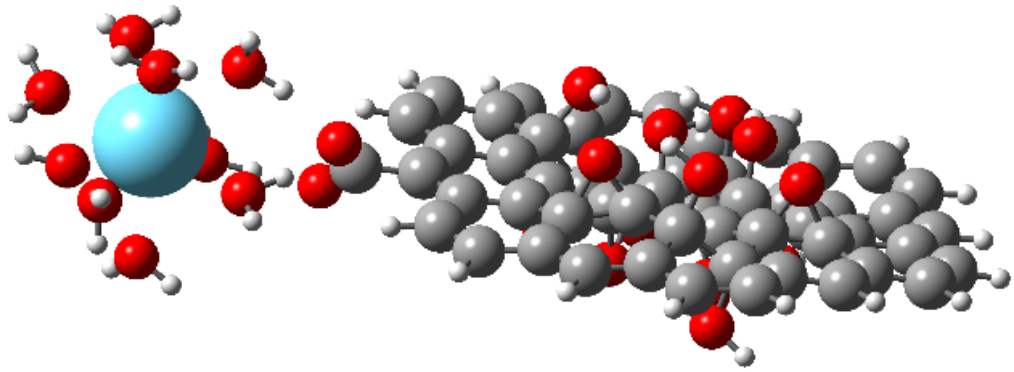

$[C_{54}H_{17}(OH)_{10}(O)_4COO.La(H_2O)_9]^{2+}$

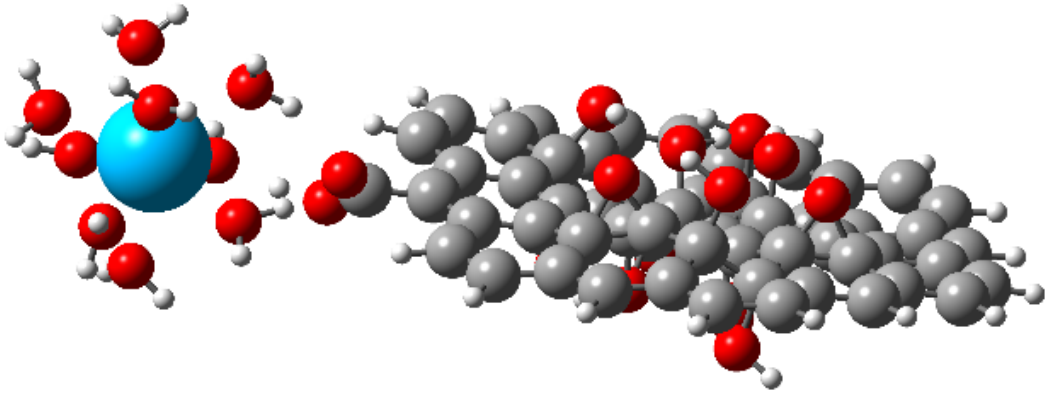

$[C_{54}H_{17}(OH)_{10}(O)_4COO.Th(H_2O)_9]^{3+}$

Figure 39: Outer-sphere binding of Sr(II), La(III), and Th(IV) aquocomplexes with the edge of the anionic GO nano-flake. Optimised at the PBE/SVP level of theory.

Binding energies calculated using equation (4.5) for outer-sphere complexation between the solvated radionuclide analogues and the edge of the anionic GO nano-flake are also presented in Table 31. Complexation geometries optimised at the PBE level of theory are presented in Figure 39, PBE0 geometries are in Appendix 4.6.1. The outer-sphere complexation of radionuclides with the edge of the anionic GO nano-flake is found to also be strongly affected by electrostatic interactions. NBO charge analysis for the aquocomplexes presented Table 24 shows there is a displacement of charge from the metal centres to water molecules in the solvation shell. Charge analysis calculations predict that around 10% of the charge of Sr(II) is transferred to water molecules in the solvation shell, 25 - 30% of the charge of the La(III) aquocomplex is transferred to the solvation shell, which is consist with results from similar calculations by Buzko *et. al.*[205,206], and approximately half of the charge of Th(IV) is transferred to the solvation shell. The cationic charge accumulated on the water molecules in the solvation shell of the radionuclide analogues interacts with the anionic charge on the COO^- group on the GO edge, stabilising the Sr(II), La(III), and Th(IV) aquocomplexes by 0.77, 0.91, and 1.47 eV, respectively, in calculation carried out using PBE compared to binding to the neutral COOH groups. The increase in stability predicted from calculations using PBE0 is 0.70, 0.81 and 1.39 eV, respectively.

A comparison between the calculated binding energies for inner-sphere and outer-sphere complexation with the edge of the anionic GO flake predicts that the formation of outer-sphere complexes is preferred by all cations. This is surprising, as has been discussed, experimental results have reported the formation of inner-sphere complexes between trivalent and tetravalent radionuclides and GO across a large pH range. Divalent radionuclides are also known to form inner-sphere complexes at pH > 6, when significant anionic charge has accumulated on COOH groups. It has been reported[186] also from FTIR spectra taken before and after adsorption that Pb(II) (and by extension other divalent cations) forms complexes mostly with COOH groups on the GO edge.

A comparison was also made for the binding preference for each of the radionuclide analogues to the surface or the edge of the anionic GO nano-flake. The surface and edge binding energies for the formation of both inner-sphere and outer-sphere

complexes is presented in Table 32. A comparison of the binding energies calculated for the formation of inner-sphere complexes with the surface and edge suggests that Sr(II) binds preferentially with the GO edge, and Th(IV) binds most readily to the GO surface, which is perhaps surprising given the significant stabilisation of the radionuclides from electrostatic interactions between the cationic aquocomplexes and anionic edge functional group, it does however highlight a preference towards complexation with highly oxidised GO which has been reported experimentally. La(III) is predicted to bind equally well with the GO surface and edge from calculations carried out with the PBE0 *xc*-functional, and is predicted to bind most readily to the GO surface from PBE calculations. A comparison of outer-sphere complexation with the surface and edge of the anionic GO nano-flake suggests that Sr(II), La(III), Th(IV) all bind preferentially with the GO nano-flake edge. This is in contrast to binding energies calculated for outer-sphere complexation with the neutral flake on which all three radionuclides binding preferentially with the surface of the nano-flake. This is due to the significant electrostatic attraction between the charged GO edge and radionuclide aquocomplexes outweighing the increased coordination by H-bonds on the surface.

Table 32: Binding energies for inner-sphere (I) and outer-sphere (O) complexation of Sr(II), La(III), and Th(IV) aquocomplexes with the surface and edge of an anionic GO nano-flake. All values are in eV. Calculations carried out in the aqueous-phase. Collated from results in other tables.

Ion	I/O	PBE		PBE0	
		Edge	Surface	Edge	Surface
Sr(II)	**I**	-1.05	-0.68	-0.91	-0.49
Sr(II)	**O**	-1.48	-0.94	-1.29	-1.03
La(III)	**I**	-1.26	-1.45	-1.09	-1.01
La(III)	**O**	-1.60	-1.18	-1.37	-0.96
Th(IV)	**I**	-1.48	-2.01	-1.30	-1.60
Th(IV)	**O**	-2.01	-1.09	-1.76	-0.84

4.4.3 Comparison of Ions

This chapter concludes with a comparison of the binding order of the radionuclide analogues to each of the GO flakes. Perhaps the most desirable potential application for GO, besides its high sorption capacity to remove radionuclides and heavy metals from contaminated aqueous environments, is a potential route towards the selective removal of radionuclides, or groups of radionuclides. Spent nuclear fuel and the effluent waste stream from nuclear energy production contains an array of potentially useful chemicals and radionuclides. The most useful are unspent fissionable material and transuranic elements, such as plutonium which has uses in nuclear weapons manufacturing and may become useful as a fuel in the next generation of nuclear reactors, and nuclear fission products which have applications in areas such as nuclear medicine[213]. An effective method for separating and categorising transuranic elements and fission products is also desirable when considering the eventual disposal route of nuclear waste. Transuranic elements can to be long-lived, highly toxic, and have low radioactivity, so many require long term storage solutions and specific disposal routes. Nuclear fission products by contrast are often highly radioactive and short lived but much less toxic, so can be treated and disposed of much more easily and in a shorter timeframe[214]. Experimental research has already revealed a pH sorption edge which is dependent on the formal charge of the radionuclides being adsorbed[1], and a sensitivity to ionic strength for monovalent and divalent cations which is pH dependent, which could potentially be exploited for the separation of groups of radionuclides. Another potential route towards nuclide separation is the tailoring of GO by selective oxidation or chemical modification, which is investigated here.

Table 33: Binding energies of inner-sphere (I) and outer-sphere (O) complexation of Sr(II), La(III), and Th(IV) aquocomplexes with the surface (S) and edge (E) of the neutral GO nano-flake. All values are in eV. Calculations carried out in the aqueous-phase. Collated from results in Section 4.4.1

		PBE			PBE0		
S/E	**I/O**	Sr(II)	La(III)	Th(IV)	Sr(II)	La(III)	Th(IV)
S	**I**	-0.63	-1.28	-1.84	-0.47	-0.90	-1.46
S	**O**	-1.08	-1.14	-1.04	-1.00	-0.93	-0.79
E	**I**	-0.54	-0.38	-0.07	-0.42	-0.31	0.10
E	**O**	-0.71	-0.69	-0.54	-0.58	-0.56	-0.37

The binding energy for both inner-sphere and outer-sphere complexation of the radionuclide analogues to the surface and edge of the neutral GO nano-flake are given in Table 33. The binding preference for each of the radionuclides is predicted to be outer-sphere complexation with the GO surface for Sr(II), inner-sphere complexation with the GO surface for Th(IV), which are both in excellent agreement with experimental results, and La(III) is predicted to form both inner-sphere and outer-sphere complexes with the GO surface. On the basis of calculated binding energies and binding preference of the radionuclides, the adsorption ability of the surface of the neutral GO nano-flake follows the order Th(IV) > La(III) > Sr (II) from PBE level calculations and Th(IV) > Sr(II) > La(III) from calculations using PBE0. The ordering of the adsorption abilities suggests that high surface oxidation and the use of a low pH environment, around the pH_{pzc} of GO, favours the sorption of radionuclides in high oxidations states. By contrast the adsorption ability of the edge of the neutral GO nano-flake follows the order Sr(II) > La(III) > Th(IV), suggesting high edge oxidation and the use of a low pH environment favours the sorption of radionuclides in low oxidation states.

It is well established from competitive sorption investigations that the sorption of cations is inhibited by the presence of cations with higher sorption capacity. This indicates a potential route towards radionuclide selectivity using GO. The selective extraction of tetravalent radionuclides may be possible in low pH environments with GO chemical modified to increase the degree of surface oxidation and reduce the occurrence of carboxylic acid edge groups. In the same conditions there may be a route towards the selective extraction of divalent and trivalent radionuclide by using GO with a high degree of edge oxidation and a low a density of surface functional groups.

Table 34: Binding energies of inner-sphere (I) and outer-sphere (O) complexation of Sr(II), La(III), and Th(IV) aquocomplexes with the surface (S) and edge (E) of the anionic GO nano-flake. All values are in eV. Calculations carried out in the aqueous-phase. Collated from results in Section 4.4.2.

		PBE			PBE0		
S/E	**I/O**	Sr(II)	La(III)	Th(IV)	Sr(II)	La(III)	Th(IV)
S	**I**	-0.68	-1.45	-2.01	-0.49	-1.01	-1.60
S	**O**	-0.94	-1.18	-1.09	-1.03	-0.96	-0.84
E	**I**	-1.05	-1.26	-1.48	-0.91	-1.09	-1.30
E	**O**	-1.48	-1.60	-2.01	-1.29	-1.37	-1.76

The binding energies for both inner-sphere and outer-sphere complexes of the radionuclide analogues with the surface and edge of the anionic GO nano-flake are presented in Table 34. The binding preference for both Sr(II) and La(III) is predicted to be outer-sphere the GO edge. Th(IV) is predicted to bind to both the anionic GO edge by the formation of outer-sphere complexes and the surface by inner-sphere complexation, although it should be noted that experimental results indicate that Th(IV) forms mostly inner-sphere complexes with GO. Calculated binding energies predict that the adsorption ability of the surface of the anionic GO nano-flake follows the order Th(IV) > La (III) > Sr (II) from calculations carried out using PBE and Th(IV) > Sr(II) > La(III) from PBE0 calculations, in agreement with calculations for the surface of the neutral GO nano-flake. The sorption ability of the edge of the anionic GO nano-flake is predicted to be Th(IV) > La (III) > Sr(II), suggesting that tetravalent cations always binds more readily with GO than cations in lower oxidation states in high pH environments.

4.5 Conclusion

The binding interactions between Sr(II), La(III), and Th(IV) aquocomplexes, and the surface and edge of GO nano-flakes was investigated using DFT. The results presented appear to be consistent with experimental data and other computational studies.

Binding energies calculated for inner-sphere complexation with the surface of GO is found to correlate with formal charge, indicating the dominance of electrostatic interactions. The La(III) and Th(IV) aquocomplexes were also found to alter the chemical structure of the GO surface to form stronger bonds. Outer-sphere binding to the GO surface was found to be independent of formal charge.

Th(IV) was found to have a much lower affinity towards the edge of the neutral GO flake, revealing a potential solution towards the selective extraction of divalent and trivalent cations using GO, which require experimental investigation.

When binding to the neutral GO nano-flake (representative of low pH environments ($pH \approx 2$)) all ions were found to bind preferably with the GO surface due to the greater availability of functional groups to form bonds with. Binding to the anionic GO nano-flake, which includes the COO^- edge group however was mostly to the flake edge due to the dominance of electrostatic forces between the cations and the anionic functional group.

4.6 Appendix

4.6.1 PBE0 Geometries

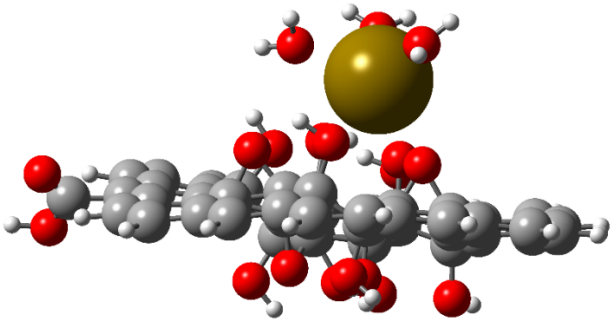

$[C_{54}H_{17}(OH)_{10}(O)_4COOH.Sr(H_2O)_3]^{2+}$

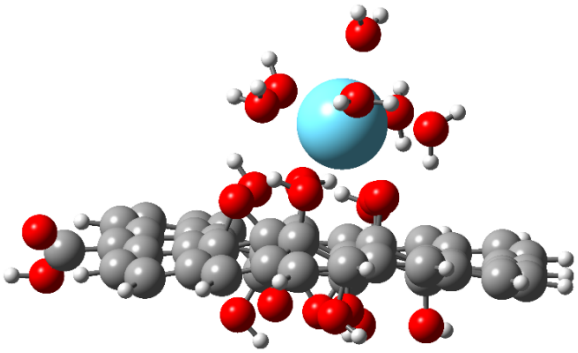

$[C_{54}H_{17}(OH)_{10}(O)_4COOH.La(H_2O)_6]^{3+}$

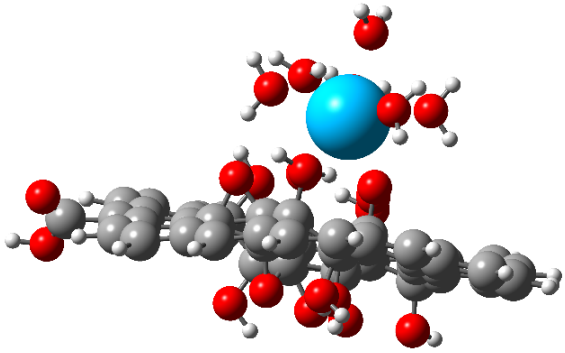

$[C_{54}H_{17}(OH)_{10}(O)_4COOH.Th(H_2O)_6]^{4+}$

Figure 40: Inner-sphere binding of Sr(II), La(III), and Th(IV) aquocomplexes with the surface of the neutral GO nano-flake. Optimised at the PBE0/SVP level of theory

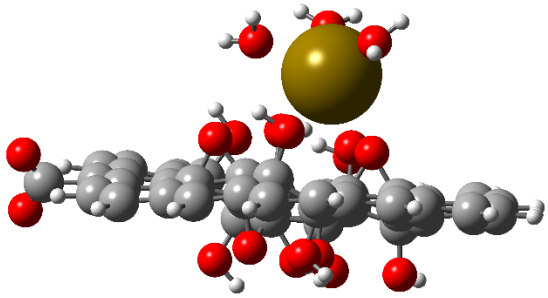

$[C_{54}H_{17}(OH)_{10}(O)_4COO.Sr(H_2O)_3]^{1+}$

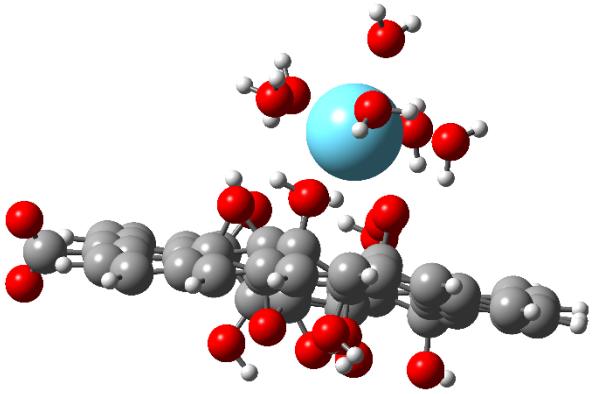

$[C_{54}H_{17}(OH)_{10}(O)_4COO.La(H_2O)_6]^{2+}$

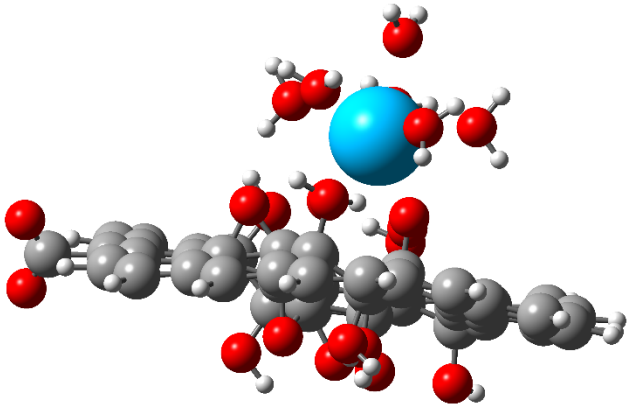

$[C_{54}H_{17}(OH)_{10}(O)_4COO.Th(H_2O)_6]^{3+}$

Figure 41: Inner-sphere binding of Sr(II), La(III), and Th(IV) aquocomplexes with the surface of the anionic GO nano-flake. Optimised at the PBE0/SVP level of theory

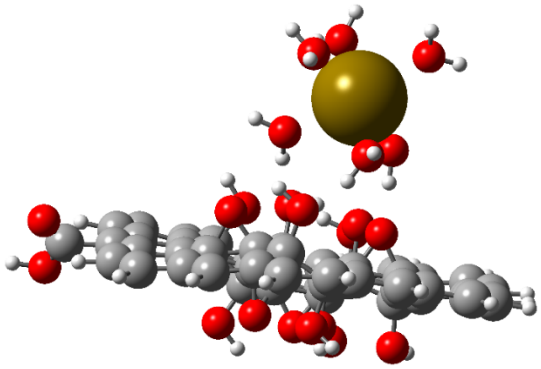

$[C_{54}H_{17}(OH)_{10}(O)_4COOH.Sr(H_2O)_6]^{2+}$

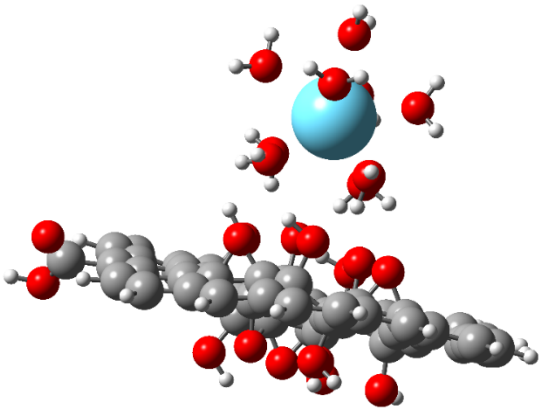

$[C_{54}H_{17}(OH)_{10}(O)_4COOH.La(H_2O)_9]^{3+}$

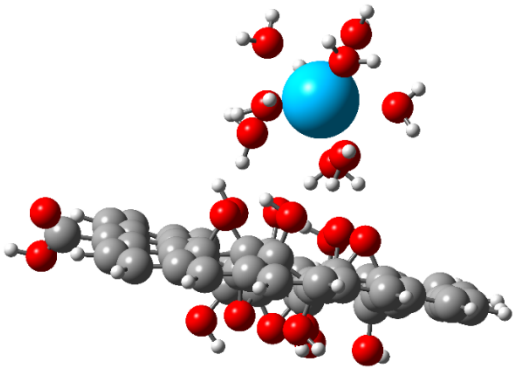

$[C_{54}H_{17}(OH)_{10}(O)_4COOH.Th(H_2O)_9]^{4+}$

Figure 42: Outer-sphere binding of Sr(II), La(III), and Th(IV) aquocomplexes with the surface of the neutral GO nano-flake. Optimised at the PBE0/SVP level of theory

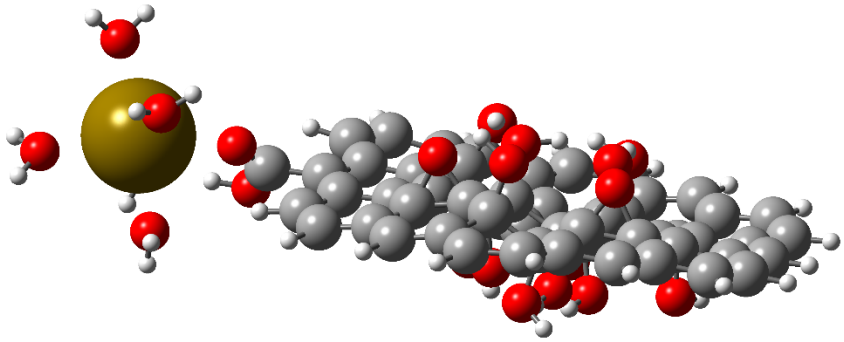

$[C_{54}H_{17}(OH)_{10}(O)_4COOH.Sr(H_2O)_5]^{2+}$

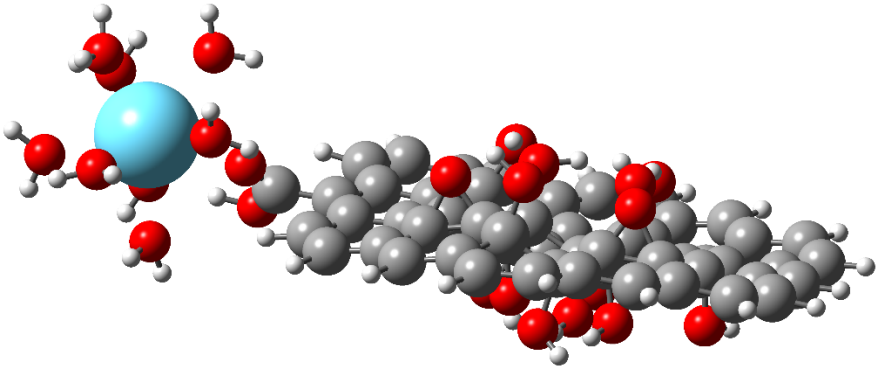

$[C_{54}H_{17}(OH)_{10}(O)_4COOH.La(H_2O)_8]^{3+}$

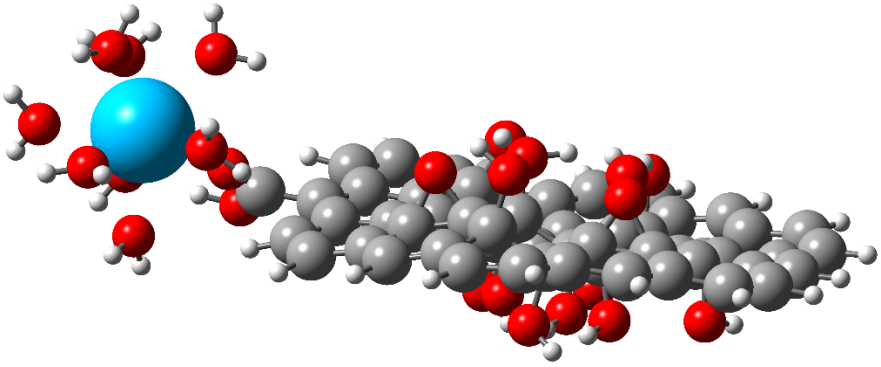

$[C_{54}H_{17}(OH)_{10}(O)_4COOH.Th(H_2O)_8]^{4+}$

Figure 43: Inner-sphere binding of Sr(II), La(III), and Th(IV) aquocomplexes with the edge of the neutral GO nano-flake. Optimised at the PBE0/SVP level of theory

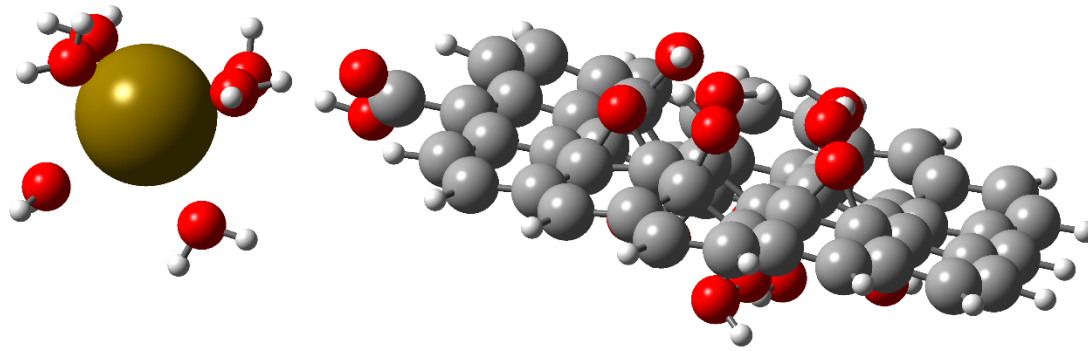

$[C_{54}H_{17}(OH)_{10}(O)_4COOH.Sr(H_2O)_6]^{2+}$

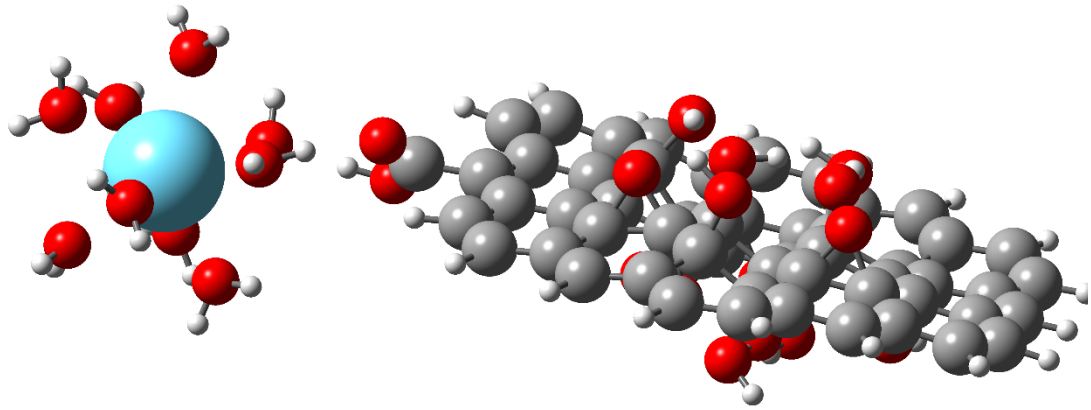

$[C_{54}H_{17}(OH)_{10}(O)_4COOH.La(H_2O)_9]^{3+}$

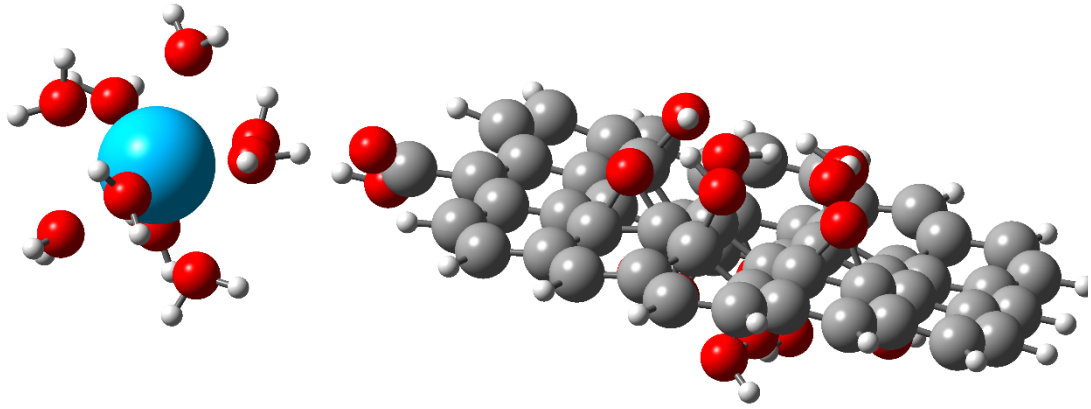

$[C_{54}H_{17}(OH)_{10}(O)_4COOH.Th(H_2O)_9]^{4+}$

Figure 44: Outer-sphere binding of Sr(II), La(III), and Th(IV) aquocomplexes with the edge of the neutral GO nano-flake. Optimised at the PBE0/SVP level of theory

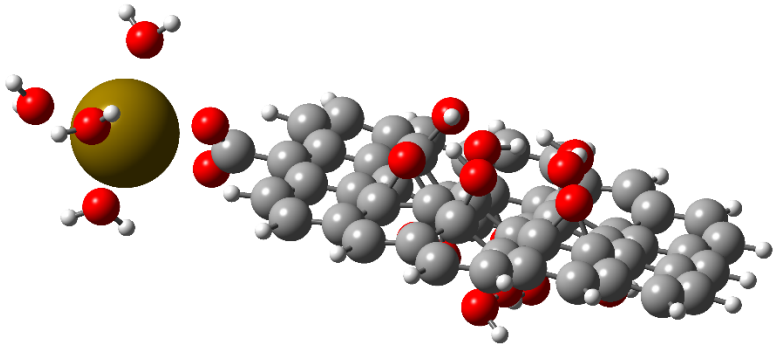

$[C_{54}H_{17}(OH)_{10}(O)_4COO.Sr(H_2O)_4]^{1+}$

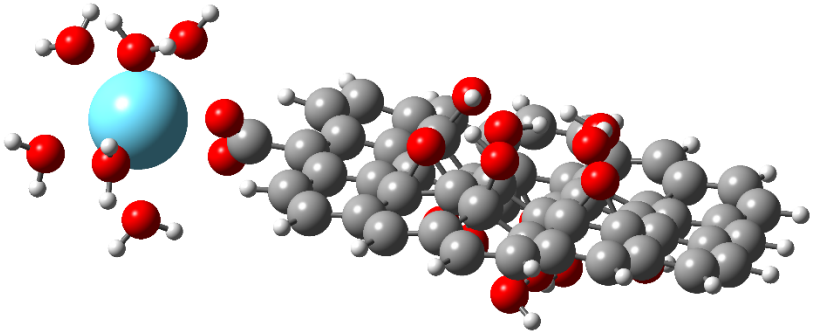

$[C_{54}H_{17}(OH)_{10}(O)_4COO.La(H_2O)_7]^{2+}$

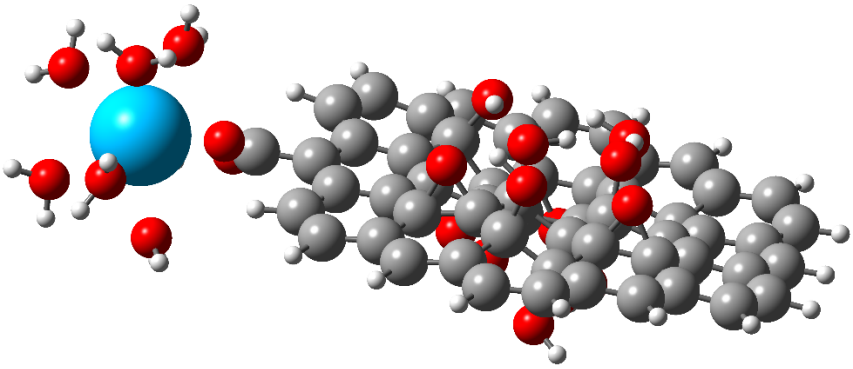

$[C_{54}H_{17}(OH)_{10}(O)_4COO.Th(H_2O)_7]^{3+}$

Figure 45: Inner-sphere binding of Sr(II), La(III), and Th(IV) aquocomplexes with the edge of the anionic GO nano-flake. Optimised at the PBE0/SVP level of theory

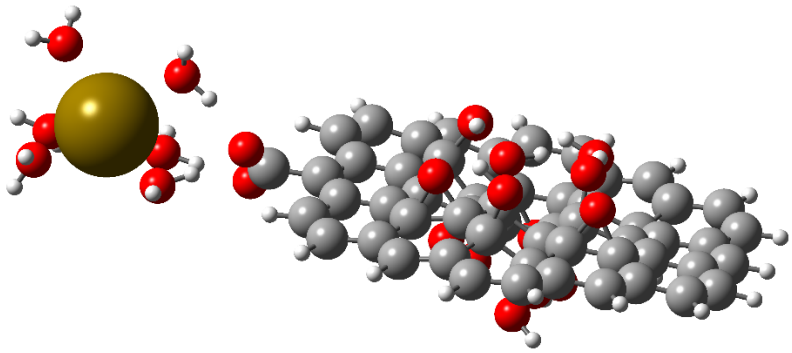

$[C_{54}H_{17}(OH)_{10}(O)_4COO.Sr(H_2O)_6]^{1+}$

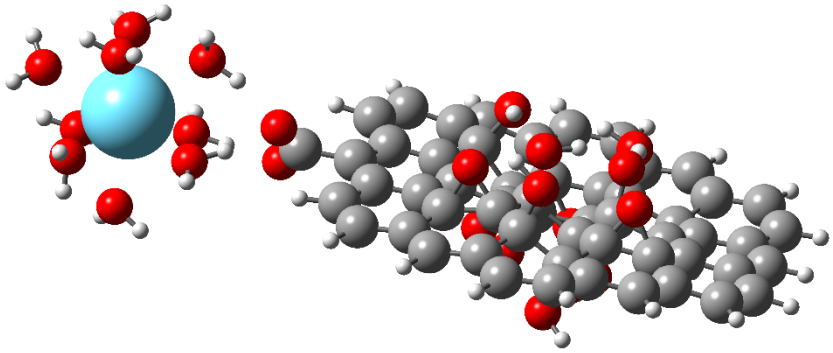

$[C_{54}H_{17}(OH)_{10}(O)_4COO.La(H_2O)_9]^{2+}$

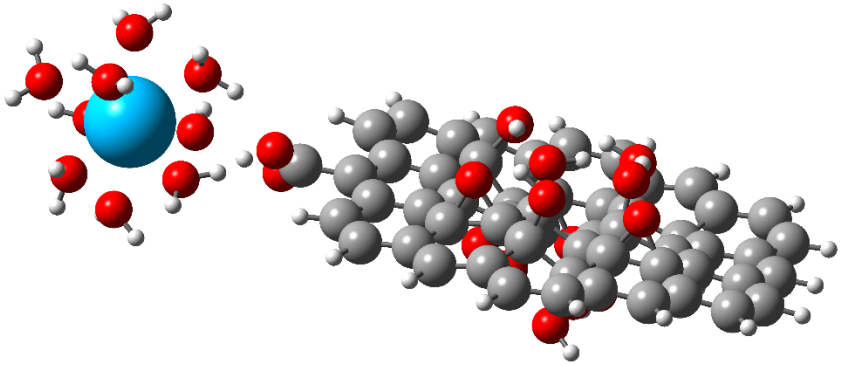

$[C_{54}H_{17}(OH)_{10}(O)_4COO.Th(H_2O)_9]^{3+}$

Figure 46: Outer-sphere binding of Sr(II), La(III), and Th(IV) aquocomplexes with the edge of the anionic GO nano-flake. Optimised at the PBE0/SVP level of theory

Chapter 5 The Adsorption of Radionuclides to the Surface and Edge of Defected Graphene Oxide Nano-flake and an Assessment of the Suitability of the Pristine GO Nano-flake Model.

5.1 Introduction

The study of the sorption of radionuclides to the surfaces and edges of graphene oxide (GO) presented in Chapter 4 investigated the interaction of the radionuclide analogues with idealised GO nano-flakes. GO is however known[215] experimentally to contain defects such as vacancies and topological changes to the GO lattice. This chapter investigates the impact of defects on the binding interactions of radionuclides with the surfaces and edges of GO nano-flakes and assesses the suitability of the idealised GO model for understanding a broader range of radionuclide-GO interactions. It was discussed in Chapter 1 that the determination of the structure of GO has been problematic and is still an area of ongoing debate. This is due mainly to GO being highly hygroscopic and having a complex structure, and there being a lack of reliable and effective methods to characterise such materials. The characterisation and quantification of defects in GO has also, predictably, been difficult for similar reasons. Studies of defects in GO are however beginning to emerge, the investigation of the effect of defects on binding interactions with radionuclides and other cationic contaminants is still however an area lacking research.

It was also discussed in Chapter 1 that there is large sample to sample variability in the structure of GO, and GO chemical compositions exist in a wide range. The composition of GO is dependent on a number of factors, such as the origin and quality of the graphite flakes used, the conditions during GO synthesis, and the chemical method used to produce the GO. The most popular methods for GO synthesis are those of Brodie[19], Staudenmaier[18], and Hummers[21] or, more commonly, some variation of these methods. The oxidation process used and the source of the graphite flakes used to produce GO are also thought to have a significant effect on the nature and degree of defects in the GO lattice.

This chapter begins with an outline of the most common defects which are thought to exist in GO, the characterisation methods which have been used to identify them, and the mechanisms by which they are thought to form. The chapter then continues with a DFT study investigating the effect of common GO defects on the sorption of radionuclides, comparisons are made to calculations for binding to defect-free GO nano-flakes presented in the previous chapter and an assessment is made on the suitability and limitations of the pristine GO nano-flake model for understanding binding in more realistic environments.

5.2 Literature Review

Defects in GO are structural alterations to the carbon lattice, for most applications the minimisation of defects is desirable, and methods and modifications to the GO production methods discussed in Chapter 1 have been developed to limit defect formation. Defects in other applications may be advantageous, so can be instead considered as structural motifs, whose formation, if controlled, may be useful[215]. The calculations presented in this chapter are aimed towards the assessment and evaluation of the effect of Stone-Wales (hereafter SW) and vacancy defects on the adsorption of radionuclides and their removal from aqueous environments. An assessment is also made towards the possible benefits or drawbacks of the presence of such structural defects in GO.

5.2.1 Vacancy Defects

One of the simplest defects which can exist in any material is the absence of an atom from its lattice. Vacancy defects have been observed in graphene-like materials experimentally, for example, Gass *et. al*[216] identified vacancies in the lattice of graphene in high-angle annular dark-field (HAADF) images from scanning transmission electron microscopy (STEM). They reported also that the vast majority of vacancy defects in graphene are single vacancies but also identified double vacancies and large pores. This is perhaps surprising based on DFT calculations by Krasheninnikov *et. al.*[217] who reported that the formation energy of single vacancy defects is around 7.6 eV, and their barrier to migration is only around 1.3 eV, meaning they may migrate under fairly mild conditions and amalgamate on the surface. They

also reported an energy barrier of 8.7 eV for double vacancy formation making them more energetically favourable than two individual vacancy defects, they are also significantly less mobile with a migration barrier calculated to be 5 eV. Meyer *et. al.*[218] also reported from high-resolution transmission electron microscopy (HRTEM) images the occurrence of both vacancies and SW defects in graphene sheets. It was also reported by Ugeda *et. al*[219] from scanning tunnelling microscope (STM) images that vacancies can also be introduced to layers of highly ordered pyrolytic graphite (HOPG) from irradiation with 140 eV Ar^+ ions. The breakdown of GO under irradiation may also be significant for its use in nuclear remediation applications, although the semi-disorder nature of GO may make it more robust to such defects than HOPG. Girit *et. al.*[220] observed the real-time evolution and formation of large vacancies in graphene surfaces under irradiation over a short time frame using TEM.

The production of GO usually requires the use of strong oxidising agents and concentrated acids. The most popular method for producing GO is that of Hummer and Offeman[21]. The Hummer method requires the use of sulphuric acid (H_2SO_4), potassium permanganate ($KMnO_4$), and sodium nitrate ($NaNO_3$). Under the harsh reactions condition of GO synthesis, over-oxidation of the GO lattice is likely to occur. It was also discussed in Chapter 4 that the sorption capacity of GO increases with increased degree of oxidation, so there is a desire for environmental applications to produce highly oxidised GO. Over oxidation of GO leads to the elimination of carbon dioxide (CO_2) from the GO lattice, and the formation of vacancy defects[221,222]. The liberation of carbon monoxide (CO) and CO_2 during GO synthesis was first reported by Hofmann *et. al.*[25] in 1937. It was proposed as a biproduct from carboxylic acid (COOH) formation, and from the formation of pores in the GO lattice, discussed in further detail in Section 1.1. The decomposition of GO and the generation of CO_2 is also reported at to occur at $T > 323$ K[222], a relatively mild condition. Vacancy sites and small holes and pores have also been identified on SEM[186] images following vigorous sonication, a necessary step in the preparation processes of GO. The Lerf-Klinowski structural model for GO discussed in Chapter 1 which is most widely accepted, neglects the formation of CO_2 during the oxidation process, and the presence of other defects. It is assumed instead that GO consists of a perfectly intact hexagonal lattice of carbon atoms, oxidised by hydroxyl and epoxy functional groups on the

surface and carboxylic acid and hydroxyl groups along the nano-flake edges (see Figure 47).

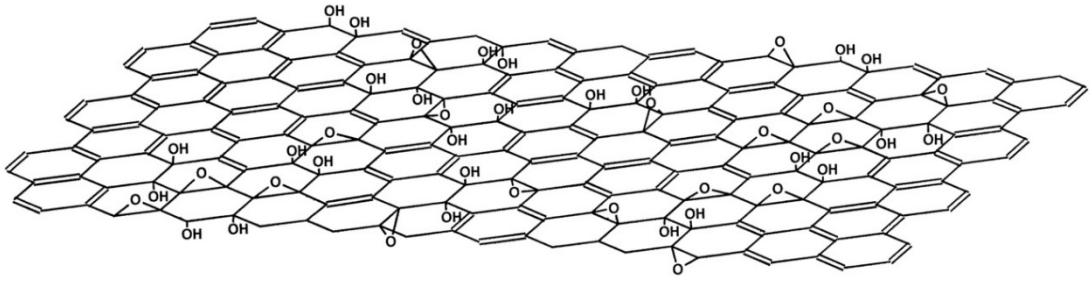

Figure 47: The Lerf-Klinowski structural model of GO [reproduced with permission from ref 20]

5.2.2 Stone-Wales Defects

Another defect which is common in GO and other carbon materials is the SW defect. The SW defect is a topological defect in the GO lattice which involves a change in the physiochemical properties of the GO system without changing the overall chemical composition or connectivity of the sp^2 and sp^3 hybridised carbon lattice. The SW defect does not involve the removal or addition of atoms to the GO lattice, unlike vacancy defect formation. It consists of a 90° rotation of a pair of carbon atoms in the GO lattice, transforming four hexagonal carbon rings into two pentagon and two heptagonal rings (see Figure 48). The formation of pentagon-heptagon defects in graphitic lattices was first proposed by Peter Thrower in 1969. The proposal of such defects is however most commonly associated with the work of Stone and Wales[223] after whom the pentagon-heptagon defect is named.

Meyer *et. al.*[218] reported from high-resolution transmission electron microscopy (HRTEM) images the occurrence of SW defects in graphene sheets. Iijima *et. al.*[224] also observed Stone-Wales defects in fullerenes and accredited them for the formation of negative curvatures. Infrared (IR) and X-ray photoelectron (XPS) spectroscopy experiments by Roh *et. al.*[225] showed that Stone-Wales defects in single-walled carbon

nanotubes (SWCNT) are much more reactive than the non-defected regions of the SWCNT surface.

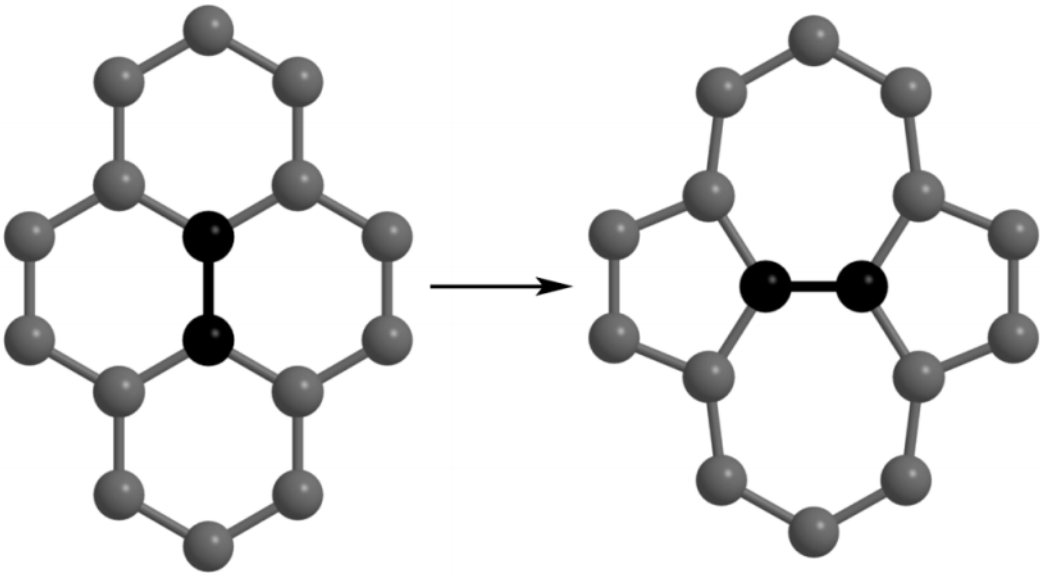

Figure 48: Stone-Wales transformation in a hexagonal lattice [reproduced with permission from ref 226]

Recent theoretical studies have also given insight into the formation of SW defects and the surface chemistry of GO around SW defects. DFT studies by Li *et. al.*[227] and Ma *et. al.*[228] reported the formation energy of a SW defect in a graphene lattice to be around 5 eV and a barrier to SW defect formation in pristine graphene of around 9 eV. It was also reported[227] that the barrier for the reverse transformation is around 5 eV. The high formation energy of SW defects suggests they are probably in low concentrations in normal environmental conditions but, if exposed to high temperatures or under irradiation they could easily form and the substantial barrier to the reverse process would warrant the stability of a significant number of SW defects when the graphene sheet is returned to normal environmental conditions. Nascimento and Nunes[229] also investigated the effect of SW defects on the chemisorption of functional groups to graphene surfaces using DFT, and the role of surface functional groups in the formation of Stone-Wales defects. Their calculations suggest the binding energy of functional groups to graphene surfaces significantly increases in the presence of Stone-Wales defects. They reported a binding energy of 0.83 eV for a single hydrogen atom to a non-defected GO surface from DFT calculations, the binding energy for the chemisorption at a SW defect site was calculated to be 2.05 eV. They

also reported a binding energy of 1.64 eV for chemisorption to carbon atoms neighbouring the Stone-Wales defect site, a significant increase on the pristine graphene nano-flake value. Another DFT study by Boukhvalov *et. al.*[230] also found that the binding energy of hydrogen atoms to graphene surfaces was significantly increased by the presence of Stone-Wales defects, particularly at low levels of surface coverage. They reported that there is also a much lower barrier to hydrogenation on defected graphene surfaces, indicating that SW defect site are much more reactive for the functional group adsorption than pristine graphene. Nascimento *et. al.*[229] reported that the stability of a hydrogen is significantly increased by the introduction of a second hydrogen atom, and the nearest neighbour opposite side (NNOS) configuration is most energetically favourable, consistent with results presented in Chapter 3. They reported also that the stability of hydrogen pairs was significantly increased by the presence of a SW defect. They calculated binding energies of 1.64 eV and 1.00 eV H^{-1} for hydrogen groups in the NNOS and next nearest neighbour opposite (NNNOS) configurations, respectively, on a pristine graphene surface, and 2.68 eV and 1.90 eV H^{-1}, respectively, on a graphene surface with a SW defect. They also calculated the binding energy of OH groups in the preferred NNOS configuration on pristine and Stone-Wales defected graphene nano-flakes. They reported a calculated binding energy of 1.55 eV OH^{-1} in the NNOS configuration on the pristine graphene surface, in good agreement with the value of 1.46 eV OH^{-1} reported in Chapter 3 for the same configuration, and 2.34 eV OH^{-1} on SW defected graphene.

The effect of surface functionalisation on the energy barrier to the formation of SW defects was also investigated by Nascimento *et. al.*[229]. They calculated energy barriers for SW defect transformations (SWT) by a series of transition state configurations in DFT. They reported a calculated energy barrier of 10.2 eV for SWT on a pristine graphene nano-flake in agreement with a similar study by Li *et. al.*[227]. The calculated energy barrier reduced to 6.8 eV for graphene functionalised with a single hydrogen atom, and reduced further to 3.7 eV for SWT on graphene functionalised with a hydrogen pair in the smallest energy barrier configuration, nearest neighbour same side (NNSS). Energy barriers calculated for hydroxylated graphene, suggest the presence of hydroxyl groups also significantly reduced the barrier to SWT.

5.3 Computational Details

Geometry optimisations were carried out using DFT in version 6.5 of the TURBOMOLE[95] code. The PBE[81] GGA *xc*-functional, along with the associated PBE0[87] hybrid GGA *xc*-functional, were used throughout. The functionals used do not include correction for dispersion energies. The def2-SVP[191,192] atom centred Ahlrich basis set of polarised double-ζ quality was used for H, C and O, and a small-core effective core potentials (ECPs) with the associated basis sets were used for Sr[193], La[194,195], and Th[196,197], as in Chapter 4. Calculations to correct for basis set superposition error were not carried out, as in calculations presented in Chapter 4.

Consideration of solvation effect was made using the conductor-like screening model (COSMO) with default parameters, *i.e.* a relative permittivity of $\varepsilon_r = \infty$, which is considered a suitable approximation for water, and molecular cavities constructed of spheres with radii which are 2.00 Å, 1.72 Å, and 1.30 Å for C, O, and H respectively, and 2.223 Å for Sr, La, and Th.

Numerical vibrational frequency calculations were carried out on geometries optimised at the PBE level of theory, in order to confirm correspondence to local energetic minima. Correspondence to energetic minima was assumed for geometry optimisations carried out using the PBE0 *xc*-functional. Such an assumption is made due to the large computational cost associated with numerical frequency analysis, especially those carried out on geometries optimised using hybrid-functionals.

5.4 Results

An investigation is carried out into the binding interactions of the radionuclide ions used in Chapter 4 (Sr(II), La(III), and Th(IV) aquocomplexes) with the surface and edge of GO nano-flakes with a single vacancy defect, a pore defect, and a Stone-Wales defect. The model GO nano-flakes are based on those used in Chapter 4 with a defect introduced close to the middle of the GO surface. Initial starting geometries for interactions with the GO surface were chosen to ensure that the defect was involved in

complexation. The initial starting geometries for complexation with the GO edge were chosen to most closely resemble the edge binding geometries in Chapter 4. Due to limitation on computational resources and the volume of calculations required, a search for lower energy geometries was not carried out. Although lower energy geometries may exist, confidence that the geometries used here allow a fair assessment of the effect of the defects on binding is obtained from comparisons with results in Chapter 4.

5.4.1 Neutral GO Nano-flakes

5.4.1.1 Vacancy Defects

An investigation was first carried out into the binding of radionuclides to the surface and edge of the neutral GO nano-flake defected with a vacancy in the carbon lattice. The neutral vacancy-defected GO nano-flake was produced by removal of a single carbon atom from the neutral GO flake presented in Figure 26 and termination of the three dangling bonds with hydrogen atoms (see Figure 49).

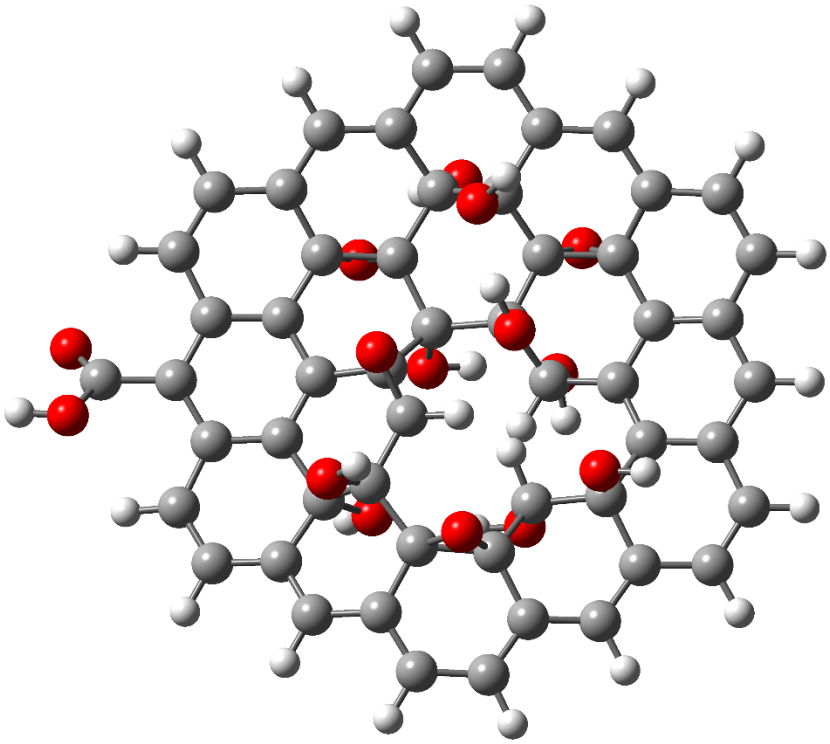

Figure 49: GO nano-flakes with a single vacancy defect incorporating both hydroxyl and epoxy groups at the 50% level of surface oxidation. Optimised at the PBE/SVP level of theory.

5.4.1.1.1 Surface Binding

The binding of the radionuclide analogues to the surface of the neutral GO nano-flake with a single vacancy defect was investigated. The calculated binding energies for inner-sphere complexation of the radionuclides with the surface of both the non-defected and vacancy defected GO nano-flake are presented in Table 35. Inner-sphere complexation energies were calculated using the method described in Section 4.3.4.2 and the following formula:

$$E_b = E_{[GO+R]^{m+}} - E_{GO} - E_{[R]^{m+}} + E_{(H_2O)_x} \quad \textbf{(5.1)}$$

Where $E_{[GO+R]^{m+}}$ is the energy of the interacting system, E_{GO} is the energy of the defected GO nano-flake, $E_{[R]^{m+}}$ is the energy of the radionuclide aquocomplex, and $E_{(H_2O)_x}$ is the energy of the water molecules eliminated from the aquocomplex solvation shell during complexation, obtained from equation (4.1).

The inner-sphere complexation of each the analogues with the vacancy defected GO surface is by the formation of 3 M-O_{GO} bonds. The Sr(II) aquocomplex forms M-O_{GO} bonds with two OH groups and an epoxy group on the GO surface, La(III) and Th(IV) both form bonds with two OH groups and one carbonyl group on a modified GO surface, as in complexation with the defect-free GO surface as in Section 4.4.1.

Table 35: Binding energies for inner-sphere complexation of Sr(II), La(III), and Th(IV) aquocomplexes with surface of defect-free (Pristine) and single vacancy defected neutral GO nano-flakes. All values are in eV. Calculations carried out in the aqueous-phase.

Ion	PBE		PBE0	
	Pristine	Defected	Pristine	Defected
Sr(II)	-0.63	-0.57	-0.47	-0.38
La(III)	-1.28	-0.92	-0.90	-0.72
Th(IV)	-1.84	-1.46	-1.46	-1.02

A clear correlation emerges between the formal charge of the radionuclide and the binding energy for inner-sphere complexation to the surface of the vacancy defected GO nano-flake. The correlation between binding energy and formal charge is also

present in calculations carried out for the defect-free GO surface. Binding energies calculated for complexation with vacancy defected GO are however smaller than those calculated for defect-free GO. Destabilisation in the presence of the defect is least significant for Sr(II). The calculated binding energy for Sr(II) is less than 0.1 eV greater on the defect-free GO surface, within the expected accuracy of DFT. The binding energies calculated for La(III) and Th(IV) are however significantly smaller. The binding energies of La(III) and Th(IV) are typically reduced by 0.35-0.45 eV in the presence of the vacancy defect, with exception of the binding energy of La(III) calculated with PBE0 which is only 0.18 eV smaller.

The energy associated with the deformation of the GO nano-flake during surface complexation, obtained from single point energy calculations carried out on the GO flakes held at their adsorptive geometries are presented in Table 36. It is noted, unsurprisingly, due to greater flexibility of the defected GO nano-flake around the vacancy site that the defected GO nano-flakes undergo greater deformation than the idealised GO nano-flakes during sorption. It is noted also that the increase in deformation energy between the defect-free and vacancy defected GO nano-flakes is less pronounced for the La(III) geometry optimised using the PBE0 *xc*-functional, which accounts for the smaller change in binding energy.

Table 36: Deformation energy of neutral defect-free (Pristine) and vacancy defected GO nano-flakes following the inner-sphere surface complexation with Sr(II), La(III), and Th(IV) aquocomplexes. All values are in eV. Calculations carried out in the aqueous-phase

Ion	PBE		PBE0	
	Pristine	Defected	Pristine	Defected
Sr(II)	0.15	0.36	0.11	0.37
La(III)	0.66	0.95	1.00	1.07
Th(IV)	0.86	1.18	1.22	1.61

A comparison of inner-sphere binding energies calculated using PBE and PBE0 reveals, as in calculations for the defect-free GO flake, that the latter predicts smaller binding energy. The same trends however emerge from calculations using both *xc*-functionals. The largest difference in calculated binding energy between the

xc-functional groups is for complexation of the Th(IV) with the GO surface which is also commensurate with the largest increase in GO nano-flake deformation energy when using PBE0.

Table 37: Binding energies for outer-sphere complexation of Sr(II), La(III), and Th(IV) aquocomplexes with surface of defect-free (Pristine) and single vacancy defected neutral GO nano-flakes. All values are in eV. Calculations carried out in the aqueous-phase.

Ion	PBE		PBE0	
	Pristine	Defected	Pristine	Defected
Sr(II)	-1.08	-0.52	-1.00	-0.42
La(III)	-1.14	-1.13	-0.93	-0.89
Th(IV)	-1.04	-1.04	-0.79	-1.06

Outer-sphere binding between the radionuclide analogues and the vacancy defected GO surface was also investigated. The calculated binding energies for outer-sphere binding with both the defect-free and vacancy defected GO nano-flake are presented in Table 37. Binding energies were calculated using the method described in Section 4.3.4.3, and the following formula:

$$E_b = E_{[GO+R]^{m+}} - E_{GO+(H_2O)_x} - E_{[R]^{m+}} + E_{(H_2O)_x} \quad \textbf{(5.2)}$$

Where $E_{[GO+R]^{m+}}$ is the energy of the interacting system, $E_{GO+(H_2O)_x}$ is the energy of the defected GO nano-flake and interacting water molecules, $E_{[R]^{m+}}$ is the energy of the radionuclide aquocomplex, and $E_{(H_2O)_x}$ is the energy of the water molecules displaced during complexation, obtained from equation (4.1).

Outer-sphere binding energies calculated using PBE predict there is no correlation between formal charge and binding energy, albeit the binding energy calculated for Sr(II) is about half that calculated for La(III) and Th(IV). Binding energies calculated using PBE0, however, predicts that binding energy increases with formal charge, the inverse correlation is predicted by PBE0 level calculations for outer-sphere complexation with the defect-free GO surface.

A comparison between the outer-sphere complexation binding energies for the defect-free and vacancy defected neutral GO surfaces using PBE predicts that the presence of a single vacancy defect has a significant effect on the binding of Sr(II), but has little to no effect on the binding energy of La(III) and Th(IV). Binding energies from calculations carried out using PBE0 suggest that the vacancy defect also has an effect on the binding energy of Th(IV), stabilising it on the defected surface by approximately 0.3 eV. Based on calculations carried out at the PBE level of theory, and the general trend towards PBE0 predicting lower binding energies than PBE, which is observed in other calculations, this is probably due to a small structural change in the GO lattice which have not been identified. Binding energies calculated for Sr(II) at both levels of theory suggest the aquocomplex is more than twice as stable on the defect-free GO surface than on the GO surface with the vacancy defect.

It is interesting to note that it is known from experimental results[143,149] that divalent cations bind to GO by outer-sphere complexation in low pH environments, whilst trivalent and tetravalent cations predominately form inner-sphere complexes[151,152,231]. Calculations presented in Table 35 predict the presence of a vacancy defect will have a significant effect on the inner-sphere complexation of La(III) and Th(IV) aquocomplexes with the GO surface, whilst there will be no significant effect on the inner-sphere binding of Sr(II). Calculated binding energies presented in Table 37 predict that the introduction of a single vacancy defect reduces the outer-sphere binding energy of the Sr(II) aquocomplex significantly but has little to no effect on the outer-sphere binding of La(III) and Th(IV).

Table 38: Binding energy for inner- and outer-sphere complexation of Sr(II), La(III), and Th(IV) aquocomplexes with the surface of a neutral GO nano-flake with a single vacancy defect. All values are in eV. Calculations carried out in the aqueous-phase.

Ion	PBE		PBE0	
	Inner	Outer	Inner	Outer
Sr(II)	-0.57	-0.52	-0.38	-0.42
La(III)	-0.92	-1.13	-0.72	-0.89
Th(IV)	-1.46	-1.04	-1.02	-1.06

A comparison between the inner-sphere and outer-sphere binding energies calculated for each of the cations to the surface of vacancy defected neutral GO flake (see Table 38) suggests there is no binding preference for Sr(II), whilst outer-sphere complexation is predicted for La(III). Calculations carried out using PBE predict that inner-sphere binding is preferred by Th(IV). PBE0 level calculations predict that there is no binding preference for Th(IV), due in part to the unusually high outer-sphere binding energy which has been calculated with the hybrid functional.

5.4.1.1.2 Edge Binding

The binding of the radionuclide analogues to the edge of the neutral vacancy defected GO nano-flake was also investigated. Binding energies calculated using equation (5.1) for inner-sphere complexation with both the vacancy-defected and defect-free nano-flakes are presented in Table 39.

Table 39: Binding energies for inner-sphere complexation of Sr(II), La(III), and Th(IV) aquocomplexes with edge of defect-free (Pristine) and single vacancy defected neutral GO nano-flakes. All values are in eV. Calculations carried out in the aqueous-phase.

Ion	PBE		PBE0	
	Pristine	Defected	Pristine	Defected
Sr(II)	-0.54	-0.60	-0.42	-0.46
La(III)	-0.38	-0.53	-0.31	-0.35
Th(IV)	-0.07	-0.27	0.10	-0.05

The calculated binding energies suggest there is an inverse correlation between formal charge and calculated binding energy, which is also predicted in calculations for inner-sphere binding to the edge of the defect-free GO nano-flake. The inner-sphere binding to the edge of the vacancy defected GO flake is by the formation of a single M-O_{GO} with the COOH group, further stabilised by a H-bond. M-O_{COOH} bonds are calculated to be 2.515 Å, 2.528 Å, and 2.309 Å for Sr(II), La(III), and Th(IV), respective, which are consistent with those calculated to the edge of the defect-free GO flake (2.516 Å, 2.516 Å, and 2.332 Å, respectively). The M-O_{COOH} bond calculated for Th(IV) is again shorter than those calculated for Sr(II) and La(III) when the respective ionic radii are taken into account, calculated binding energies however suggest again that Th(IV) is significantly less stable on the neutral GO edge than the other

radionuclides. Th(IV) is however predicted to be slightly more stable on the edge of the vacancy-defected GO flake than the defect-free flake. Binding energies calculated for Sr(II) are not significantly different on the edge of the defect-free and vacancy defected flakes. Binding energies calculated for La(III) using PBE predict it will be more stable on the vacancy-defected nano-flake, PBE0 calculations however predict no significant change in binding energy. The binding energies suggest that inner-sphere complexation of radionuclides with the edge of the GO flake is generally insensitive to the presence of a vacancy defect on the GO surface. There is however a broad trend which emerges from PBE calculations that suggests there is increased stability associated with the vacancy defect with increases cation charge. This may be due to the vacancy site allowing for greater lateral flexibility of the GO flake allowing for better coordination between the ions and the nano-flake edge and overcoming some of the steric effects inhibiting the binding of Th(IV).

Table 40: Binding energies for outer-sphere complexation of Sr(II), La(III), and Th(IV) aquocomplexes with edge of defect-free (Pristine) and single vacancy defected neutral GO nano-flakes. All values are in eV. Calculations carried out in the aqueous-phase.

Ion	PBE		PBE0	
	Pristine	Defected	Pristine	Defected
Sr(II)	-0.71	-0.78	-0.58	-0.64
La(III)	-0.69	-0.72	-0.56	-0.57
Th(IV)	-0.54	-0.55	-0.37	-0.40

The binding energies calculated for outer-sphere binding to the edge of the defect-free and vacancy defected neutral GO nano-flakes are presented in Table 40. The calculated binding energies predict that Sr(II) and La(III) are stabilised approximately equally to the edge of the vacancy defected GO nano-flake, whilst the binding energy for Th(IV) is about 0.2 eV smaller, in agreement with calculations for binding to the edge of the defect-free GO flake. The smaller binding energy for Th(IV) was attributed to a structural change in one of the water molecules in the solvation shell of Th(IV) in Chapter 4, this structural change has also occurred here. A comparison of the values calculated for the defect-free and vacancy defected GO flake reveals that the presence

of a vacancy on the GO surface has essentially no effect on outer-sphere binding to the GO nano-flake edge.

Table 41: Binding energy for inner- and outer-sphere complexation of Sr(II), La(III), and Th(IV) aquocomplexes with the edge of a neutral GO nano-flake with a single vacancy defect. All values are in eV. Calculations carried out in the aqueous-phase.

Ion	PBE		PBE0	
	Inner	Outer	Inner	Outer
Sr(II)	-0.60	-0.78	-0.46	-0.64
La(III)	-0.53	-0.72	-0.35	-0.57
Th(IV)	-0.27	-0.55	-0.05	-0.40

A comparison was also made for the binding preference for each of the radionuclide analogues for inner-sphere or outer-sphere complexation with the edge of vacancy defected GO (see Table 41). It is predicted that outer-sphere complexation is the preferred mode of binding for all ions, as with the defect-free GO nano-flake.

Consideration of the data presented in Table 38 and Table 41 suggest that Sr(II) binds most readily to the edge of the GO nano-flake with a vacancy-defect forming outer-sphere complexes, whilst La(III) and Th(IV) both bind most readily with the GO surface.

5.4.1.2 Pore Defects

The binding of radionuclides to the surface and edge of the neutral GO nano-flakes defected with a pore was also investigated. The pore-defected GO nano-flake was produced by removal of the central six-membered carbon ring from the neutral GO flake presented in Figure 26 and termination of the six dangling bonds with hydrogen atoms (see Figure 50). The pore defect can be considered as a large vacancy in the GO lattice rather than a hole. Space-filling models produced by Feicht and Eigler[215] for a similar 7-carbon vacancy suggested that diffusion is not allowed for vacancy defects of this size. Holes can form in GO surfaces from the accumulation of vacancy defects in close proximity, their investigation would however require a much larger GO model than those used in this research, which would be computationally prohibitive at the level of theory used.

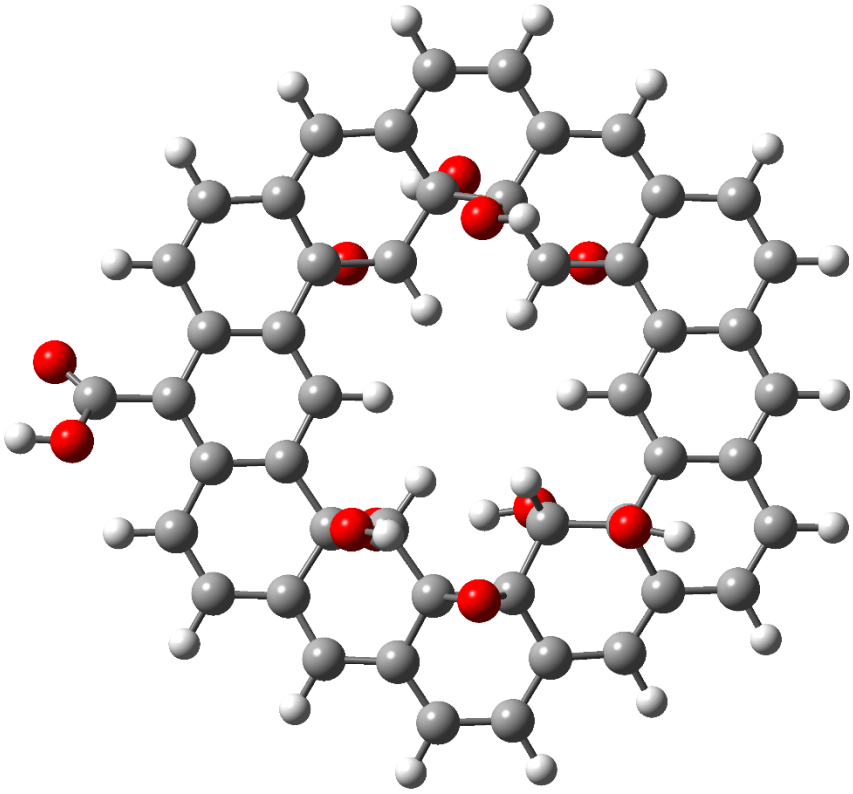

Figure 50: GO nano-flakes with a pore defect incorporating both hydroxyl and epoxy groups at the 50% level of surface oxidation. Optimised at the PBE/SVP level of theory

5.4.1.2.1 Surface Binding

The binding energies calculated using equation (5.1) for the inner-sphere complexation of the radionuclide analogues with the surface of the defect-free and pore-defected neutral GO nano-flakes are presented in Table 42. Inner-sphere complexation to the pore defected surface is by the formation of two M-O_{GO} bonds with functionals groups on the GO surface, which is one fewer than form with the pristine GO surface (see Figure 51). Binding also involves the formation of H-bonds, which will contribute to stability.

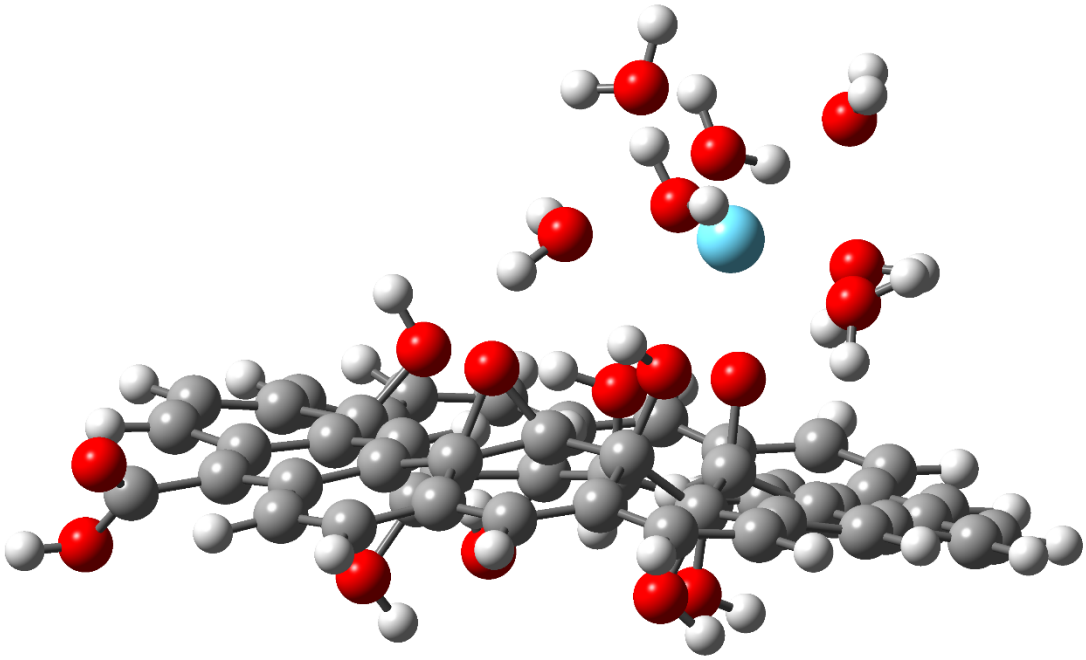

Figure 51: Inner-sphere binding of the La(III) aquocomplex with the surface of the neutral GO nano-flake with a pore defect. Optimised at the PBE/SVP level of theory.

The Sr(II) aquocomplex forms M-O_{GO} bonds with an epoxy group and a OH group, which are calculated to be 2.498 Å and 2.836 Å, respectively, at the PBE level of theory (complexation to the surface of defect-free GO is by the formation of a M-O_{epoxy} bond calculated to be 2.529 Å and two M-O_{OH} with an average calculated bond length of 2.629 Å). The La(III) aquocomplex modified the surface structure of the GO nano-flake to form M-O_{GO} bonds with a carbonyl group and a OH group, with bond lengths calculated to be 2.347 Å and 2.651 Å, respectively. The La(III) complex was also found to alter the GO surface on the defect-free flake to form a M-$O_{carbonyl}$ bond calculated to be 2.348 Å and two M-O_{OH} bonds with an average length of 2.671 Å. The inner-sphere complexation between Th(IV) and GO surface also involves the formation of a bond with a carbonyl group by breaking a C-O bond in an epoxy group. The M-O_{GO} bond to the carbonyl group on the pore-defected surface was calculated to have a bond length 2.126 Å, consistent with the M-$O_{carbonyl}$ bond calculated to the surface of defect-free GO (calculated to be 2.137 Å), and an M-O_{OH} bond calculated to be 2.611 Å. The two M-O_{OH} bonds formed between Th(IV) and the pristine GO surface were calculated to have an average length of 2.583 Å.

The calculated binding energies to the pore defected surface reveal a correlation between formal change and binding energy, which is consistent with calculations for

inner-sphere binding with the defect-free GO surface. Binding energies are consistent between the two GO flakes, which is perhaps surprising given that fewer M-O_{GO} bonds form with the pore defected flake, due to spatial constraints and the availability of fewer surface functional groups for binding. It was reported by Yang *et. al.*[160] from DFT calculations that there is a significant increase in the inner-sphere binding energy when a complex is formed with a second epoxy group on a GO surface. Results presented here suggest there is no significant increase in binding energy when complexing with a triplet of surface functional groups rather than a pair, predicting an upper limit for binding energy to the GO surface.

Table 42: Binding energies for inner-sphere complexation of Sr(II), La(III), and Th(IV) aquocomplexes with surface of defect-free (Pristine) and pore-defected neutral GO nano-flakes. All values are in eV. Calculations carried out in the aqueous-phase.

Ion	PBE		PBE0	
	Pristine	Defected	Pristine	Defected
Sr(II)	-0.63	-0.70	-0.47	-0.48
La(III)	-1.28	-1.23	-0.90	-0.84
Th(IV)	-1.84	-1.81	-1.46	-1.45

A comparison of inner-sphere binding energies calculated using PBE and PBE0 reveals again that the latter predicts smaller binding energies. The same trends in binding energy however again emerge from calculations using both *xc*-functionals.

The outer-sphere binding of the radionuclide analogues with the pore-defected GO surface was also investigated. Binding energies for outer-sphere complexation to the defect-free and pore-defected GO nano-flake surfaces calculated using equation (5.2) are presented in Table 43. Outer sphere complexation with the neutral pore-defected GO surface is by the formation of H-bonds between surface functional groups and three water molecules from the solvation shell of Sr(II), or four water molecules from the solvation shells of La(III) and Th(IV). Outer-sphere complexation with the defect-free GO surface also involves three water molecules from the Sr(II) solvation shell or four from La(III) or Th(IV). Binding energies calculated for Sr(II) and La(III) to the pore-defected flake are consistent with those calculated for the defect-free GO surface, suggesting an independence to formal charge for divalent and trivalent cation

adsorption, and an insensitivity to the surface defect. The binding energy calculated for Th(IV) on the pore-defected surface is, however, around 1 eV greater than those calculated for the divalent and trivalent radionuclides, and significant greater than the binding energies calculated to the surface of the defect-free GO nano-flake.

Table 43: Binding energies for outer-sphere complexation of Sr(II), La(III), and Th(IV) aquocomplexes with surface of defect-free (Pristine) and pore-defected neutral GO nano-flakes. All values are in eV. Calculations carried out in the aqueous-phase.

Ion	PBE		PBE0	
	Pristine	Defected	Pristine	Defected
Sr(II)	-1.08	-1.13	-1.00	-0.89
La(III)	-1.14	-1.12	-0.93	-0.87
Th(IV)	-1.04	-2.20	-0.79	-1.86

Analysis of the Th(IV) adsorbed geometry on the pore defected surface (see Figure 52) reveals that the aquocomplex has undergone hydrolysis. The eliminated proton from the solvation shell of the Th(IV) aquocomplex has also allowed the formation of a OH group on the GO surface through transformation of an epoxy groups. It was reported from calculations in Chapter 3 that OH groups are much more stable on the surface of GO flakes than epoxy groups, which is presumably contributing towards the greatly increased stability of the system here. It is also reported in the literature that Th(IV) aquocomplexes are prone to hydrolysis and form highly stable hydrolysed complexes[209,232]. Yang *et. al.*[160] and Sun *et. al.*[180] also reported from DFT calculations that the stability of Pb(II) and U(IV) increases significantly on GO surfaces when they form the Pb(OH) and U(OH) complexes by abstraction of a hydroxyl group from the GO surface.

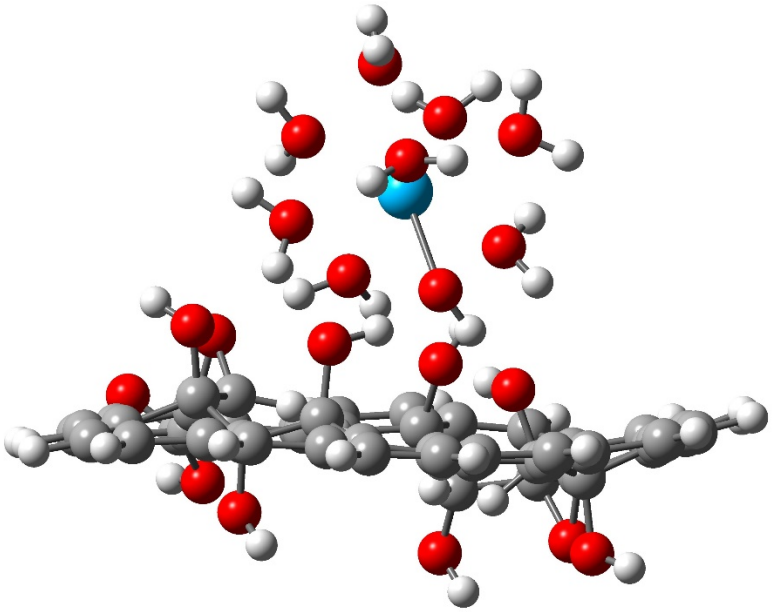

Figure 52: Outer-sphere binding of the Th(IV) aquocomplex with the surface of the neutral GO nano-flake with a pore defect. Optimised at the PBE/SVP level of theory. The Th-O bond indicates the location of the hydroxide.

A comparison of the inner-sphere and outer-sphere binding energies calculated for each of the cations to the surface of the pore-defected neutral GO (see Table 44) predict that Sr(II) strongly prefers the formation of outer-sphere complexes, which is in agreement with experimental results and consistent with calculations for binding to the defect-free GO surface. Binding energies calculated for La(III) predict no clear preference for binding interaction, which is again consistent with binding energies calculated for complexation with the defect-free GO surface. The binding energy calculated for Th(IV) predicts that the formation of an outer-sphere complex is preferred, which does not agree with experimental observations or other theoretical studies. It is reported that Th(IV) and other tetravalent cations mostly form inner-sphere complexes with GO. It is has been discussed however, that the high stabilisation energy calculated for the outer-sphere complexation of Th(IV) to the pore-defected GO surface is due to the hydrolysis of the Th(IV) aquocomplex, and it is likely that the modification of the chemical structure on the GO nano-flake surface through formation of a OH group in place of a surface epoxy group may also be contributing to stability. The hydrolysis of Th(IV), although not found in other calculations, could also occur in other environments, under normal environmental conditions, and in the dynamic environment of radionuclide complexation with GO, it is unlikely that Th(IV) will exist solely as the nonacoordinated aquocomplex.

Table 44: Binding energy for inner- and outer-sphere complexation of Sr(II), La(III), and Th(IV) aquocomplexes with the surface of a neutral GO nano-flake with a pore-defect. All values are in eV. Calculations carried out in the aqueous-phase.

Ion	PBE		PBE0	
	Inner	Outer	Inner	Outer
Sr(II)	-0.70	-1.13	-0.48	-0.89
La(III)	-1.23	-1.12	-0.84	-0.87
Th(IV)	-1.81	-2.20	-1.45	-1.86

5.4.1.2.2 Edge Binding

The binding of the radionuclide analogues to the COOH group on the edge of the neutral GO nano-flake with a pore-defect was also investigated. The binding energies calculated using equation (5.1) for inner-sphere complexation with the edge of both the defect-free and pore-defected nano-flakes are presented in Table 45.

Table 45: Binding energies for inner-sphere complexation of Sr(II), La(III), and Th(IV) aquocomplexes with edge of defect-free (Pristine) and pore-defected neutral GO nano-flakes. All values are in eV. Calculations carried out in the aqueous-phase.

Ion	PBE		PBE0	
	Pristine	Defected	Pristine	Defected
Sr(II)	-0.54	-0.52	-0.42	-0.40
La(III)	-0.38	-0.40	-0.31	-0.26
Th(IV)	-0.07	-0.19	0.10	-0.01

The calculated binding energies again suggest there is an inverse correlation between formal charge and calculated binding energy, consistent with calculations for inner-sphere binding to the edge of the defected-free and vacancy-defected GO flakes. Inner-sphere complexation is also again by the formation of a single M-O_{COOH} bond and a H-bond with the hydroxyl group of the carboxylic acid moiety. M-O_{COOH} bond lengths were calculated to be 2.507 Å, 2.516 Å, and 2.315 Å for Sr(II), La(III), and Th(IV), respective, in PBE level calculations, which are consistent with the bonds formed to the edge of the defect-free and vacancy-defected GO nano-flakes. The binding energies are also consistent with those calculated to the edge of the defect-free

GO flake. It is predicted again that Th(IV) has much lower affinity to the COOH group on the edge of the neutral flake than La(III) and Sr(II). The results also indicate again that the defect-free GO flake model is suitable for modelling inner-sphere binding interactions with the edge of neutral, defected GO.

Table 46: Binding energies for outer-sphere complexation of Sr(II), La(III), and Th(IV) aquocomplexes with edge of defect-free (Pristine) and pore-defected neutral GO nano-flakes. All values are in eV. Calculations carried out in the aqueous-phase.

Ion	PBE		PBE0	
	Pristine	Defected	Pristine	Defected
Sr(II)	-0.71	-0.70	-0.58	-0.58
La(III)	-0.69	-0.72	-0.56	-0.57
Th(IV)	-0.54	-0.54	-0.37	-0.41

The binding energies calculated for outer-sphere binding to the edge of the defect-free and pore-defected neutral GO nano-flake are presented in Table 46. Binding energies calculated for interaction with the edge of defected GO are in very close agreement with those calculated for the idealised system. The calculated binding energy of Th(IV) is again around 0.2 eV smaller than that calculated for Sr(II) and La(III), which is again commensurate with an elongation of one of the O-H bonds in a water molecule interacting with the GO edge. A comparison of the binding energies calculated for the two GO flakes shows the presence of a pore on the GO surface has little to no effect on outer-sphere binding to the edge.

5.4.1.3 Stone-Wales Defects

The binding of radionuclides to the surface and edge of the neutral GO nano-flakes with a SW defect was also investigated. The SW-defected nano-flake was produced by rotation of a C-C bond in the central carbon ring of the defect-free GO nano-flake by 90° (see Figure 53). This resulted in a GO nano-flake with the same sp^2-sp^3 connectivity as the pristine GO nano-flake and the occurrence of 5 and 7 membered carbon rings in the GO lattice.

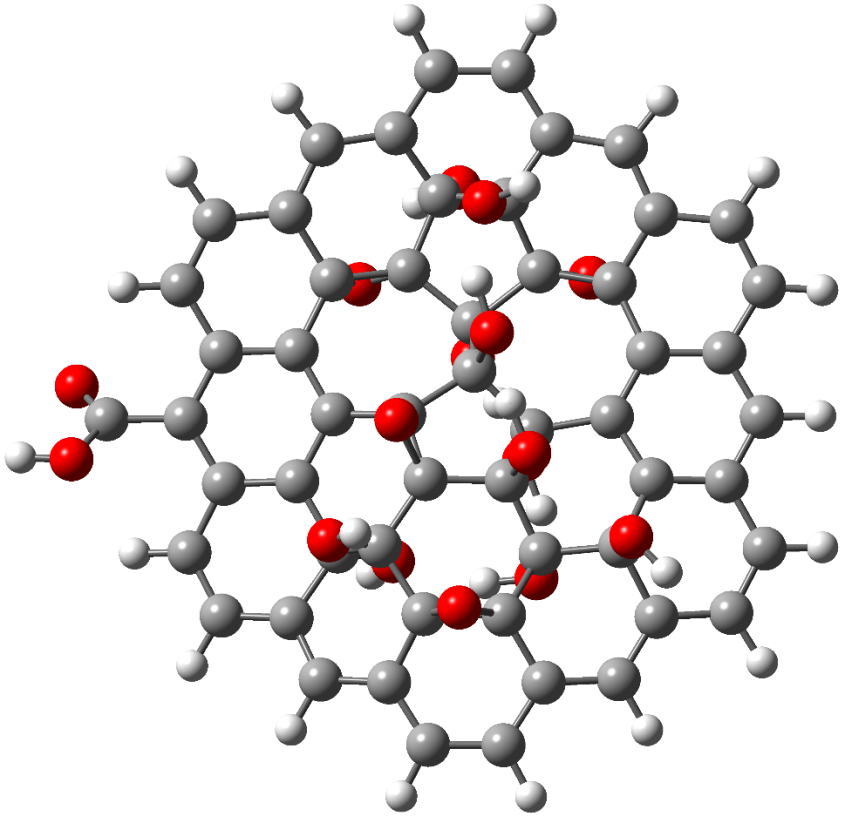

Figure 53: GO nano-flakes with a Stone-Wales defect incorporating both hydroxyl and epoxy groups at the 50% level of surface oxidation. Optimised at the PBE/SVP level of theory

5.4.1.3.1 Surface Binding

The binding energies for the inner-sphere complexation of the radionuclides analogues with the surface of the defect-free and SW-defected GO nano-flakes calculated using equation (5.1) are presented in Table 47. A clear correlation between formal charge and calculated binding energy emerges from the data, in agreement with calculations carried out for binding to the defect-free, vacancy defected GO surfaces. A comparison of the binding energies calculated for inner-sphere complexation using PBE predicts that Sr(II) will be stabilised on the GO surface by the SW defect, the increase in binding energy is however not predicted by calculations carried out with PBE0. The binding of La(III) and Th(IV) are both predicted to be inhibited by the presence of the SW defect.

Table 47: Binding energies for inner-sphere complexation of Sr(II), La(III), and Th(IV) aquocomplexes with surface of defect-free (Pristine) and SW-defected neutral GO nano-flakes. All values are in eV. Calculations carried out in the aqueous-phase.

Ion	PBE		PBE0	
	Pristine	Defected	Pristine	Defected
Sr(II)	-0.63	-0.87	-0.47	-0.48
La(III)	-1.28	-1.16	-0.90	-0.74
Th(IV)	-1.84	-1.62	-1.46	-1.35

Inner-sphere complexation with the SW defected GO surface is by the formation of 3 M-O_{GO} bonds. The complexation of all three of the ions involved the breaking of a C-O bond in a surface epoxy group to form a M-$O_{carbonyl}$ bond and two M-O_{OH} bonds. The C-O bond was not found to break during complexation of Sr(II) with the surface of the defect-free GO flake, it is presumably then, the reason for stabilisation of Sr(II) in PBE calculations. The bond formed between Sr(II) and the carbonyl group on the SW-defected GO surface was calculated to be 2.442 Å at the PBE level of theory, shorter than the M-O_{epoxy} bond formed with the pristine GO surface (2.529 Å). M-O_{OH} bonds were calculated to have an average length of 2.639 Å on the SW-defected and 2.629 Å on the defect-free GO surface. The bonds formed between La(III) and the SW-defected surface were a M-$O_{carbonyl}$ bond calculated to be 2.346 Å and two M-O_{OH} bonds with an average bond length of 2.669 Å, which are consist with the equivalent bonds for complexation to the defect-free GO surface calculated to be 2.348 Å and 2.671 Å, respectively. The bonds formed between Th(IV) and the SW-defected surface were a M-$O_{carbonyl}$ bond calculated to be 2.150 Å and two M-O_{OH} bonds with an average length calculated to be 2.598 Å, consistent with the M-$O_{carbonyl}$ and average M-O_{OH} bonds calculated to be 2.137 Å and 2.583 Å on the defect-free GO surface, respectively.

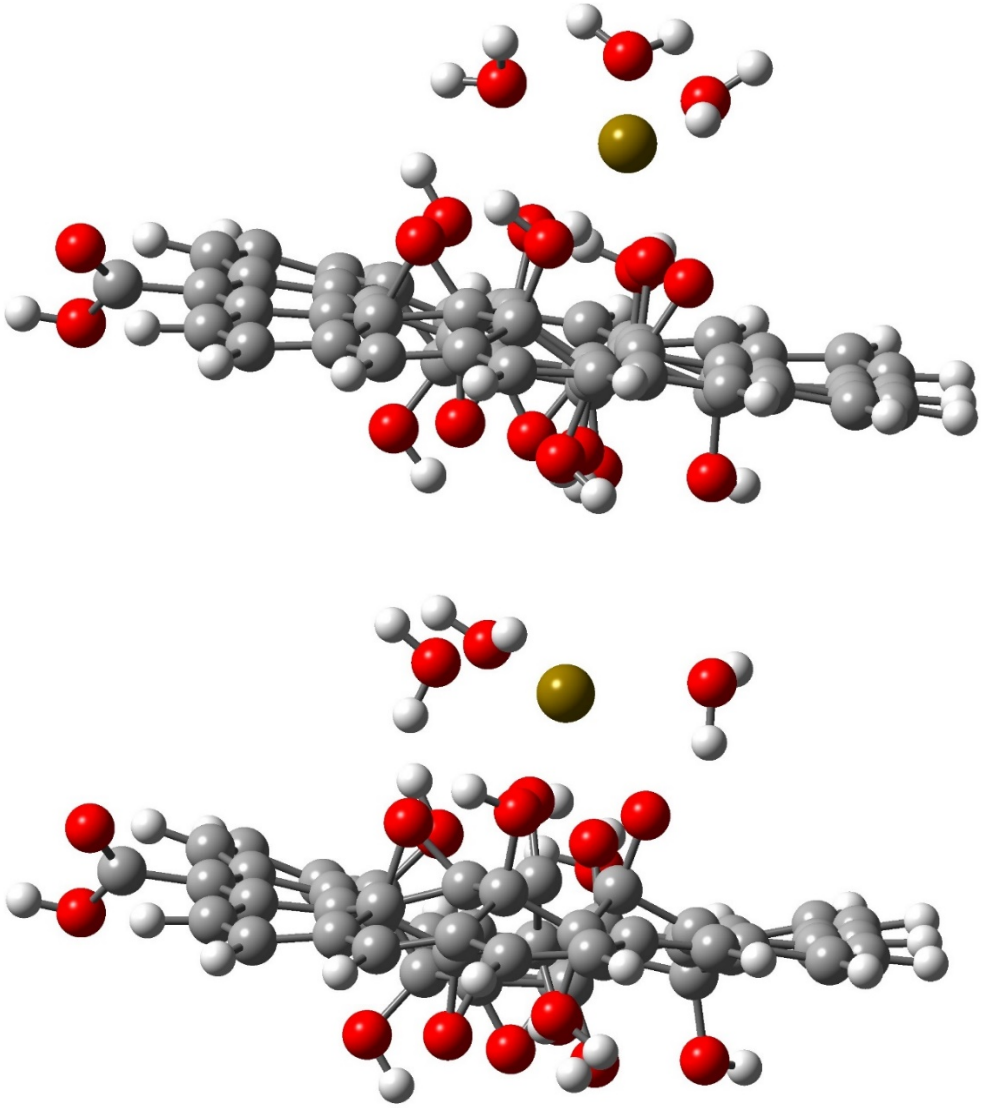

Figure 54: Inner-sphere binding of the Sr(II) aquocomplex with the surface of the defect-free (top) and SW-defect(bottom) neutral GO nano-flake. Optimised at the PBE/SVP level of theory.

The inner-sphere complexation geometries for Sr(II) to the surface of the defect-free and SW-defected GO nano-flakes are presented in Figure 54. It is noted that the SW-defected nano-flake is less planar than the pristine nano-flake, presumably due to greater flexibility around the defect site. The reduced planarity of the defected GO flake results in the formation of two additional H-bonds and distortion of the Sr(II) solvation shell. The formation of additional H-bonds is presumably also contributing towards the increased stability of the Sr(II) aquocomplex predicted by PBE calculations, it should be noted also however that the formation of additional H-bonds also occurs in complexation geometries optimised using PBE0, where no increase in binding energy is predicted. It was established in Chapter 3 however that the

deformation of the GO lattice has a greater effect in calculations carried out using PBE0, revealing two competing effects on the energetics of the system, one which relates to the stabilisation of the Sr(II) complex on the SW-defected GO surface by the formation of additional H-bonds, the other associated with the energy associated with the distortion of the GO nano-flake from planarity. The formation of additional H-bonds is not observed in La(III) and Th(IV) inner-sphere complexation geometries with the SW defected GO surface, although the SW defected nano-flake is again less planar than the pristine flake, which could be the reason for the lower calculated binding energies.

Table 48: Binding energies for outer-sphere complexation of Sr(II), La(III), and Th(IV) aquocomplexes with surface of defect-free (Pristine) and SW-defected neutral GO nano-flakes. All values are in eV. Calculations carried out in the aqueous-phase.

Ion	PBE		PBE0	
	Pristine	Defected	Pristine	Defected
Sr(II)	-1.08	-1.32	-1.00	-1.10
La(III)	-1.14	-1.33	-0.93	-1.08
Th(IV)	-1.04	-1.25	-0.79	-1.00

The outer-sphere complexation between the SW-defected GO surface and the radionuclide analogues was also investigated. The binding energies calculated for binding to the defect-free and SW-defected flakes using equation (5.2) are presented in Table 48. The binding energies suggest that the radionuclides are all stabilised at the SW defect. Outer-sphere complexation with the SW-defected GO surface is by the formation of H-bonds between surface functional groups and four water molecules in the solvation shell of all of the analogue ions. Outer-sphere complexation of Sr(II) with the defect-free surface involved only three water molecules from the radionuclide solvation shell, the same trends however emerge for complexation with both the defect-free and SW-defected GO surfaces. The calculated binding energies suggest that the ions are all stabilised on the GO surface approximately equally, indicating that binding to the neutral SW-defected surface is insensitive to formal charge. The defect-free GO nano-flake model qualitatively described the interactions with the SW-defected GO surface but underestimates the binding energy of cations by outer-

sphere complexation. The presence of SW defects may increase the binding efficiency of GO, particular for the removal of monovalent and divalent radionuclides which are known from experimental data[143,149] to form outer-sphere complexes with GO. SW defects are also predicted to inhibit the adsorption of trivalent and tetravalent radionuclides by inner-sphere complexations, their preferred mode of binding interaction from experimental results[151,152,231], increasing further the expected uptake of divalent (and monovalent) cations in competitive environments.

Table 49: Binding energy for inner- and outer-sphere complexation of Sr(II), La(III), and Th(IV) aquocomplexes with the surface of a neutral GO nano-flake with a SW-defect. All values are in eV. Calculations carried out in the aqueous-phase.

Ion	PBE		PBE0	
	Inner	Outer	Inner	Outer
Sr(II)	-0.87	-1.32	-0.48	-1.10
La(III)	-1.16	-1.33	-0.74	-1.08
Th(IV)	-1.62	-1.25	-1.35	-1.00

A comparison between the calculated inner-sphere and outer-sphere complexation energies for each of the radionuclide analogues to the surface of the neutral GO nano-flake with a SW-defect (see Table 49) predicts that Sr(II) strongly prefers outer-sphere binding, in agreement with experimental results and other GO models presented in this research. The binding energies calculated for La(III) predict a preference towards outer-sphere binding, and Th(IV) is predicted to form inner-sphere complexes, consistent with experimental results and calculations carried out for the pristine GO model.

5.4.1.3.2 Edge Binding

The binding of the radionuclide analogues to the COOH group at the edge of the neutral SW-defected GO flake was also investigated. The binding energies for inner-sphere complexation with the edge of the neutral defect-free and SW-defected GO flakes, calculated using equations (5.1) are presented in Table 50.

Table 50: Binding energies for inner-sphere complexation of Sr(II), La(III), and Th(IV) aquocomplexes with edge of defect-free (Pristine) and SW-defected neutral GO nano-flakes. All values are in eV. Calculations carried out in the aqueous-phase.

Ion	PBE		PBE0	
	Pristine	Defected	Pristine	Defected
Sr(II)	-0.54	-0.52	-0.42	-0.41
La(III)	-0.38	-0.44	-0.31	-0.29
Th(IV)	-0.07	-0.15	0.10	0.03

Calculated binding energies again suggest there is an inverse correlation between formal charge and binding energy, as in calculations for inner-sphere complexation with the edge of the defect-free and vacancy-defected GO nano-flakes. Inner-sphere complexation is also again by the formation of a single M-O_{COOH} bond and a H-bond. The M-O_{COOH} bonds are calculated to be 2.522 Å, 2.537 Å, and 2.332 Å for Sr(II), La(III), and Th(IV), respective, which are consistent with the bonds which formed with the edge of the other GO nano-flakes. The binding energies are also in agreement with those calculated at the edge of the other GO flake models. Th(IV) is predicted to have a much lower affinity to the edge of the neutral flake than La(III) and Sr(II). The defect-free GO flake model is therefore suitable for modelling edge binding interactions to neutral SW-defected GO flakes.

Table 51: Binding energies for outer-sphere complexation of Sr(II), La(III), and Th(IV) aquocomplexes with edge of defect-free (Pristine) and SW-defected neutral GO nano-flakes. All values are in eV. Calculations carried out in the aqueous-phase.

Ion	PBE		PBE0	
	Pristine	Defected	Pristine	Defected
Sr(II)	-0.71	-0.76	-0.58	-0.62
La(III)	-0.69	-0.69	-0.56	-0.56
Th(IV)	-0.54	-0.51	-0.37	-0.36

The binding energies calculated for outer-sphere binding to the edge of the defect-free and SW-defected neutral GO nano-flake are presented in Table 51. Binding energies calculated for interaction with the edge of defected GO are in very close agreement

with those calculated for the idealised system. The binding energies for Sr(II) and La(III) are within 0.1 eV of one another. The calculated binding energy of Th(IV) is again around 0.2 eV smaller than that calculated for Sr(II) and La(III), this is again commensurate with an elongation of one of the O-H bonds in a water molecule interacting with the GO edge.

5.4.2 Anionic GO Nano-Flakes

The analysis of binding interaction between the radionuclide analogues and the surface and edge of anionic defected GO nano-flakes which include the carboxylate (COO^-) functional group at the edge was also carried out. Many of the results and trends which emerge from calculations carried out on the surface of the anionic GO surface are consistent with those from calculations on the neutral GO surface, so the data is presented here, but the trends are not explicitly discussed again. The binding interaction with the anionic COO^- group on the GO edge, as was shown in Chapter 4, are significantly different than the interactions with the edge of the neutral GO flake, they are therefore the main focus of the discussion in this section. The anionic defected GO nano-flakes have the same surface structure as the neutral defected GO flakes in Section 5.4.1.

5.4.2.1 Vacancy Defects

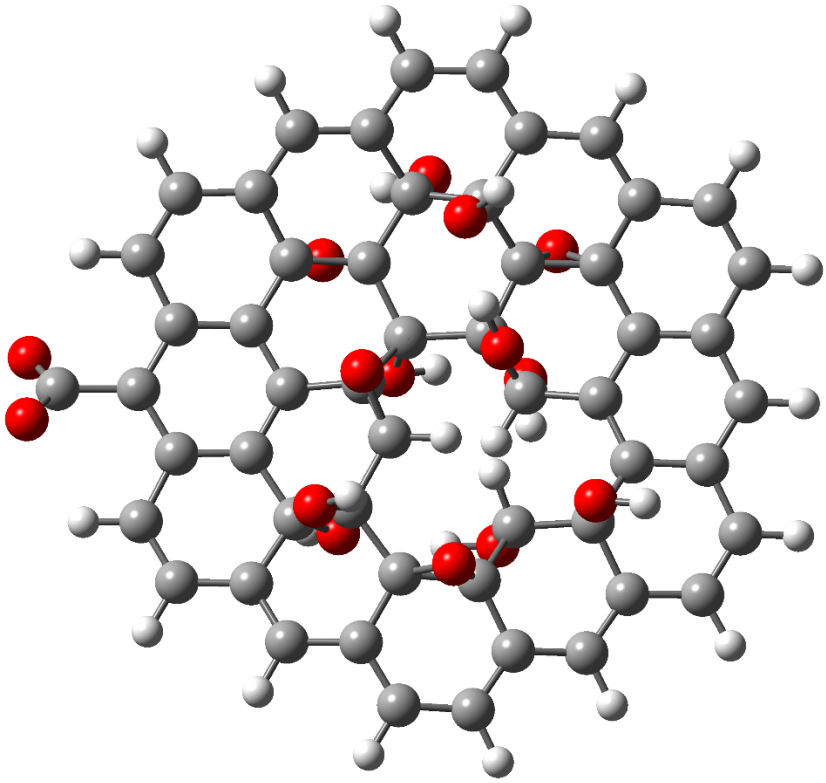

Figure 55: Anionic GO nano-flakes with a single vacancy defect incorporating both hydroxyl and epoxy groups at the 50% level of surface oxidation. Optimised at the PBE/SVP level of theory.

5.4.2.1.1 Surface Binding

The binding energies calculated for inner-sphere surface complexation of the ions with the surface of the defect-free and vacancy-defected anionic GO nano-flakes are presented in Table 52. Inner-sphere complexation energies were calculated using the method outlined in Section 4.3.4.2 and the following formula:

$$E_b = E_{[GO+R]^{(m-1)+}} - E_{[GO]^-} - E_{[R]^{m+}} + E_{(H_2O)_x} \quad \textbf{(5.3)}$$

Where $E_{[GO+R]^{(m-1)+}}$ is the energy of the interacting system, $E_{[GO]^-}$ is the energy of the defected anionic GO nano-flake, $E_{[R]^{m+}}$ is the energy of the radionuclide aquocomplex, and $E_{(H_2O)_x}$ is the energy of the water molecules eliminated from the aquocomplex solvation shell during complexation, obtained from equation (4.1).

A clear correlation emerges between the formal charge of the radionuclide and the binding energy for inner-sphere complexation to the surface of the vacancy-defected anionic GO nano-flake, in agreement with calculations for the defect-free GO surface. The binding energies calculated for the complexation of La(III) and Th(IV) predict they are 0.35-0.45 eV less stable for inner-sphere binding in the presence of a vacancy defect, whilst Sr(II) is predicted to have little or no sensitive to the present of the vacancy defect, which is consistent with the binding energies calculated for complexation with the surface of the neutral vacancy-defected flake.

Table 52: Binding energies for inner-sphere complexation of Sr(II), La(III), and Th(IV) aquocomplexes with surface of defect-free (Pristine) and single vacancy defected anionic GO nano-flakes. All values are in eV. Calculations carried out in the aqueous-phase.

Ion	PBE		PBE0	
	Pristine	Defected	Pristine	Defected
Sr(II)	-0.68	-0.63	-0.49	-0.45
La(III)	-1.45	-1.06	-1.01	-0.57
Th(IV)	-2.01	-1.64	-1.60	-1.17

The outer-sphere complexation between the surface of the vacancy-defected anionic GO flake and the ion complexes was also investigated. The calculated binding energies were calculated using the method outlined in Section 4.3.4.3 and the following formula:

$$E_b = E_{[GO+R]^{[m-1]+}} - E_{[GO+(H_2O)_x]^-} - E_{[R]^{m+}} + E_{(H_2O)_x} \quad \textbf{(5.4)}$$

Where $E_{[GO+R]^{[m-1]+}}$ is the energy of the interacting system, $E_{[GO+(H_2O)_x]^-}$ is the energy of the defected anionic GO nano-flake and interacting water molecules, $E_{[R]^{m+}}$ is the energy of the radionuclide aquocomplex, and $E_{(H_2O)_x}$ is the energy of the water molecules displaced during complexation, , obtained from equation (4.1).

Outer-sphere binding energies calculated using PBE predict there is no correlation between the formal charge of the radionuclide and binding energy, albeit the binding energy for Sr(II) is predicted to be about half that of La(III) and Th(IV), and also

around half that calculated for binding to the pristine GO surface. The significant reduction in the outer-sphere binding energy of Sr(II) in the presence of the vacancy defect was also predicted from calculations for outer-sphere binding to the surface of the neutral vacancy-defected flake. Calculations carried out using PBE0 predict an increase in binding energy with increased charge, consistent with results from the neutral vacancy-defected flake. The inverse correlation between binding energy and formal charge was also predicted from calculations for outer-sphere binding to the defect-free GO surface.

Table 53: Binding energies for outer-sphere complexation of Sr(II), La(III), and Th(IV) aquocomplexes with surface of defect-free (Pristine) and single vacancy defected anionic GO nano-flakes. All values are in eV. Calculations carried out in the aqueous-phase.

Ion	PBE		PBE0	
	Pristine	Defected	Pristine	Defected
Sr(II)	-0.94	-0.53	-1.03	-0.43
La(III)	-1.18	-1.04	-0.96	-0.79
Th(IV)	-1.09	-1.01	-0.84	-1.04

Binding energies calculated using PBE from Table 52 and Table 53 predict that Sr(II) and La(III) form both inner-sphere and outer-sphere complexes with the defected GO surface, whilst Th(IV) is predicted to most readily form inner-sphere complexes. Binding energies calculated at the PBE0 level of theory however, predicts La(III) most readily forms outer-sphere complexes. PBE0 calculations for complexation with the neutral vacancy defected surface (see Section 5.4.1.1.1) predicted no binding preference for Th(IV), due to an unusually high binding energy calculated with the hybrid functional. Calculations presented here also predict an usually high binding energy for outer-sphere complexation of Th(IV) with the defected surface. Inner-sphere complexation is however, predicted to be the preferred method for binding of Th(IV) to the vacancy defected surface, albeit the inner-sphere and outer-sphere calculated binding energies are much closer to one another than in calculations carried out with PBE.

5.4.2.1.2 Edge Binding

The binding of radionuclides to the COO^- group on the edge of the anionic vacancy-defected GO nano-flake was also investigated. Binding energies calculated using equation (5.3) for the inner-sphere complexation of the radionuclides ions with the edge of the defect-free and vacancy-defected anionic GO flake are presented in Table 54.

Table 54: Binding energies for inner-sphere complexation of Sr(II), La(III), and Th(IV) aquocomplexes with edge of defect-free (Pristine) and single vacancy defected anionic GO nano-flakes. All values are in eV. Calculations carried out in the aqueous-phase.

Ion	PBE		PBE0	
	Pristine	Defected	Pristine	Defected
Sr(II)	-1.05	-1.16	-0.91	-0.99
La(III)	-1.26	-1.36	-1.09	-1.16
Th(IV)	-1.48	-1.68	-1.30	-1.47

Inner-sphere complexation with the edge of the anionic vacancy-defected GO nano-flake is by the formation of 2 M-O_{COO^-} bonds. The M-O_{COO^-} bonds are calculated to have average lengths of 2.559 Å, 2.558 Å, and 2.423 Å for Sr(II), La(III), and Th(IV), respectively, which are in close agreement with the M-O_{COO^-} bond calculated to the edge of the anionic defect-free GO nano-flake, which had calculated average bond lengths of 2.575 Å, 2.561 Å, and 2.407 Å, respectively. The binding energies calculated for inner-sphere complexation with the edge of the anionic vacancy-defected GO flake predict a clear correlation between formal charge and binding energy, which is also present in calculations for binding to the edge of the defect-free flake. Th(IV) is predicted to be more stable on the edge of the defected GO nano-flake than the defect-free flake, an increase in binding energy was also predicted for binding to the edge of the vacancy defected neutral nano-flake. Binding energies calculated for Sr(II) and La(III) also predict an increase in stability, albeit is it less pronounced than the increase in stability predicted for Th(IV). The binding energies calculated using PBE0 are smaller than those calculated using PBE, as found throughout this research.

Table 55: Binding energies for outer-sphere complexation of Sr(II), La(III), and Th(IV) aquocomplexes with edge of defect-free (Pristine) and single vacancy defected anionic GO nano-flakes. All values are in eV. Calculations carried out in the aqueous-phase.

Ion	PBE		PBE0	
	Pristine	Defected	Pristine	Defected
Sr(II)	-1.48	-1.49	-1.29	-1.29
La(III)	-1.60	-1.62	-1.37	-1.38
Th(IV)	-2.01	-2.03	-1.76	-1.78

Binding energies for the outer-sphere complexation of the radionuclide analogues with the edge of the defect-free and vacancy-defected anionic GO nano-flakes calculated using equation (5.4) are presented in Table 55. The calculated binding energies for complexation with the edge of both the idealised and defected GO nano-flakes predict that the stability of the radionuclide increases with formal charge. The calculated binding energies also show that outer-sphere binding to the edge of anionic GO is insensitive to the presence of a vacancy-defect on the GO surface. The idealised GO model is therefore well suited for predicting the binding interactions with the edge of a vacancy-defected GO nano-flake. All calculated binding energies for complexation with the edge of the defect-free nano-flake are within 0.02 eV of those calculated for binding to the edge of the vacancy-defected flake, which is negligible.

Table 56: Binding energy for inner- and outer-sphere complexation of Sr(II), La(III), and Th(IV) aquocomplexes with the edge of an anionic GO nano-flake with a single vacancy defect. All values are in eV. Calculations carried out in the aqueous-phase.

Ion	PBE		PBE0	
	Inner	Outer	Inner	Outer
Sr(II)	-1.16	-1.49	-0.99	-1.29
La(III)	-1.36	-1.62	-1.16	-1.38
Th(IV)	-1.68	-2.03	-1.47	-1.78

A comparison of the calculated binding energies for inner-sphere and outer-sphere complexations with the edge of the vacancy defected anionic GO flake (see Table 56) predicts that the formation of outer-sphere complexes is preferred by all cations. This

is surprising, it was discussed in Chapter 4 that experimental results report the formation of inner-sphere complexes between trivalent and tetravalent radionuclides and GO across a large pH range. Divalent radionuclides are also known from experimental results[145–147] to form inner-sphere complexes with GO at pH > 6, when significant anionic charge has accumulated on the flake, albeit that is probably more than the single unit of negative charge in the anionic model presented here. It has also been reported[186] from spectral analysis of Pb(II) and GO before and after complexation that binding occurs mostly with carboxylate groups.

5.4.2.2 Pore Defects

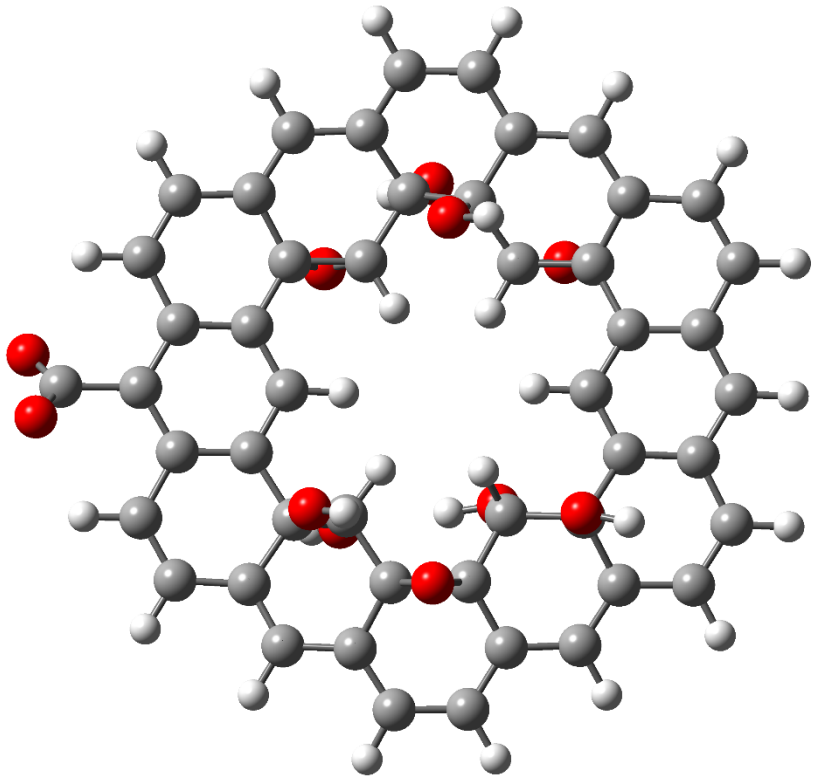

Figure 56: Anionic GO nano-flakes with a pore defect incorporating both hydroxyl and epoxy groups at the 50% level of surface oxidation. Optimised at the PBE/SVP level of theory.

5.4.2.2.1 Surface Binding

The binding energies calculated for the inner-sphere complexation of the ions with the surface of defect-free and pore-defected anionic GO nano-flakes are presented in Table 57. Complexation with the surface of the anionic pore-defected GO nano-flake is again by the formation of only two M-O_{GO} bonds with functional groups on the GO surface, one fewer than a formed with the defect-free surface. Sr(II) forms M-O_{GO} bonds with an epoxy and an OH groups, and H-bonds form with functional groups on the GO surface. La(III) and Th(IV) both modify the chemical structure of the GO surface to form M-O_{GO} bonds with a carbonyl group and an OH groups, and 2 H-bonds with surface functional groups. The bond lengths are consistent with those calculated to the surface of the neutral pore-defected GO nano-flake. The calculated binding energies are also consistent with those calculated to the defect-free anionic GO nano-flake surface, despite the formation of fewer M-O_{GO} bonds.

Binding energies calculated for La(III) and Th(IV) predict they are more stable on the surface of the anionic than neutral pore defected nano-flake. The increased stability on the surface of the anionic nano-flake is also present in calculations for binding to the surface of the idealised GO flake. NBO charge analysis presented in Chapter 4 suggested this may be due to the displacement of anionic charge from the edge of the GO flake to functional groups on the modified surface, which also the most likely cause for the increase in binding energy.

Table 57: Binding energies for inner-sphere complexation of Sr(II), La(III), and Th(IV) aquocomplexes with surface of defect-free (Pristine) and pore-defected anionic GO nano-flakes. All values are in eV. Calculations carried out in the aqueous-phase.

Ion	PBE		PBE0	
	Pristine	Defected	Pristine	Defected
Sr(II)	-0.68	-0.74	-0.49	-0.51
La(III)	-1.45	-1.35	-1.01	-0.96
Th(IV)	-2.01	-1.98	-1.60	-1.60

Binding energies calculated for the formation of outer-sphere complexes between the radionuclide analogues and the surface of the anionic pore-defected GO nano-flake are

presented in Table 58. Binding energies are consistent with those calculated for outer-sphere complexation with the surface of the neutral defected GO nano-flake.

The binding energy calculated for Th(IV) is again significantly greater than that calculated for outer-sphere binding to the surface of the defect-free GO nano-flake, and also significantly greater than those calculated for Sr(II) and La(III). Analysis of the Th(IV) sorption geometry (see Figure 57) reveals that hydrolysis of the Th(IV) complex has again occurred. The resulting complex is however different than in the outer-sphere complex of Th(IV) with the neutral pore defected GO nano-flake. Complexation between the Th(IV) aquocomplex and the surface of the neutral pore-defected flake involved the elimination of a single proton from a water molecule in the Th(IV) solvation shell, resulting in the formation of the $[Th(OH)(H_2O)_8]^{3+}$ solvated thorium complex, interacting with a pore defected GO surface which is modified to include a OH group formed by protonation of an epoxy group. Analysis of the outer-sphere surface complex formed with the anionic pore defected GO nano-flake, however, reveals a geometry in which the Th(IV) complex has migrated on the GO surface to the periphery of the pore defect and undergone hydrolysis by elimination of two protons from a single water molecule in the Th(IV) solvation shell. This results in the formation a $[Th(O)(H_2O)_8]^{2+}$ complex coordinated to a defected GO nano-flake surface whose surface chemistry has been modified to incorporate two additional OH groups from protonation of two epoxy groups.

Table 58: Binding energies for outer-sphere complexation of Sr(II), La(III), and Th(IV) aquocomplexes with surface of defect-free (Pristine) and pore-defected anionic GO nano-flakes. All values are in eV. Calculations carried out in the aqueous-phase.

Ion	PBE		PBE0	
	Pristine	Defected	Pristine	Defected
Sr(II)	-0.94	-1.20	-1.03	-0.98
La(III)	-1.18	-1.30	-0.96	-0.92
Th(IV)	-1.09	-2.41	-0.84	-1.83

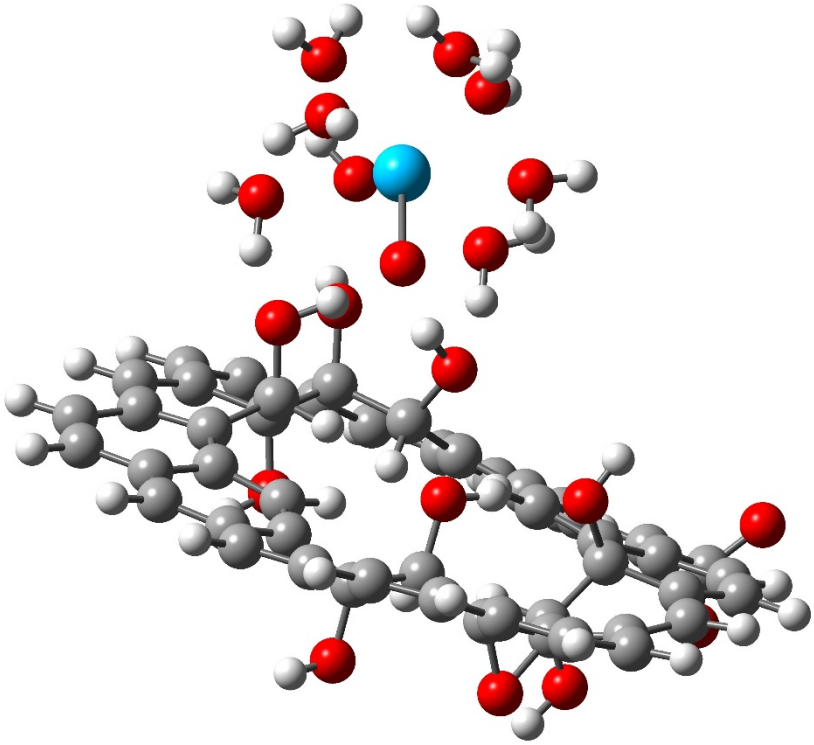

Figure 57: Outer-sphere binding of the Th(IV) aquocomplex with the surface of the anionic GO nano-flake with a pore defect. Optimised at the PBE/SVP level of theory. The Th-O bond highlights the location of the oxo-ligand

A comparison of the calculated binding energy for outer-sphere complexation of Th(IV) with the surface of the neutral (see Table 43) and anionic (see Table 58) pore-defected GO nano-flakes, suggests there is no further increase in stability from elimination of a second proton to form the $[Th(O)(H_2O)_8]^{2+}$ solvated complex. Calculations carried out using PBE predict an increase in stability of the system of around 0.2 eV following elimination of the second proton from the solvation shell water molecule. Calculations carried out using PBE0 however predict no significant change in energy. There is little currently known about the stability of the functional groups in the vicinity of pore defects on GO nano-flake surfaces. This would be a useful avenue of further research for a greater understanding of the binding energies calculated here.

5.4.2.2.2 Edge Binding

The binding energies calculated using equation (5.3) for the inner-sphere complexation of the radionuclide analogues with the edge of the defect-free and pore-defected anionic GO nano-flakes are presented in Table 59.

Table 59: Binding energies for inner-sphere complexation of Sr(II), La(III), and Th(IV) aquocomplexes with edge of defect-free (Pristine) and pore-defected anionic GO nano-flakes. All values are in eV. Calculations carried out in the aqueous-phase.

Ion	PBE		PBE0	
	Pristine	Defected	Pristine	Defected
Sr(II)	-1.05	-1.04	-0.90	-0.90
La(III)	-1.26	-1.28	-1.09	-1.12
Th(IV)	-1.48	-1.59	-1.30	-1.41

The inner-sphere complexation with the COO^- group on the edge of the anionic pore-defected GO nano-flake is by the formation of 2 M-O_{COO^-} bonds which are calculated to have average bond lengths of 2.573 Å, 2.559 Å, and 2.423 Å for Sr(II), La(III), and Th(IV), respectively, which are in close agreement with the those calculated to the edge of the defect-free and vacancy-defected GO flakes. The calculated binding energies also predict a clear correlation between formal charge and binding energy, in agreement with calculations for complexation with the edge of the other GO flakes. Binding energies calculated using PBE0 are also smaller than those calculated using PBE, in agreement with other results.

Table 60: Binding energies for outer-sphere complexation of Sr(II), La(III), and Th(IV) aquocomplexes with edge of defect-free (Pristine) and pore-defected anionic GO nano-flakes. All values are in eV. Calculations carried out in the aqueous-phase.

Ion	PBE		PBE0	
	Pristine	Defected	Pristine	Defected
Sr(II)	-1.48	-1.46	-1.29	-1.27
La(III)	-1.60	-1.61	-1.37	-1.38
Th(IV)	-2.01	-1.97	-1.76	-1.74

Binding energies calculated for the outer-sphere complexation of the radionuclide analogues with the edge of the defect-free and pore-defected anionic GO nano-flake are also presented in Table 60. The calculated binding energies predict that the stability of the radionuclide increases with formal charge, as in calculations for outer-sphere binding to edge of the defect-free and vacancy-defected GO flakes. The binding

energies suggest that interactions with the edge of a pore defected GO nano-flake are modelled well by the defect-free GO nano-flake model. All calculated binding energies are within 0.1 eV of those calculated for binding to the edge of the other GO flakes, revealing outer-sphere edge binding to be insensitive to the presence of a vacancy defect on the GO surface.

5.4.2.3 Stone-Wales Defects

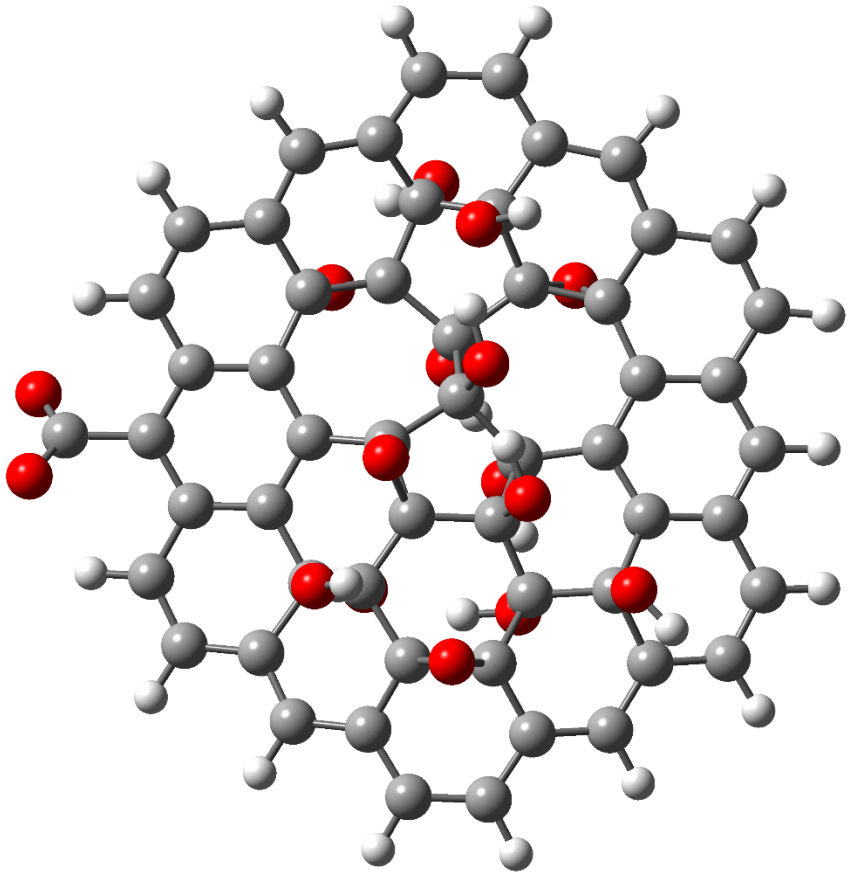

Figure 58: Anionic GO nano-flakes with a SW defect incorporating both hydroxyl and epoxy groups at the 50% level of surface oxidation. Optimised at the PBE/SVP level of theory.

5.4.2.3.1 Surface Binding

The binding energies for the inner-sphere complexation of the radionuclide analogues to the surface of the defect-free and SW-defected anionic GO nano-flakes are presented in Table 61. A comparison of the binding energies reveals the SW-defect is predicted

to have the same effect on inner-sphere binding to the anionic surface as it was predicted to have to the neutral surface (see Table 47). Calculations carried out using PBE predict that Sr(II) is stabilised on the GO surface by the SW defect, the increase in binding energy is however not predicted by calculations carried out using PBE0. The binding of La(III) and Th(IV) is predicted to be inhibited by the SW-defect by both *xc*-functionals.

Table 61: SW Binding energies for inner-sphere complexation of Sr(II), La(III), and Th(IV) aquocomplexes with surface of defect-free (Pristine) and SW-defected anionic GO nano-flakes. All values are in eV. Calculations carried out in the aqueous-phase.

Ion	PBE		PBE0	
	Pristine	Defected	Pristine	Defected
Sr(II)	-0.68	-0.98	-0.49	-0.58
La(III)	-1.45	-1.32	-1.01	-0.87
Th(IV)	-2.01	-1.82	-1.60	-1.40

Similarly to the binding interactions with the neutral SW-defected surface, the inner-sphere complexation of the Sr(II) aquocomplex to the surface of the anionic SW-defected GO nano-flakes results in the formation of two additional H-bonds and distortion of the Sr(II) solvation shell. The formation of additional H-bonds is again commensurate with an increase in binding energy in the PBE calculation. Additional H-bonds also form in the complexation geometries optimised using PBE0, where no increase in binding energy is predicted. This is again most presumably due to a greater effect of deformation of the GO flake on binding energies in calculations using PBE0 as established in Chapter 3. The formation of additional H-bonds is not observed in La(III) and Th(IV) inner-sphere complexation geometries with the SW-defected GO surface, although the SW-defected nano-flake is again less planar than the defect-free flake.

Table 62: Binding energies for outer-sphere complexation of Sr(II), La(III), and Th(IV) aquocomplexes with surface of defect-free (Pristine) and SW-defected anionic GO nano-flakes. All values are in eV. Calculations carried out in the aqueous-phase.

Ion	PBE		PBE0	
	Pristine	Defected	Pristine	Defected
Sr(II)	-0.94	-1.23	-1.03	-1.03
La(III)	-1.18	-1.23	-0.96	-1.01
Th(IV)	-1.09	-1.17	-0.84	-0.93

Binding energies calculated for the outer-sphere complexation of the radionuclide analogues with the surface of the defect-free and SW-defected anionic flakes using equation (5.4) are presented in Table 62. The binding energies calculated using PBE predict that the radionuclides are all stabilised at the SW defect, albeit the predicted increase in stability is less significant than that predicted from calculations of binding to the surface of the neutral SW-defected flake (see Table 48). Calculations carried out with PBE0 predict little to no increase in stability. The binding energies indicate that the radionuclides bind to the defected GO surface approximately equally and binding is insensitive to the formal charge, in agreement with calculation for outer-sphere complexation with the neutral surface.

5.4.2.3.2 Edge Binding

The binding energies calculated using equation (5.3) for the inner-sphere complexation of the radionuclide analogues with the edge of the defect-free and SW-defected anionic GO nano-flakes are presented in Table 63.

Table 63: Binding energies for inner-sphere complexation of Sr(II), La(III), and Th(IV) aquocomplexes with edge of defect-free (Pristine) and SW-defected anionic GO nano-flakes. All values are in eV. Calculations carried out in the aqueous-phase.

Ion	PBE		PBE0	
	Pristine	Defected	Pristine	Defected
Sr(II)	-1.05	-1.07	-0.91	-0.94
La(III)	-1.26	-1.25	-1.09	-1.10
Th(IV)	-1.48	-1.52	-1.30	-1.36

The inner-sphere complexation with the edge of the anionic SW-defected GO nano-flake is also by the formation of 2 M-O_{COO^-} bonds which are calculated to have average bond lengths of 2.562 Å, 2.562 Å, and 2.419 Å for Sr(II), La(III), and Th(IV), respectively, which are in close agreement with the those calculated to the edge of the defect-free, and other defected GO flakes. The calculated binding energies are also in very good agreement with those calculated for binding to the edge of other GO nano-flakes and predict a clear correlation between formal charge and binding energy. Binding energies calculated using PBE0 are also smaller than those calculated at the PBE level of theory, in agreement with other results.

Table 64: Binding energies for outer-sphere complexation of Sr(II), La(III), and Th(IV) aquocomplexes with edge of defect-free (Pristine) and SW-defected anionic GO nano-flakes. All values are in eV. Calculations carried out in the aqueous-phase.

Ion	PBE		PBE0	
	Pristine	Defected	Pristine	Defected
Sr(II)	-1.48	-1.48	-1.29	-1.29
La(III)	-1.60	-1.59	-1.37	-1.37
Th(IV)	-2.01	-1.96	-1.76	-1.73

Binding energies calculated for the outer-sphere complexation of the radionuclide analogues with the edge of the defect-free and SW-defected anionic GO nano-flakes are presented in Table 64. The calculated binding energies are also in very good agreement with those calculated for binding to the edge of the other GO nano-flakes and predict that the stability of the radionuclides increases with formal charge, as in calculations for outer-sphere binding to edge of the other GO flakes. The binding energies suggest that the defect-free GO model is suitable for understanding binding to the edge of a SW-defected GO nano-flake. All calculated binding energies are within 0.05 eV of those calculated for binding to the edge of the vacancy-defected and defect-free flakes, revealing outer-sphere edge binding is insensitive to the SW-defect on the flake surface.

5.5 Conclusion

The binding interactions between Sr(II), La(III), and Th(IV) aquocomplexes, and the surfaces and edges of GO nano-flakes with vacancies, pores and Stone-Wales defects has been investigated. The results from calculations were compared to those for binding to the surface and edge of defect-free GO nano-flakes presented in Chapter 4.

The presence of a vacancy defect in the GO surface is found in calculations presented here to inhibit the inner-sphere complexation of La(III) and Th(IV) with the surface but has little to no effect on the inner-sphere binding of Sr(II). Conversely, the defect is found to inhibit the outer-sphere binding of Sr(II) but has little to no effect on the outer-sphere binding of La(III) and Th(IV). It should be noted however that the dangling bonds created by the vacancy have been terminated here with hydrogen atoms for simplicity. It is likely in realistic environments that other moieties would occupy these positions on the GO surface. The stability of functional groups around defect sites and their effect on the binding of radionuclide complexes is an area which requires further investigation.

Inner-sphere complexation with the pore-defected GO surface involves the formation of fewer M-O_{GO} bonds than complexation with the defect-free surface but gives broadly similar binding energies. Outer-sphere binding of Th(IV) with the pore defected surface is however found to promote the hydrolysis of the Th(IV) aquocomplex which significantly contributes towards stability. It should be noted that the hydrolysis of Th(IV) and other polyvalent cations could occur much more frequently under non-idealised conditions, and is unlikely to occur only in the presence of the pore defect. It should be noted also that like the vacancy defect model, all dangle bonds in the pore are saturated with hydrogen atoms in the models presented here, it is likely that other functional groups will form here, which could significantly affect the binding interactions between radionuclides and the GO surface. This is something which also requires further investigation.

Binding to the SW-defected GO surface by inner-sphere complexation is broadly the same as complexation with the defect-free surface. Outer-sphere binding is however,

more stable on the SW-defected surface, which may be due to greater spatial density of oxygen groups on the 5-membered carbon ring.

The binding to the surface of the neutral and anionic defected GO nano-flakes is broadly the same, suggesting that the majority of the anionic charge is localised on the flake edge. Complexation with the nano-flake edge is also largely insensitive to the presence of defects on the surface, although there is a small stabilisation of inner-sphere binding to the flake edge which may be due to greater lateral flexibility in the defected flakes.

The results do not reveal a possible route towards cation selectivity based on the introduction of defects into the GO lattice. Binding to the surface of all GO nano-flakes is dominated mostly by electrostatic interactions so Th(IV) binds most preferably, likewise electrostatic interactions are also dominant for binding to the edge of the anionic GO flakes. A potential route towards the selective extraction of divalent and trivalent radionuclides is however identified again in GO with a low density of surface functional groups and high degree of edge oxidation, due to the low affinity of the Th(IV) aquocomplex to the edge of the neutral GO nano-flakes.

Chapter 6 General Conclusions and Future Work

Graphene oxide (GO) has been shown under laboratory conditions to be a highly effective and potentially versatile sorbent material for the removal of a wide range of radionuclides and heavy metals from contaminated aqueous environments. It is effective for the removal of cations over a wide pH range and in the presence of competing ions. It is however useful for the removal of anions such as Tc(VII), which exists mostly as the pertechnetate anion (ThO_4^-) only at extremely low pH, due to the accumulation of anionic change on GO at pH > 2. It has a large surface area and a lack of internal surfaces making it highly efficient and giving it fast sorption kinetics. It can be produced on an industrial scale using readily available laboratory equipment and chemicals and consists of only CHON (carbon, hydrogen, oxygen and nitrogen) chemicals meaning it has little environmental impact and can be incinerated, reducing the production of secondary waste. Sorption and desorption experiments have also indicated that it may be reusable. The research presented in this thesis has been a computational study to better understand the binding interaction between radionuclides and the surface and edge of GO to encourage its development as sorption materials for use in nuclear decommissioning.

A model for graphene oxide based on the widely accepted Lerf-Klinowski model was developed using DFT in Chapter 3. The development of the model revealed an insensitivity to the lateral size of the nano-flake for functional group stability on the surface at high level of oxidation, which had not been reported previously. It was also found from calculations that the formation of epoxy groups is unlikely at low levels of surface oxidation and functional groups tend to aggregate on GO surfaces, which is consistent with experimental observations.

In Chapter 4, the GO model developed in the proceeding chapter was used to understand the mechanisms of binding interactions with GO surfaces and edges. The results from DFT calculations were broadly similar to experimental results and those from other theoretical studies. The binding of cations to GO it was found, is due mainly to electrostatic interactions so highly charged cations (or anions at extremely low pH) are absorbed most efficiently by GO. A potential route towards cation separation was identified at extremely low pH ≈ 2 using GO which has been chemically

modified to reduce the degree of surface oxidation and increase the degree of edge oxidation, due to an extremely low affinity of Th(IV) (and potentially other actinides) towards the neutral carboxylic acid group. It is noted however that the GO model used in the calculations is highly idealised, particularly there is only a lone functional group on the GO flake edge, and hydroxyl and carbonyl groups, which are thought to occur along GO flake edges are not considered. Further computational and experimental studies are therefore required to verify this observation.

In Chapter 5 an investigation into the effect of single vacancies, pores and Stone-Wales (SW) defects on the sorption capacity of GO was presented. It was found that the occurrence of defects on the GO surface has little to no effect on binding to the flake edge. It was found also that the binding interactions with defected surfaces considered are broadly similar to those with the surface of defect-free GO. The results from calculations presented in Chapter 5 do not identify a likely route towards radionuclide selectivity based on the introduction of defects, nor do they suggest that the sorption capacity of GO will be significantly increased or reduced with the accumulation of defects in the surfaces.

The results from sorption investigations presented in this thesis however, should be treated with caution, particularly those in Chapter 5. The GO flake models used are highly simplified, albeit less simplistic than many of those found elsewhere in the open literature. The termination of all dangling bonds left behind by the creation of vacancies in the GO lattice, for example, is by the addition of hydrogen atoms, in real-world conditions other chemical species are likely to form in these positions. Likewise, the solvation shell of the radionuclide complexes consist of only water molecules, in real-world conditions a wide range of ligands can form the solvation shell. It is shown in Chapter 5 that the occurrence of even a single hydroxyl group in the solvation shell of Th(IV) has a profound effect on its binding with the pore-defected GO surface. Solvation shells are also known to change in varying environments, for example, Pb(II) is known to form $Pb(OH)^{+}$, $Pb(OH)_2^{0}$, and $Pb(OH)_3^{-}$ complexes at various pHs, which could significantly affect its affinity towards GO. The consideration of solvation shells consisting of different ligands could therefore also be useful as an indirect route to quantifying pH effects.

Results presented in this thesis, and both experiment and computational studies found elsewhere show GO to have great potential as a sorbent material. The next phase of research, it is suggested, should take the form of both further computational studies and an industrial scale investigation. Sufficient confidence in the potential of GO, particularly that obtained from laboratory based experimental research, should now exist to warrant investment in large-scale investigations. There are however, also several areas of outstanding knowledge which would be best obtained by further computational studies. These include verifying the results obtained in Chapter 4 with additional radionuclides and extending results obtained in Chapter 5 by termination of dangling bonds arising from the introduction of defects with more realistic moieties. Investigations should also be carried out into the effect of different ligands in the radionuclide solvation shell, which can also be used to indirectly investigate the binding interactions in different pH environments. Greater understanding of the mechanisms involved in GO coagulations when introduced to radionuclide contaminated water should also be sought, potentially through the use of molecular dynamics (MD) simulations.

From the results and discussion presented in this thesis, it is suggested that the binding and aggregation of GO with cations could make it directly useful in storage ponds, tanks and wet silo as a scavenger. It could also potentially be used within current methods and apparatus as a direct substitution for existing sorbent materials, or to complement other sorbent materials such as TiO_2 or activated carbon. It could also be integrated into semi permeable membranes and barriers for the remediation of contaminated groundwater and plumes.

References

1. Romanchuk, A. Y., Slesarev, A. S., Kalmykov, S. N., Kosynkin, D. V & Tour, J. M. Graphene oxide for effective radionuclide removal. *Phys. Chem. Chem. Phys.* **15**, 2321–7 (2013).

2. Chiba, S. *et al.* Method to Reduce Long-lived Fission Products by Nuclear Transmutations with Fast Spectrum Reactors. *Sci. Rep.* **7**, 1–10 (2017).

3. Hastings, J. J., Rhodes, D., Fellerman, A. S., Mckendrick, D. & Dixon, C. New approaches for sludge management in the nuclear industry. *Powder Technol.* **174**, 18–24 (2007).

4. Sohlenius, G., Saetre, P., Norde, S., Grolander, S. & Sheppard, S. Inferences About Radionuclide Mobility in Soils Based on the Solid / Liquid Partition Coefficients and Soil Properties. *Ambio* **42**, 414–424 (2013).

5. Dreyer, D. R., Park, S., Bielawski, C. W. & Ruoff, R. S. The chemistry of graphene oxide. *Chem. Soc. Rev.* **39**, 228–40 (2010).

6. Chen, J., Yao, B., Li, C. & Shi, G. An improved Hummers method for eco-friendly synthesis of graphene oxide. *Carbon N. Y.* **64**, 225–229 (2013).

7. Tang, L. *et al.* Bottom-up synthesis of large-scale graphene oxide nanosheets. *J. Mater. Chem.* **22**, 5676 (2012).

8. Lerf, A., He, H., Forster, M. & Klinowski, J. Structure of Graphite Oxide Revisited. *J. Phys. Chem. B* **102**, 4477–4482 (1998).

9. The Nuclear Decommissioning Authority. *Taking forward decommissioning*. (2008).

10. Gabaldón, C., Marzal, P., Ferrer, J. & Seco, A. Single and competitive adsorption of Cd and Zn onto a granular activated carbon. *Water Res.* **30**, 3050–3060 (1996).

11. Omar, H., Arida, H. & Daifullah, A. Adsorption of 60Co radionuclides from aqueous solution by raw and modified bentonite. *Appl. Clay Sci.* **44**, 21–26 (2009).

12. Sheng, G. *et al.* Enhanced removal of uranium(VI) by nanoscale zerovalent iron supported on na-bentonite and an investigation of mechanism. *J. Phys. Chem. A* **118**, 2952–2958 (2014).

13. Brings, B. Use of modern ion exchange resins for removing radionuclides using a German PWR reactor as an example. *Therm. Eng.* **57**, 538–542 (2010).

14. Montaña, M. *et al.* Removal of radionuclides in drinking water by membrane treatment using ultrafiltration, reverse osmosis and electrodialysis reversal. *J. Environ. Radioact.* **125**, 86–92 (2013).

15. Ding, C., Cheng, W., Sun, Y. & Wang, X. Novel fungus-Fe3O4 bio-nanocomposites as high performance adsorbents for the removal of radionuclides. *J. Hazard. Mater.* **295**, 127–137 (2015).

16. Pehlivan, E., Altun, T., Cetin, S. & Iqbal Bhanger, M. Lead sorption by waste biomass of hazelnut and almond shell. *J. Hazard. Mater.* **167**, 1203–1208 (2009).

17. TEPCO. Multi-nuclide Removal Equipment (ALPS) Confirmatory Testing, Installation and Characteristics of Radioactive Waste. https://www7.tepco.co.jp/wp-content/uploads/hd03-02-03-001-m120625_01-e.pdf (2012).

18. Staudenmaier, L. Verfahren zur Darstellung der Graphitsaure. *Ber. Dtsch. Chem. Ges.* **31**, 1481–1487 (1898).

19. Brodie, B. C. On the Atomic Weight of Graphite. *Philos. Trans. R. Soc. London* **149**, 249–259 (1859).

20. He, H., Klinowski, J., Forster, M. & Lerf, A. A new structural model for graphite

oxide. *Chem. Phys. Lett.* **287**, 53–56 (1998).

21. William S. Hummers, J. & Offeman, R. E. Preparation of Graphitic Oxide. *J. Am. Chem. Soc* **80**, 1339 (1958).

22. Marcano, D. C. *et al.* Improved Synthesis of Graphene Oxide. *ACS Nano* **4**, 4806–4814 (2010).

23. Schafhaeutl, C. LXXXVI. On the combinations of carbon with silicon and iron, and other metals, forming the different species of cast iron, steel, and malleable iron. *Philos. Mag.* **16**, 570–590 (1840).

24. Hofmann, U., Frenzel, A. & Csalan, E. Die Konstitution der Graphitsaure und ihre Reaktionen. *Ann. der Chemie* **510**, 1–41 (1934).

25. Hofmann, U. & König, E. Untersuchungen über Graphitoxyd. *Zeitschrift für Anorg. und Allg. Chemie* **80**, 1- (1937).

26. Hofmann, U. & Holst, R. Über die Säurenatur und die Methylierung von Graphitoxyd. *Berichte der Dtsch. Chem. Gesellschaft* **72**, 754–771 (1939).

27. Thiele, H. Uber Salzbildung und Basenaustausch der Graphitsaure. *Kolloid-Zeitschrift* **145**, 1–20 (1937).

28. Ruess, G. Uber das Graphitoxyhydroxyd (Graphitoxyd). *Monatshefte fur Chemie* **76**, 381–417 (1946).

29. Ruff, O. & Bretschneider, O. Die Reaktionsprodukte der verschiedenen Kohlenstoffformen mit Fluor II (Kohlenstoff-monofluorid). *Zeitschrift fur Anorg. und Allg. Chemie* **217**, 1–18 (1934).

30. Cooper, D. R. *et al.* Experimental Review of Graphene. *ISRN Condens. Matter Phys.* **2012**, 1–56 (2012).

31. Scholz, W. & Boehm, H. P. Betrachtungen zur Struktur des Graphitoxids.

Zeitschrift für Anorg. und Allg. Chemie **369**, 327–340 (1969).

32. Hadži, D. & Novak, A. Infra-red spectra of graphitic oxide. *Trans. Faraday Soc.* **51**, 1614–1620 (1955).

33. Nakajima, T., Mabuchi, A. & Hagiwara, R. A new structure model of graphite oxide. *Carbon N. Y.* **26**, 357–361 (1988).

34. Nakajima, T. & Matsuo, Y. Formation process and structure of graphite oxide. *Carbon N. Y.* **32**, 469–475 (1994).

35. Kita, Y., Watanabe, N. & Fujii, Y. Chemical Composition and Crystal Structure of Graphite Fluoride. *J. Am. Chem. Soc.* **101**, 3832–3841 (1979).

36. Touhara, H., Kadono, K., Fujii, Y. & Watanabe, N. On the Structure of Graphite Fluoride. *ZAAC - J. Inorg. Gen. Chem.* **544**, 7–20 (1987).

37. Mermoux, M., Chabre, Y. & Rousseau, A. FTIR and 13C NMR study of graphite oxide. *Carbon N. Y.* **29**, 469–474 (1991).

38. Lerf, A., He, H., Riedl, T., Forster, M. & Klinowski, J. 13C and 1H MAS NMR studies of graphite oxide and its chemically modified derivatives. *Solid State Ionics* **101**–**103**, 857–862 (1997).

39. Dimiev, A. M., Alemany, L. B. & Tour, J. M. Graphene oxide. Origin of acidity, its instability in water, and a new dynamic structural model. *ACS Nano* **7**, 576–588 (2013).

40. Szabó, T. *et al.* Evolution of surface functional groups in a series of progressively oxidized graphite oxides. *Chem. Mater.* **18**, 2740–2749 (2006).

41. Szabó, T., Berkesi, O. & Dékány, I. DRIFT study of deuterium-exchanged graphite oxide. *Carbon N. Y.* **43**, 3186–3189 (2005).

42. Mkhoyan, K. A. *et al.* Atomic and electronic structure of graphene-oxide. *Nano*

Lett. **9**, 1058–1063 (2009).

43. Stobinski, L. *et al.* Graphene oxide and reduced graphene oxide studied by the XRD, TEM and electron spectroscopy methods. *J. Electron Spectros. Relat. Phenomena* **195**, 145–154 (2014).

44. Pimenta, M. A. *et al.* Studying disorder in graphite-based systems by Raman spectroscopy. *Phys. Chem. Chem. Phys.* **9**, 1276–1290 (2007).

45. Wilson, N. R. *et al.* Graphene oxide: structural analysis and application as a highly transparent support for electron microscopy. *ACS Nano* **3**, 2547–2556 (2009).

46. Gómez-Navarro, C. *et al.* Electronic transport properties of individual chemically reduced graphene oxide sheets. *Nano Lett.* **7**, 3499–3503 (2007).

47. Zhengtang, L., Lu, Y., Somers, L. & Johnson, C. High Yield Preparation of Macroscopic Graphene Oxide Membranes High Yield Preparation of Macroscopic Graphene Oxide Membranes. *J. Am. Chem. Soc* **131**, 898–899 (2009).

48. Dave, S. H., Gong, C., Robertson, A. W., Warner, J. H. & Grossman, J. C. Chemistry and Structure of Graphene Oxide via Direct Imaging. *ACS Nano* **10**, 7515–7522 (2016).

49. Gómez-Navarro, C. *et al.* Atomic structure of reduced graphene oxide. *Nano Lett.* **10**, 1144–1148 (2010).

50. Liu, Z. *et al.* Direct observation of oxygen configuration on individual graphene oxide sheets. *Carbon N. Y.* **127**, 141–148 (2018).

51. Dimiev, A. M. & Polson, T. A. Contesting the two-component structural model of graphene oxide and reexamining the chemistry of graphene oxide in basic media. *Carbon N. Y.* **93**, 544–554 (2015).

52. Wilson, N. R. *et al.* Graphene oxide: structural analysis and application as a highly transparent support for electron microscopy. *ACS Nano* **3**, 2547–56 (2009).

53. Malard, L. M., Pimenta, M. A., Dresselhaus, G. & Dresselhaus, M. S. Raman spectroscopy in graphene. *Phys. Rep.* **473**, 51–87 (2009).

54. Hanninen, V. Lecture 5. Basis functions. *Introduction to Computational Chemistry* 1–24 http://www.helsinki.fi/kemia/fysikaalinen/opetus/jlk/luennot/Lecture5.pdf (2012).

55. Ouellete, R. & Rawn, D. 1 - Structure and Bonding in Organic Compounds. in *Organic Chemistry Study Guide* 1–16 (2015).

56. Magnasco, V. Chapter 12 - Atomic orbitals. in *Elementary Molecular Quantum Mechanics (Second Edition)* 467–481 (2013).

57. Slater, J. C. Atomic shielding constants. *Phys. Rev.* **36**, 57–64 (1930).

58. Boys, S. F. A General Method of Calculation for the Stationary States of Any Molecular System. *Proc. R. Soc. Lond. A. Math. Phys. Sci.* **200**, 542–554 (1950).

59. Hoggan, P. E. Molecular Integrals over Slater-type Orbitals . From pioneers to recent progress. *Quantum Front. Atoms Mol. Physics, Chem. Biol.* 63–90 (2010).

60. Szabo, A. & Ostlund, N. *Modern Quantum Chemistry: Introduction to Advanced Electronic Structure Theory*. (1996).

61. Faegri, K. & Speis, H. J. Basis set quality vs size. Approximate Gaussian-type orbital (GTO) wave functions for first row transition metal atoms. *J. Chem. Phys.* **86**, 7035–7040 (1987).

62. Hehre, W. J., Stewart, R. F. & Pople, J. A. Self-Consistent Molecular-Orbital Methods. I. Use of Gaussian Expansions of Slater-Type Atomic Orbitals. *J. Chem. Phys.* **51**, 2657 (1969).

63. Davidson, E. R. & Feller, D. Basis set selection for molecular calculations. *Chem. Rev.* **86**, 681–696 (1986).

64. Ditchfield, R., Hehre, W. J. & Pople, J. A. Self-Consistent Molecular-Orbital Methods. IX. An Extended Gaussian-Type Basis for Molecular-Orbital Studies of Organic Molecules. *J. Chem. Phys.* **54**, 724–728 (1971).

65. Schäfer, A., Horn, H. & Ahlrichs, R. Fully Optimized Contracted Gaussian-Basis Sets for Atoms Li to Kr. *J. Chem. Phys.* **97**, 2571–2577 (1992).

66. Schäfer, A., Huber, C. & Ahlrichs, R. Fully optimized contracted Gaussian basis sets of triple zeta valence quality for atoms Li to Kr. *J. Chem. Phys.* **100**, 5829 (1994).

67. Dunning Jr, T. H. Gaussian basis sets for use in correlated molecular calculations. I. The atoms boron through neon and hydrogen. *J. Chem. Phys.* **90**, 1007 (1989).

68. Pyykko, P. & Desclaux, J. P. Relativity and the Periodic System of Elements. *Acc. Chem. Res.* **12**, 276–281 (1979).

69. Norrby, L. J. Why is mercury liquid? Or, why do relativistic effects not get into chemistry textbooks? *J. Chem. Educ.* **68**, 110 (1991).

70. Anderson, C. D. The positive electron. *Phys. Rev.* **43**, 491–494 (1933).

71. Boys, S. F. & Bernardi, F. The calculation of small molecular interactions by the difference of separate total energies. Some procedures with reduced errors. *Mol. Phys.* **19**, 553–566 (1970).

72. Roothaan, C. C. J. New developments in molecular orbital theory. *Rev. Mod.*

Phys. **23**, 69–89 (1951).

73. Hall, G. G. The Molecular Orbital Theory of Chemical Valency. VIII. A Method of Calculating Ionization Potentials. *Proc. R. Soc. Ser. A* **205**, 541–552 (1951).

74. Hohenberg, P. & Kohn, W. Inhomogeneous Electron Gas. *Phys. Rev.* **136**, B864 (1964).

75. Kohn, W. & Sham, L. J. Self-consistent equations including exchange and correlation effects. *Phys. Rev.* **140**, A1133 (1965).

76. Perdew, J. P. & Schmidt, K. Jacob's ladder of density functional approximations for the exchange-correlation energy. *AIP Conf. Proc.* **577**, 1–20 (2001).

77. Perdew, J. P. & Zunger, A. Self-interaction correction to density-functional approximations for many-electron systems. *Phys. Rev. B* **23**, 5048–5079 (1981).

78. Ceperley, D. M. & Alder, B. J. Ground state of the electron gas by a stochastic method. *Phys. Rev. Lett.* **45**, 566–569 (1980).

79. Rappoport, D., Crawford, N. R. M., Furche, F. & Burke, K. Approximate Density Functionals: Which Should I Choose? in *Encyclopedia of Inorganic Chemistry* 159–172 (2009). doi:10.1002/0470862106.ia615.

80. Becke, A. D. Density-functional exchange-energy approximation with correct asymptotic behavior. *Phys. Rev. A* **38**, 3098–3100 (1988).

81. Perdew, J. P., Burke, K. & Ernzerhof, M. Generalized Gradient Approximation Made Simple. *Phys. Rev. Lett.* **77**, 3865–3868 (1996).

82. Perdew, J. *et al.* Atoms, molecules, solids, and surfaces: Applications of the generalized gradient approximation for exchange and correlation. *Phys. Rev. B* **46**, 6671–6687 (1992).

83. Hammer, B., K W Jacobsen & J K Norskov. Role of Nonlocal Exchange

Correlation in Activated Adsorption. *Phys. Rev. Lett.* **70**, 3971–3974 (1993).

84. Tao, J., Perdew, J. P., Staroverov, V. N. & Scuseria, G. E. Climbing the Density Functional Ladder: Non-Empirical Meta-Generalized Gradient Approximation Designed for Molecules and Solids. *Phys. Rev. Lett.* **91**, 146401 (2003).

85. Furche, F. & Perdew, J. P. The performance of semilocal and hybrid density functionals in 3d transition-metal chemistry. *J. Chem. Phys.* **124**, (2006).

86. Mardirossian, N. & Head-Gordon, M. Thirty years of density functional theory in computational chemistry: An overview and extensive assessment of 200 density functionals. *Mol. Phys.* **115**, 2315–2372 (2017).

87. Perdew, J. P., Ernzerhof, M. & Burke, K. Rationale for mixing exact exchange with density functional approximations. *J. Chem. Phys.* **105**, 9982 (1996).

88. Becke, A. D. Density-functional thermochemistry.III. The role of exact exchange. *J. Chem. Phys.* **98**, 5648 (1993).

89. Lee, C., Yang, W. & Parr, R. G. Development of the Colle-Salvetti correlation-energy formula into a functional of the electron density. *Phys. Rev. B* **37**, 785–789 (1988).

90. Vetere, V., Adamo, C. & Maldivi, P. Performance of the 'parameter free' PBE0 functional for the modeling of molecular properties of heavy metals. *Chem. Phys. Lett.* **325**, 99–105 (2000).

91. Furche, F. *et al.* Turbomole. *Wiley Interdiscip. Rev. Comput. Mol. Sci.* **4**, 91–100 (2014).

92. Sierka, M., Hogekamp, A. & Ahlrichs, R. Fast evaluation of the Coulomb potential for electron densities using multipole accelerated resolution of identity approximation. *J. Chem. Phys.* **118**, 9136–9148 (2003).

93. California, U. C. D. U. of. Potential Energy Surface.

https://chem.libretexts.org/Core/Physical_and_Theoretical_Chemistry/Quantum_Mechanics/11%3A_Molecules/Potential_Energy_Surface (2017).

94. Fletcher, R. *Practical Methods of Optimization*. (John Wiley & Sons, 2000).

95. TURBOMOLE v6.5 2013. http://www.turbomole.com (2013).

96. Schlegel, H. B. Geometry optimization. *Wiley Interdiscip. Rev. Comput. Mol. Sci.* **1**, 790–809 (2011).

97. Mulliken, R. S. Electronic population analysis on LCAO-MO molecular wave functions. I. *J. Chem. Phys.* **23**, 1833–1840 (1955).

98. Reed, Alan E.; Weinstock, Robert B.; Weinhold, F. Natural population analysis. *J. Chem. Phys.* **83**, 735–746 (1985).

99. McNaught, A. D. & Wilkinson, A. *IUPAC. Compendium of Chemical Terminology*. *IUPAC. Compendium of Chemical Terminology* (Blackwell Scientific Publications, 1997). doi:10.1351/goldbook.NT07080.

100. Glendening, E. D., Landis, C. R. & Weinhold, F. Natural bond orbital methods. *Wiley Interdiscip. Rev. Comput. Mol. Sci.* **2**, 1–42 (2012).

101. Berland, K. *et al.* van der Waals forces in density functional theory: a review of the vdW-DF method. *Reports Prog. Phys.* **78**, 66501 (2015).

102. Chen, J. Chen Research Groups, Computational Biochemistry & Biophysics. https://www.k-state.edu/bmb/labs/jc/research.html.

103. Kirkwood, J. G. On the Theory of Strong Electrolyte Solutions. *J. Chem. Phys.* **2**, 767 (1934).

104. Kirkwood, J. G. The Dielectric Polarization of Polar Liquids. *J. Chem. Phys.* **7**, 911 (1939).

105. Onsager, L. Electric moments of molecules in liquids. *J. Am. Chem. Soc.* **58**, 1486–1493 (1936).

106. Jacopo Tomasi, Benedetta Mennucci & Cammi, R. Quantum Mechanical Continuum Solvation Models. *Chem. Rev.* **105**, 2999–3093 (2005).

107. Klamt, A. & Schüürmann, G. COSMO: a new approach to dielectric screening in solvents with explicit expressions for the screening energy and its gradient. *J. Chem. Soc., Perkin Trans. 2* 799–805 (1993) doi:10.1039/P29930000799.

108. Truong, T. N. & Stefanovich, E. V. A new method for incorporating solvent effect into the classical, ab initio molecular orbital and density functional theory frameworks for arbitrary shape cavity. *Chem. Phys. Lett.* **240**, 253–260 (1995).

109. Barone, V. & Cossi, M. Quantum calculation of molecular energies and energy gradients in solution by a conductor solvent model. *J. Phys. Chem. A* **102**, 1995–2001 (1998).

110. Pye, C. C. & Ziegler, T. Regular article An implementation of the conductor-like screening model of solvation within the Amsterdam density functional package. *Theor. Chem. Acc.* **101**, 396–408 (1999).

111. Schäfer, A., Klamt, A., Sattel, D., Lohrenz, J. C. W. & Eckert, F. COSMO Implementation in TURBOMOLE: Extension of an efficient quantum chemical code towards liquid systems. *Phys. Chem. Chem. Phys.* **2**, 2187–2193 (2000).

112. Park, S. & Ruoff, R. S. Chemical methods for the production of graphenes. **4**, 45–47 (2009).

113. Jiang, X., Ma, Y., Li, J., Fan, Q. & Huang, W. Self-Assembly of Reduced Graphene Oxide into Three-Dimensional Architecture by Divalent Ion Linkage. *J. Phys. Chem. C* **114**, 22462–22465 (2010).

114. Ray, S. C. Chapter 2: Application and Uses of Graphene Oxide and Reduced Graphene Oxide. in *Applications of Graphene and Graphene-Oxide Based*

Nanomaterials 39–55 (2015). doi:10.1016/B978-0-323-37521-4.00002-9.

115. Pei, S. & Cheng, H. M. The reduction of graphene oxide. *Carbon N. Y.* **50**, 3210–3228 (2012).

116. Boukhvalov, D. W. & Katsnelson, M. I. Modeling of graphite oxide. *J. Am. Chem. Soc.* **130**, 10697–701 (2008).

117. Ghaderi, N. & Peressi, M. First-principle study of hydroxyl functional groups on pristine, defected graphene, and graphene epoxide. *J. Phys. Chem. C* **114**, 21625–21630 (2010).

118. Bond, C. S. On the Length of the Carbon-Carbon Single Bond' BY. (1959).

119. Tachikawa, H., Iyama, T. & Kawabata, H. Interaction of Hydroxyl OH Radical with Graphene Surface : A Density Functional Theory Study Interaction of Hydroxyl OH Radical with Graphene Surface : *Jpn. J. Appl. Phys.* **52**, 01AH01 (2013).

120. Lahaye, R. J. W. Ed. functional theory study of graphite oxide for different oxidation levels, Jeong, H. K., Park, C. Y. & Lee, Y. H. Density functional theory study of graphite oxide for different oxidation levels. *Phys. Rev. B - Condens. Matter Mater. Phys.* **79**, 1–8 (2009).

121. Hellweg, A., Hattig, C., Hofener, S. & Klopper, W. Optimized accurate auxiliary basis sets for RI-MP2 and RI-CC2 calculations for the atoms Rb to Rn. *Theor. Chem. Acc.* **117**, 587–597 (2007).

122. Chen, J. *et al.* Size distribution-controlled preparation of graphene oxide nanosheets with different C/O ratios. *Mater. Chem. Phys.* **139**, 8–11 (2013).

123. Kim, M. C., Hwang, G. S. & Ruoff, R. S. Epoxide reduction with hydrazine on graphene: A first principles study. *J. Chem. Phys.* **131**, 1–6 (2009).

124. Xu, S. C., Irle, S., Musaev, D. G. & Lin, M. C. Quantum Chemical Study of the

Dissociative Adsorption of OH and H2O on Pristine and Defected Graphite (0001) Surfaces: Reaction Mechanisms and Kinetics. *J. Phys. Chem. C* **111**, 1355–1365 (2007).

125. Boukhvalov, D. W. Modeling of hydrogen and hydroxyl group migration on graphene. *Phys. Chem. Chem. Phys.* **12**, 15367 (2010).

126. Boukhvalov, D. W. & Katsnelson, M. I. Modeling of graphite oxide. *J. Am. Chem. Soc.* **130**, 10697–10701 (2008).

127. Krishnamoorthy, K., Veerapandian, M., Yun, K. & Kim, S. The chemical and structural analysis of graphene oxide with different degrees of oxidation. *Carbon N. Y.* **53**, 38–49 (2012).

128. Yan, J. A. & Chou, M. Y. Oxidation functional groups on graphene: Structural and electronic properties. *Phys. Rev. B - Condens. Matter Mater. Phys.* **82**, 21–24 (2010).

129. Li, J. L. *et al.* Oxygen-driven unzipping of graphitic materials. *Phys. Rev. Lett.* **96**, 5–8 (2006).

130. Pandey, D., Reifenberger, R. & Piner, R. Scanning probe microscopy study of exfoliated oxidized graphene sheets. *Surf. Sci.* **602**, 1607–1613 (2008).

131. Ghaderi, N. & Peressi, M. First-principle study of hydroxyl functional groups on pristine, defected graphene, and graphene epoxide. *J. Phys. Chem. C* **114**, 21625–21630 (2010).

132. Lerf, A., He, H., Forster, M. & Klinowski, J. Structure of Graphite Oxide Revisited ǁ. *J. Phys. Chem. B* **102**, 4477–4482 (1998).

133. Weiwei Cai, Richard D. Piner, Frank J. Stadermann, Sungjin Park, Medhat A. Shaibat, Yoshitaka Ishii, Dongxing Yang, Aruna Velamakanni, Sung Jin An, Meryl Stoller, Jinho An, Dongmin Chen, R. S. R. Structural Characterization of C-Labeled Graphite Oxide. *Science (80-.).* **321**, 1815–1818 (2008).

134. Kudin, K. N. *et al.* Raman spectra of graphite oxide and functionalized graphene sheets. *Nano Lett.* **8**, 36–41 (2008).

135. Tchounwou, P. B., Yedjou, C. G., Patlolla, A. K. & Sutton, D. J. Heavy Metal Toxicity and the Environment. *Mol. Clin. Environ. Toxicol.* **101**, 133–164 (2012).

136. Jensen, S. E. & Nonbol, E. *Description of the Magnox Type of Gas Cooled Reactor (MAGNOX)*. *Nordic Nuclear Safety Research* vol. 2 (1998).

137. Tabish, T. A., Memon, F. A., Gomez, D. E., Horsell, D. W. & Zhang, S. A facile synthesis of porous graphene for efficient water and wastewater treatment. *Sci. Rep.* **8**, 1–14 (2018).

138. Zhao, G., Li, J., Ren, X., Chen, C. & Wang, X. Few-Layered Graphene Oxide Nanosheets As Superior Sorbents for Heavy Metal Ion Pollution Management. 10454–10462 (2011) doi:10.1021/es203439v.

139. Zhao, G. *et al.* Removal of Pb(ii) ions from aqueous solutions on few-layered graphene oxide nanosheets. *Dalt. Trans.* **40**, 10945 (2011).

140. Sitko, R. *et al.* Adsorption of divalent metal ions from aqueous solutions using graphene oxide. *Dalton Trans.* **42**, 5682–9 (2013).

141. Kumar, M. & Puri, A. A review of permissible limits of drinking water. *Indian J. Occup. Environ. Med.* **16**, 40–44 (2012).

142. Anantharaman, K., Shivakumar, V. & Saha, D. Utilisation of thorium in reactors. *J. Nucl. Mater.* **383**, 119–121 (2008).

143. Romanchuk, A. Y., Kuzenkova, A. S., Slesarev, A. S., Tour, J. M. & Kalmykov, S. N. Cs(I) and Sr(II) Sorption onto Graphene Oxide. *Solvent Extr. Ion Exch.* **34**, 594–602 (2016).

144. Yang, S. T. *et al.* Folding/aggregation of graphene oxide and its application in

Cu2+ removal. *J. Colloid Interface Sci.* **351**, 122–127 (2010).

145. Zhao, G., Li, J., Ren, X., Chen, C. & Wang, X. Few-layered graphene oxide nanosheets as superior sorbents for heavy metal ion pollution management. *Environ. Sci. Technol.* **45**, 10454–10462 (2011).

146. Showalter, A. R. *et al.* Sorption mechanisms of metals to graphene oxide. *J. Phys. Conf. Ser.* **712**, 012094 (2016).

147. Zhao, G. *et al.* Removal of Pb(II) ions from aqueous solutions on few-layered graphene oxide nanosheets. *Dalton Trans.* **40**, 10945–52 (2011).

148. Minitha, C. R., Lalitha, M., Jeyachandran, Y. L., Senthilkumar, L. & Rajendra Kumar, R. T. Adsorption behaviour of reduced graphene oxide towards cationic and anionic dyes: Co-action of electrostatic and π – π interactions. *Mater. Chem. Phys.* **194**, 243–252 (2017).

149. Yang, S. *et al.* Investigation of 90 Sr (II) sorption onto graphene oxides studied by macroscopic experiments and theoretical calculations. *J. Radioanal. Nucl. Chem.* **308**, 721–732 (2016).

150. Sun, Y., Wang, Q., Chen, C., Tan, X. & Wang, X. Interaction between Eu(III) and graphene oxide nanosheets investigated by batch and extended X-ray absorption fine structure spectroscopy and by modeling techniques. *Environ. Sci. Technol.* **46**, 6020–7 (2012).

151. Pan, N. *et al.* Removal of Th4+ ions from aqueous solutions by graphene oxide. *J. Radioanal. Nucl. Chem.* **298**, 1999–2008 (2013).

152. Ye, F. & Tang, Y. The modeling evidences for Th(IV) sorption on graphene oxide. *J. Radioanal. Nucl. Chem.* **310**, 565–571 (2016).

153. Zhao, G. *et al.* Preconcentration of U(VI) ions on few-layered graphene oxide nanosheets from aqueous solutions. *Dalt. Trans.* **41**, 6182 (2012).

154. Wang, C. L., Li, Y. & Liu, C. L. Sorption of uranium from aqueous solutions with graphene oxide. *J. Radioanal. Nucl. Chem.* **304**, 1017–1025 (2015).

155. Li, Z. *et al.* Uranium(VI) adsorption on graphene oxide nanosheets from aqueous solutions. *Chem. Eng. J.* **210**, 539–546 (2012).

156. Wilkins, E. & Yang, Q. Comparison of the heavy metal removal efficiency of biosorbents and granular activated carbons. *J. Environ. Sci. Heal. Part A Environ. Sci. Eng. Toxicol.* **31**, 2111–2128 (1996).

157. An, H. K., Park, B. Y. & Kim, D. S. Crab shell for the removal of heavy metals from aqueous solution. *Water Res.* **35**, 3551–3556 (2001).

158. Li, Y.-H. *et al.* Competitive adsorption of Pb2+, Cu2+ and Cd2+ ions from aqueous solutions by multiwalled carbon nanotubes. *Carbon N. Y.* **41**, 2787–2792 (2003).

159. Bosso, S. . & Enzweiler, J. Evaluation of heavy metal removal from aqueous solution onto scolecite. *Water Res.* **36**, 4795–4800 (2002).

160. Yang, S. *et al.* Competitive adsorption of Pb(II), Ni(II), and Sr(II) ions on graphene oxides: A combined experimental and theoretical study. *Chempluschem* **80**, 480–484 (2015).

161. Yu, Q., Matheickal, J. T., Yin, P. & Kaewsarn, P. Heavy metal uptake capacities of common marine macro algal biomass. *Water Res.* **33**, 1534–1537 (1999).

162. Rao, M. M., Ramana, D. K., Seshaiah, K., Wang, M. C. & Chien, S. W. C. Removal of some metal ions by activated carbon prepared from Phaseolus aureus hulls. *J. Hazard. Mater.* **166**, 1006–1013 (2009).

163. Xu, D., Tan, X., Chen, C. & Wang, X. Removal of Pb(II) from aqueous solution by oxidized multiwalled carbon nanotubes. *J. Hazard. Mater.* **154**, 407–416 (2008).

164. Rafatullah, M., Sulaiman, O., Hashim, R. & Ahmad, A. Adsorption of copper (II), chromium (III), nickel (II) and lead (II) ions from aqueous solutions by meranti sawdust. *J. Hazard. Mater.* **170**, 969–977 (2009).

165. Nassar, N. N. Rapid removal and recovery of Pb(II) from wastewater by magnetic nanoadsorbents. *J. Hazard. Mater.* **184**, 538–546 (2010).

166. Wang, S., Dong, Y., He, M., Chen, L. & Yu, X. Characterization of GMZ bentonite and its application in the adsorption of Pb(II) from aqueous solutions. *Appl. Clay Sci.* **43**, 164–171 (2009).

167. Bouby, M. *et al.* Sorption of Eu(III) onto titanium dioxide: Measurements and modeling. *J. Colloid Interface Sci.* **350**, 551–562 (2010).

168. Fan, Q. H. *et al.* Adsorption of humic acid and Eu(III) to multi-walled carbon nanotubes: Effect of pH, ionic strength and counterion effect. *Radiochim. Acta* **97**, 141–148 (2009).

169. Shao, D. D. *et al.* Removal of Eu(III) from aqueous solution using ZSM-5 zeolite. *Microporous Mesoporous Mater.* **123**, 1–9 (2009).

170. Sun, Y. *et al.* Comparison of U(VI) removal from contaminated groundwater by nanoporous alumina and non-nanoporous alumina. *Sep. Purif. Technol.* **83**, 196–203 (2011).

171. Carboni, M., Abney, C. W., Taylor-Pashow, K. M. L., Vivero-Escoto, J. L. & Lin, W. Uranium Sorption with Functionalized Mesoporous Carbon Materials. *Ind. Eng. Chem. Res.* **52**, 15187–15197 (2013).

172. Goldberg, S., Criscenti, L. J., Turner, D. R., Davis, J. A. & Cantrell, K. J. Adsorption–Desorption Processes in Subsurface Reactive Transport Modeling. *Vadose Zo. J.* **6**, 407 (2007).

173. Li, Y., Wang, C. & Guo, Z. Sorption of thorium (IV) from aqueous solutions by graphene oxide. *J. Radioanal. Nucl. Chem.* **299**, 1683–1691 (2014).

174. Noh, J. S. & Schwarz, J. A. Effect of HNO 3 treatment on the surface acidity of activated carbons. *Carbon N. Y.* **28**, 675–682 (1990).

175. Konkena, B. & Vasudevan, S. Understanding aqueous dispersibility of graphene oxide and reduced graphene oxide through p K a measurements. *J. Phys. Chem. Lett.* **3**, 867–872 (2012).

176. Chowdhury, I., Duch, M. C., Mansukhani, N. D., Hersam, M. C. & Bouchard, D. Colloidal properties and stability of graphene oxide nanomaterials in the aquatic environment. *Environ. Sci. Technol.* **47**, 6288–6296 (2013).

177. Madadrang, C. J. *et al.* Adsorption Behaviour of EDTA-Graphene Oxide for Pb(II) Removal. *ACS Appl. Mater. Interfaces* **4**, 1186–1193 (2012).

178. Bai, Z. Q. *et al.* Interactions between Th(IV) and graphene oxide: experimental and density functional theoretical investigations. *Rsc Adv.* **4**, 3340–3347 (2014).

179. Wu, Q. Y. *et al.* Understanding the interactions of neptunium and plutonium ions with graphene oxide: Scalar-relativistic DFT investigations. *J. Phys. Chem. A* **118**, 10273–10280 (2014).

180. Sun, Y. *et al.* Adsorption and Desorption of U(VI) on Functionalized Graphene Oxides: A Combined Experimental and Theoretical Study. *Environ. Sci. Technol.* **49**, 4255–4262 (2015).

181. Wang, X. *et al.* High sorption of U(VI) on graphene oxides studied by batch experimental and theoretical calculations. *Chem. Eng. J.* **287**, 448–455 (2016).

182. Wu, Q. Y. *et al.* Understanding the bonding nature of uranyl ion and functionalized graphene: A theoretical study. *J. Phys. Chem. A* **118**, 2149–2158 (2014).

183. Cheng, W. *et al.* Mutual effect of U(VI) and Sr(II) on graphene oxides: evidence from EXAFS and theoretical calculations. *Environ. Sci. Nano* **4**, 1124–1131 (2017).

184. Yusan, S. (Doyurum) & Akyil, S. Sorption of uranium(VI) from aqueous solutions by akaganeite. *J. Hazard. Mater.* **160**, 388–395 (2008).

185. Sheng, L. & Fein, J. B. Uranium reduction by Shewanella oneidensis MR-1 as a function of NaHCO 3 concentration: Surface complexation control of reduction kinetics. *Environ. Sci. Technol.* **48**, 3768–3775 (2014).

186. Wang, X., Chen, Z. & Yang, S. Application of graphene oxides for the removal of Pb(II) ions from aqueous solutions: Experimental and DFT calculation. *J. Mol. Liq.* **211**, 957–964 (2015).

187. Koh, Y. W., Westerman, K. & Manzhos, S. A computational study of adsorption and vibrations of UF6 on graphene derivatives: Conditions for 2D enrichment. *Carbon N. Y.* **81**, 800–806 (2015).

188. Austin, J. P., Burton, N. A., Hillier, I. H., Sundararajan, M. & Vincent, M. A. Which density functional should be used to study actinyl complexes? *Phys. Chem. Chem. Phys.* **11**, 1143–1145 (2009).

189. Sun, Y., Shao, D., Chen, C., Yang, S. & Wang, X. Highly efficient enrichment of radionuclides on graphene oxide-supported polyaniline. *Environ. Sci. Technol.* **47**, 9904–10 (2013).

190. Liu, Q. & Liu, Y. Distribution of Pb(II) species in aqueous solutions. *J. Colloid Interface Sci.* **268**, 266–269 (2003).

191. Eichkorn, K., Weigend, F., Treutler, O. & Ahlrichs, R. Auxiliary basis sets for main row atoms and transition metals and their use to approximate Coulomb potentials. *Theor. Chem. Acc.* **97**, 119–124 (1997).

192. Weigend, F. & Ahlrichs, R. Balanced basis sets of split valence, triple zeta valence and quadruple zeta valence quality for H to Rn: Design and assessment of accuracy. *Phys. Chem. Chem. Phys.* **7**, 3297–3305 (2005).

193. Kaupp, M., Schleyer, P. v. R., Stoll, H. & Preuss, H. Pseudopotential approaches

to Ca, Sr, and Ba hydrides. Why are some alkaline earth MX_2 compounds bent? *J. Chem. Phys.* **94**, 1360–1366 (1991).

194. Dolg, M., Stoll, H. & Preuss, H. Energy-adjusted *ab initio* pseudopotentials for the rare earth elements. *J. Chem. Phys.* **90**, 1730–1734 (1989).

195. Dolg, M., Stoll, H. & Preuss, H. A combination of quasirelativistic pseudopotential and ligand field calculations for lanthanoid compounds. *Theor. Chim. Acta* **85**, 441–450 (1993).

196. Cao, X., Dolg, M. & Stoll, H. Valence basis sets for relativistic energy-consistent small-core actinide pseudopotentials. *J. Chem. Phys.* **118**, 487–496 (2003).

197. Küchle, W., Dolg, M., Stoll, H. & Preuss, H. Energy-adjusted pseudopotentials for the actinides. Parameter sets and test calculations for thorium and thorium monoxide. *J. Chem. Phys.* **100**, 7535–7542 (1994).

198. Sure, R., Brandenburg, J. G. & Grimme, S. Small Atomic Orbital Basis Set First-Principles Quantum Chemical Methods for Large Molecular and Periodic Systems: A Critical Analysis of Error Sources. *ChemistryOpen* **5**, 94–109 (2016).

199. Schreckenbach, G. & Shamov, G. A. Theoretical Actinide Molecular Science. *Acc. Chem. Res.* **43**, 19–29 (2010).

200. Wang, J., Becke, A. D. & Smith, V. H. Evaluation of $\langle S2 \rangle$ in restricted, unrestricted Hartree-Fock, and density functional based theories. *J. Chem. Phys.* **102**, 3477–3480 (1995).

201. Cohen, A. J., Tozer, D. J. & Handy, N. C. Evaluation of $\langle \hat{S}2 \rangle$ in density functional theory. *J. Chem. Phys.* **126**, 214104 (2007).

202. Wittbrodt, J. M. & Schlegel, H. B. Some reasons not to use spin projected density functional theory. *J. Chem. Phys.* **105**, 6574–6577 (1996).

203. Kerridge, A. & Kaltsoyannis, N. Quantum Chemical Studies of the Hydration of Sr2+ in Vacuum and Aqueous Solution. *Chem. Eur. J.* **17**, 5060–5067 (2011).

204. Makkos, E., Kerridge, A. & Kaltsoyannis, N. The importance of second shell effects in the simulation of hydrated Sr2+ hydroxide complexes. *Dalt. Trans.* **44**, 11572–11581 (2015).

205. Buzko, V., Sukhno, I. & Buzko, M. Ab Initio and DFT Study of La3+ Hydration. *Int. J. Quantum Chem.* **107**, 2353–2360 (2007).

206. Buzko, V. Y., Sukhno, I. V., Buzko, M. B., Polushin, A. A. & Panyushkin, V. T. Study of the Structure and Stability of Aqua Complexes La(H2O)n (n = 8, 9) by Ab Initio Methods. *Russ. J. Inorg. Chem.* **53**, 1249–1255 (2008).

207. Allen, P. G., Bucher, J. J., Shuh, D. K., Edelstein, N. M. & Craig, I. Coordination chemistry of trivalent lanthanide and actinide ions in dilute and concentrated chloride solutions. *Inorg. Chem.* **39**, 595–601 (2000).

208. Yang, T., Tsushima, S. & Suzuki, A. Quantum mechanical and molecular dynamical simulations on thorium(IV) hydrates in aqueous solution. *J. Phys. Chem. A* **105**, 10439–10445 (2001).

209. Torapava, N., Persson, I., Eriksson, L. & Lundberg, D. Hydration and hydrolysis of thorium(IV) in aqueous solution and the structures of two crystalline thorium(IV) hydrates. *Inorg. Chem.* **48**, 11712–11723 (2009).

210. Ludwig, R. & Weinhold, F. Quantum cluster equilibrium theory of liquids: Freezing of QCE/3-21G water to tetrakaidecahedral 'bucky-ice'. *J. Chem. Phys.* **110**, 508–515 (1999).

211. Makkos, E. Computational investigations of the speciation of Sr 2+ in aqueous solution, and its interactions with the hydrated brucite (0001) surface. (2017).

212. Shannon, R. D. Revised effective ionic radii and systematic studies of interatomic distances in halides and chalcogenides. *Acta Crystallogr. Sect. A* **32**,

751–767 (1976).

213. Hladik, O., Bernhardt, G., Boessert, W. & Munze, R. Production of Fission 99Mo by Processing Irradiated Natural Uranium Targets. in *Fission Molybdenum for Medical Use* 65–81 (1987).

214. World Nuclear Association - Storage and Disposal of Radioactive Waste. http://www.world-nuclear.org/information-library/nuclear-fuel-cycle/nuclear-waste/storage-and-disposal-of-radioactive-waste.aspx (2018).

215. Feicht, P. & Eigler, S. Defects in Graphene Oxide as Structural Motifs. *ChemNanoMat* **4**, 244–252 (2018).

216. Gass, M. H. *et al.* Free-standing graphene at atomic resolution. *Nat. Nanotechnol.* **3**, 676–681 (2008).

217. Krasheninnikov, A. V., Lehtinen, P. O., Foster, A. S. & Nieminen, R. M. Bending the rules: Contrasting vacancy energetics and migration in graphite and carbon nanotubes. *Chem. Phys. Lett.* **418**, 132–136 (2006).

218. Meyer, J. C., Kisielowski, C., Erin, R., Rossell, M. D. & Crommie, M. F. Direct Imaging of Lattice Atoms and Topological Defects in Graphene Membranes Direct Imaging of Lattice Atoms and Topological Defects in Graphene Membranes. *Nano Lett.* **8**, 3582–3586 (2008).

219. Ugeda, M. M., Brihuega, I., Guinea, F. & Gómez-Rodríguez, J. M. Missing atom as a source of carbon magnetism. *Phys. Rev. Lett.* **104**, 1–4 (2010).

220. Tan, Y. W. *et al.* Graphene at the Edge. *Science (80-.).* **666**, 1705–1708 (2009).

221. Morimoto, N. *et al.* Real-Time, in Situ Monitoring of the Oxidation of Graphite: Lessons Learned. *Chem. Mater.* **29**, 2150–2156 (2017).

222. Eigler, S., Dotzer, C., Hirsch, A., Enzelberger, M. & Müller, P. Formation and decomposition of CO2intercalated graphene oxide. *Chem. Mater.* **24**, 1276–

1282 (2012).

223. Stone, A. J. & Wales, D. J. Theoretical Studies of Icosahedral C60 and Some Related Species. *Chem. Phys. Lett.* **128**, 501–503 (1986).

224. Iijima, S., Ichihashi, T. & Yoshinori, A. Pentagons, heptagons and negative curvature in graphite microtubule growth. *Nature* **356**, 776–778 (1992).

225. Roh, S. *et al.* Characteristic features of stone-wales defects in single-walled carbon nanotube; Adsorption, dispersion, and field emission. *J. Nanomater.* **2010**, (2010).

226. Podlivaev, a. I. & Openov, L. a. Dynamics of the Stone-Wales defect in graphene. *Phys. Solid State* **57**, 820–824 (2015).

227. Li, L., Reich, S. & Robertson, J. Defect energies of graphite: Density-functional calculations. *Phys. Rev. B* **72**, 184109 (2005).

228. Ma, J., Alfe, D., Michaelides, A. & Wang, E. Stone-Wales defects in graphene and other planar sp2-bonded materials. *Phys. Rev. B* **80**, 033407 (2009).

229. Nascimento, A. J. M. & Nunes, R. W. Lubrication of Stone-Wales transformations in graphene by hydrogen and hydroxyl functional groups. *Nanotechnology* **24**, (2013).

230. Boukhvalov, D. W. & Katsnelson, M. I. Chemical functionalization of graphene with defects. (2008) doi:10.1021/nl802234n.

231. Sun, Y., Wang, Q., Chen, C., Tan, X. & Wang, X. Interaction between Eu(III) and Graphene Oxide Nanosheets Investigated by Batch and Extended X-ray Absorption Fine Structure Spectroscopy and by Modeling Techniques. (2012) doi:10.1021/es300720f.

232. Okamoto, Y., Mochizuki, Y. & Tsushima, S. Theoretical study of hydrolysis reactions of tetravalent thorium ion. *Chem. Phys. Lett.* **373**, 213–217 (2003).